RESEARCH INTO THE INTERPRETATION OF DEFORMATION MEASURED BY EXTENSOMETERS

A Thesis Submitted to the College of

Graduate and Postdoctoral Studies

In Partial Fulfillment of the Requirements

For the Degree of Master of Science

In the Department of Civil, Geological and Environmental Engineering

University of Saskatchewan

Saskatoon

By

DYLAN SHACKER

PERMISSION TO USE

In presenting this thesis in partial fulfillment of the requirements for a Postgraduate degree from the University of Saskatchewan, I agree that the Libraries of this University may make it freely available for inspection. I further agree that permission for copying of this thesis in any manner, in whole or in part, for scholarly purposes may be granted by the professor or professors who supervised my thesis work or, in their absence, by the Head of the Department or the Dean of the College in which my thesis work was done. It is understood that any copying or publication or use of this thesis or parts thereof for financial gain shall not be allowed without my written permission. It is also understood that due recognition shall be given to me and to the University of Saskatchewan in any scholarly use which may be made of any material in my thesis.

Requests for permission to copy or to make other uses of materials in this thesis/dissertation in whole or part should be addressed to:

Head of the Department of Civil, Geological and Environmental Engineering
University of Saskatchewan
3B48 Engineering Building, 57 Campus Drive
Saskatoon, Saskatchewan S7N 5A9
Canada

OR

Dean
College of Graduate and Postdoctoral Studies
University of Saskatchewan
116 Thorvaldson Building, 110 Science Place
Saskatoon, Saskatchewan S7N 5C9
Canada

ABSTRACT

This thesis interprets data collected by extensometers installed to monitor underground excavations in open stope mining environments. The interpretation of the extensometer data includes assessment of the measurements to determine the validity of the data and if the measurements are suitable for use in estimation of stress and/ or a geometry of potential instability.

A new method for estimating a change in stress based on the elastic properties of the rock mass and the measured strains is introduced and applied. This method can be applied to estimate the pre-mining stress, normal to an opening, based on the normal strain caused by mining.

The recently developed Strain Effective Radius Factor (SERF) method for estimating a potential geometry of instability is reviewed and applied to additional datasets. The SERF method is an empirical tool that can be applied to predict unstable stope hanging wall geometries based on trends in strain measurements. This is a useful development for interpreting the meaning of increasing hanging wall deformation and can provide insights into potential risks of continued stope excavation.

This research interprets historic instrumentation datasets from two mining operations and introduces and analyzes a new instrumentation dataset from the Santoy mine in northern Saskatchewan. The two historical instrumentation datasets included stopes with hanging wall instability allowing the estimation of both pre-mining stress and a geometry of instability. The new instrumentation dataset monitored hanging walls without any recorded instability, therefore only the pre-mining stress could be estimated. It was found that pre-mining stress could be reasonably estimated. A variation to the SERF method is proposed to improve the prediction of a geometry of instability and appears promising based on its application to a limited number of case histories.

ACKNOWLEDGMENTS

First and foremost, I would like to recognize and thank Dr. Doug Milne for his wit and dogged patience during my studies, research, and our many editing sessions. I would also like to thank Donna Beneteau for her support and encouragement as well as Brandon Fell and Michael van Dyke for their contributions.

I would like to thank NSERC and SSR Mining for their financial support of my research. In particular I would like to thank the staff at Seabee Gold Operation for allowing me access to the mine to collect data, keeping me safe while I was on site, and answering a wide array of questions both during and after primary data collection.

Last but certainly not least, I thank my wife for her continuous support and encouragement throughout my studies. I can imagine having completed this work without her.

TABLE OF CONTENTS

LIST OF FIGURES

LIST OF TABLES

NOTATION

a = Radius of Opening

A = Fukuzono Slope Constant

CHILE = Continuous, homogenous, isotropic, linear elastic

CMS = Cavity Monitoring System

d = Distance to Point from the Surface of a Sphere

D_e = Equivalent Dimension / Span

E = Elastic Modulus

E_i = Reference Voltage

ELOS = Equivalent Linear Overbreak / Slough

ELRD = Equivalent Linear Relaxation Depth

E_o = Voltage Drop

ERF = Effective Radius Factor

ERF_f = Effective Radius Factor of failure

ERF_p = Predicted Effective Radius Factor of instability

ESR = Excavation Support Ratio

Extensometer = Multi Point Borehole Extensometer

Factor A = Stress Factor

Factor B = Joint Defect Orientation Factor

Factor C = Gravity Factor

FEM = Finite Element Model

G = Shear Modulus

HR = Hydraulic Radius

J_a = Joint Set Alteration Number

J_n = Joint Set Number

J_r = Joint Set Roughness

J_v = Number of Joints Visible per Unit Volume

J_w = Joint Water Reduction Factor

K = Ratio between the Horizontal and Vertical Stresses

Modified SERF = Modified Strain Effective Radius Factor

MRMR = Modified Rock Mass Rating

n = Number of Distances

N = Stability Number

N' = Modified Stability Factor

NGI = Norwegian Geotechnical Institute

OOA = Onset of Acceleration

Q = Tunnel Quality Index

Q' = Modified Tunnel Quality Index

r = Distance to Point from the Centre of a Sphere

r_1 = Distance to Closest Point (1) from the Centre of a Sphere

r_2 = Distance to Furthest Point (2) from the Centre of a Sphere

RF = Radius Factor

RF_f = Radius Factor of failure

RF_p = Predicted Radius Factor of Instability

R_h = Harmonic Average

RMR = Rock Mass Rating

RQD = Rock Quality Designation

r_θ = Distance from the Surface Centre to the Abutment

S = Shape Factor

SERF = Strain Effective Radius Factor

SGO = Seabee Gold Operation

SRF = Stress Reduction Factor

t = Time of Measurement

TARP = Trigger Action Response Plan

t_f = Time of Failure

TU = Trend Update

u_r = Radial Displacement

ur_1 = Radial Displacement of Closest Point (1) to the Centre of the Circle

ur_2 = Radial Displacement of Furthest Point (2) to the Centre of the Circle

u_θ = Tangential Displacement

V_{-1} = Inverse Velocity

z = Depth Below Surface

α = Fukuzono Slope Constant

γ = Unit Weight

$\Delta\sigma_n$ = Induced Stress Change Normal to the Opening

$\Delta\sigma_z$ = Induced Stress Change Along Tunnel Axis

$\varepsilon_{a\text{-}b}$ = Strain between two Points

ε_n = Induced Strain Normal to the Opening

ε_r = Radial Strain

ε_{rr} = Induced Radial Strain

ε_z = Induced Axial Strain Along Tunnel Axis

θ = Counter-Clockwise Angle to Point from the orientation of Kσ

θ = Angle Interval of Distance Measurements

ν = Poisson's Ratio

σ_1 = Largest Principal Compressive Stress

σ_3 = Smallest Principal Compressive Stress

σ_h = Horizontal Stress

σ_n = Normal Stress

σ_{pre} = Pre-mining Stress

σ_{rr} = Induced Radial Stress

$\sigma_{r\theta}$ = Induced Tangential Stress

σ_v = Vertical Stress

$\sigma_{\theta\theta}$ = Induced Tangential Stress

1 INTRODUCTION

1.1 Background

This thesis interprets data collected from extensometers installed to monitor underground excavations in open stope mining environments and focussed on two main areas. Research was conducted to estimate the stress change due to stope hanging wall relaxation. The objective was to quantify the pre-mining stress normal to stope hanging walls. An existing methodology was also tested and improved for monitoring the strain response in stope hanging walls as stope excavation progresses to predict instability.

Currently, the measurement of stresses in mining environments is seldom conducted due to cost. The measurement of stress change can be conducted at less cost; however, the initial stress state is still difficult to estimate with any accuracy. As underground mining activity continues, stresses are redistributed around openings leading to stress concentration and zones of relaxation which can induce instability. Realistic modelling, to determine zones of stress driven potential instability, require improved inputs to reasonably represent stress conditions in underground mines.

Historically the design of an open stope's final geometry is done using empirical or numerical tools. Following the completion of mining of the open stope, the stability result of either stable or unstable may be added to a database which can be used to adjust future designs of open stope geometries. Although open stopes may be instrumented to monitor deformation and strain, there are limited methods for interpreting the collected data or for using the data to predict when instability might occur. The Strain Effective Radius Factor (SERF) method is a new method that has been proposed as an empirical means of predicting a geometry at which instability might occur based on monitoring accelerating strain in the open stope hanging wall. The predicted geometry of instability provides information that operations can use to adjust the final geometry of the monitored open stope. This thesis tests the validity of this new method on existing data bases, suggests revisions to the technique, and includes the design and interpretation of a new monitoring program at Santoy mine to check the application of the revised method.

Figure 1-1 illustrates a generic underground mining operation and is presented to introduce several terms that will be used throughout the thesis. A stope refers to an underground excavation, with a height and width that are generally larger than a normal development tunnel. The stope that is

bounded in cross section view by the back, hanging wall, floor, and footwall (Figure 1-1a). Sublevel sills are located within the open stope with the overcut sill serving as the access point for drilling and blasting of the open stope and the undercut sill providing access to the stope for the removal of broken ore (mucking). Sills are generally accessed from the haulage drift through a crosscut (Figure 1-1b).

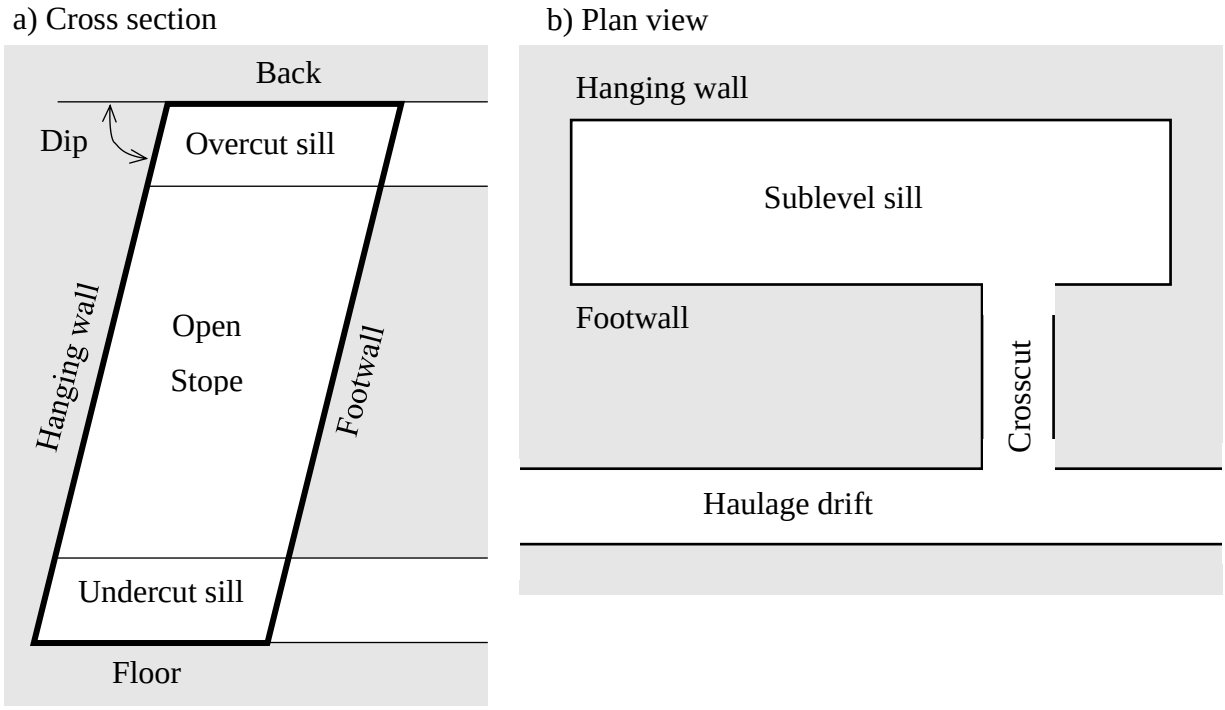

Figure 1-1: Labelled schematic (a) cross section and (b) plan view of an open stope.

1.1.1 Pre-mining

The pre-mining stress state refers to the stress state of the rock mass prior to any excavation and is expressed as the magnitudes and directions of the 3 orthogonal principal stresses. The principal stresses often consist of a vertical, or sub-vertical stress related to the depth of overlying rock, and two horizontal or sub-horizontal stresses which are related to the vertical stress and other possible factors. Brady and Brown (2006) suggest some of the factors influencing the in-situ stress state are the current surface topography, erosion of the historic surface topography, the presence and melting of glaciers, residual stress from chemical or physical processes, inclusions or intrusions of younger rock formations, tectonic activity, and fractures and discontinuities within the rock mass.

When stress measurements are not available, the vertical stress (σ_v) can be estimated based on the average unit weight of the overlying rock (γ) and the depth below surface (z).

$$\sigma_v = \gamma z \qquad \text{EQUATION 1-1}$$

Herget (1987) compiled a database of 54 Canadian Shield stress measurements and developed equations for calculating the ratio between the horizontal and vertical stresses (K) at different depths. Using this K-ratio, the horizontal stresses acting at depth z can be used to estimate the horizontal stress (σ_h).

$$\sigma_h = K\sigma_v = K\gamma z \qquad \text{EQUATION 1-2}$$

1.2 Objectives of Research

The objective of this thesis is to assess if it is reasonable to estimate pre-mining stress normal to the stope hanging wall and to predict a geometry of instability, based on extensometer data. A process for assessing extensometer data for stress estimation and a revised methodology for predicting a geometry of instability is proposed. Analysis required a dataset that included extensometer measurements of hanging wall deformation from a mine with appropriate geology, records of blast times and geometries, and a hanging wall failure comparison to the predicted geometry of instability. Datasets including all of these elements were not readily available for analysis.

If the pre-mining stress can be reasonably estimated from extensometer data, this could justify increasing the number of stress measurements and measurement locations and provide improved data for numerical models. Additionally, since the required measurements can be extracted from instrumentation already installed to monitor open stopes, the additional cost related to interpreting the data would be minimal.

The SERF method is a new method that has only been applied to the back analysis of one open stope by Milne and Snell (2018). This thesis will apply the SERF method to additional open stopes to test the validity of the predicted geometries of instability and investigate the theory supporting the method.

1.3 Thesis Overview

The objective of this thesis is to provide a methodology to estimate the stress normal to a stope hanging wall prior to mining, based on recorded deformations, and predict possible underground open stope instability. Section 2 reviews stress theory, stope design, rock mass deformation, instrumentation, opening geometry, empirical methods for predicting instability, and response plans for approaching instability. Section 3 applies and expands upon the concepts introduced in Section 2 and details the process that is applied to assess extensometer data for measurement reliability, stress estimation, and estimation of instability using the SERF method.

Sections 4 and 5 apply the approach outlined in Section 3 to extensometer datasets. Sections 4 reviews historical data from the 1990s collected from Brunswick Mine (Canada) and Mount Isa Mine (Australia) to estimate pre-mining stresses and compare predicted and actual unstable stope geometries. Section 5 describes the design and implementation of a new instrumentation program at Santoy Mine (Canada) and the resulting estimation of pre-mining stress and prediction of geometries of instability. The thesis conclusions can be found in Section 6.

2 LITERATURE REVIEW

2.1 Open Stope Mining

There are a wide range of underground mining methods that can be applied to extract ore from a deposit. Open stoping refers to a category of unsupported underground mining methods that are characterized by:

- being a non-entry mining method. Once production begins, workers are restricted to operate within the sublevel sill and are not permitted within the open stope itself.
- following production blasts, the broken ore (muck) is removed to create an open geometry that remains open until the excavation is completed. Once the final geometry is reached following the completion of excavation, the stope may be backfilled.
- the open geometry is designed to be stable. No caving or significant hanging wall spalling or sloughing are expected for the final geometry.

Various forms of open stope mining can be applied depending on the orebody and geological conditions. Due to the unsupported nature of open stopes, the rock mass generally needs to have a strength of at least "fair" (Potvin, 1988) and the more competent the rock mass, the larger the opening geometry can be. Larger opening geometries are generally preferred as they can decrease both the amount of development needed and the overall cost of extracting the ore.

Depending on the orebody width and the allowable back span for sills, open stopes can be mined in either a longitudinal or transverse direction. In a longitudinal orientation, sill development is generally aligned with the orebody strike with the sill width approximately equalling the orebody width (Figure 2-1a). In a transverse orientation, sill development is generally aligned perpendicular to the orebody strike with the sill width defined by the stable back dimension (Figure 2-1b). A transverse orientation involves the mining of primary and secondary stopes where the primary stopes must be filled with cemented backfill prior to excavation of the secondary stopes.

Depending on the strength of the rock mass and the stress environment, pillars and or backfill may be required to stabilize the opening and allow for the extraction of subsequent stopes within the orebody. Open stopes may either be left open with no pillars, left open with pillars, or backfilled to enable pillar recovery at a later date (Potvin, 1988).

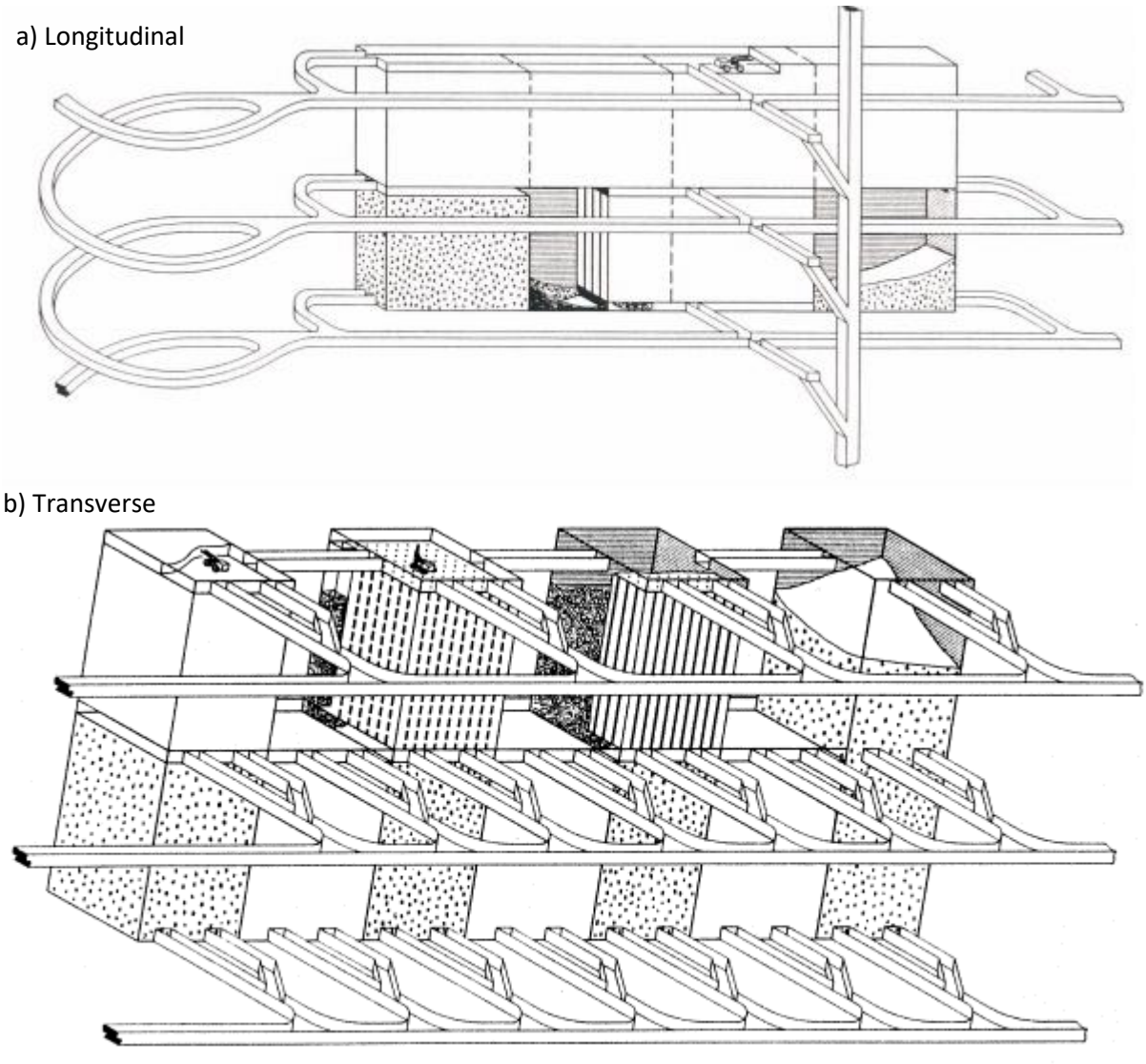

Figure 2-1: Isometric schematic of (a) longitudinal and (b) transverse open stope mining (from Potvin and Hudyma, 2000; after Potvin and Hudyma, 1989).

2.2 Rock Mass Deformation

Deformation often serves as an indirect measure used for calculating stresses and strains around underground openings. By monitoring deformation, analyses can be completed to provide information about the stability of the rock mass. Historically, deformation data has been collected to monitor approaching instability and for design optimization with numerical modelling (Brady and Brown, 1985). Although extensively collected, there is a lack of guidance for what constitutes stable deformations in underground operations.

2.2.1 Stages of ground response

As sequential production blasting and mucking of an underground orebody progresses, the ground response of the stope hanging wall varies based upon the size of the opening, the material properties of the rock mass, and the local stress conditions. The analysis of deformation data collected from extensometers can provide insight into the type of deformation that the hanging wall is undergoing at the location of the extensometer.

The term "undercutting" refers to when the mining front passes the location that extensometer anchors are projected onto the stope hanging wall. The result of undercutting is that the extensometer anchor locations are no longer supported by the in-situ rock mass and stresses cannot pass through the open stope resulting in stress redistribution. Figure 2-2 illustrates the undercutting of an extensometer by a horizontal advance.

When extensometer anchors are projected onto the stope hanging wall, they are projected in a direction normal to the stope hanging wall. This projection plane is referred to as a true longitudinal view or section. A cross section showing the projection of extensometer anchors onto the stope hanging wall is shown along with the resulting true longitudinal view of the stope hanging wall in Figure 2-2.

Milne et al. (1996) suggest that after undercutting, the initial deformation measured by the extensometer is associated with the redistribution of stresses around the opening and the resulting elastic relaxation. As the geometry of the open stope increases, the continued deformation measured by the extensometer may be a result of the dilation of fractures within the rock mass. A decrease in the elastic modulus of the rock mass may occur which, if it continues, could result in the rock mass starting to deform with a discontinuum mechanism, such as arching.

(a) Prior to mining by extensometer

Longitudinal Section

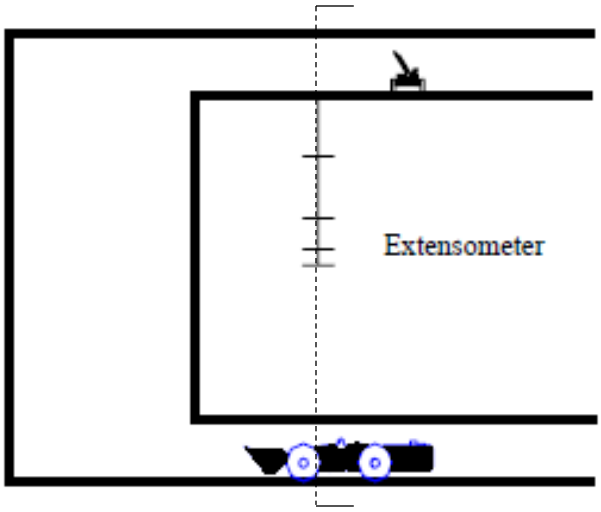

Cross Section A – A’

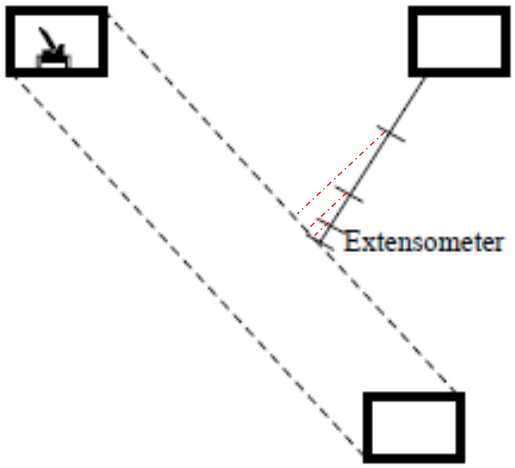

(b) After mining by extensometer

Longitudinal Section

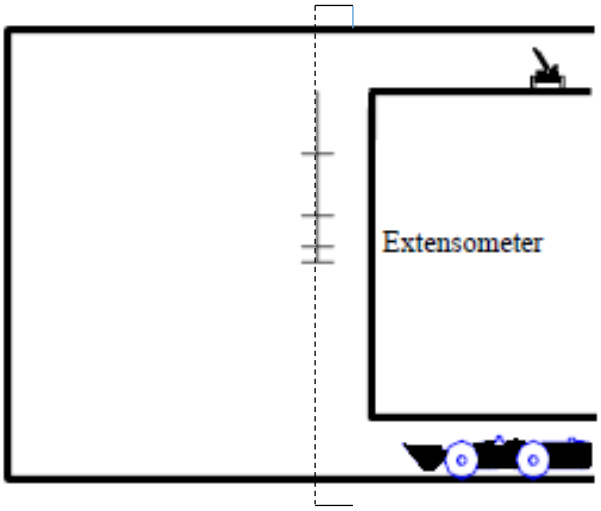

Cross Section A – A’

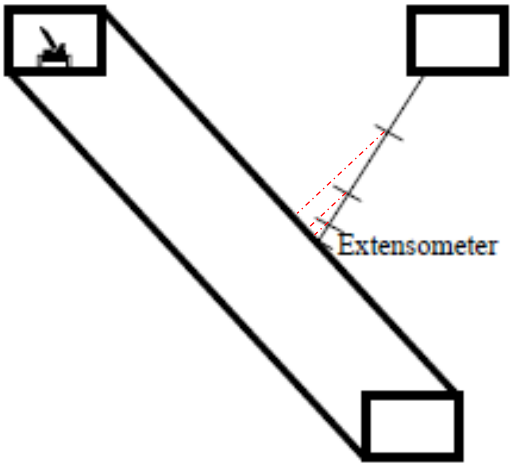

Figure 2-2: Schematic showing a stope hanging wall being monitored by an extensometer both before (a) and after (b) the extensometer is undercut or “mined by” for horizontal stope excavation (after Milne, 1997).

The variations in ground response to increases in the size of the stope and hanging wall geometry were divided into four idealized stages by Milne (1997) (Figure 2-3). Eventually, the result is an opening that is either stable or fails. The identification of the idealized stage of deformation from strain measurements provides an indication of the way that the stope hanging wall is behaving. While these stages of ground response can occur anywhere on the stope hanging wall, this thesis refers to the response of the rock mass at the location of an extensometer.

In Figure 2-3, Stage 1 is the elastic compressive response as the excavation approaches the extensometer location, prior to undercutting, and stresses are shed around the opening, concentrating in the abutment containing the extensometer. Stage 2 is the elastic extension of the rock mass following undercutting of the extensometer location as the rock mass above the excavation is destressed. Stage 3 is the non-linear extension of the rock mass as the geometry of the stope hanging wall continues to increase and the hanging wall continues to relax and "sag" into the open stope. Stage 4 is separated to describe the two eventual conditions for the stope hanging wall. Stage 4a relates to a hanging wall that has stabilized, either reaching a natural equilibrium or through the addition of backfill or some other stabilizing influence. Stage 4b shows a failed hanging wall where the non-linear extension continues to the point of failure. It is possible for a hanging wall failure to occur during stope excavation or at some point after stope excavation has concluded if the hanging wall geometry is increased beyond what local conditions can support.

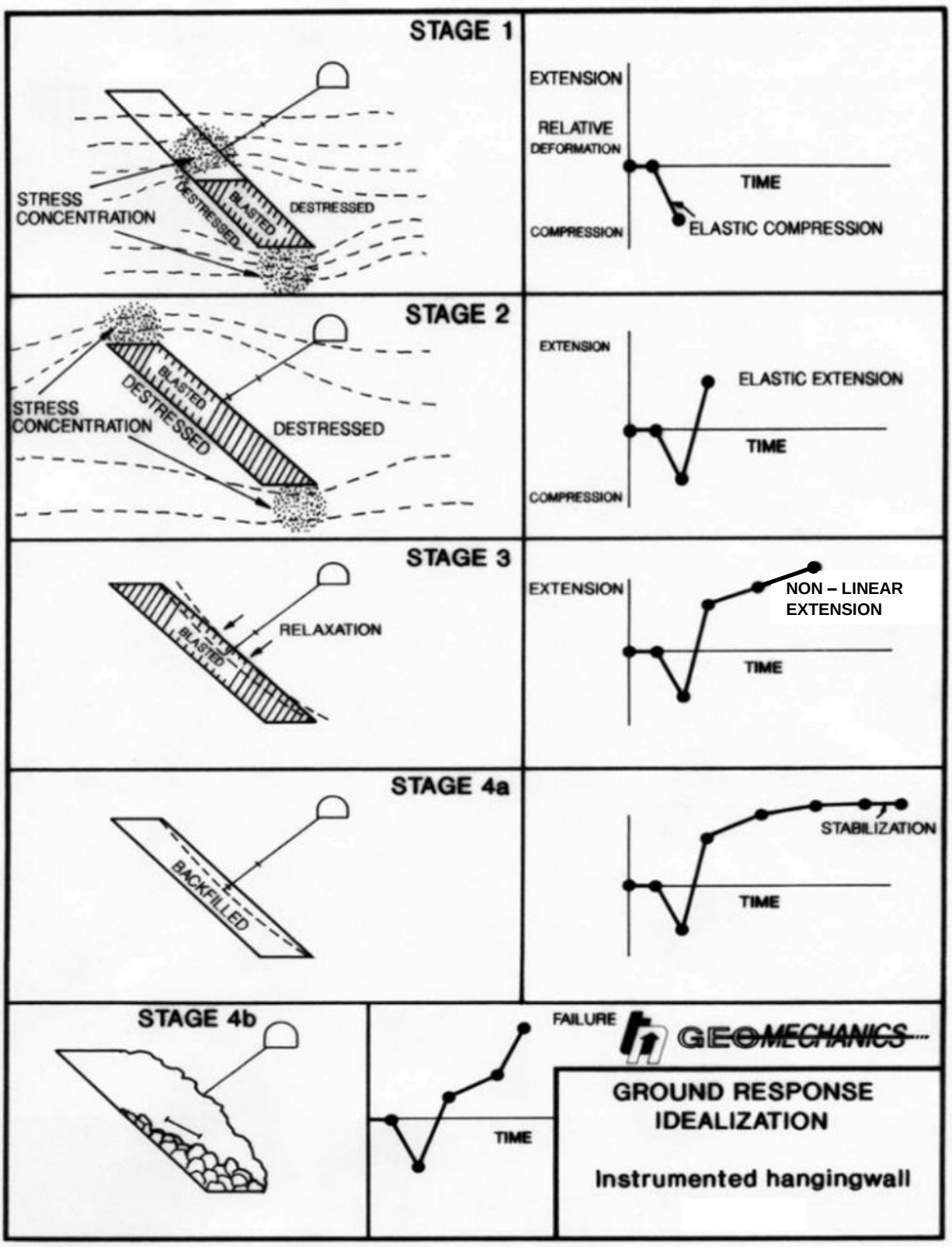

Figure 2-3: Idealization of the deformation of a stope hanging wall, measured by an extensometer, in response to stope excavation (after Milne, 1997).

2.2.2 Measurement

Rock mass deformation can be measured on the walls and back of an open stope using survey scanning technology to capture point clouds. Deformation can also be measured at different depths into the rock mass using extensometers.

The primary source of deformation data required to produce the graphs illustrated in Figure 2-3 were multi-point borehole extensometer (extensometer) installations. The extensometers installed consisted of six anchors that were grouted in place such that they would deform along with the surrounding rock mass. A schematic of a typical extensometer is shown in Figure 2-4.

Each anchor is independently connected to a linear potentiometer in the extensometer head by fibreglass rods (Figure 2-5). The linear potentiometer converts a change in the position of the anchor to a change in resistance (Figure 2-6). By passing a known reference voltage (Ei) over the linear potentiometers, the corresponding voltage drop (Eo) can be converted to a displacement, which is assumed to equal the change in distance of the anchor from the instrument head at the time of measurement.

$$\frac{Displacement}{Length_{potentiometer}} = \frac{[Voltage_{current} - Voltage_{baseline}]}{[Voltage_{reference}]} = \frac{E_{o2} - E_{01}}{E_i} \qquad \text{EQUATION 2-1}$$

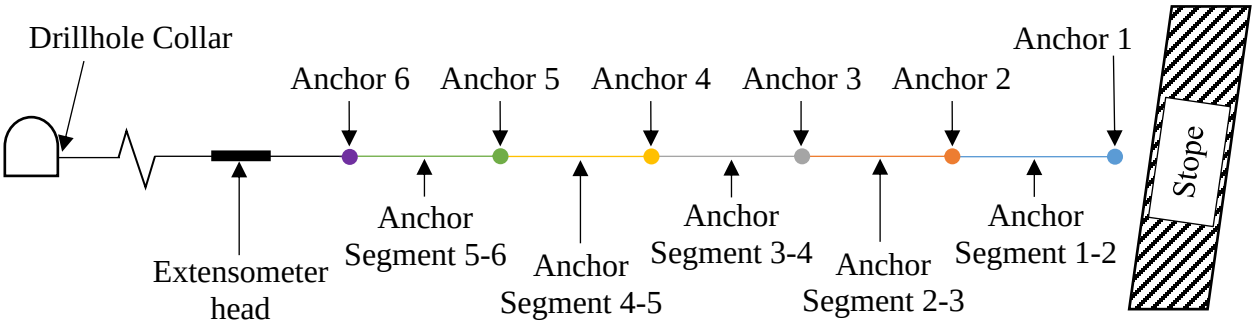

Figure 2-4: Representation of the extensometer anchor and segment locations and the relative position of the stope hanging wall.

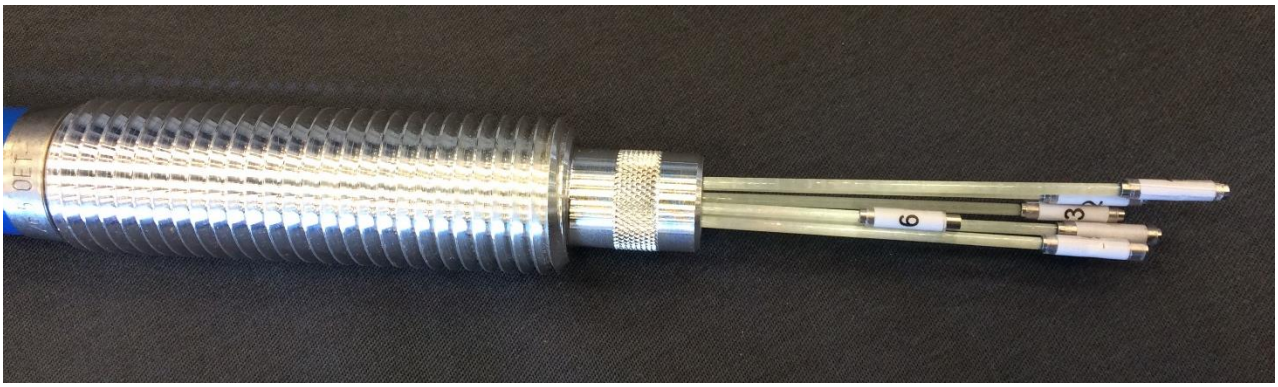

Figure 2-5: Close up view of an extensometer anchor and the individual cables connecting the anchor to the potentiometer.

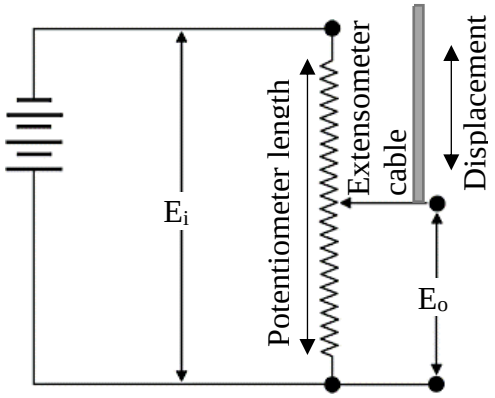

Figure 2-6: Circuit diagram of a basic potentiometer connected to an extensometer cable.

Measurements of voltage were collected both manually and using a datalogger programmed to collect measurements at a regular time interval. Using a datalogger provides a much more robust dataset as continuous measurements can be collected from the instrument at discrete intervals. This can allow data collection at regular intervals, independent of the availability of a person to physically travel to the instrument to collect an individual measurement. Dataloggers function by outputting a voltage (E_i) to the instrument and recording the returned voltage (E_o).

Ideally, instrumentation programs are scheduled to have the extensometers installed before production drilling and blasting of a stope begins. This ensures that the extensometers have established baseline measurements for each anchor before the extensometer is influenced by stress changes associated with stope excavation. Data analysis associated with this research program began when the extensometer anchors were undercut by stope excavation.

2.3 Stress

Prior to mining, a rock mass is subject to gravitational, tectonic, and other stresses. Resulting stress fields can be represented as three stresses acting normal to 3 orthogonal planes. Each orthogonal plane also has 2 shear stresses acting on it. The magnitude and direction of the normal stresses corresponding to the orientation where all the shear stresses have a magnitude of zero, corresponds to the principal stresses. Stress fields are defined by their principal stress magnitudes and directions.

2.3.1 Induced

The induced stress state describes the increases and decreases in the initial stress fields caused by the excavation of a portion of the rock mass. Since stress cannot propagate through voids, the induced stresses are often visualized as streamlines, associated with the largest principal stress, flowing around the excavation, similar to the flow of water around an obstruction (Hoek and Brown, 1980). Areas where stream lines bunch up are indicative of stress concentration and high stresses, while areas where stream lines are absent are indicative of areas of stress relaxation and low or tensile stresses (Figure 2-7). For openings with a circular cross-section, stresses deviate along the opening boundary (Figure 2-7a) while for openings with a tabular cross-section the geometry results in a zone of stress relaxation along the boundary (Figure 2-7b). As a convention, compressive stresses are positive with the largest principal compressive stress being σ_1 and the smallest principal stress being σ_3.

In a jointed rock mass, stress relaxation reduces the confinement of joints, which can allow for the movement of intact blocks within the joint system. As a result, it is reasonable to assume that tensile stresses cannot develop within a rock mass (Potvin, 1988). A jointed rock with little or no confinement may experience spalling in drift walls and backs. When confinement reduces, but the rock mass is still contiguous, dilation of fracture infill may lower the effective elastic modulus.

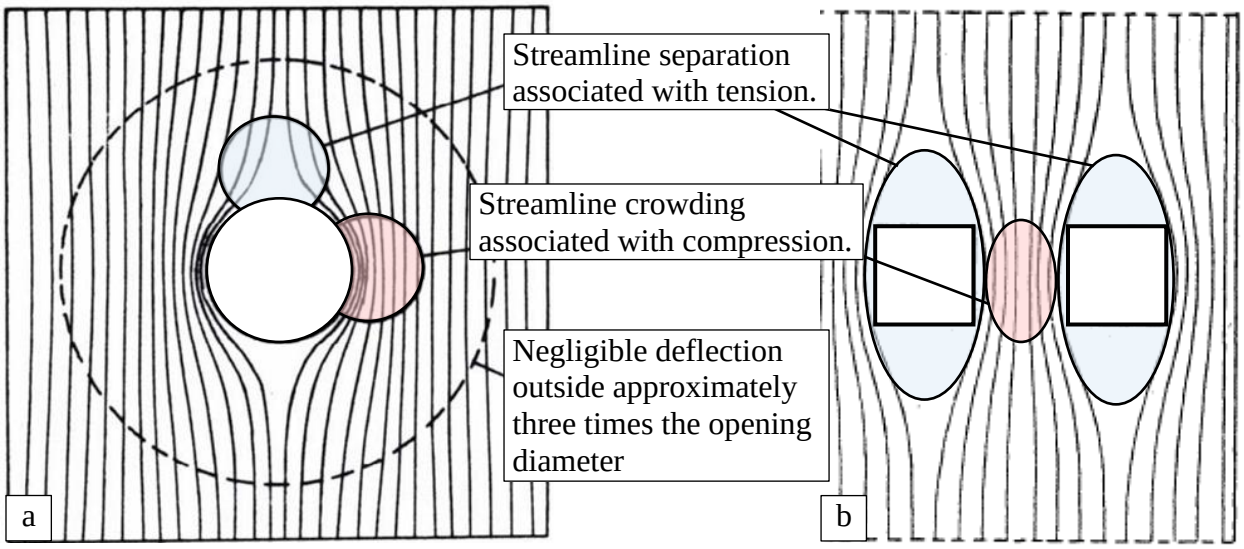

Figure 2-7: Theoretical stress flow lines around: (a) circular shape and (b) tabular shape (after Hoek and Brown, 1980).

Potvin (1988) conducted a parametric study of longitudinal open stopes to analyze the induced principal tangential stresses on stope surfaces of different geometries and under different stress conditions. In his modelling, Potvin (1988) considered surface geometries based on their stope aspect ratio, which is the stope length divided by the stope height. The stress normal to the stope hanging wall is equal to zero at the stope boundary and the induced vertical and horizontal stresses on the stope boundary are estimated. Results of the parametric modelling study were plotted to show the induced stresses for surfaces with different stope aspect ratios associated with the pre-mining K-ratios for horizontal stress and for the horizontal to vertical stress, as shown in Figure 2-8 and Figure 2-9 respectively. For tangential stresses induced in the horizontal direction, the induced stress increased as the stope length increased with respect to height and reduced to a tensile stress as the K-ratio increased. For stresses induced in the vertical direction, the induced stress decreased as the stope length increased with respect to height and reduced to a tensile stress as the K-ratio increased.

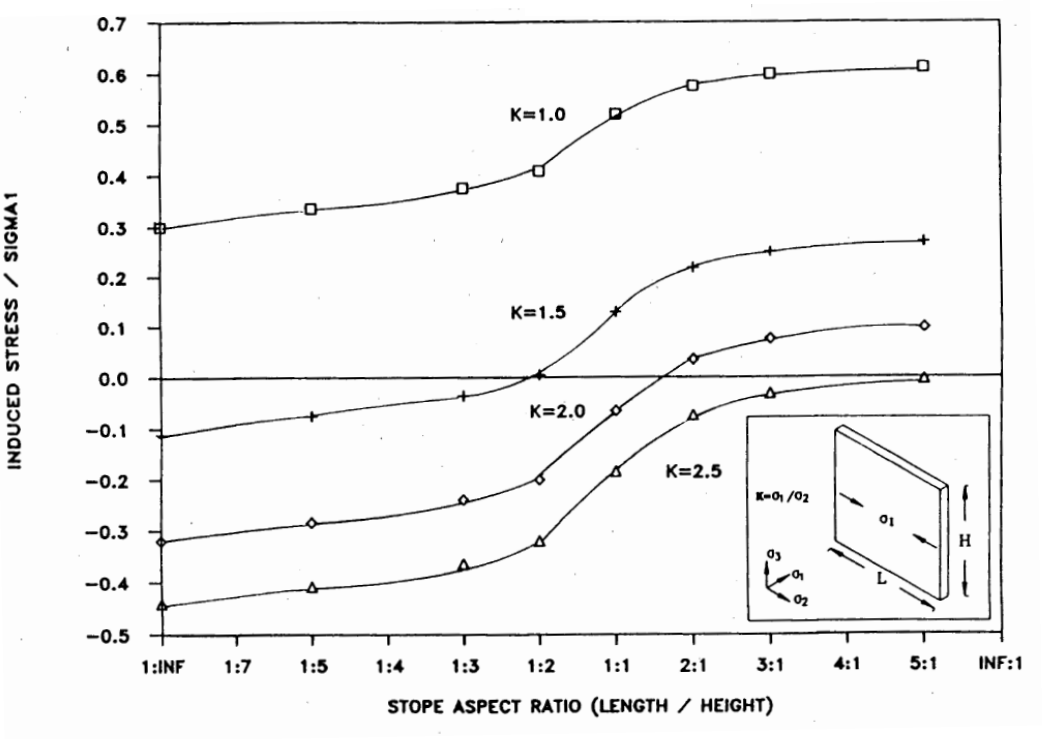

Figure 2-8: Induced stresses along the horizontal axis of a stope hanging wall for different stope aspect ratio and K-ratio (from Potvin, 1988).

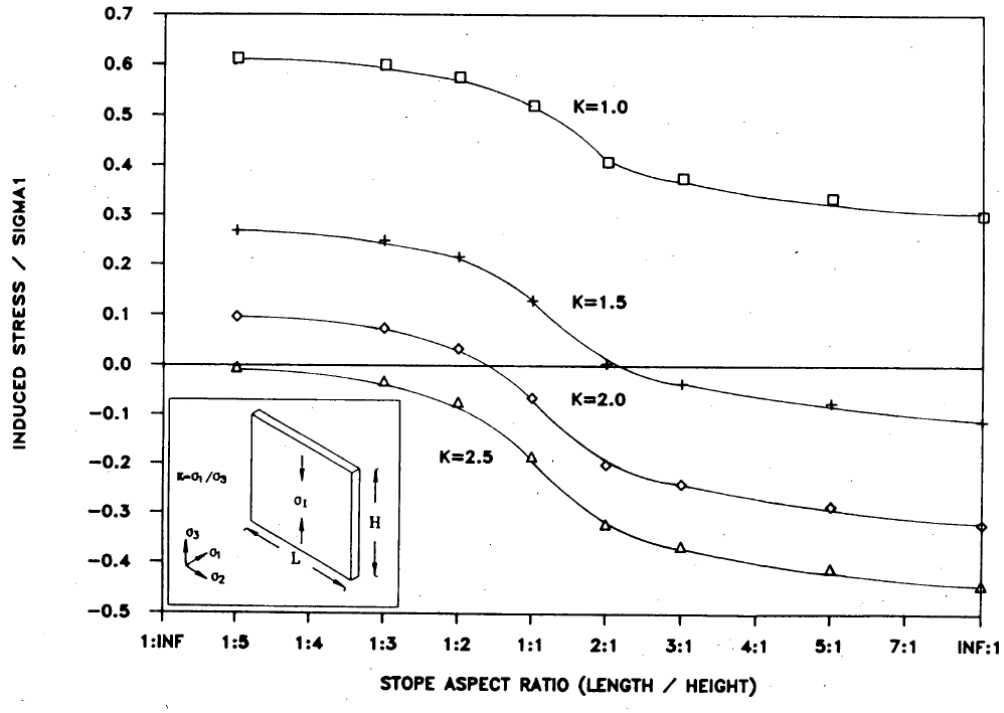

Figure 2-9: Induced stresses along the vertical axis of a stope hanging wall for different stope aspect ratio and K-ratio (from Potvin, 1988).

2.3.2 Measurement

Due to variability in geological history, a wide range of in situ stress conditions exist (Hoek and Brown, 1980). Although field stress measurement is generally expensive and subject to experimental challenges, resulting in inaccuracies (Potvin, 1988), they are required to provide representative measures of local stress conditions. Field stress measurements can be collected from drill holes or exposed rock faces using a variety of stress measurement techniques which are generally associated with either stress relief or stress balancing. Examples of some of the most common measurement techniques are overcoring, the flat jack method, and hydraulic fracturing.

2.4 Calculation of Stress and Deformation

Understanding the ground response to excavations is required to assess the stability of the excavations. Initially, analytical solutions were developed as simplified representations of ground movement in response to stress changes. In cases where the assumptions made in closed form solutions are not appropriate, numerical modelling may be required to consider non-circular geometries, inhomogeneous materials, and non-linear behaviour. The development of more powerful computers has allowed for more complexity to be added into numerical models, although challenges remain in the accurate collection of input data.

2.4.1 Cylinder

A closed form solution for calculating displacement and stresses around circular openings was developed by Kirsch (1898). The tangential (u_θ) and radial (u_r) displacements induced by a circular opening can be calculated using Equation 2-2 and total stresses can be calculated using Equation 2-3. A schematic is shown in Figure 2-10 that includes definitions of the variables. The Kirsch solution assumes plane strain and is applicable to long openings such as tunnels. In these settings, tunnel closure measurements can be taken to monitor stress changes based on the radial closure of several points around the opening.

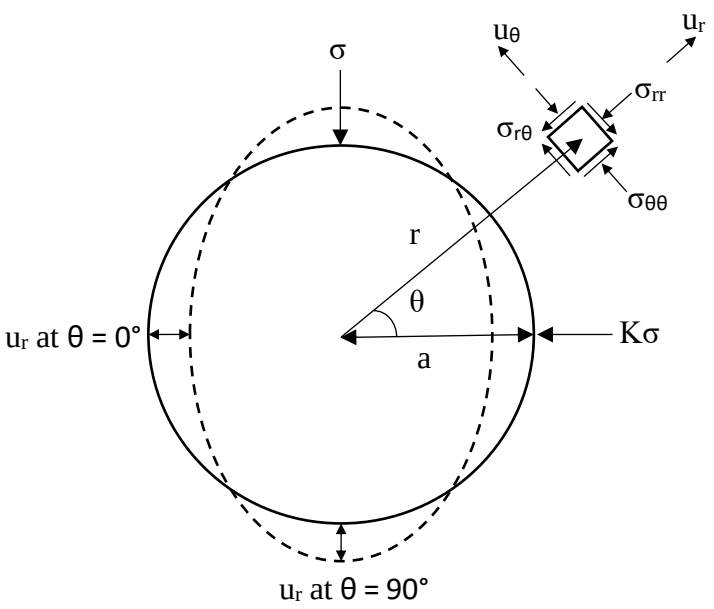

σ = Axial Stress

a = Radius of Opening

G = Shear Modulus

r = Distance to Point from the Centre of the Sphere

K = Stress Concentration Ratio

υ = Poisson's Ratio

θ = Counter-clockwise Angle to Point from Direction of Kσ

Figure 2-10: Schematic showing radial deformation of a circular opening and the variables used in the Kirsch closed form solution (after Brady and Brown, 1985).

$$u_\theta = -\frac{\sigma a^2}{4Gr}\left[(1-K)\left\{2(1-2\nu)+\frac{a^2}{r^2}\right\}sin2\theta\right]$$

$$u_r = -\frac{\sigma a^2}{4Gr}\left[(1+K)-(1-K)\left\{4(1-\nu)-\frac{a^2}{r^2}\right\}cos2\theta\right] \qquad \text{EQUATION 2-2}$$

$$\sigma_{rr} = \frac{\sigma}{2}\left[(1+K)\left(1-\frac{a^2}{r^2}\right)-(1-K)\left(1-\frac{4a^2}{r^2}+\frac{3a^4}{r^4}\right)cos2\theta\right]$$

$$\sigma_{r\theta} = \frac{\sigma}{2}\left[(1-K)\left(1+\frac{2a^2}{r^2}-\frac{3a^4}{r^4}\right)sin2\theta\right]$$

$$\sigma_{\theta\theta} = \frac{\sigma}{2}\left[(1+K)\left(1+\frac{a^2}{r^2}\right)+(1-K)\left(1+\frac{3a^4}{r^4}\right)cos2\theta\right] \qquad \text{EQUATION 2-3}$$

Boundary stresses can be calculated from Equation 2-3 when r = a.

$$\sigma_{rr} = 0$$

$$\sigma_{r\theta} = 0$$

$$\sigma_{\theta\theta} = \sigma[(1+K)+2(1-K)cos2\theta]$$

When θ = 0 and the stress estimate is aligned with the Kσ stress,

$$\sigma_{\theta\theta} = \sigma(3-K) \qquad \text{EQUATION 2-4}$$

2.4.2 Sphere

Brady and Brown (2006) summarized equations developed by Poulos and Davies (1974) to calculate the elastic deformation radially inwards towards a spherical opening in a hydrostatic stress field. Spherical solutions are applied by Milne (1997) to represent three-dimensional stope geometries because they are considered to be the closest geometry to have a closed form solution

$$u_r = -\frac{\sigma a^3}{4Gr^2} \qquad \text{EQUATION 2-5}$$

Where: u_r = Radial Displacement

σ = Hydrostatic Stress Field

a = Sphere Radius

G = Shear Modulus

r = Distance to the Point from the Centre of the Sphere

Milne (1997) replaced the "r" in Equation 2-5 with the term "a+d" where d is the distance from the surface of the sphere to the point. Then, based on the approximation that $\frac{a-d}{a} \approx \frac{a}{a+d}$ when the distance to the point is much smaller than the radius of the sphere, Milne (1997) derived Equation 2-6 from Equation 2-5. Equation 2-6 can be used to approximate the radial displacement around a sphere in a hydrostatic stress field in terms of stress (σ), the elastic rock properties, geometry of the sphere, and the distance to the point from the surface of the sphere (d).

$$u_r \approx \frac{\sigma_n(1+\upsilon)}{2E}(a-2d) \qquad \text{EQUATION 2-6}$$

Milne (1997) then calculated the relative displacement between two points near a spherical opening to calculate radial strain (ε_r). Equation 2-7 shows that the strain approaches a constant value when the distance from the points to the opening is much smaller than the opening radius.

$$\varepsilon_r \approx \frac{\sigma_n(1+\upsilon)}{E} \qquad \text{EQUATION 2-7}$$

2.4.3 Tabular

Milne (1997) completed numerical modelling of the elastic strains induced in the backs of tabular openings with variable geometries and initial stress states using Map3D boundary element models. The modelling was conducted for an elastic modulus of 60 GPa and a Poisson's ratio of 0.25. Empirical analysis of the modelled elastic strains ($\varepsilon_{a\text{-}b}$) at different locations within the back resulted in strain plots that appeared to approach a maximum constant value as the distance to the abutments increased. Using the same form as the equation for estimating the radial strain between two points near a spherical opening (Equation 2-7), Milne (1997) formulated Equation 2-8 to estimate if measurements are within a probable elastic range given the assumed elastic properties of the rock mass and an initial pre-mining stress acting normal to the opening (σ_n).

$$\varepsilon_{a-b} \approx \frac{0.64\Delta\sigma_n(1+\nu)}{E}$$

$$\Delta\sigma_n \approx \frac{\varepsilon_{a-b}E}{0.64(1+\nu)} \qquad \text{EQUATION 2-8}$$

2.4.4 Numerical modelling of stress and deformation

Numerical models can be applied to model continuum or discontinuum behaviour. In continuum models, the rock mass remains intact and the response can range from elastic to plastic. In discontinuum models, the rock mass is comprised of individual components that can respond individually to changes in stress. Regardless of the type of numerical model being used, it is important to calibrate the model with local case histories.

In boundary element models, only the excavation boundary is divided into elements while the rock mass is considered to be a continuum. As a result, boundary element models are generally restricted to modelling elastic responses. While the simplicity associated with modelling the rock mass as a continuum is a primary benefit of boundary element models, it also creates challenges in modelling discontinuities and incorporating variations in the material properties of the rock mass. Details relating to the calculations in boundary element models can be found in Brady and Brown (2006).

Examine2D (RocScience Inc., n.d. a) is an example of a boundary element program that models elastic displacements and stresses in two dimensions by assuming plane strain conditions. The model assumes that the rock mass is continuous, homogeneous, isotropic, and linear elastic

(CHILE), so the degree to which these assumptions deviate from the actual rock mass should be considered when interpreting the model outputs. Despite these limitations, the modelled stresses and displacements provide useful insights into potential stress conditions in an elastic environment and in identifying areas where stresses may exceed material strength (Capes, 2009).

The displacements modelled in Examine2D are elastic displacements and are reliant on the elastic modulus of the rock mass (RocScience Inc., n.d. a). The correct selection of the elastic modulus can be challenging due to variability within the rock mass and deterioration of the initial elastic modulus due to blast damage and stress relaxation. The elastic deformation response generally comprises a small fraction of the total displacement, especially in weak fractured rock, as non-linear deformation can be orders of magnitude larger than the elastic response (RocScience Inc., n.d. a).

RS3 (RocScience Inc., n.d. b) is an example of a finite element model (FEM) that models displacement and stress in a three-dimensional environment. FEM are domain discretization models in which the entire rock mass is divided into simple elements with assigned properties. The collective interaction of the simple elements model the behaviour of the overall rock mass.

FEM can model non-linear behaviour in inhomogeneous rock masses. Since FEM models have boundaries, these boundaries need to be designed to avoid influencing the area of interest and appropriate boundary loading conditions must be applied (Potvin, 1988, Hoek, 2006). The precision of the model can be modified by changing the element size. FEM allow yielding to occur within the rock mass and model the stress interactions in the yielded zones within the overall model (Capes, 2009). It is unclear if the perceived certainty associated with modelling inelastic behaviour outweighs the added uncertainty associated with the larger number of input parameters.

2.5 Opening geometry

Stope sizes are usually designed to their maximum stable geometry, based on variable rock mass properties, local stresses, orebody dimensions, mining method, and other factors. To account for these variables, various empirical design methods have been developed to compare stope geometries for stopes mined in similar conditions. Depending on the dimension being designed, different measures are used to represent the geometry. This study only considers the hanging wall geometry.

2.5.1 Hydraulic Radius

Most commonly, the geometry of a stope hanging wall is represented by its hydraulic radius (HR). The term hydraulic radius has been in use since it was borrowed from fluid mechanics and introduced to mining by Laubscher (1977). It is used to represent the average distance from the centre of a geometry to the supporting abutments. For a geometry of length (a) and height (b), it is generally calculated by dividing the 2-dimensional area of the hanging wall by the perimeter of the 2-dimensional area as per Equation 2-9.

$$HR = \frac{area}{perimeter} = \frac{a \times b}{2a + 2b} \qquad \text{EQUATION 2-9}$$

Milne (1997) reformatted the formula to better illustrate the influence of abutments on the calculation of HR, as shown in Equation 2-10.

$$HR = \frac{2}{\frac{1}{0.5a} + \frac{1}{0.5b} + \frac{1}{0.5a} + \frac{1}{0.5b}} \qquad \text{EQUATION 2-10}$$

Although HR is widely used, there are some limitations to its ability to represent different geometries. Milne (1997) identified that the HR is the same for both square and circular shaped geometries, even though the extra surface area associated with the corners of a rectangular opening should be detrimental to stability (Figure 2-11). Another limitation is the ability of HR to represent an irregular geometry. Usually HR is calculated for the largest rectangle that can be formed without crossing an abutment. While it may be possible to represent the geometry using a shape with more than four sides, generally the largest HR is calculated for a four-sided shape. For irregular shapes, the accepted practice is to calculate multiple HR values for different approximating geometries and use the largest value (Figure 2-12).

Circle

$$HR = \frac{Area}{Perimeter} = \frac{\pi r^2}{2\pi r} = \frac{\pi(0.5a)^2}{2\pi(0.5a)} = 0.25a$$

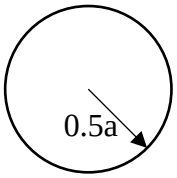

Square

$$HR = \frac{Area}{Perimeter} = \frac{a^2}{4a} = 0.25a$$

$$HR = \frac{4 \times 0.5}{\frac{1}{0.5a} + \frac{1}{0.5a} + \frac{1}{0.5a} + \frac{1}{0.5a}} = \frac{2 \times 0.5a}{4} = 0.25a$$

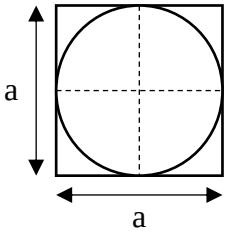

Figure 2-11: Calculation of HR for a rectangle and ellipse surface geometries (after Milne, 1997).

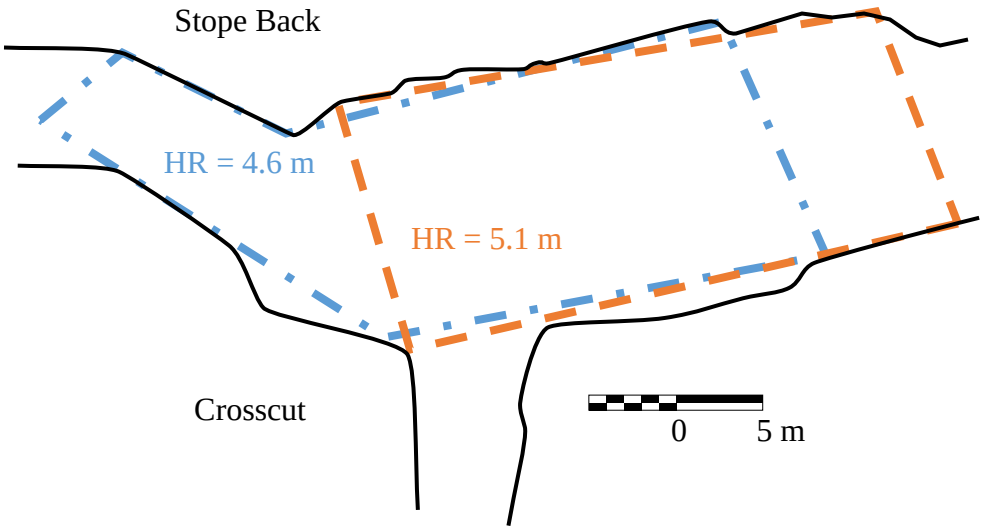

Figure 2-12: Calculation of multiple HR for an irregular stope geometry (after Milne, 1997).

2.5.2 Radius Factor and Effective Radius Factor

Another form of HR, called the harmonic average (R_h), was proposed by Milne (1997). The harmonic average is double the HR as shown by Equation 2-11, and represents the average distance to the surface abutments as measured from the surface centre. It can be derived by reformatting Equation 2-10 as the summation of a number (n) of distances from the surface centre to the abutment (r_θ) at angle intervals (θ) (Equation 2-11). It is assumed that the harmonic average is

better represented by averaging distance measurements from a large number of measurements taken at small angular intervals.

$$HR = \frac{2}{\frac{1}{0.5a} + \frac{1}{0.5b} + \frac{1}{0.5a} + \frac{1}{0.5b}} = \frac{0.5}{\frac{1}{4}\left(\frac{1}{0.5a} + \frac{1}{0.5b} + \frac{1}{0.5a} + \frac{1}{0.5b}\right)}$$

$$R_h = \frac{1}{\frac{1}{4}\left(\frac{1}{0.5a} + \frac{1}{0.5b} + \frac{1}{0.5a} + \frac{1}{0.5b}\right)} = \frac{1}{\frac{1}{n}\sum_{\theta=1}^{n}\frac{1}{r_\theta}}$$ EQUATION 2-11

Milne (1997) proposed the term radius factor (RF), which is half the harmonic radius, be used as a replacement to HR. Similar to both the harmonic average and HR, radius factor is measured from the centre of the surface geometry.

$$RF = \frac{R_h}{2} = \frac{0.5}{\frac{1}{n}\sum_{\theta=1}^{n}\frac{1}{r_\theta}}$$ EQUATION 2-12

The RF can be calculated at any point on a surface, having a maximum value at the surface centre and reducing to zero at the abutments. Milne (1997) introduced the term Effective Radius Factor (ERF) for calculation of RF at all surface points other than the centre of the surface. The calculation of RF and ERF are shown in Figure 2-13 for the same irregular geometry used to calculate HR (Figure 2-12).

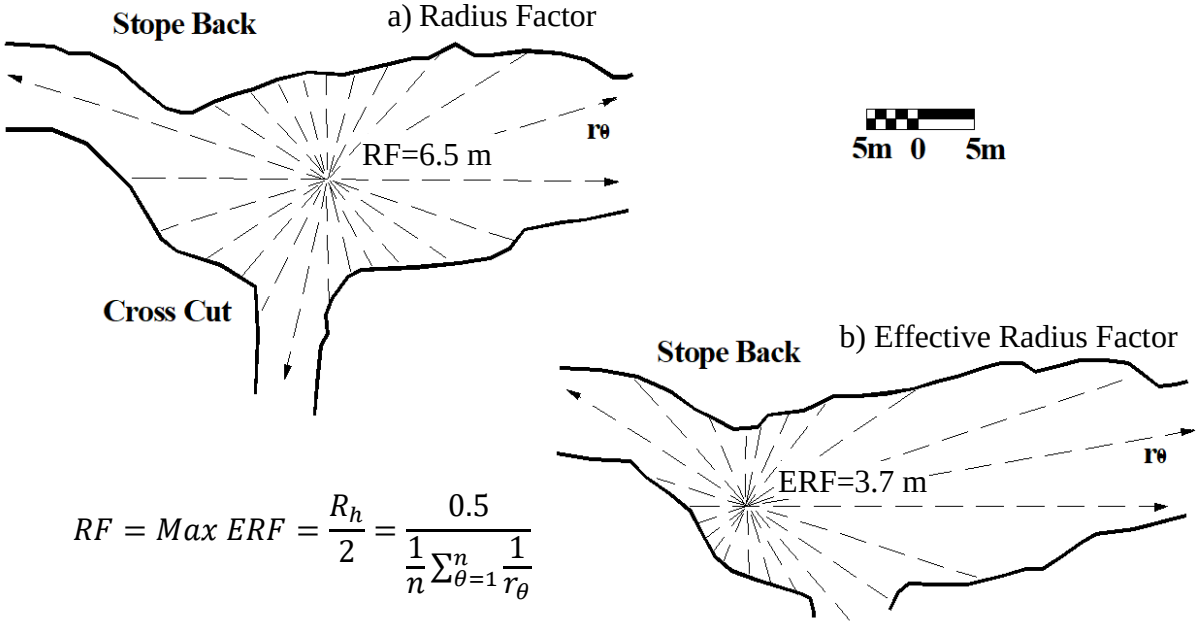

Figure 2-13: Calculation of RF and ERF for an irregular stope geometry (after Milne et al, 1996).

2.6 Stope Design

The development of empirical tools for designing open stopes is dependent on rock mass classification systems to compare local conditions to previous stability results. Following the advent of the Tunnel Quality Index by Barton et al. (1974) and the Rock Mass Rating by Bieniawski (1974, 1976), case histories for open stopes were compiled and analyzed, resulting in the development of the Stability Graph (Nickson, 1981; Potvin, 1988; Nickson, 1992; Stewart and Forsyth, 1995) and later the Dilution Graph (Clark 1998; Capes, 2009). In addition to empirical tools, stopes can also be designed using numerical models that assess the induced stresses after excavation against different rock mass failure criteria.

2.6.1 RQD

The Rock Quality Designation (RQD) was developed by Deere (1964) to quantify the competence of rock from drill core and is most commonly used for selecting tunnel support and as an input parameter in other rock mass classification systems. RQD is a measure of the intact core recovered from a core run as shown in Equation 2-13. RQD is intended to represent the in-situ rock mass so care is required to identify and discount mechanical breaks or other instances of core damage so as not to artificially degrade the calculated RQD.

$$\text{RQD} = \frac{\text{Cumulative length of core pieces} > 100\text{mm}}{\text{Total length of core run}} \times 100\% \qquad \text{EQUATION 2-13}$$

RQD can also be estimated from the number of joints visible per unit volume (J_v) on a rock surface, if drill core is not available (Palmström, 1982) as per Equation 2-14. As when assessing core, it is important to exclude joints created by blasting or other mechanical means when estimating RQD from visible joints.

$$\text{RQD} = 115 - 3.3\text{J}_\text{v} \qquad \text{EQUATION 2-14}$$

2.6.2 NGI Tunnel Quality Index (Q)

Barton et al. (1974) developed the Norwegian Geotechnical Institute (NGI) Tunnel Quality Index (Q), to estimate support requirements for tunnelling based on six variables representing different attributes of the rock mass. The pairs of variables in the Q equation (Equation 2-15) represent block size, discontinuity condition, and stress modifiers. A summary for the calculation of each of the independent variables is outlined in Table 2-1. For full details, see Hoek (2006).

$$Q = \frac{RQD}{J_n} \times \frac{J_r}{J_a} \times \frac{J_w}{SRF}$$ EQUATION 2-15

Where: RQD = Rock Quality Designation

J_n = Joint Set Number

J_r = Joint Set Roughness

J_a = Joint Set Alteration Number

J_w = Joint Water Reduction Factor

SRF = Stress Reduction Factor

Values of Q range from 0.001 to 1000, on a logarithmic scale, and are associated with rock quality assessments ranging from exceptionally poor to exceptionally good. Barton et al. (1974) consider the support requirements relative to the opening geometry, represented by the Equivalent Dimension (D_e), which is calculated as the maximum span divided by the Excavation Support Ratio (ESR). The ESR is related to the degree of conservatism required of the design and is similar to an inverse of the factor of safety.

The Modified Tunnelling Quality Index (Q') is used to classify the inherit rock mass properties for the purpose of design modelling and is calculated in the same manner as Q except with a SRF of one (Hutchinson and Diederichs, 1995). Equation 2-16 shows the calculation.

$$Q' = \frac{RQD}{J_n} \times \frac{J_r}{J_a} \times \frac{J_w}{1}$$ EQUATION 2-16

Table 2-1: Definition of the variables and ratings used in calculation of the Tunnelling Quality Index Q (after Barton et al., 1974).

Rock Quality Designation	**RQD**
Very Poor	0 – 25
Poor	25 – 50
Fair	50 – 75
Good	75 – 90
Excellent	90 - 100

Joint Set Number	**J_n**
Massive, No or few joints	0.5 – 1.0
One joint set	2
One joint set plus random	3
Two joint sets	4
Two joint sets plus random	6
Three joint sets	9
Three joint sets plus random	12
Four or more joint sets, random heavily jointed, ‘sugar cube’, etc.	15
Crushed rock, earth like	20

Joint Roughness Number	**J_r**
Discontinuous joints	4
Rough, undulating	3
Smooth, undulating	2
Rough, planar	1.5
Smooth, planar	1
Slickensided, planar	0.5
Thick infill, no rock contact	1.0

Joint Alteration Number	**J_a**
Tightly healed	0.75
Surface staining only	1.0
Low friction coating (chlorite, talc, etc.)	4.0
Thin swelling clay	10.0
Thick swelling clay	20.0

Joint Water Reduction	**J_w**
Dry to minor inflow	1.0
Medium inflow	0.66
Large inflow	0.5
Exceptionally high flow (reduces with time)	0.1 – 2
Exceptionally high flow (no reduction with time)	0.05 – 0.1

Stress Reduction Factor	**SRF**
Low stress near surface	2.5
Medium confining stress	1.0
Mild rock burst	5 – 10
Heavy rock burst	10 – 20
Single, shear zone, clay free	2.5
Multiple shear zones, with clay	10
Squeezing rock	5 – 20
Swelling rock	5 – 20

2.6.3 Rock Mass Rating (RMR)

The Rock Mass Rating (RMR) system was developed by Bieniawski (1974, 1976) based on observations during civil tunnelling work. The rock mass is characterized by five parameters which are used to calculate the RMR_{76}. These parameters represent the drill core quality, rock strength, groundwater condition, joint spacing, and joint condition (Table 2-2). Depending on the orientation of the opening relative to the joint sets, a sixth parameter may also be applied. RMR_{76} ranges in value from 8 to 100 and is calculated by taking the sum of variables one through five and then adding the value associated with the joint orientation.

A relationship was developed by Bieniawski (1978) relating the RMR_{76} to the elastic modulus of the rock mass (Equation 2-17). In poorer quality rock masses, this can provide a better indication of the elastic modulus than a lab-based measure as it incorporates jointing, which may be absent in test specimens.

$$E = 2RMR_{76} - 100 \qquad \text{EQUATION 2-17}$$

An approximation can also be made relating the RMR and Q values (Bieniawski, 1976), if design purposes require a value in the other system, although the preference should be to calculate the new value rather than relying on this approximation (Equation 2-18).

$$RMR_{76} = 9\ln Q + 44 \qquad \text{EQUATION 2-18}$$

Table 2-2: Definition of the variables and ratings for the RMR76 system (after Bieniawski, 1976).

A, CLASSIFICATION PARAMETERS AND THEIR RATINGS

PARAMETER			RANGES OF VALUES						
1	Strength of intact rock material	Point-load strength index	> 8 MPa	4 - 8 MPa	2 - 4 MPa	1 - 2 MPa	For this low range - uniaxial compressive test is preferred		
		Uniaxial compressive strength	> 200 MPa	100 - 200 MPa	50 - 100 MPa	25 - 50 MPa	10 - 25 MPa	3 - 10 MPa	1 - 3 MPa
	Rating		15	12	7	4	2	1	0
2	Drill core quality RQD		90% - 100%	75% - 90%	50% - 75%	25% - 50%	< 25%		
	Rating		20	17	13	8	3		
3	Spacing of joints		> 3 m	1 - 3 m	0.3 - 1 m	50 - 300 mm	< 50 mm		
	Rating		30	25	20	10	5		
4	Condition of joints		Very rough surfaces. Not continuous, No separation, Hard joint wall rock	Slightly rough surfaces. Separation < 1 mm. Hard joint wall rock	Slightly rough surfaces. Separation > 1 mm. Soft joint wall rock.	Slickensided surfaces, OR Gouge < 5 mm thick, OR Joint open 1-5 mm. Continuous joints.	Soft gouge > 5 mm thick. OR Joint open > 5mm. Continuous joints.		
	Rating		25	20	12	6	0		
5	Ground water	Inflow per 10 m tunnel length	None		< 25 litres/min	25 - 125 litres/min	> 125 litres/min		
		Ratio $\frac{\text{joint water pressure}}{\text{major principal stress}}$	OR 0		OR 0.0 - 0.2	OR 0.2 - 0.5	OR > 0.5		
		General conditions	OR Completely dry		OR Moist only (interstitial water)	OR Water under moderate pressure	OR Severe water problems		
	Rating		10		7	4	0		

B. RATING ADJUSTMENT FOR JOINT ORIENTATIONS

Strike and dip orientations of joints		Very favourable	Favourable	Fair	Unfavourable	Very unfavourable
Ratings	Tunnels	0	-2	-5	-10	-12
	Foundations	0	-2	-7	-15	-25
	Slopes	0	-5	-25	-50	-60

C. ROCK MASS CLASSES DETERMINED FROM TOTAL RATINGS

Rating	100 ← 81	80 ← 61	60 ← 41	40 ← 21	< 20
Class No.	I	II	III	IV	V
Description	Very good rock	Good rock	Fair rock	Poor rock	Very poor rock

D. MEANING OF ROCK MASS CLASSES

Class No.	I	II	III	IV	V
Average stand-up time	10 years for 5 m span	6 months for 4 m span	1 week for 3 m span	5 hours for 1,5 m span	10 minutes for 0,5m span
Cohesion of the rock mass	> 300 kPa	200 - 300 kPa	150 - 200 kPa	100 - 150 kPa	< 100 kPa
Friction angle of the rock mass	> 45°	40° - 45°	35° - 40°	30° - 35°	< 30°

2.6.4 Stability Graph

Mathews et al. (1981) introduced the Stability Graph as an empirical method for assessing open stope stability in deep mining environments based upon 26 cases from three mines and 29 cases from literature. In developing the stability graph, stability results for open stopes were plotted based on a Stability Number (N) and the Shape Factor (S) or HR and regions associated with the stability result were developed. The regions included in Mathews' Stability Graph are stable, potentially unstable, and potentially caving.

The Stability Number (N) is calculated using Q' and three stability factors, called the Stress Factor (A), Joint Defect Orientation Factor (B), and Gravity Factor (C).

$$N = Q' \times A \times B \times C \qquad \text{EQUATION 2-19}$$

Factor A is estimated using Figure 2-14a, which is based upon the ratio between the intact strength of the rock mass and the induced tangential stress acting parallel to the stope surface. The uniaxial compressive strength of the rock is generally taken as the intact strength.

Factor B considers the orientation of geological structures relative to the stope surface and is estimated using Figure 2-14b. If multiple structures exist, the most predominant structure should be considered when determining Factor B.

Factor C considers the influence of gravity on the stope hanging wall by assessing the inclination of the surface and is estimated using Figure 2-14c. For this factor, stability is highest for vertical surfaces and decreases as the surface becomes more horizontal.

Potvin (1988) expanded the database of case histories to include over 250 cases from 34 Canadian mines and modified the weighting of the three stability factors introduced by Mathews et al. (1981) (Figure 2-14). This resulted in the calculation of the Modified Stability Number (N') and a modification to the stable and caved zones.

Nickson (1992) compiled a new database with 59 case histories from 13 mines and compared his database with the Modified Stability Graph (Potvin, 1988). Following this comparison, Nickson (1992) proposed a revision to the Modified Stability Graph to include a stable with support zone and a supported transition zone (Figure 2-15).

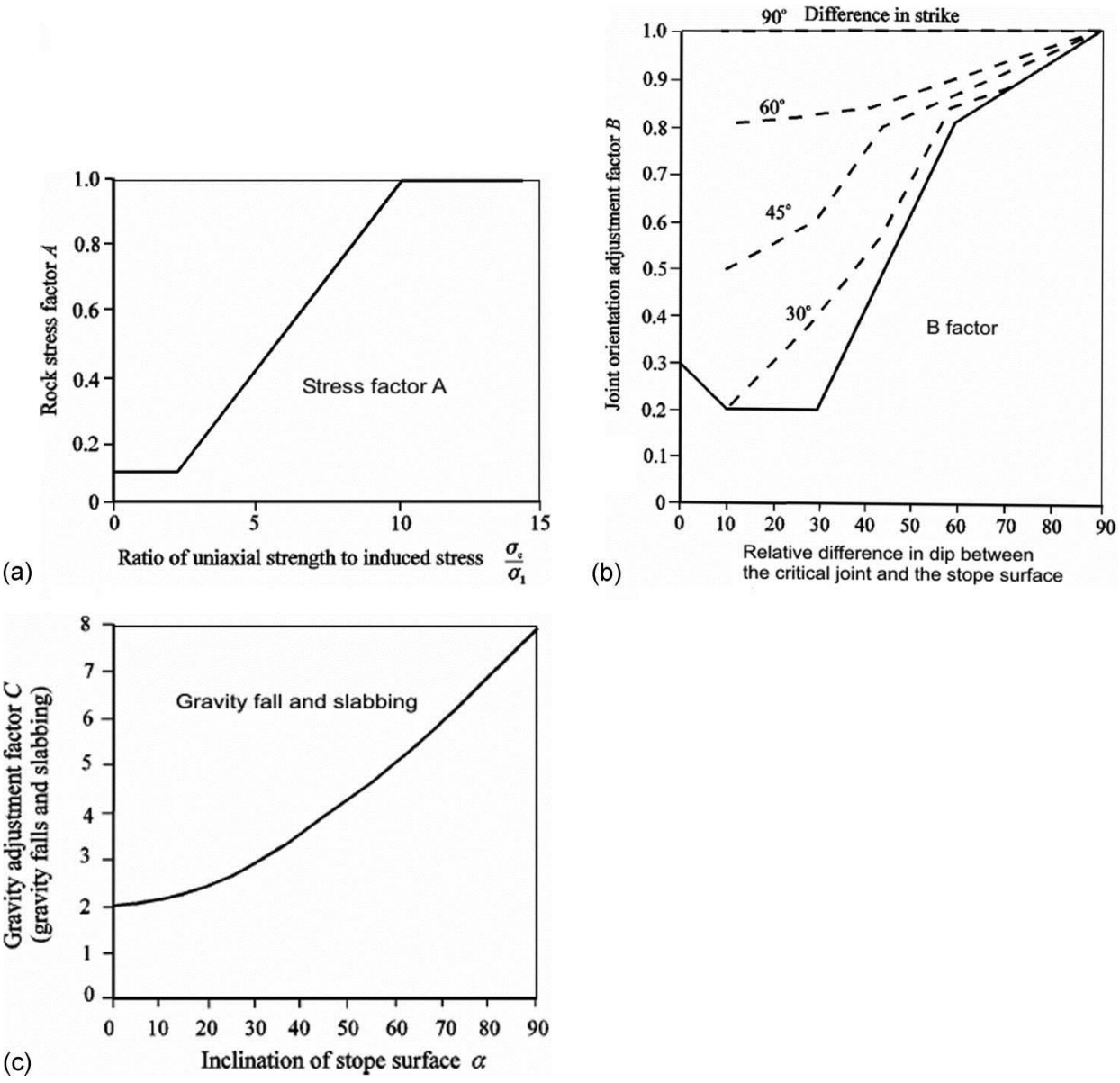

Figure 2-14: Graphs for determining the stability factors (from Suorineni, 2010; after Potvin, 1988)

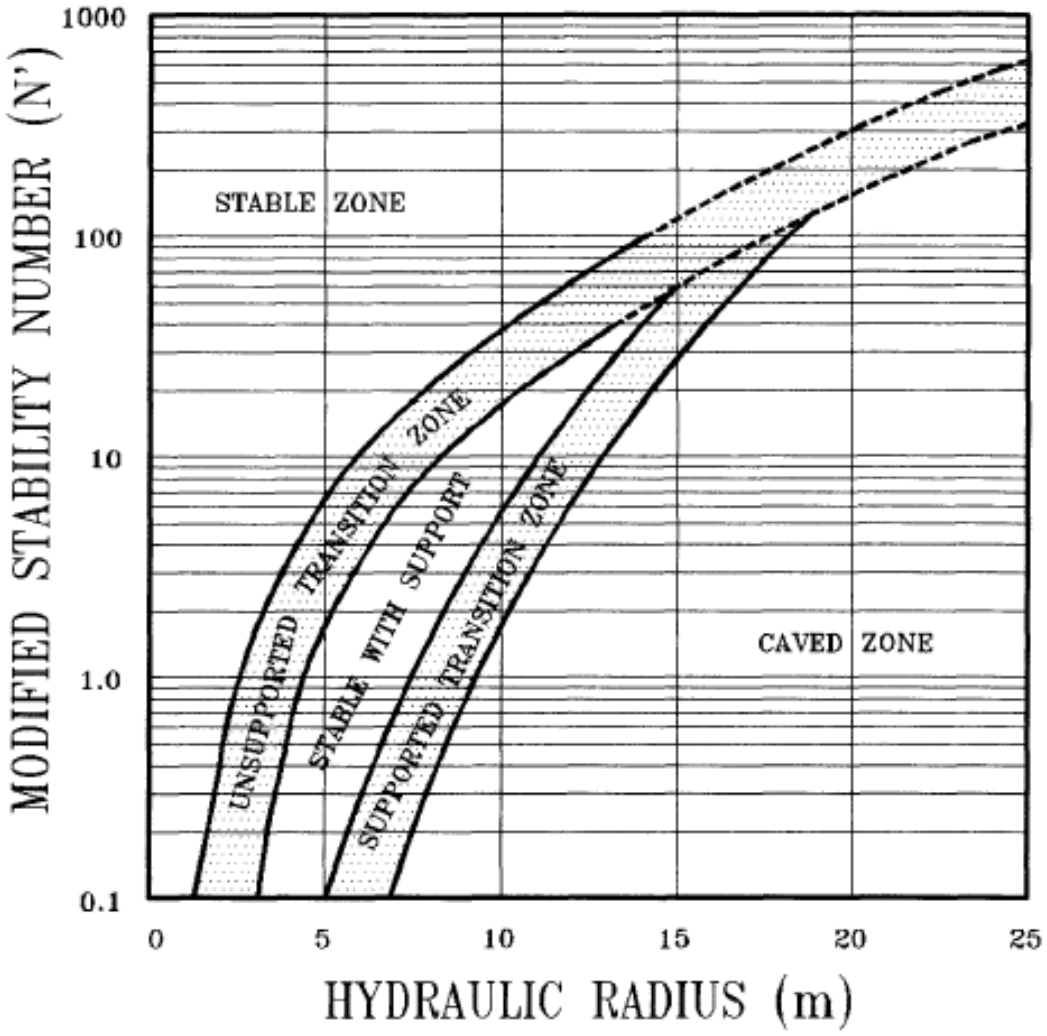

Figure 2-15: The Nickson Stability Graph (from Nickson, 1992).

An additional stability factor has been developed as a correction for sliding but it is seldom used, due to challenges in application, so it is not shown here.

Another variation of the Modified Stability Graph was developed by Stewart and Forsyth (1995) who argued that the Stability Graph provides a non-rigorous solution and the single Potvin (1988) transition zone may be an oversimplification of the possible stability results. To capture other possible stability results, Stewart and Forsyth (1995) identified additional transitions between zones associated with potential caving, potential major failure, potentially unstable, and potentially stable.

Suorineni (2010) completed a review of the original and modified stability graphs. He identified the subjectivity involved in creating the stability graph zones, lack of consideration for faults or stand-up time, influence of poor blasting, oversimplification of complex geometries, Stress Factor A not accounting for tension, and the poor representation of footwall failures due to sliding as significant limitations to the use of Stability Graphs. To address the limited ability of the Stability Graph to account for faults and other discrete geological structures, a fault factor was developed for use with the Stability Graph (Suorineni, 1998; Suorineni et al., 1999; Suorineni et al., 2001).

Part of the challenge associated with the definition of the Stability Graph zones lies in classifying the result of the case studies into the zones that are to be included in the graph. As an example, depending on the orebody width, overbreak or dilution of one metre could be considered as either stable or caving. As a result, the application of the stability graphs to narrow orebody widths has not worked well (Suorineni, 1998; Stewart and Trueman, 2003).

While the Stability Graph has proven to be useful for determining the dimension of open stopes, actual stope stability is dependent on local rock mass properties, which may be difficult to identify during the design phase. In the case where adverse conditions exist, which were not identified during the design phase, a failure could occur for a stope believed to have a conservative design. Restricted access to open stopes to investigate failures may prevent a proper reconciliation of the stability factors and the resulting zone the surface would plot to.

2.6.5 Dilution Graph

The term Equivalent Linear Overbreak/Slough (ELOS) was developed by Clark (1998) as an alternative means to quantify the volume of overbreak or slough associated with stope dilution (Equation 2-20). To calculate ELOS, the volume of dilution is divided by the approximate area of the stope hanging wall to calculate an average depth associated with the dilution volume. By considering dilution as an equivalent thickness rather than a volume, the magnitude of the dilution is more apparent when compared with the stope width.

$$ELOS = \frac{Volume\ of\ slough}{Stope\ height \times Wall\ strike\ length} \qquad \text{EQUATION 2-20}$$

Clark (1998) developed the Dilution Graph from a database of 88 measurements from six Canadian mines.by plotting the ELOS values on the Modified Stability Graph. He then identified and plotted contours associated with the calculated ELOS as a means of estimating the amount of dilution based on then N' and HR of a stope (Figure 2-16a).

Capes (2009) expanded the database associated with the Dilution Graph by collecting an additional 169 cases. Using the expanded database, he was able refine the ELOS contours shown in the Modified Dilution Graph (Figure 2-16b).

Through development of the Dilution Graph, Clark (1998) demonstrated that dilution and relaxation are both associated with the stope geometry. During theoretical analysis of the ELOS parameter, Clark (1998) compiled and plotted the maximum depth of the induced relaxation zones for models run with various geometries and K-ratios.

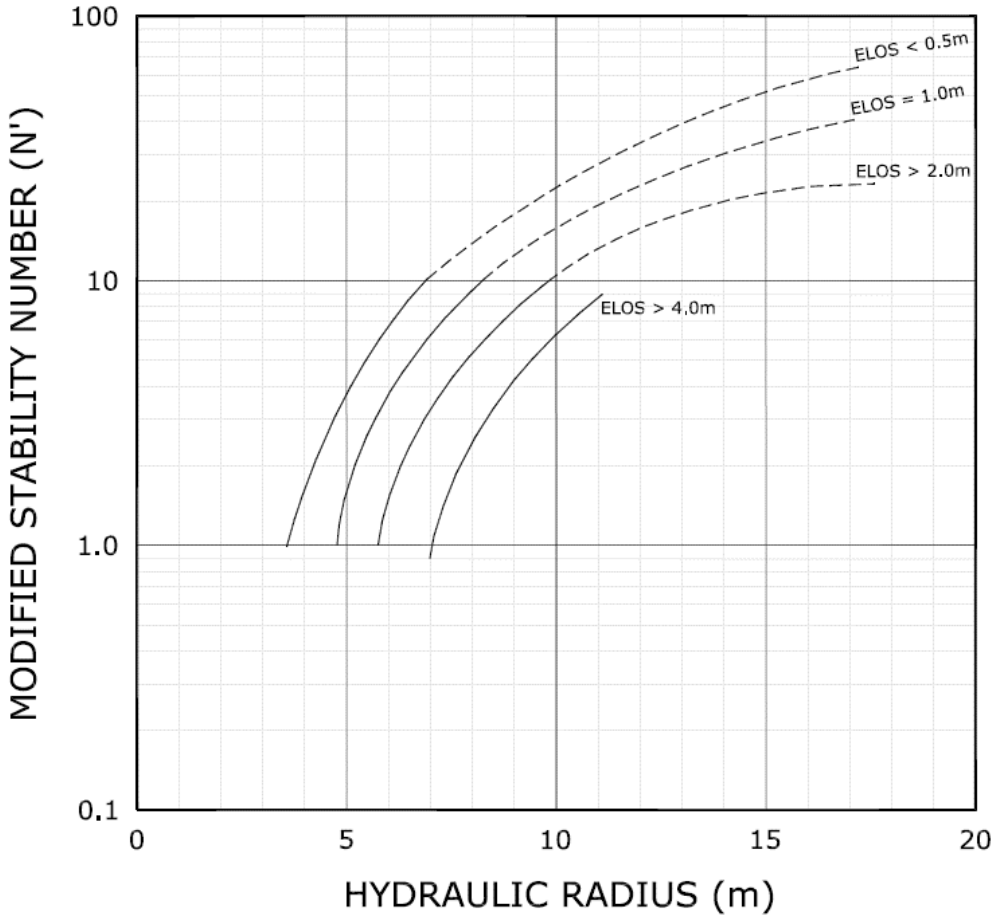

Figure 2-16: Empirical estimation of dilution as ELOS using the Dilution Graph (from Schartner, 2018; after Capes, 2009).

At the same time as Clark (1998) was completing his research, Milne (1997) assessed the elastic strain responses at different locations on a surface, represented by the ERF of that point, and found that the elastic strain converged to a constant when the ERF was approximately equal to the distance of the anchor furthest from the surface. The constant strain value is associated with the upper bound to the elastic response predicted by Equation 2-8, suggesting that when the ERF is larger than then maximum distance of the anchor segment to the surface, the anchor segment is fully relaxed.

Wang (2007) introduced the term Equivalent Linear Relaxation Depth (ELRD), which is similar to ELOS, to represent the average depth of the zone of relaxation based on Equation 2-21.

$$ELRD = \frac{Volume\ of\ relaxation\ on\ a\ Stope\ Surface}{Stope\ Surface\ Area} \qquad \text{EQUATION 2-21}$$

Wang (2007) then created a similar plot to Clark (1998) for his model results, representing the zone of relaxation with ELRD instead of maximum depth of relaxation (Figure 2-17b).

Although the results for the data series K=1.5 differ, similar trends are apparent in the plots by both Clark (1998) and Wang (2007). Generally speaking, the zone of relaxation expands as the geometry becomes larger and the rate of expansion increases for bigger K-ratios (Figure 2-17).

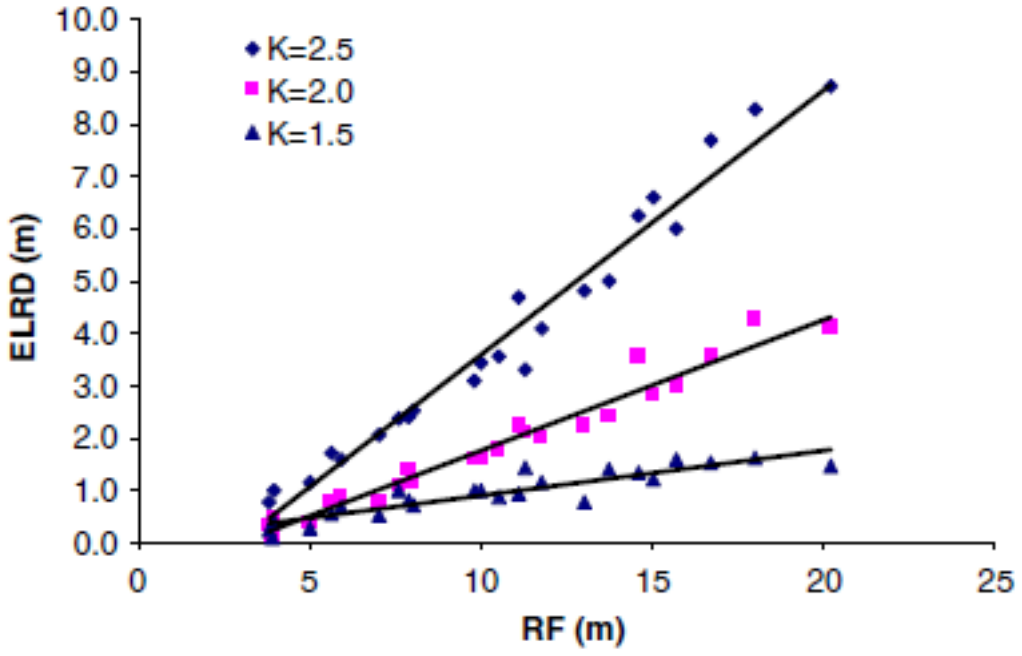

Figure 2-17: Average depth of relaxation for different geometries and K-ratios (from Wang et al., 2004).

2.6.6 Numerical modelling for stope design

Numerical models combine empirical and theoretical calculations to assess rock mass stability both within the rock mass and along the opening boundary (Potvin, 1988). In stope designs, numerical models are generally used to determine the stress field induced by excavating the stope. The calculated stresses can then be assessed against indicators of compressive or tensile failure. Unconfined compressive failure is expected if the induced stress exceeds half of the uniaxial compressive strength of the rock mass, or tensile failure is modelled in rock masses that have a low tensile strength (Potvin, 1988).

Modelling results can be analyzed to identify zones of potential shear, compressive, or tensile failure. Designs can then be modified to mitigate the risk to an acceptable level. Sensitivity analysis can also be performed that test the influence of different parameters on the design. Some numerical models can run multiple iterations where rock that fails in either compression or tension is removed from the rock mass and the model is re-run until a stable geometry is achieved (Potvin, 1988).

Although modelling can be a powerful tool when used appropriately, it relies on complex mathematical computations, intrinsic assumptions, and a number of user inputs to represent a real-world problem. Even assuming flawless programming logic, the model results will only be as good as the input parameters, which are based on a relatively small number of field observations. Case histories can be used to calibrate model results; however, this assumes that future areas will have similar rock mass properties and respond similarly to previously excavated areas, which is not always the case.

2.7 Failure Prediction Based on Monitoring

Excavations do not always preform as predicted by models and other design tools. While monitoring can provide measurements on the behaviour of the excavations, these measurements are of limited use if not analyzed using appropriate tools. The development of techniques to interpret measurements and provide a prediction of approaching instability are an important tool to mitigate risks or avert the predicted instability.

2.7.1 Inverse Velocity Method

The inverse velocity method was developed by Fukuzono (1985) to monitor surface slopes in soil and was later adapted to hard rock by Rose and Hungr (2007). The inverse velocity method monitors trends in deformation over time to predict the time at which instability is expected to occur and has been used to accurately predict large surface slope failures with sizes ranging from 1 to 18 million cubic metres.

The inverse velocity method relies on time-dependent deformation data which indicates accelerating creep as the slope becomes less stable (Rose and Hungr, 2007). The concept was developed by Fukuzono (1985) and was based on the analysis of rain induced landslides in large scale laboratory tests. As the time of failure is approached, the displacement velocity increases asymptotically towards infinity and the inverse of velocity decreases towards zero. Although deformation rates never reach infinity (Carla et al., 2017a), and in some cases decrease prior to failure (Mazzanti et al., 2015), the observation of the raw trend, or data averaged trend, still provides a useful estimate of failure time, although estimates should be used with caution with a margin for error (Crosta and Agliardi, 2003; Carla et al., 2017a).

Through observing plots of the inverse of the observed displacement over an interval of time (inverse velocity) versus time, Fukuzono proposed a trend defined by Equation 2-22. The slope of the trend has a different form depending on the constant α such that the trend is linear when α equals two, decreases with time for α less than two, and increases with time for α greater than two (Figure 2-18a). Although non-linear forms of trend were proposed, Fukuzono suggested that the linear trend ($\alpha = 2$) provides a reasonable approximation, especially closer to the time of failure, which was later supported by other authors (Voight, 1988; Voight, 1989; Kilburn and Petley, 2003; Rose and Hungr, 2007; Mazzanti et al., 2015). Consideration should still be given to the non-linear trends, as there are some cases where non-linear trends provide a better fit (Crosta and Agliardi, 2003), though this might not be recognized until after failure occurs.

$$V^{-1} = [A(\alpha - 1)]^{\frac{1}{\alpha-1}}(t_f - t)^{\frac{1}{\alpha-1}}$$ EQUATION 2-22

Where: V^{-1} = Inverse Velocity

A = Fukuzono Slope Constant

α = Fukuzono Slope Constant

t = Time of Measurement

t_f = Time of Failure

Being an empirical method, the influence of various environmental elements, which can be difficult to identify and model independently, are accounted for within the trend (Costa and Agliardi, 2003). The effect of individual factors, such as groundwater, can result in periodic changes that are superimposed on the overall trendline (Rose and Hungr, 2007). Appropriate filtering and averaging can improve the reliability of the trendline; however, the periodic change may be enough to drive the slope to instability closer to the time of failure (Rose and Hungr, 2007).

The inverse velocity method was applied to rock slopes in mining environments by Rose and Hungr (2007) and used to predict failure times in three case studies. Both the inverse velocity plot and the velocity plot for the Betze-Post pit case study are shown in Figure 2-18b. Subsequently, additional case studies have been published that explore the application of the inverse velocity method, coupled with various methods of measuring slope movement to predict slope failures in both mining and non-mining applications (Dick et al., 2014, Mazzanti et al., 2015, Carla et al., 2017b). The use of the inverse velocity method is also described in guidelines for open pit design (Read and Stacey, 2009; Martin and Stacey, 2018) and practitioners have tried to standardize its application (Carla et al., 2017a; Bozzano et al., 2018; Carla et al., 2018).

To improve predictions from the inverse velocity method, it is important to adjust the prediction to reflect changes in the rate of deformation (Rose and Hungr, 2007). The term *Onset of Acceleration* (OOA) was introduced by Dick et al. (2014) to describe the beginning of an increase in the rate of measured displacement from baseline levels. This is an important trigger point and Carla et al. (2017b) suggest initiating slope monitoring, using the inverse velocity method, following the OOA. The term *Trend Update* (TU) was also introduced by Dick et al. (2014) to

describe a point at which there is a significant change in the deformation rate, following the initial OOA. Carla et al. (2017b) suggested that positive crossovers, where the long-term moving average is crossed by the short-term moving average, can assist in the identification of either the OOA or trend update. In cases where the slope deformation accelerates, a failure to identify a trend update will likely result in a failure time prediction that is too long, due to the inclusion of lower deformation velocities in the data averaging and trending.

Surface applications are sensitive to noise from both natural sources and measurement devices. To properly identify the underlying trend, measurement error associated with noise needs to be accounted for and eliminated (Rose and Hungr, 2007; Dick et al., 2014; Mazzanti et al., 2014; Carla et al., 2017b). Different filtering techniques have been proposed and often take the form of averaging displacements and velocities over several measurements. Selection of an appropriate filter can assist in the identification of the OOA and trend updates, which may be missed if only real-time data is reviewed (Carla et al., 2017b).

Results from the inverse velocity method improve as the density of measurement points on the slope increase. Initially, slopes were only monitored at a small number of locations through manual survey or instrumentation. As a result, the inverse velocity method could only be applied to large-scale failures, as there was insufficient measurement resolution to analyze smaller blocks or discrete wedge failures. With technological developments, such as Slope Stability Radar (SSR) and Terrestrial Synthetic Aperture Radar Interferometry (TInSAR) (Mazzanti et al., 2014), the density of measurement has increased, allowing the monitoring of smaller failures.

(a)

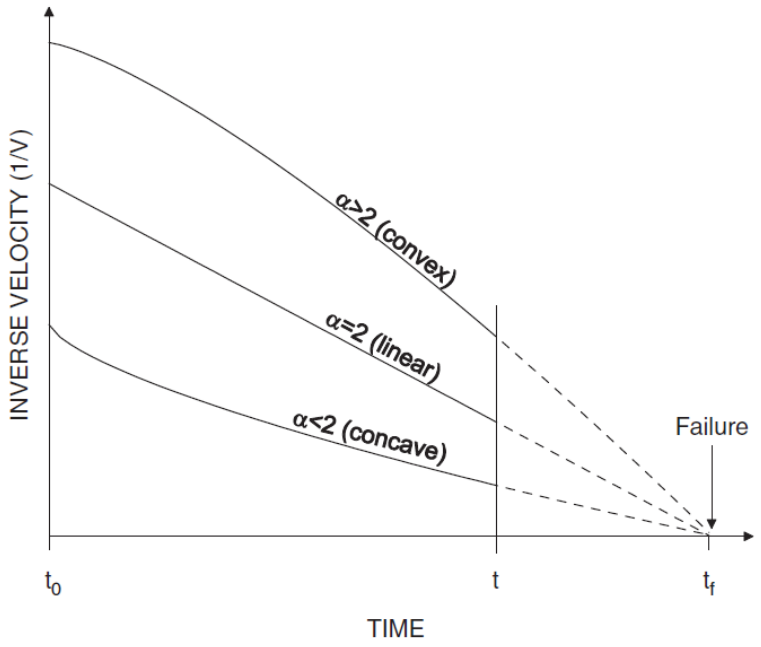

(b)

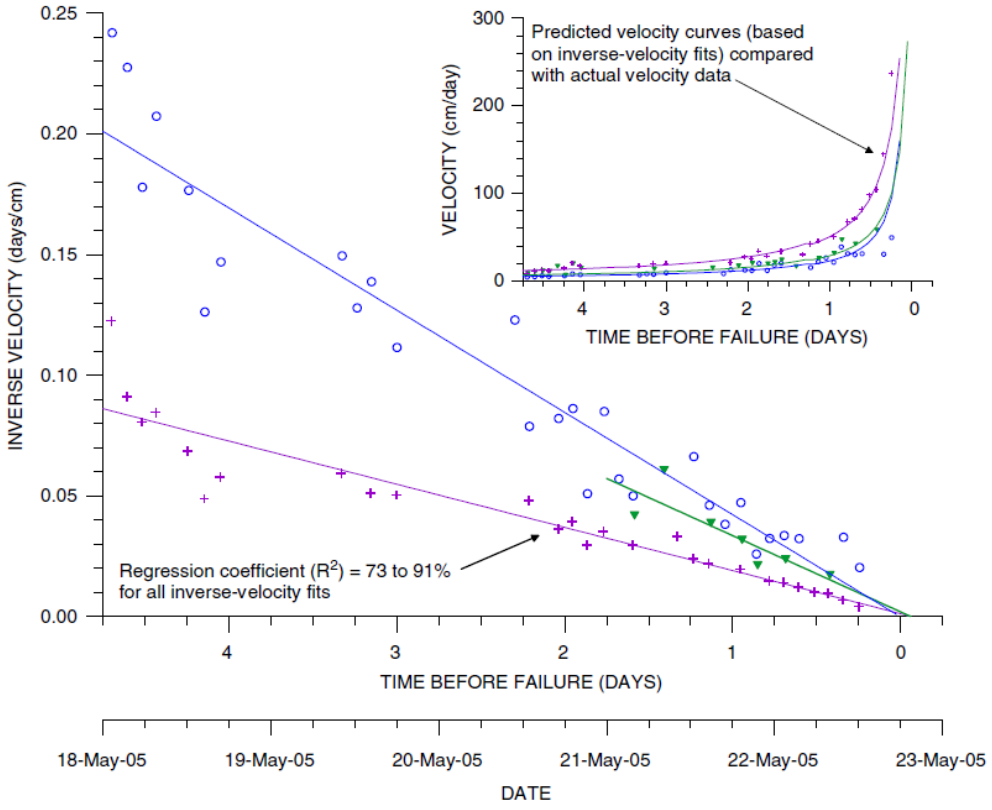

Figure 2-18: Inverse velocity plots showing (a) different trends based on different values of α (after Fukuzono, 1985; from Rose and Hungr, 2007) and (b) Inverse velocity and velocity plots of movement of the Betze-Post pit's southeast wall (after Rose and Hungr, 2007).

2.7.2 Strain Effective Radius Factor

The Strain Effective Radius Factor (SERF) method is an empirical technique for predicting a hanging wall geometry at which instability may occur (Milne and Snell, 2018). It applies a similar methodology to the inverse velocity method described in Section 2.7.1, but instead predicts a geometry of instability based on measured hanging wall strain. The time scale on the horizontal axis of Figure 2-18 is replaced with the hanging wall geometry, represented by ERF (Section 2.5.2), as shown in Figure 2-19f and the inverse velocity on the vertical axis of Figure 2-18 is replaced by ERF/ strain.

While increased hanging wall strain has been associated with increases in hanging wall geometry (Milne et al., 1996, Milne, 1997, Milne et al., 2004), this relationship was not applied to predict instability. The ERF workflow developed by Milne (1997) to monitor hanging wall deformation and strain using extensometers was modified by Milne and Snell (2016) to consider the SERF method as shown in shown in Figure 2-19. An extensometer is installed in the stope hanging wall prior to undercutting as shown in cross section (Figure 2-19a) and a true longitudinal view (Figure 2-19b). Following undercutting, the subsequent stope blasts are shown in a true longitudinal view along with the anchor locations (Figure 2-19c). The resultant theoretical segment strain associated with the response to these blasts is shown in Figure 2-19d, and the ERF calculation for extensometer anchor projections for each blast geometry (Figure 2-19e). The strain plots generally produce a step-like data series with the majority of the stain change occurring near the time of the blast. In some cases, there are additional strain changes between blasts which are attributed to the change in geometry when using the SERF method. Depending on the orientation of the extensometer relative to the stope hanging wall, it is possible that multiple anchors may project to the same location. The final SERF stage (Figure 2-19f) adds to the analysis approach outlined by Milne (1997) by plotting the inverse of strain against the ERF as introduced by Milne and Snell (2016).

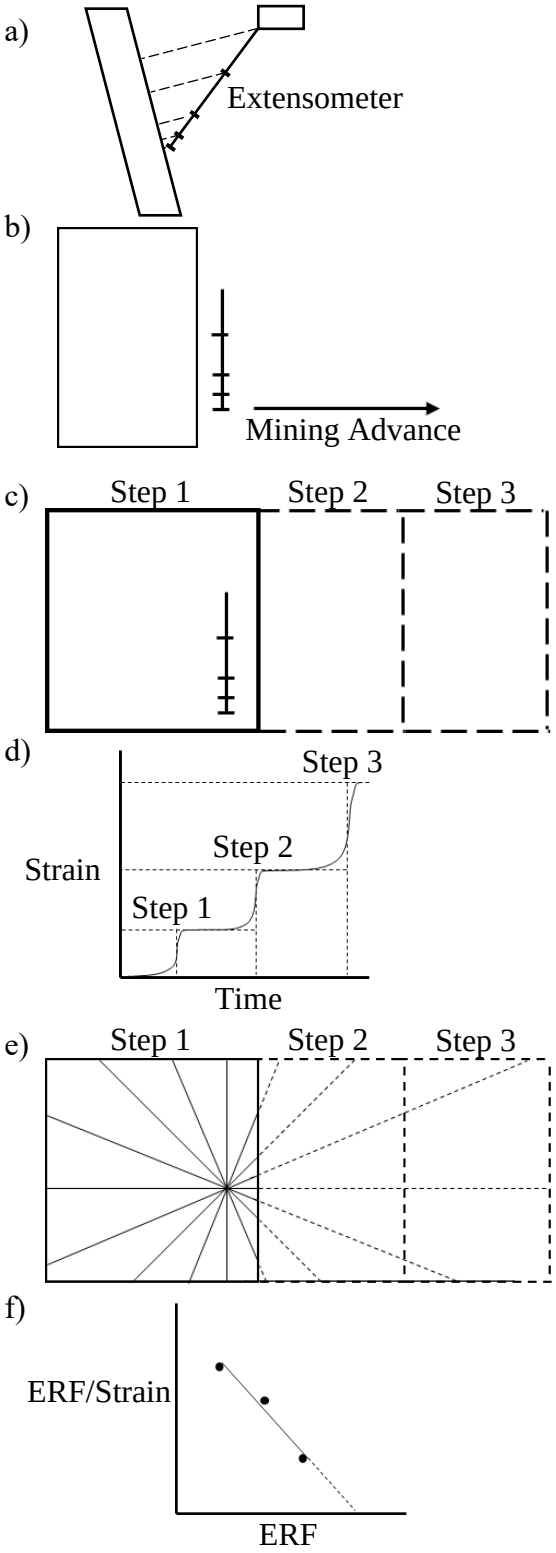

Extensometer cross section with anchor locations projected onto the hanging wall.

Extensometer located in the stope abutment, prior to undercutting. Deformation during this stage is ignored.

Extensometer has been undercut. Deformation is obtained for each subsequent mining step.

Conventional plotting of strain data versus time for each extensometer anchor

ERF calculated for each extensometer anchor location, for each step.

Inverse of strain plotted against stope geometry, expressed as the ERF value.

Figure 2-19: Steps involved in the SERF workflow to assess the extensometer dataset using instrument locations, opening geometry, and the ground response to mining (after Milne, 1997; Milne and Snell, 2016).

The SERF method was developed by combining the observation that the strain between anchors increases as the stope ERF increases (Milne et al., 2004) with the prediction of instability based on taking the inverse of velocity (Fukuzono, 1985). As hanging wall instability, in this application, is driven by the opening size, rather than time, the SERF method replaces time with ERF on the horizontal axis (Milne and Snell, 2016) in a modification of the inverse velocity plot (Figure 2-20). As a result of changing the variable on the horizontal axis, the SERF method predicts a geometry of instability, instead of a time of instability, at the point where the trendline intercepts the horizontal axis. Although the predicted instability is associated with a geometry, considering the production schedule and blast designs, a time until instability can be inferred. As with the inverse velocity method, as additional data is collected following subsequent production blasts, the SERF plot should be queried to identify trend updates, which could result in a change to the predicted geometry of instability (Rose and Hungr, 2007; Dick et al., 2014).

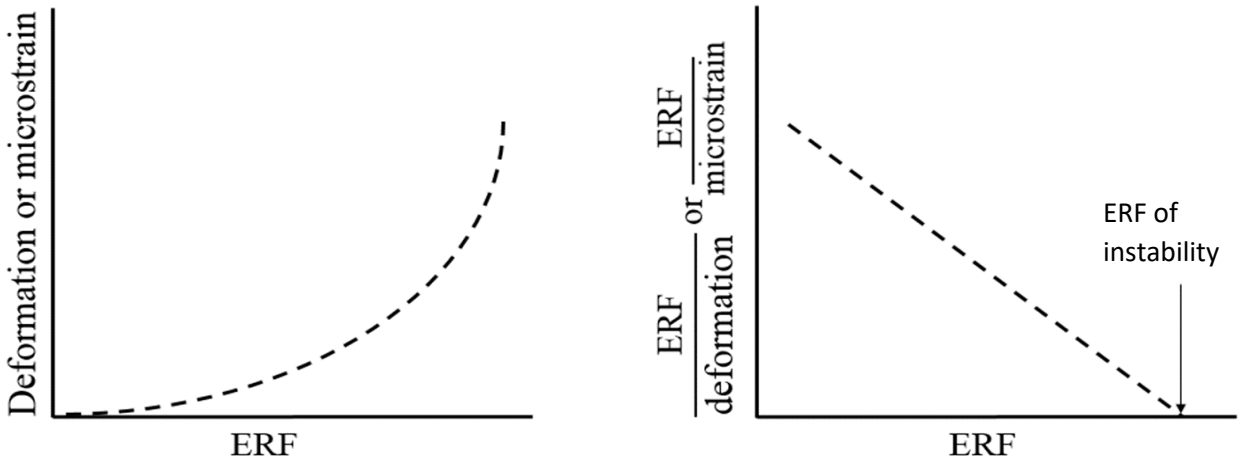

Figure 2-20: Theoretical plots of the relationship between microstrain and ERF and the inverse of microstrain and ERF (after Milne and Snell, 2018).

The form of instability predicted by the SERF method is related to the non-linear sag of the hanging wall into the opening (Figure 2-3 Stage 3). Deposits with a hanging wall consisting of a stratified or bedded rock type are well suited to this form of instability (Figure 2-21). A theoretical section through a stope showing the progression from an initial stope geometry to a failed geometry, through the opening of cracks in the hanging wall, is shown in Figure 2-22. Examples of this form of instability, where the hanging wall spalls and fails back to planar features parallel to the original hanging wall, are shown for two case studies in Figure 2-23. By monitoring hanging walls with

extensometers containing multiple anchor segments, it is possible to apply the SERF method to predict a geometry of instability based on each anchor segment (Milne and Snell, 2018). The depth of the predicted instability is associated with the segment farthest from the opening predicting instability.

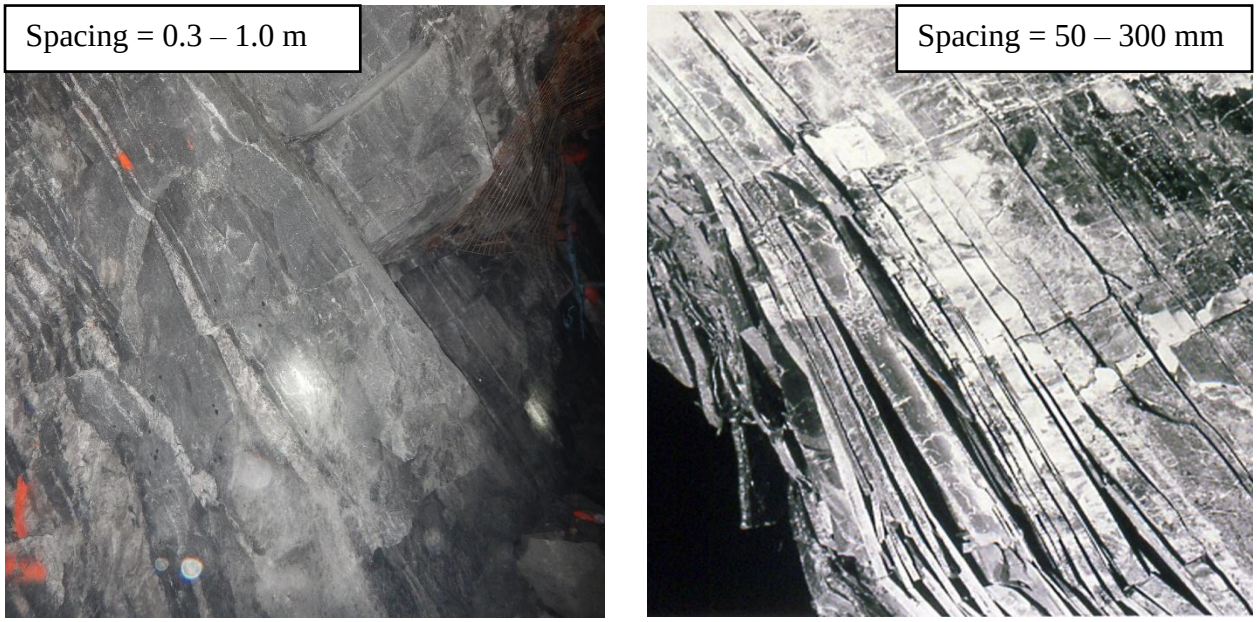

Figure 2-21: Stratified bedding of hanging wall rock. Left image-Seabee Gold Operation, Right image- Mount Isa Mine (Mount Isa Mines, 1984).

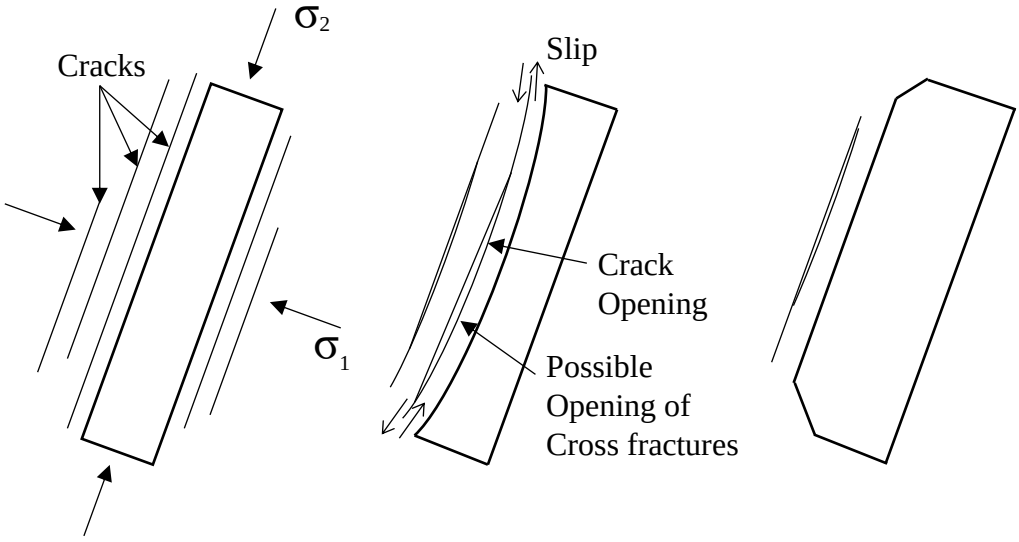

Figure 2-22: Crack opening and propagation in a stope hanging wall (after Beer et al., 1983).

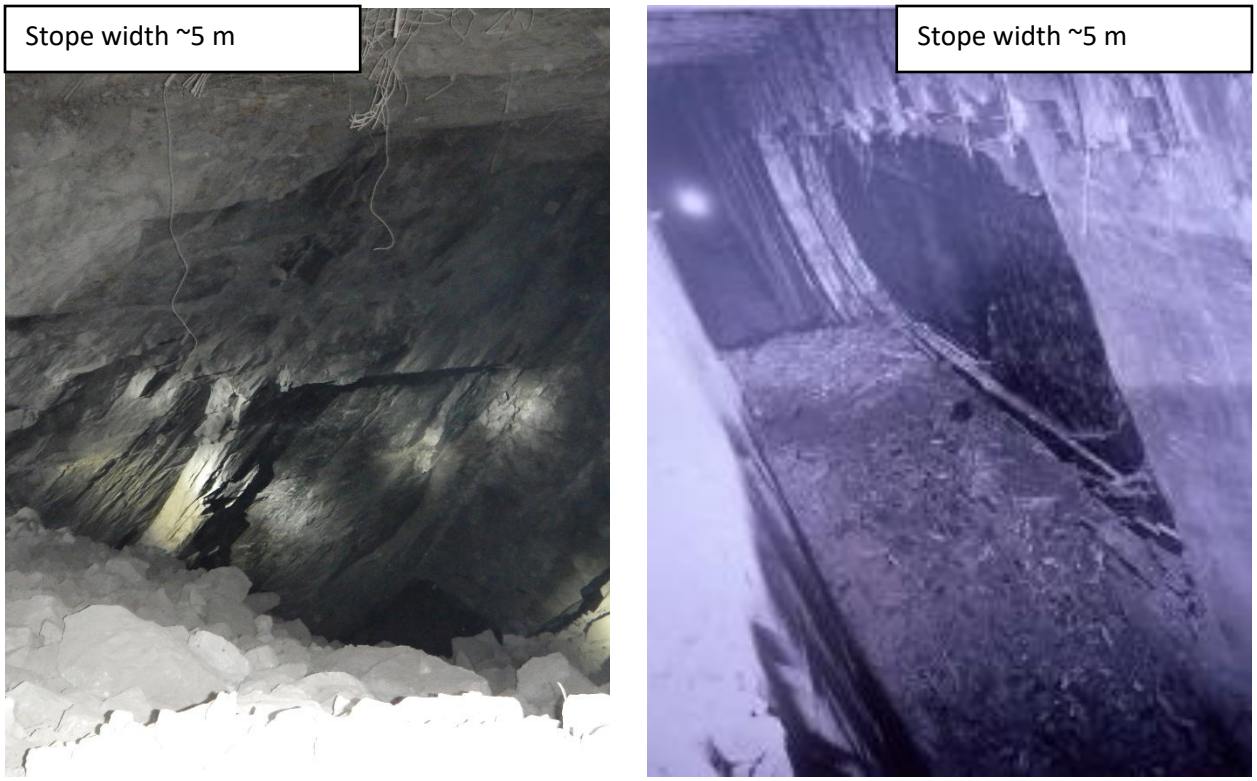

Figure 2-23: Form of hanging wall instability predictable by the SERF method. Left image- Seabee Gold Operation (2017), Right image- Mount Isa Mine (Mount Isa Mines, 1984).

Milne and Snell (2018) highlighted several assumptions related to the inverse velocity method and their equivalent assumptions for the SERF method. These assumptions have been compiled in Table 2-3. As noted in Section 2.7.1, the size of instability that can be predicted is dependent on the resolution of the data collection network. If additional monitoring points were available, it is possible that smaller scale instability could be identified.

The application of the SERF method to predict a geometry of hanging wall instability requires increasing, non-linear anchor segment strains as the ERF increases due to subsequent stope blasting. The SERF method also requires that the dataset contains measurements from sufficient hanging wall geometries to confirm the onset of increasing non-linear strain and establish a trend of inverse strain that can predict a geometry of instability. If the dataset does not meet these requirements, or the strain trend changes to indicate hanging wall stabilization, the effectiveness of the SERF method cannot be determined. To date, only one case history has been published using the SERF method, where a geometry of instability was predicted for a failed hanging wall at Brunswick mine (Milne and Snell, 2018). This case history is detailed in Section 4.

Table 2-3: Comparison between assumptions required for the application of the inverse velocity and SERF methods.

Inverse Velocity	SERF
Slope geometry is relatively constant and time is the governing factor for instability.	Excavation time is relatively brief and hanging wall geometry is the governing factor for instability.
Rock mass conditions are relatively constant and groundwater relatively static.	Rock mass conditions are relatively constant and groundwater relatively static.
Does not predict discrete wedge or block failures.	Does not predict discrete wedge or block failures.
Is not applicable for the prediction of stress driven failure.	Is not applicable for the prediction stress driven failure.

2.8 Trigger Action Response Plan

Although presented in the context of open pit mining, Read and Stacey (2009) note that most ground control programs include a series of planned responses to probable events, referred to as a Trigger Action Response Plan (TARP). Dick et al (2014) suggest the integration of slope deformation alarms, associated with a deformation velocity exceeding a defined threshold, into a mine's TARP. Once the implementation of TARP is triggered, the methodology may elevate TARP to critical alert levels if failure is imminent or result in the removal of TARP following an assessment of the slope deformation behaviour and associated risks. A similar approach of escalating the alert level, and increasing the number of measurements, is described by Crosta and Agliardi (2003).

3 APPROACH TO FIELD DATA ANALYSIS

The analysis of the hanging wall deformation response to sequential excavation, outlined in Section 2.2.1, includes the assessment of the type of deformation being measured. For this assessment, deformation is considered as the strain between anchor points. Elastic strain can be related to changing stresses due to blasting and the undercutting blast can be used to estimate the pre-mining stresses at the measurement location. When the data indicates that the rock mass is no longer behaving elastically, the SERF method may be applied to predict a geometry of hanging wall instability.

3.1 Data reliability

The extensometer datasets should be reviewed to assess the reliability of the data for stress estimation and SERF analysis, prior to detailed analysis. Potential problems with the data can be broken into mechanical / electrical problems and rock mass behaviour problems. Possible mechanical / electrical problems include the following:

- Loose or poorly bonded anchors which can be identified when strain between two adjacent anchor segments have a combined strain approximately equal to zero. This occurs when the shared anchor between two segments is loose and moves independently, resulting in compressional strain in one anchor segment and approximately the same magnitude of tensile strain in the adjacent anchor segment. Some useful data may still be obtained by combining the two segments and assessing the total strain, although the magnitude may be lower due to the longer anchor segment length.
- Broken or shorted wiring can indicate an anchor that has been excavated, or simply failed, leaving the anchor intact. In either case, failed wires can be identified by a lack of anchor response to subsequent stope mining.
- Water ingress into the wiring can result in random fluctuations in readings. As long as the fluctuations are not continuous, these fluctuations can often be filtered out through averaging.

Problems associated with the interpretation of deformation data can also pertain to the behaviour of the rock mass which sometimes cannot be associated with changing stress conditions, changes

in the stope geometry, or approaching instability based on the SERF analysis. Discrete wedges or other structural instability may create conditions where the SERF method is not expected to work.

If extensometers are installed normal to the stope wall, strains can more easily be related to changes in the stress normal to the stope. As discussed in Section 2.2.1, as mining approaches and subsequently undercuts an extensometer location, stress related strains between anchor locations can be expected to initially increase with approaching mining and then decrease after undercutting. If mining is approaching the instrument location from only one direction, a stress increase of up to approximately three times the initial stress may be expected based on considering the excavation as a cylindrical opening (Equation 2-4). Near openings, an elastic compressive stress response should not be expected to exceed the intact rock strength, since substantial rock mass confinement is unlikely. If the compressive strains exceed the expected limits, and the cause does not appear to be mechanical / electrical, the following rock mass behaviour may be the cause:

- The rock mass may have failed under high stress, creating new fractures, and reducing the overall elastic modulus. The resulting strains would then be very hard to interpret.
- Stress induced shearing could cause very high apparent compressive strains.
- Gravity induced shearing could cause very high apparent compressive or tensile strains. This would be more likely if extensometers were not installed normal to the stope hanging wall, as shown in Figure 3-1.

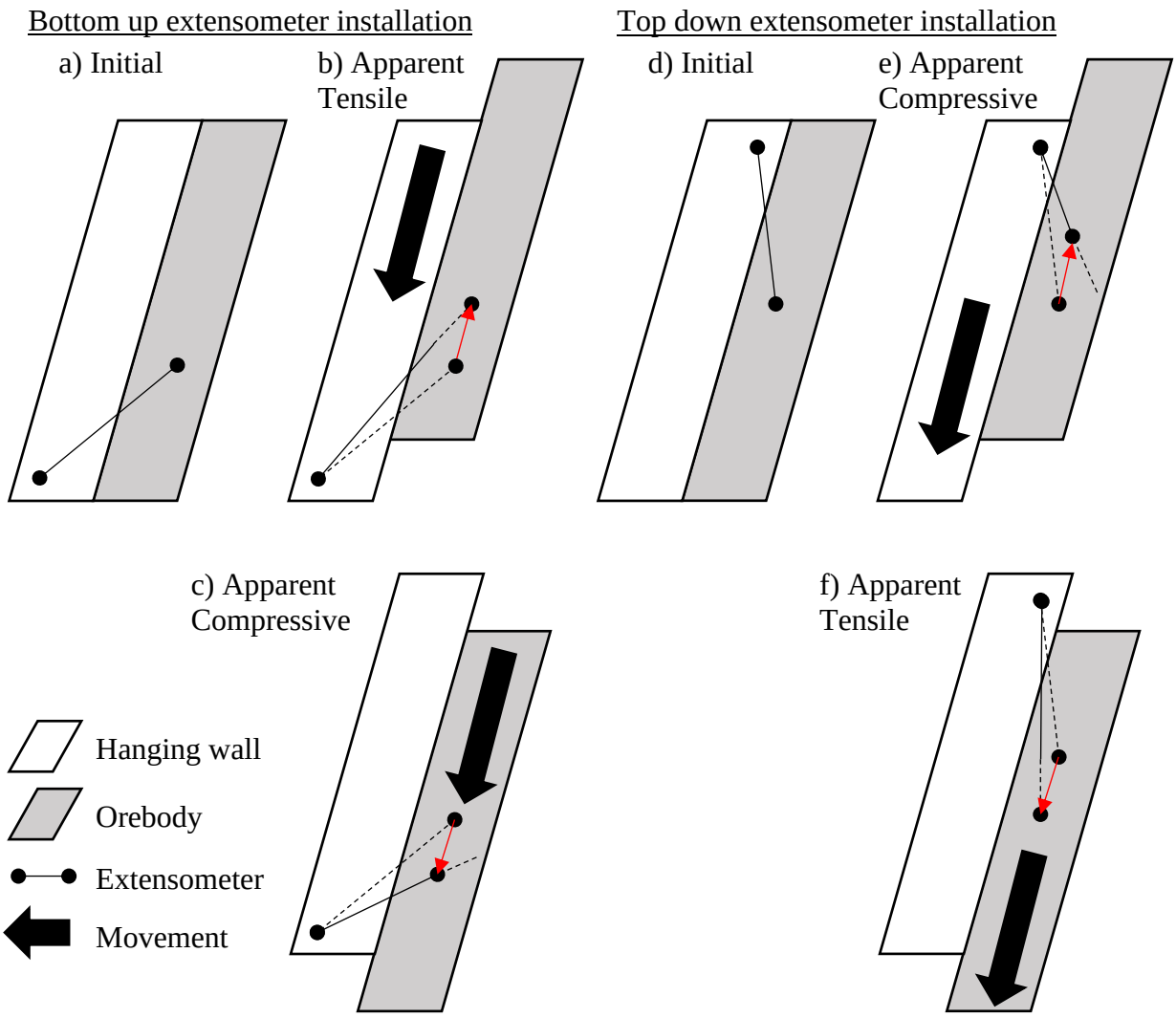

Figure 3-1: Schematic of gravity or stress induced shearing resulting in different strain responses for a bottom up extensometer installation showing (a) initial anchor positions, (b) shearing resulting in an apparent tensile strain, and (c) shearing resulting in an apparent compressive strain or for a top down installation showing (d) initial anchor positions, (e) shearing resulting in an apparent compressive strain, and (f) shearing resulting in an apparent tensile strain

3.2 Stress estimation

3.2.1 Cylindrical openings

One of the objectives of this thesis is to estimate the stress normal to an excavation, based on measured displacement, or the resulting strain. The equations to calculate displacement around a simple cylindrical opening were considered first, to build on Kirsch's closed form solutions. The radial displacements of two points (r_1 and r_2), induced by the creation of a cylindrical opening, can be determined from Equation 2-2. The strain between the two points (r_1 and r_2) (Figure 3-2), can be calculated using Equation 3-1.

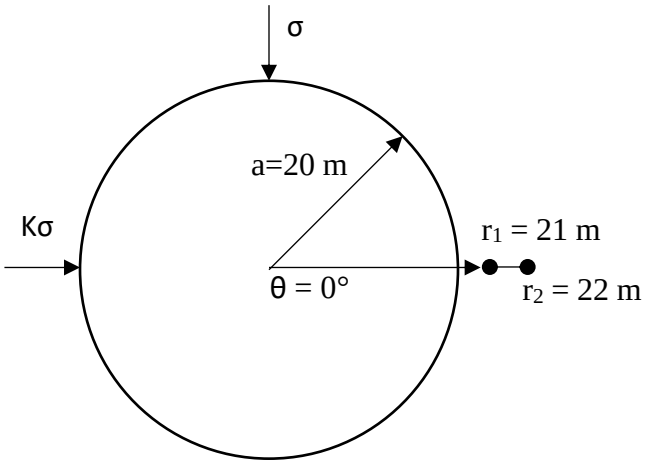

$$\varepsilon_{rr} = \frac{u_{r1} - u_{r2}}{r_2 - r_1} \qquad \text{EQUATION 3-1}$$

Figure 3-2: Schematic showing two points near a cylindrical opening from which a strain can be calculated from the difference in displacement due to the opening and the distance between the points.

Another approach is to use the Kirsch solution to calculate the stresses induced by the excavation (Equation 2-4) to determine the change in stress. Assuming plane strain, the strain normal to an excavation can be expressed in terms of the initial stresses and elastic constants. Since the radial strain will decrease with distance from the opening, strain is calculated near the opening at points r_1 and r_2. For this example, consider the cylinder to represent a horizontal tunnel, where the pre-mining stress (σ_{pre}) are equal to σ for the vertical stress and Kσ for the horizontal stress. The ground response at the boundary of the cylinder is considered to assess the largest theoretical stress change. The stress change at the boundary, and for θ = 0 where the radial stress is aligned with the horizontal stress such that the Kirsch stress changes in the plane of the excavation are:

$$\Delta\sigma_{rr} = \sigma_{rr(induced)} - \sigma_{horiz(pre)} = \sigma_{rr} - K\sigma = 0 - K\sigma = -K\sigma$$

$$\Delta\sigma_{\theta\theta} = \sigma_{\theta\theta(induced)} - \sigma_{vert(pre)} = \sigma(3 - K) - \sigma = 2\sigma - K\sigma$$

By applying Hooke's Law, the induced stress along the tunnel axis required for plane strain conditions can be calculated at points r_1 and r_2.

$$\varepsilon_z = 0 = \frac{1}{E}[\Delta\sigma_z - \nu(\Delta\sigma_{rr} + \Delta\sigma_{\theta\theta})]$$

$$\Delta\sigma_z = \nu(\Delta\sigma_{rr} + \Delta\sigma_{\theta\theta})$$

Solving for the radial strain at the boundary,

$$\varepsilon_{rr} = \frac{1}{E}[\Delta\sigma_{rr} - \nu(\Delta\sigma_{\theta\theta} + \Delta\sigma_z)]$$

$$\varepsilon_{rr} = \frac{1}{E}\left[\Delta\sigma_{rr} - \nu\left(\Delta\sigma_{\theta\theta} + \nu(\Delta\sigma_{rr} + \Delta\sigma_{\theta\theta})\right)\right]$$

$$\varepsilon_{rr} = \frac{1}{E}\left[(-K\sigma) - \nu\left((2\sigma - K\sigma) + \nu((-K\sigma) + (2\sigma - K\sigma)\right)\right]$$

$$\varepsilon_{rr} = \frac{1}{E}\left[-K\sigma - \nu(2\sigma - K\sigma) - \nu^2(2\sigma - 2K\sigma)\right]$$

$$\varepsilon_{rr} = \frac{-\sigma}{E}\left[K + \nu(2 - K) + 2\nu^2(1 - K)\right] \qquad \text{EQUATION 3-2}$$

A simple numerical model was run in Examine2D and the modelled displacement, and associated strain, were compared to the strains calculated using both the Kirsch solution (Equation 2-2) and the combined Kirsch and Hooke solution (Equation 3-2). The circular opening modelled had a radius of 20 metres and the rock mass had a Poisson's ratio of 0.25 and an elastic modulus of 50 GPa. The modelled anchors were located one metre and two metres from the opening as shown in Figure 3-2 so that a model result could be returned and compared to the stress change derived from the closed form solution for displacement (Equation 2-2). After the relationship was verified, the strain estimate from the closed form solution was compared to the estimate from Equation 3-2. The plot of the model results (Figure 3-3 and Table 3-1) shows reasonable correlation between the model, Kirsch, and Kirsch/ Hooke strain values. The correlation is further improved when considering the comparison of the microstrain between the two anchors or at the excavation boundary. Full details of the modelling are available in Appendix A.

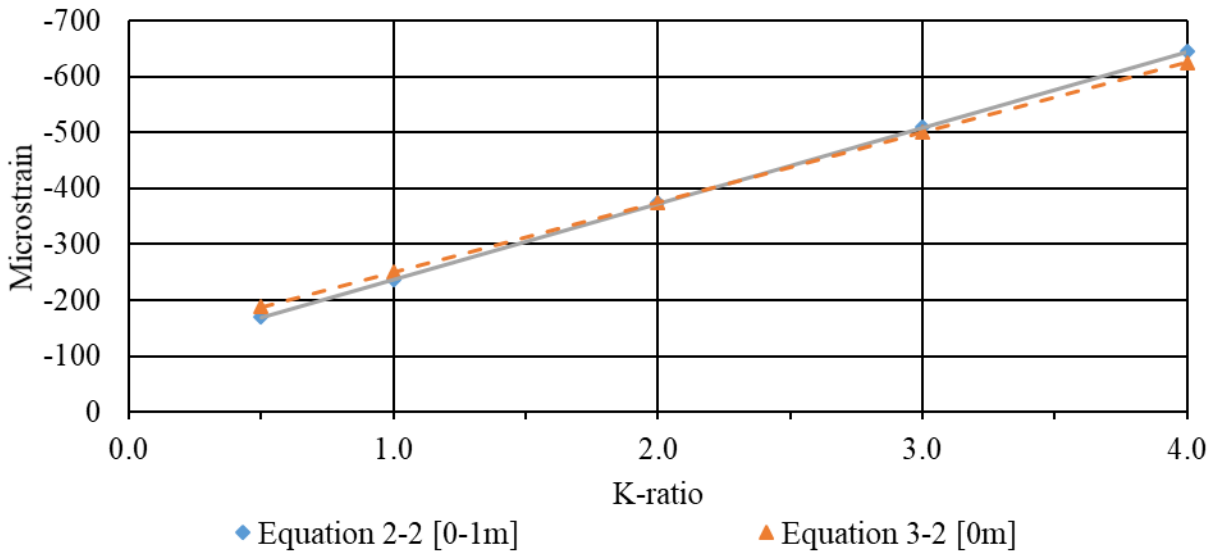

Figure 3-3: Comparison of the modelled induced strains around a circular opening, under different horizontal to vertical stress ratios.

Table 3-1: Comparison of the modelled induced strains around a circular opening, under different horizontal to vertical stress ratios.

K	Microstrain				
	Examine 2D [1-2m]	Equation 2-2 [1-2m]	Equation 2-2 [0-1m]	Equation 3-2 [0m]	Delta* (%)
0.5	-143	-141	-170	-188	11%
1.0	-219	-216	-238	-250	5%
2.0	-372	-368	-374	-375	0%
3.0	-524	-520	-510	-500	-2%
4.0	-677	-671	-645	-625	-3%

*Delta = (Equation 3.2 – Equation 2.2) / Equation 2.2

3.2.2 Tabular openings

Despite the limitations in applying the Kirsch closed form solution for circular openings to tabular openings, which are more indicative of geometries in mining applications, the ability to reasonably estimate induced strains around a circular opening from the elastic properties of the rock mass suggest a similar approach may be possible for tabular openings.

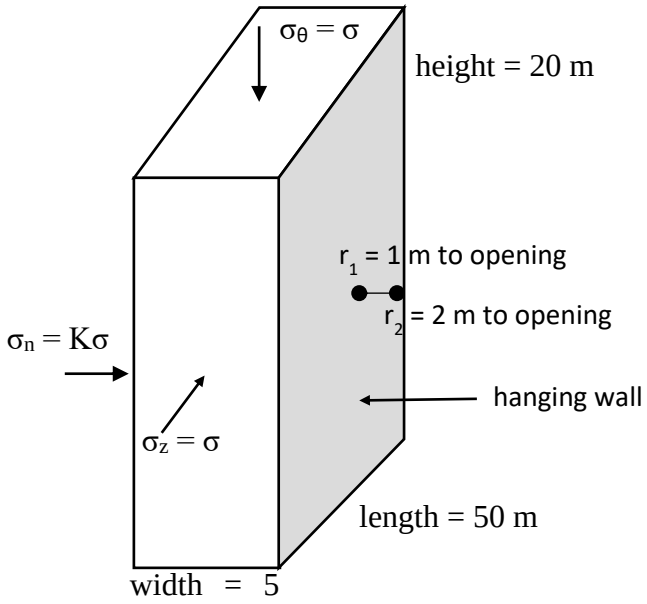

Figure 3-4: Schematic showing two points near a tabular opening from which a strain can be calculated from the difference in displacement due to the opening and the distance between the points.

For the simple stope geometry shown in Figure 3-4, a simplification was considered where plane strain was not assumed and both of the induced tangential stresses (σ_θ and σ_z), at the midpoint of the stope hanging wall, were assumed to equal zero. It is also assumed that the measurement points are close enough to the boundary that the induced normal stress (σ_n) is zero.

$$\Delta\sigma_n = \sigma_{n(induced)} - \sigma_{normal(pre)} = 0 - K\sigma = -K\sigma$$

$$\Delta\sigma_\theta = \sigma_{\theta(induced)} - \sigma_{vert(pre)} = 0 - \sigma = -\sigma$$

$$\Delta\sigma_z = \sigma_{z(induced)} - \sigma_{axial(pre)} = 0 - \sigma = -\sigma$$

Solving for the strain normal to the opening:

$$\varepsilon_n = \frac{1}{E}\left(\Delta\sigma_n - \nu(\Delta\sigma_\theta + \Delta\sigma_z)\right)$$

$$\varepsilon_n = \frac{1}{E}\left(-K\sigma - \nu(-\sigma - \sigma\ )\right)$$

$$\varepsilon_n = \frac{-\sigma}{E}(K - 2\nu) \qquad \text{EQUATION 3-3}$$

$$\Delta\sigma_n = K\sigma = \mathrm{K}\frac{\varepsilon_n E}{(\mathrm{K}-2\upsilon)}$$

$$\Delta\sigma_n = \frac{K\varepsilon E}{K\left(1-\frac{2\upsilon}{K}\right)}$$

$$\Delta\sigma_n = \frac{\varepsilon E}{\left(1-\frac{2\upsilon}{K}\right)} \qquad \text{EQUATION 3-4}$$

$$\Delta\sigma_n = 0 - \sigma_{pre}$$

$$\sigma_{pre} = -\frac{\varepsilon E}{\left(1-\frac{2\upsilon}{K}\right)}$$

As a simplification for when K=2

$$\Delta\sigma_n = \frac{\varepsilon E}{\left(1-\frac{2\upsilon}{K}\right)} = \frac{\varepsilon E}{\left(1-\frac{2\upsilon}{2}\right)}$$

$$\Delta\sigma_n = \frac{\varepsilon E}{(1-\upsilon)} \qquad \text{EQUATION 3-5}$$

$$\Delta\sigma_n = 0 - \sigma_{pre}$$

$$\sigma_{pre} = -\frac{\varepsilon E}{(1-\upsilon)} \qquad \text{EQUATION 3-6}$$

The form of Equation 3-5 is similar to the empirical equation that Milne (1997) developed for estimating the probable upper range for the elastic response of a rock mass due to adjacent mining of a tabular excavation (Equation 2-8). The difference is that Equation 2-8 is adapted from deformation around a circular opening, which tends to increase tangential stresses which induce greater strain normal to the opening and needed to be scaled down for a tabular opening. Comparing the calculations from Equation 2-8 and Equation 3-5, for a Poisson's ratio (0.25), results in a similar value.

$$\Delta\sigma_{\text{Equation 2-8}} \cong \Delta\sigma_{\text{Equation 3-5}}$$

$$\frac{\varepsilon E}{0.64(1+\nu)} \cong \frac{\varepsilon E}{(1-\nu)}$$

For $\upsilon = 0.25$

$$\frac{1}{0.64(1+(0.25))} \cong \frac{1}{(1-(0.25))}$$

$$1.25 \cong 1.33\ (within\ {\sim}7\%)$$

As for the circular opening, a tabular opening was modelled in Examine2D and the modelled displacement, and associated strain, were compared to the modelled stress. The modelled geometry was 20 metres high by five metres wide by 50 metres long in a rock mass with a Poisson's ratio of 0.25 and an elastic modulus of 50 GPa. The modelled anchors were located one metre and two metres from the opening at mid-height (Figure 3-4).

The plot of the model results (Figure 3-5) shows the input K-ratio and normal stress, as well as the modelled strains calculated from the modelled displacement of points r_1 and r_2. The modelled strains were then used to calculate the normal stress using the different formulas (Equation 2-8, Equation 3-4, and Equation 3-5). It is interesting to note that although Equation 3-5 is a simplification of Equation 3-4 when K=2, it appears to provide the best estimate of induced normal stress when K is greater than one, with the calculated values within 10% of the expected values. Additional numerical modelling was completed in Examine2D and RS3 for rock masses with different elastic properties and K-ratios to empirically validate Equation 3-5. Consistently, the stress predicted by Equation 3-5 was within 10% of the input normal stress, suggesting that it is a reasonable formula for predicting the pre-mining stress from the elastic strain response of a fully relaxed rock mass. Modelling results are available in Appendix A.

The underling assumption that tangential and normal stresses approach zero at the middle of a boundary surface is supported by the parametric study completed by Potvin (1988) and summarized in Figure 2-8 and Figure 2-9. Although modelling may indicate negative tangential stresses for models with higher K-ratios, it should be remembered tensile stresses in a fractured rock mass cannot be supported and will result in a relaxed or unstressed condition.

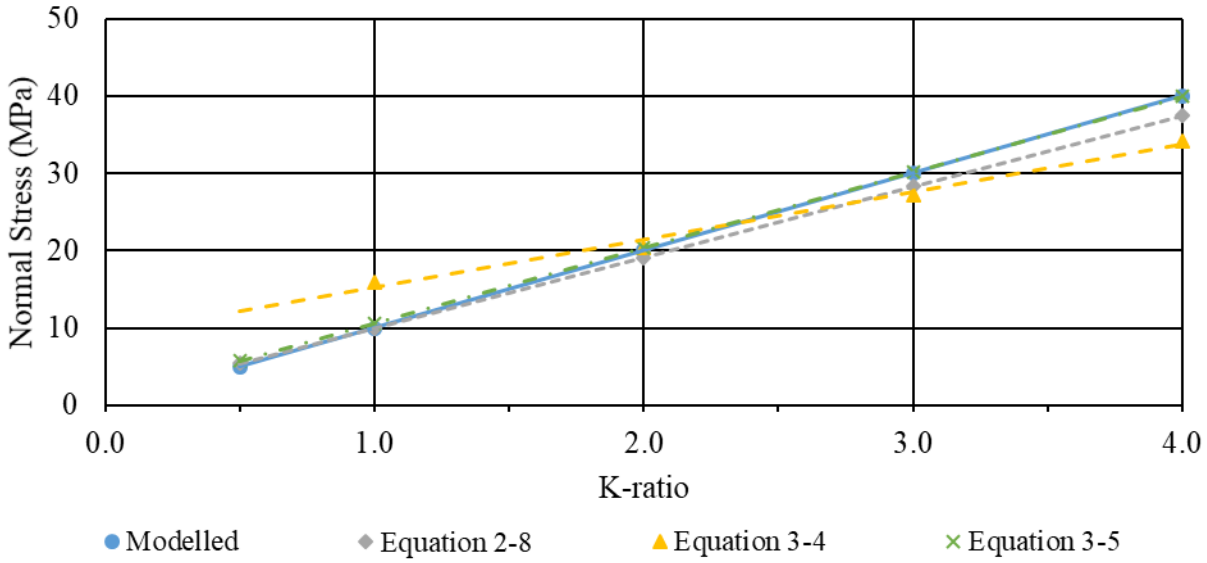

Figure 3-5: Comparison of the modelled induced normal stress around a tabular opening to the normal stress calculated from modelled strains, under different horizontal to vertical stress ratios.

Table 3-2: Comparison of the modelled induced normal stress around a tabular opening to the normal stress calculated from modelled strains, under different horizontal to vertical stress ratios.

K	Normal Stress						
	Modelled	Equation 2-8		Equation 3-4		Equation 3-5	
	(MPa)	(MPa)	Delta* (%)	(MPa)	Delta* (%)	(MPa)	Delta* (%)
0.5	5.0	5.4	8%			5.8	15%
1.0	10.0	10.0	0%	16.0	60%	10.6	6%
2.0	20.0	19.1	-4%	20.4	2%	20.4	2%
3.0	30.0	28.3	-6%	27.2	-9%	30.2	1%
4.0	40.0	37.4	-6%	34.2	-14%	39.9	0%

*Delta = (Calculated Stress-Modelled Stress) / Modelled Stress

3.2.3 Estimated Upper Bound to Elastic Deformation

Just as measured strain values can be used to estimate the pre-mining stress normal to a stope surface, estimated stress changes can be used to approximate the onset of non-linear deformation, which would be expected prior to rock instability.

An estimate of a strain associated with an upper bound to elastic deformation can assist with the identification of the onset of non-linear extension. As shown in Section 0, Equation 3-5 can be used to estimate an elastic response, normal to a surface. When measured strain due to mining a tabular excavation exceeds values calculated with Equation 3-7, the rock mass is either reacting to a drop in the effective elastic modulus, or the rock is responding non-linearly. Either response indicates a decrease in overall rock mass stability.

$$\Delta\sigma_n = \frac{\varepsilon_{(a-b)}\, E}{(1-\upsilon)}$$

$$\varepsilon_{(a-b)} = \frac{\Delta\sigma_n}{E}(1-\upsilon) \qquad \text{EQUATION 3-7}$$

Where: $\varepsilon_{(a-b)}$ = estimated upper bound to elastic deformation

$\Delta\sigma_n$ = change in stress acting normal to the opening

υ = Poisson's ratio

E = Elastic modulus

If unavailable from direct measurement or numerical modelling, an approximation for pre-mining stress normal to a planned opening can be made based on the depth of the opening, the expected K-ratio, and the unit weight of rock using Equation 1-2. Once estimates or measurements of the pre-mining stress have been made, the estimate of the upper bound to elastic deformation can be updated.

3.2.4 Pre-mining stress

The estimation of the pre-mining stress, for each extensometer location, is based on the short-term response of the stope hanging wall to undercutting. Once the undercutting blast is identified, the change in strain, due to undercutting, is measured and used to calculate the pre-mining stress based on Equation 3-6. Depending on the position of the extensometer relative to the stope abutments, the abutment may influence the zone of relaxation, as shown in Figure 3-6. As a general rule, if the normal distance to the furthest anchor considered is less than the ERF value of the anchors, Equation 3-6 should be valid (Figure 3-6a).

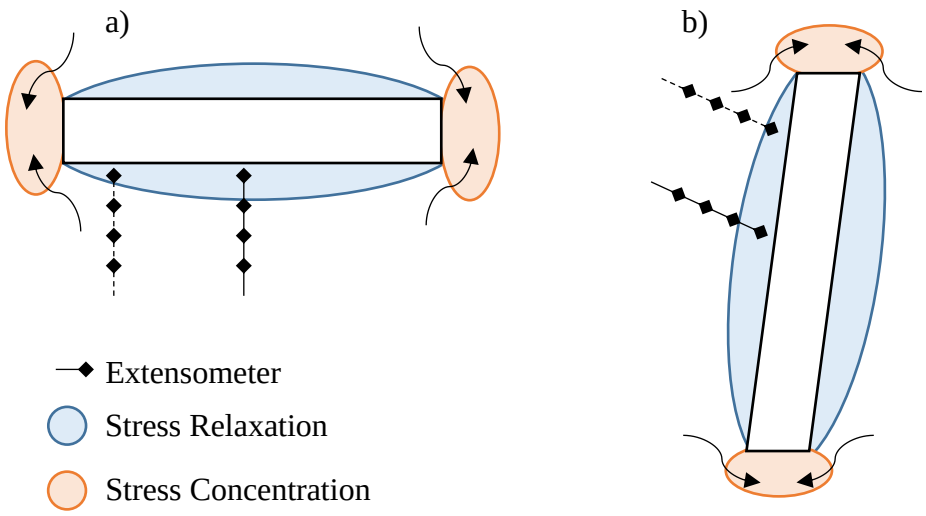

Figure 3-6: (a) Plan and (b) cross section of a stope showing stress deviation around the opening.

The undercutting blast can be identified by comparing the blast design and blast records to the extensometer anchor locations. The same true longitudinal view, including projected extensometer anchor positions and blast outlines, used to calculate the anchor ERF, can be used to identify the undercutting blast. Due to potential variations in the planned and 'as built' location of the extensometer anchors, the actual blast advance, and variability in the zone of relaxation, the predicted undercutting blast should be verified by examining the measured deformation response. This is especially true when the anchor locations are close to the opening abutment following undercutting (Figure 3-7).

The deformation data can be used to identify or verify the undercutting blast. Considering the theoretical ground response to mining, it is reasonable to expect a compressive response to be measured up to the point of undercutting, at which point the deformation trend would reverse and extension should be measured. In practice, this may be misleading as small magnitude extension may be measured that is unrelated to undercutting, the initial ground response may be reduced by ground support, and the depth of stress relaxation may not reach anchors further from the opening (Figure 3-6). Milne (1997) suggested that the depth of the zone of relaxation is approximately equal to the ERF of that point on the surface of the opening. This relationship can be used to predict if the anchor segment is fully relaxed, partially relaxed, or potentially still measuring a compressive response.

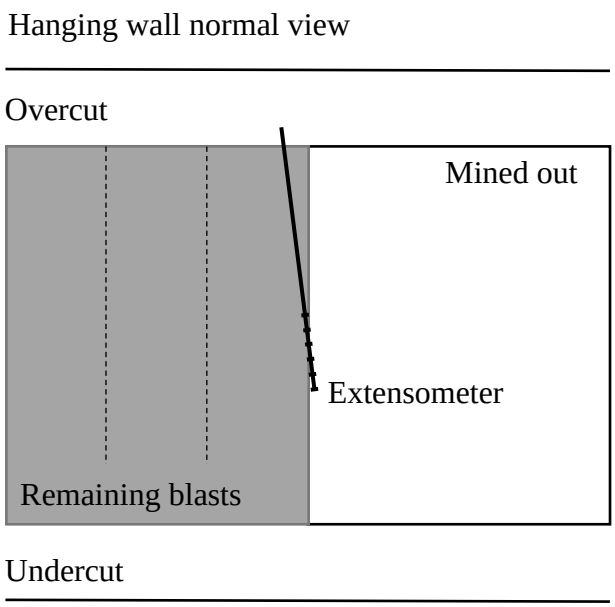

Figure 3-7: Illustration of extensometer anchors close to an undercutting blast front which should be verified by assessing the deformation measured in response to assumed undercutting.

Once the date and time of the undercutting blast are identified, the short-term strain change due to the blast can be identified. When data loggers are used, frequent measurements are collected and the strain just prior to the blast and within a couple of hours following the blast can be identified and used to calculate the change in strain (Figure 3-8). When manual readings are used, only a pre and post blast reading may be available for calculating the strain.

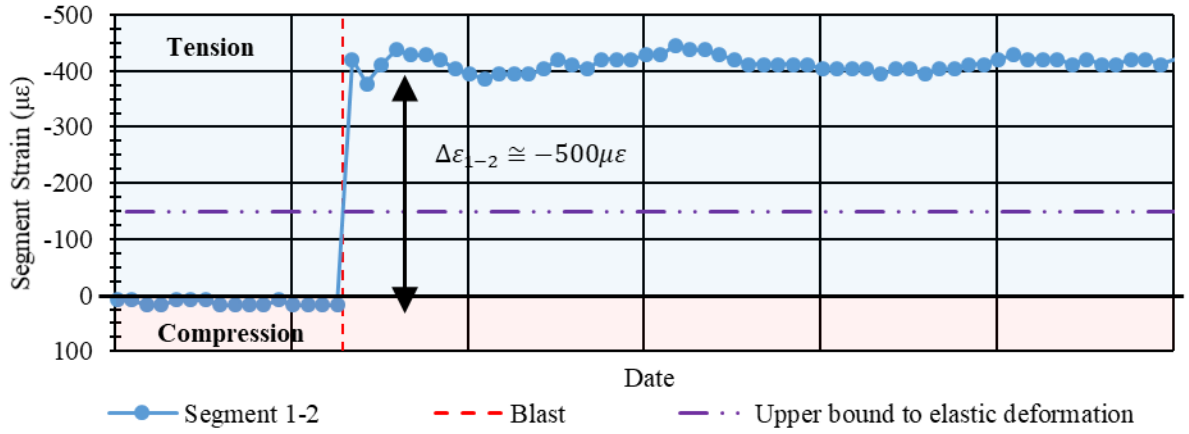

Figure 3-8: Plot of the short-term strain response over time to undercutting.

The measured change in strain can be used to estimate the associated change in stress, as described in Section 0. Because the principal stress normal to a surface of an opening reduces to zero, the change in stress can be used to predict a pre-mining stress using Equation 3-6. Depending on the initial stress state, and mining geometry, this can either be an estimate of the concentrated stress, just prior to undercutting, or the stress state prior to the beginning of stope extraction.

Possible issues with the estimated pre-mining stress can occur if the rock mass is not fully relaxed or if non-linear extension is occurring. Partial relaxation will result in an underestimation of the pre-mining stress. A simple comparison of the distance of the anchor segment from the surface to the ERF of the anchor location can provide insight into the extents of the zone of relaxation (Milne, 1997). When the ERF of the anchor is larger than the distance of the anchor segment to the surface, full relaxation can be expected.

Non-linear extension can be more difficult to identify. The estimated upper bound to elastic deformation can serve as an indicator of the transition from elastic to non-linear extension, which also serves as a bound to the effectiveness of Equation 3-6 to predict the pre-mining stress. If the estimated upper bound is exceeded, non-linear extension may be occurring, or, the elastic modulus of the rock mass may be deteriorating due to joint dilation. Knowing how to adjust the elastic modulus to be indicative of the deteriorating rock mass is challenging. It should be also be re-iterated that the estimated upper bound to elastic deformation is associated with the estimated pre-mining stress normal to the surface

3.3 Ground Response to Mining

This study is focused on the analysis of hanging wall deformation data, collected by extensometers, resulting from undercutting of the extensometer and during continued non-linear extension with continued mining. The estimation of the pre-mining stress occurs following undercutting of the extensometer and analysis using the SERF method can be conducted when non-linear extension is being measured. Application of the SERF method involves the identification of non-linear extension and can only be applied to continued non-linear extension with continued mining.

While the estimation of the elastic deformation limit can provide an indication of the transition from elastic to non-linear extension, it is best used in conjunction with the analysis of changes in the trend of strain measurements following subsequent stope blasting. Although the estimated

upper bound to elastic deformation may be exceeded following a stope blast, the increases in strain may be small relative to changes following subsequent stope blasts. This is illustrated following undercutting and the initiation of elastic extension (Figure 3-9a) when a smaller strain change was measured for the next blast. After this, subsequent blasts result in a trend of larger strain increases suggesting this to be the actual initiation of non-linear extension (Figure 3-9b).

If continued blasting and excavation of the stope does not result in additional deformation, the application of the SERF method is likely not applicable. In some cases, some form of intervention, such as stope backfilling, can reduce the rate of deformation and eventually stabilize a stope hanging wall. The influence of backfill on measured deformation can be seen in Figure 3-10c where the measured strain change following a blast reduces to near zero, suggesting the stabilization of the hanging wall. The backfill acts as a weak abutment and would reduce the effective ERF and RF for the unsupported hanging wall. When stabilization occurs, a trend update occurs and the SERF method should not be continued until a new trend of increasing non-linear extension is detected. In this example the transition from elastic compression to elastic extension (Figure 3-10a) and elastic extension to non-linear extension (Figure 3-10b) both appear to occur following the same blast.

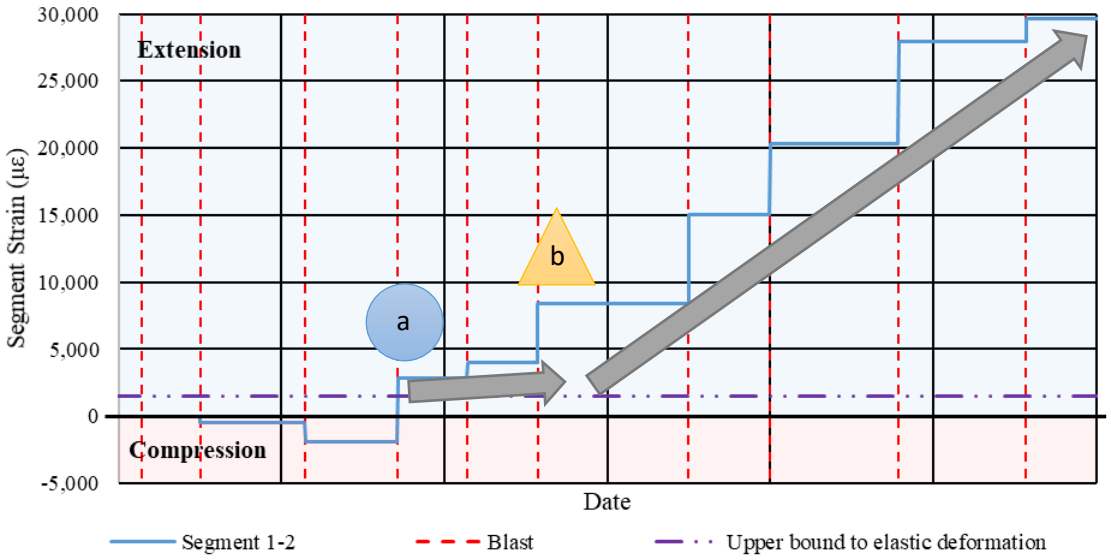

Figure 3-9: Time scale plot of the strain response to blasting showing larger strain increases for larger stope hanging wall geometries, (a) the transition from elastic compression to elastic extension following undercutting, and (b) the potential transition from elastic extension to non-linear extension.

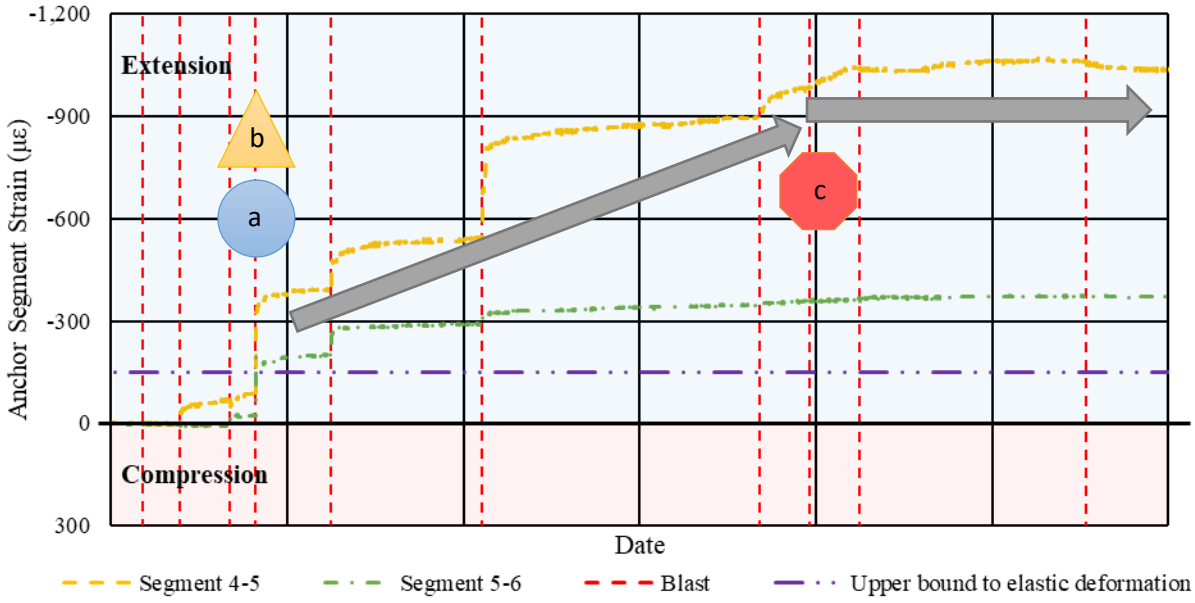

Figure 3-10: Time scale plot of the strain response to blasting showing larger strain increases for larger stope hanging wall geometries (a) the transition from elastic compression to elastic extension following undercutting, (b) the potential transition from elastic extension to non-linear extension, and (c) stabilization of the stope hanging wall.

3.4 SERF Method

3.4.1 Theory

The SERF method modifies the inverse velocity method to plot the inverse of strain against the hanging wall geometry, expressed as ERF, as described in Section 2.7.2. An important distinction during the application of the SERF method is that the predicted geometry of instability is expected to be associated with the hanging wall RF, while the datapoints are associated with the ERF of the measurement location. Since the measurement location is often closer to an abutment, the measurement location may remain stable while instability occurs at a different location on the stope hanging wall.

The SERF method relies on increases in the measured strain to drive the inverse strain value towards zero as ERF increases. In its original form (Milne and Snell, 2018), this is countered by the inclusion of the ERF term in the numerator, which increases the value of the plotted point. Figure 3-11 shows hypothetical strain curves for a simple hanging wall surface, which only changes along one dimension. Two scenarios are considered where the hanging wall fails at either a large or small geometry. As the surface length increases, the ERF of the measurement location

initially increases rapidly before levelling off as the surface length continues to increase. This is contrasted by the strain curves which follow an exponential form, initially increasing slowly and accelerating with time. For the scenario where the hanging wall fails at a smaller geometry, the strain begins to accelerate at a smaller surface length.

Figure 3-12 shows the impact of including ERF in the numerator, during the application of the SERF method. The inclusion of ERF in the numerator of the inverse strain plot initially suppresses the trend towards zero (Figure 3-12b), or potentially reverses it (Figure 3-12a). Especially for openings with a limited number of blasts until instability (Figure 3-12b), the delay in establishing the trend towards zero can result in a Predicted Radius Factor of instability (RF_p) that is non-conservative and may suggest that continued mining may be possible, resulting in hanging wall instability.

The same issues were not present when the ERF term was not included in the numerator during application of the SERF method. As a result, it is suggested that the SERF method be modified to plot 1/ strain instead of ERF/strain. This variation will be referred to as the modified SERF method and is applied to case histories in Sections 4 and 5.

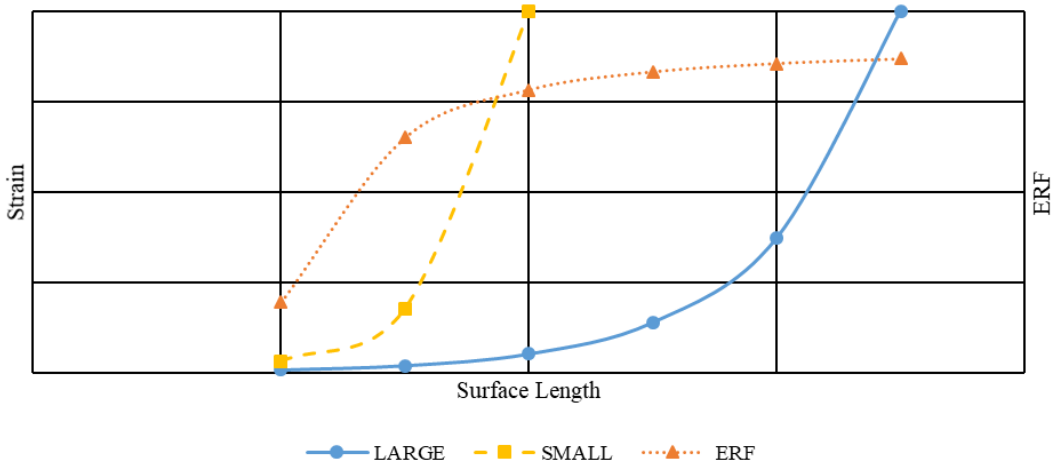

Figure 3-11: Changes to ERF and a 1/microstrain series for instability occurring at a large and small geometry.

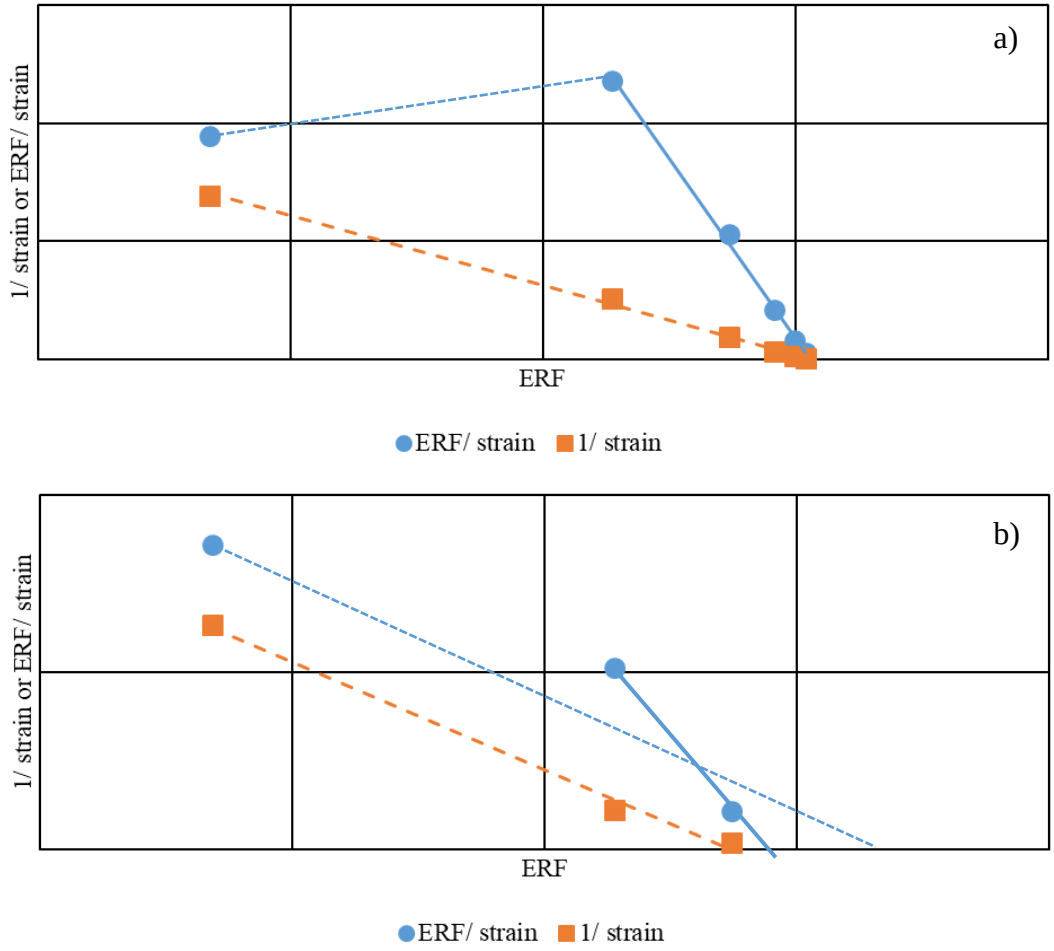

Figure 3-12: Difference in RF_p using ERF/strain and 1/strain for the (a) large geometry of instability and (b) small geometry of instability.

3.4.2 Applications

The primary benefit of the modified SERF method is the real time insight into the approach of potential hanging wall instability. The application of the modified SERF method can identify a RF_p that is smaller than the final RF of the designed final stope. When this is the case, the modified SERF method suggests that hanging wall instability may occur prior to, or as a result of, the final designed production blast being taken. To reduce the risk of instability, the final hanging wall RF may be reduced. Possible means of reducing the hanging wall RF include terminating stope production early (Figure 3-13a), modifying the remaining blasts to reduce the RF (Figure 3-13b), or stabilizing the hanging wall with backfill.

Alternatively, the application of the modified SERF method may result in a RF_p that is larger than the final RF of the designed stope. Depending on the degree to which the RF_p is larger than the designed final stope RF, and when level development allows it, the stope may be mined as designed (Figure 3-13c) or additional production blasts could be added to the stope (Figure 3-13d). For a theoretical longhole open stope, as shown in Figure 3-13, increasing the strike length of the stope may provide the opportunity to reduce the amount of waste development, reduce the number of rib pillars, and/ or increase the amount of production before backfilling is required.

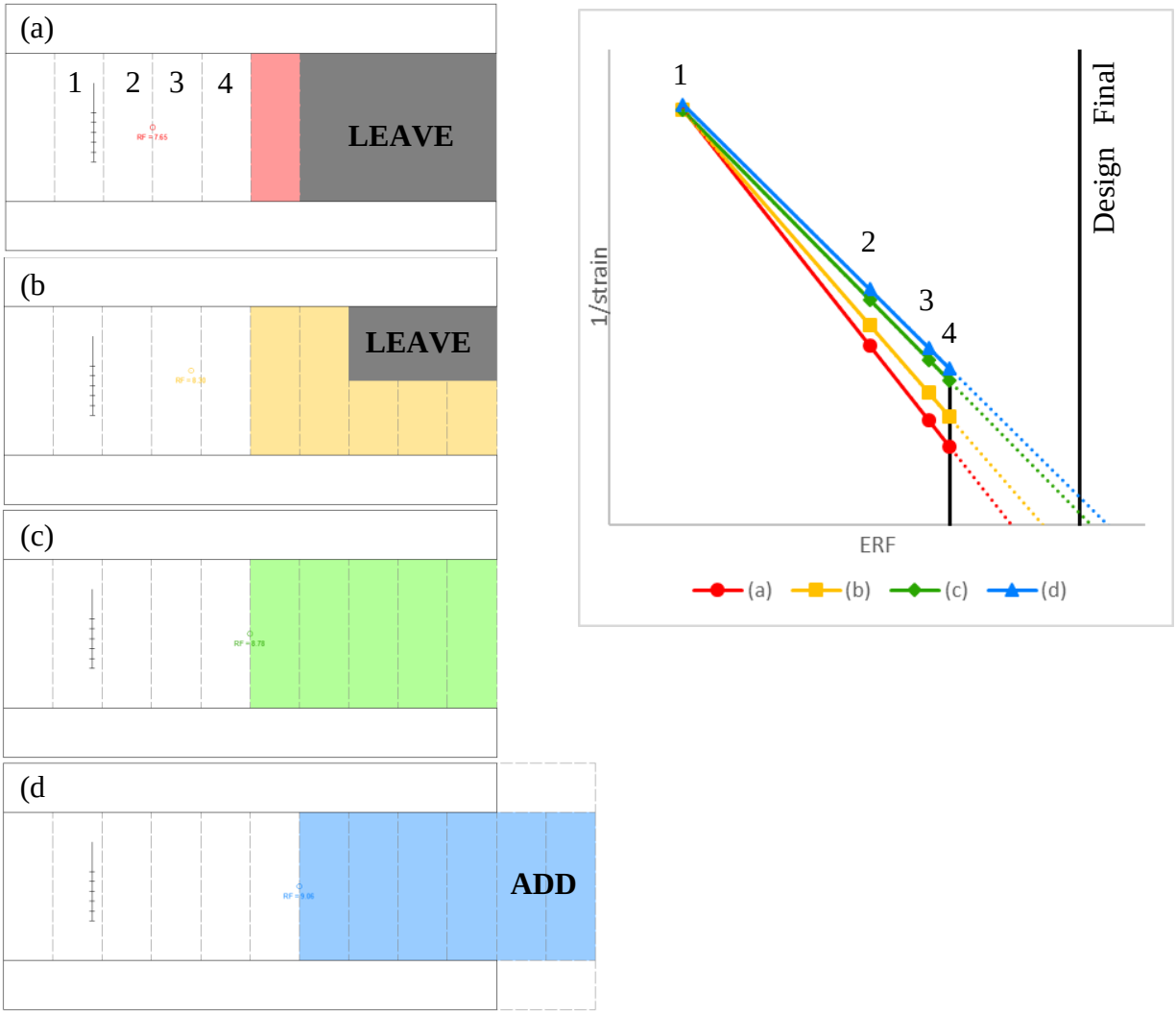

Figure 3-13: Hypothetical long-section of a stope hanging wall and associated SERF method predictions and possible actions including reducing the final hanging wall RF by (a) stop mining early or (b) modify the remaining blast extents; (c) mining to design; or (d) mining past design.

3.5 Trigger Action Response Plan

The integration of deformation alarms into a TARP can be adapted to underground operations if the SERF method (Section 3.4) is found to be effective and applies in the area under observation. This can be done by modifying the methodology outlined for open pits, by Dick et al. (2014). The inverse velocity method is replaced with the SERF method and time with geometry (Figure 3-14). Once the TARP is implemented, following the identification of non-linear extension (instead of the onset of acceleration), a prediction of a geometry of instability, associated with the RF of instability (RF_p), can be made following the subsequent production blast. As additional production blasts are taken, additional points are plotted to establish a trend and search for a possible trend update. As the actual geometry approaches the RF_p, through sequential blast activity, a decision point exists to elevate the TARP alert level with possible actions, including the continuation of mining based on the original design, modification of the final hanging wall geometry, or the termination of mining from the stope.

Similar to open pit applications, the decision to elevate the TARP alert level should be associated with a number of blasts, or time remaining, before predicted instability. The RF_p should be compared to the hanging wall RF for each of the remaining production blasts to determine how many additional production blasts are required to reach the RF_p, or if the RF_p will be reached at all. The mine production schedule can then be reviewed to determine the time remaining until the blast that may result in instability based on the SERF method.

It is important to note that each mine should develop and implement its own TARP based upon local conditions and the risk associated with hanging wall instability. As is to be expected, and is demonstrated by the case histories, there is variance between the RF_p and the actual RF of failure (RF_f). Depending on the economic consequences of dilution associate with the potential hanging wall instability, the user may wish to keep the design stope RF a certain size smaller than the RF_p.

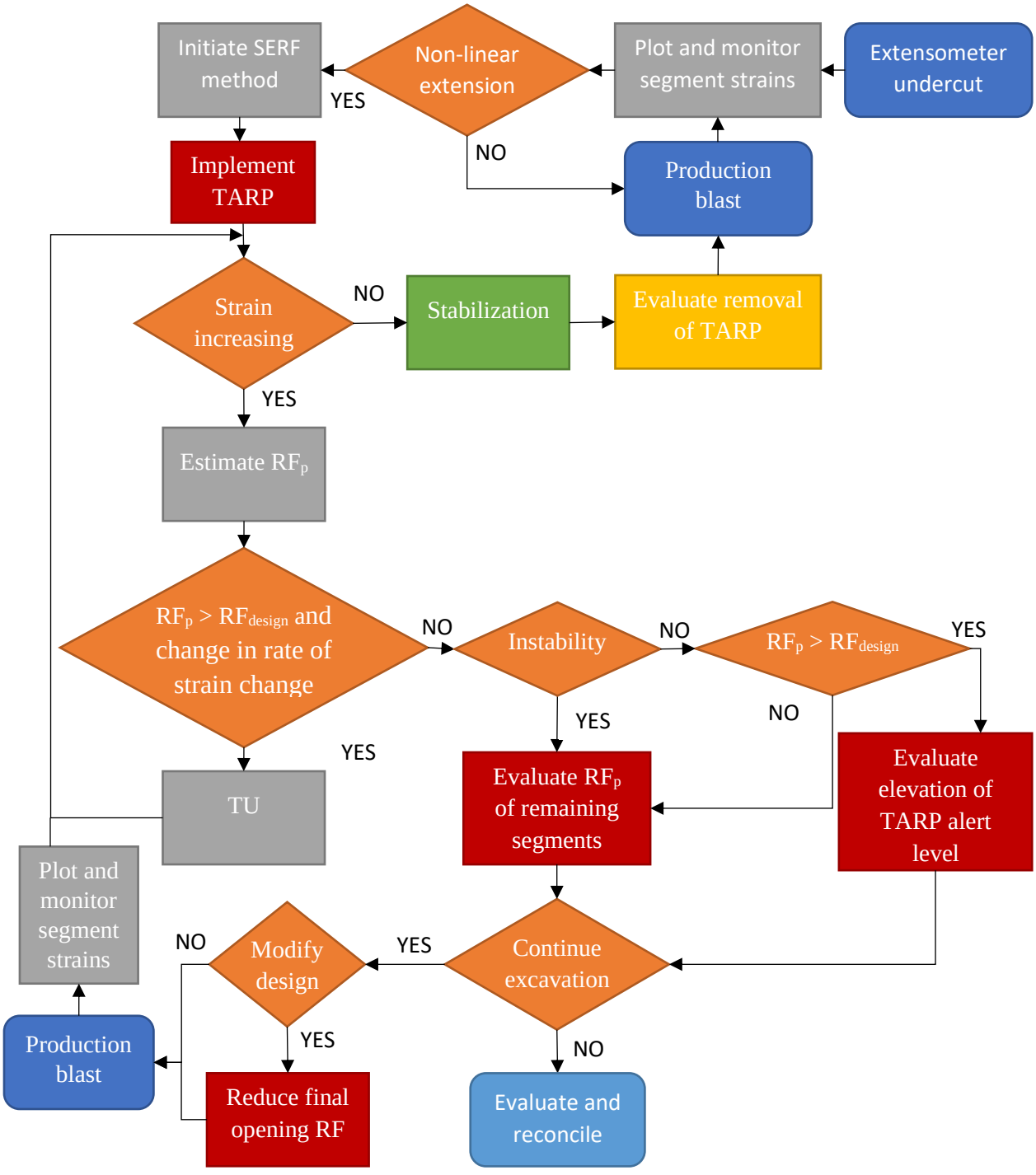

Figure 3-14: Flowchart of SERF method for monitoring of geometry driven instability after extensometer undercutting.

4 INTERPRETATION OF HISTORIC INSTRUMENTATION DATA

Historic datasets from Brunswick Mine and Mount Isa Mine were analyzed to test the reasonableness of estimating pre-mining stresses and a potential geometry of instability from extensometer measurements. The datasets were analyzed following the approach outlined in Section 3 and an overview of the results of the analysis are provided in Table 4-1. A full analysis of the Brunswick Mine dataset is provided in Section 4.1 while the analysis of the Mount Isa Mine datasets are summarized in Sections 4.2 and 4.3 , with full detail available in Appendix D.

Table 4-1: Overview of the outcome of the estimates of pre-mining stress and a geometry of instability using the SERF method for different stopes.

Mine	Stope	Pre-mining stress	SERF
Brunswick Mine	16N	Inconclusive	Valid
Mount Isa Mine	5FP1	Reasonable	Not applicable
	5HP1	Reasonable	Promising

4.1 Brunswick Mine – 16N Stope

Prior to applying the SERF method to new case histories, the Brunswick case history, presented by Milne and Snell (2018), was recreated to confirm the predictions using the SERF method and to assess both the ground response to mining and estimate the pre-mining stress from the extensometer data.

The Brunswick mine produced lead, zinc, copper, and silver ore for nearly 50 years near Bathurst, New Brunswick (Figure 4-1). The case study data analyzed in this study was collected from 1992 to 1993 while the mine was owned by Noranda Inc. and was producing approximately 10,500 tonnes of ore per day. At the time, ore was mined using overhand cut-and-fill or open stoping, depending on the stope location and stress levels. In this Section, the instrumentation program, data, and analysis are presented for the 16N stope.

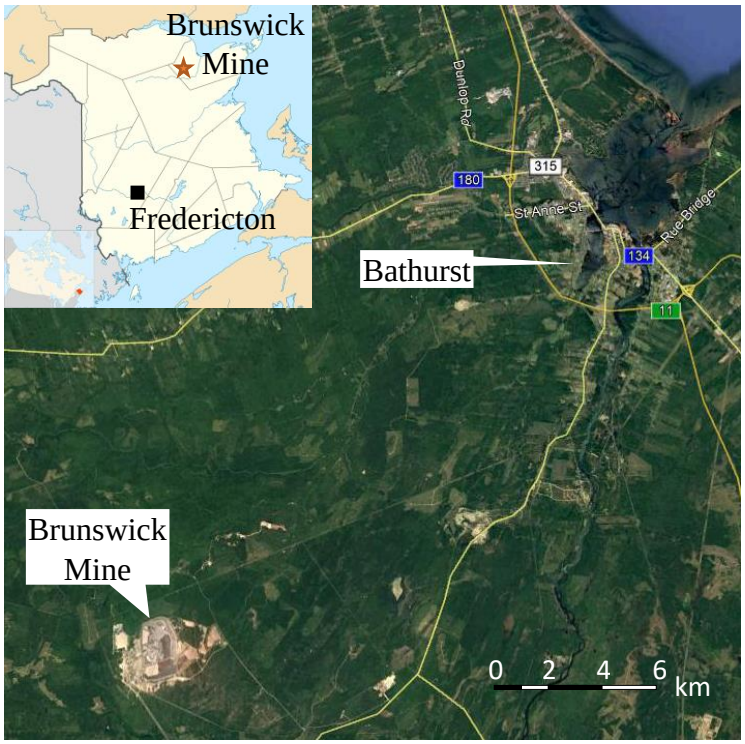

Figure 4-1: Location of the Brunswick Mine (after Google, n.d.; Wikipedia, n.d. a).

4.1.1 General rock mass properties

The main ore zone dipped to the west at approximately 70 to 75° and ranged from 5 to 10 metres thick (Hudyma et al., 1993). The ore was hosted in a massive sulfide with a hanging wall composed of a chloritic schist with a Q' ranging from 4.0 to 8.0 due to variations in the chloritic infilling of joints. Mapping identified three primary joint sets with orientations of approximately 90°/270° (A), 90°/000° (B), 20°/230° (C) as shown in Figure 4-2 (Esmaeili et al., 2010; Milne and Snell, 2018). Other rock mass properties associated with the Brunswick mine are summarized in Table 4-2.

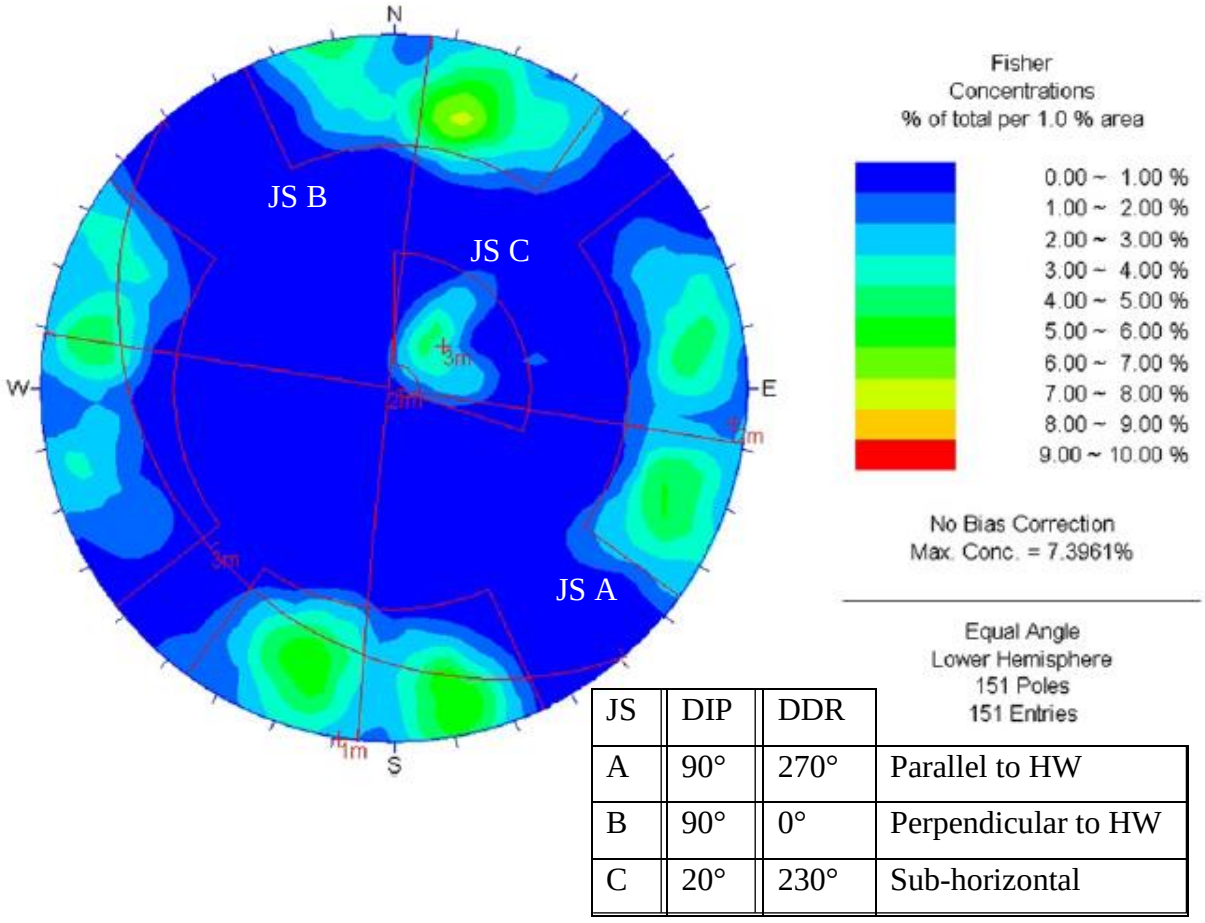

JS	DIP	DDR	
A	90°	270°	Parallel to HW
B	90°	0°	Perpendicular to HW
C	20°	230°	Sub-horizontal

Figure 4-2: Stereonet of the Brunswick Mine joint orientations (after Esmaeili et al., 2010).

Table 4-2: Summary of rock mass properties at Brunswick Mine (Hudyma et al., 1993; Esmaeili et al., 2010).

Property	Symbol	Chloritic Schist (hanging wall)
Average Q’		4
Elastic Modulus	E	63 GPa ±11
Poisson’s Ratio	ν	0.22 ± 0.001
Unit weight	γ	26 kN/m^3
Unconfined compressive strength	UCS	70 MPa

4.1.2 Mining Overview

A long section of the main ore zone at Brunswick Mine is shown in Figure 4-3. The case study data is associated with the 16N stope, located in the 725 sill pillar between two production levels. The mining method for this area was open stoping due to high stress concentration in the pillar. The sill pillar's initial stress levels were measured using the borehole slotting technique. The principal stresses were calculated as summarized in Table 4-3. Estimating the vertical stress based on the sill pillar depth (16 MPa) compares favourably with the calculated vertical stress (14-19 MPa).

Table 4-3: Calculated initial stresses in the 725 sill pillar (Hudyma et al., 1993).

Principal Stress	Direction	Magnitude
σ_1	E-W	30 MPa
σ_2	N-S	25 MPa
σ_3	Vertical	16 MPa

Figure 4-3: Longitudinal projection of the main ore zone at the Brunswick mine showing the location of the 16N stope (from Milne, 1997).

The 16N stope was an open stope located in the main ore zone between the 575 and 725 levels in a sill pillar at a depth of approximately 600 metres (Figure 4-3), corresponding to a vertical stress of approximately 16 MPa. The stope has an approximate north-south strike with an east/west stress, normal to the stope hanging wall, of approximately 30 MPa (σ_1). The approximate dimensions of the final opening were 58 metres along strike and an up dip length of 45 metres at an average dip of 78°. A research project was conducted during the mining of the 16N stope and is detailed in numerous publications (Hudyma et al., 1993; Kanduth et al., 1993; Milne, 1993; Hudyma et al., 1994; Milne, 1997).

Site engineers had developed a ground support program for the 16N stope. The ground support included a fan pattern of three seven-metre-long double strand, cable bolts installed into the hanging wall on one-metre spacing along the 6-sub (Hudyma et al., 1993). The cable bolts were installed for the remainder of the stope length, starting from the slot associated with blasts 13 to 16 (Figure 4-4).

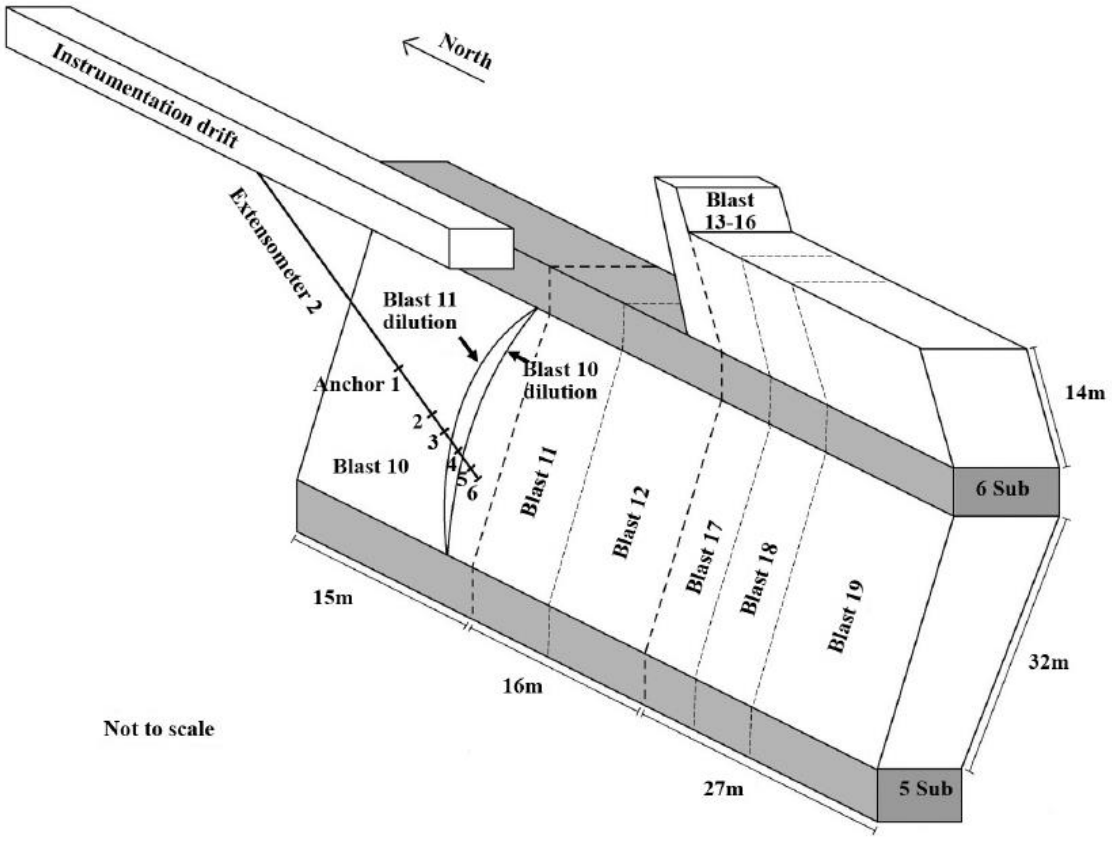

Figure 4-4: Isometric view of the N16 stope hanging wall showing major production blast and the location of extensometer 2 (from Milne and Snell, 2018).

4.1.3 Instrumentation program design

The 16N stope at the Brunswick mine was instrumented with 11 extensometers, several ground movement monitors, and 10 strain gauges (Figure 4-6). Measurements from the extensometers were collected from a hanging wall instrumentation drift, as shown in Figure 4-4. Anchor 6 was located closest to the designed stope hanging wall, with the anchor numbers decreasing as the distance from the designed stope hanging wall increased (Figure 4-5). The distances between adjacent anchors are also shown in Figure 4-5.

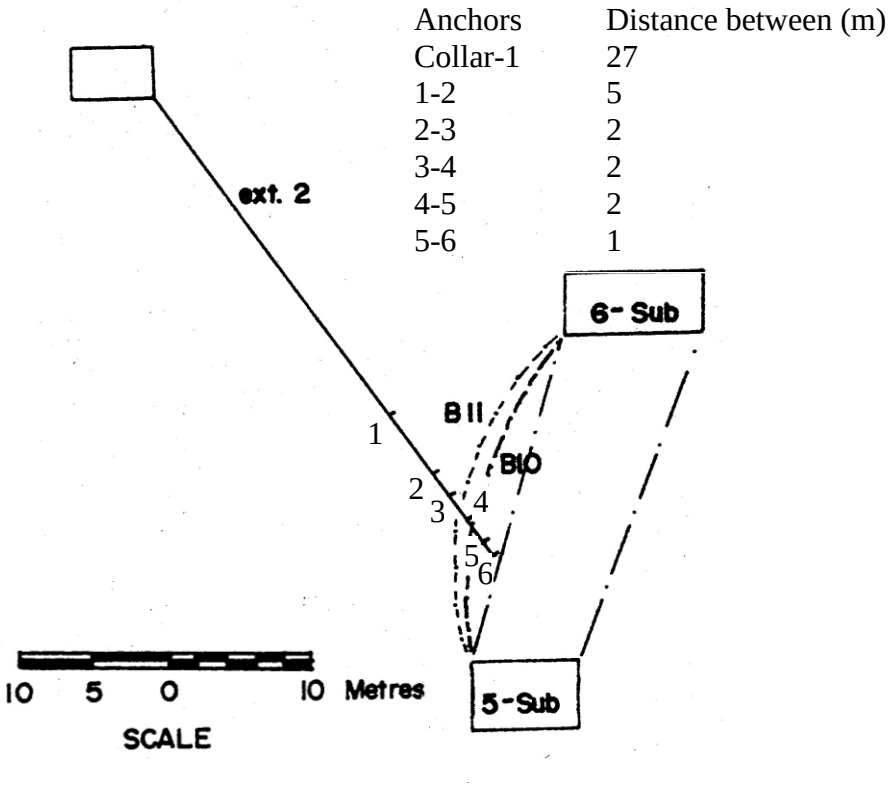

Figure 4-5: Cross section of the 16N stope at Brunswick mine showing the position of extensometer 2 anchors relative to the stope hanging wall before and after local sloughing (after Milne, 1993).

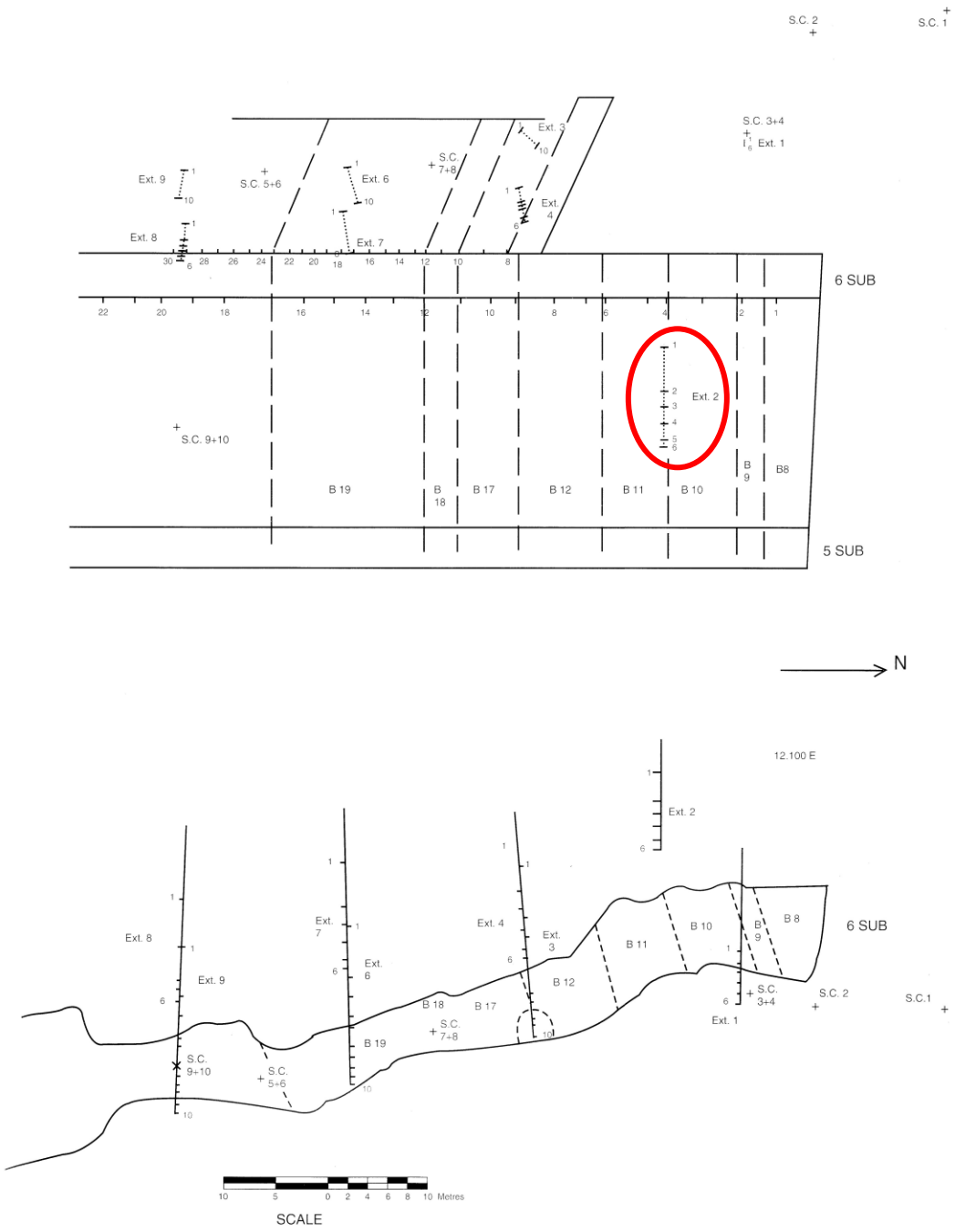

Figure 4-6: Long view and plan section of the 16N stope hanging wall at Brunswick mine showing the major blast extents and instrumentation locations (from Hudyma et al, 1993).

4.1.4 Stope mining

Figure 4-4 shows the north to south mining of the Brunswick 16N stope, along with the location of extensometer 2. The main blasts are shown in Figure 4-6, but not the slot blasts. The first seven blasts (slot blasts), were used to develop the slot between sub 6 and sub 5. The next five blasts (8 to 12) were longhole production blasts between sub 6 and sub 5. Following blast 12, the next four blasts (13 to 16) were used to develop a slot from sub 6 to 575 level to allow uppers to be taken along with the longhole blasts for the remainder of the production blasts (Hudyma et al, 1993). Extensometer data is available starting with production blast 10 on 20-August, 1992 through blast 19 on 14-November, 1992 (Milne, 1993; Hudyma et al, 1993).

As mining progressed, there were challenges with hanging wall stability. Following blast 10 there was significant dilution from the hanging wall which increased from 40% to 90% dilution by blast 17. Following blast 19, a hanging wall failure occurred which extended over 10 metres into the hanging wall from the designed surface. Following this failure, a rib pillar was left before additional blast production blasts could be fired to mine the remainder of the stope (Hudyma et al., 1993).

The rib pillar provided a break in the unsupported hanging wall geometry and separated the instrumented opening from the remaining stope blasts. For the purpose of this analysis, mining that took place on the other side of the rib pillar is not considered.

4.1.5 Ground response to mining

For the stope location, a pre-mining stress of approximately 30 MPa, oriented normal to the hanging wall, was measured by Hudyma et al. (1993). Prior to undercutting, there was minimal concentration of compressive strain indicated by the data from extensometer 2.

Applying Equation 3-7, the estimated upper bound to elastic deformation in the hanging wall, adjacent and normal to the stope, due to hanging wall stress relaxation following undercutting by stope mining, is estimated to be approximately 375 microstrain of tension. Assuming a one metre anchor segment length, this strain would be associated with a deformation of approximately 0.4 millimetres.

$$\varepsilon_{(a-b)} = \frac{\Delta\sigma_n}{E}(1-\upsilon) = \frac{0-30MPa}{63GPa}(1-0.22) \cong -375\mu\varepsilon$$

Of the installed instrumentation, only the extensometer 2 dataset contained measurements of hanging wall deformation for enough production blasts to be relevant for analysis using the SERF method.

EXTENSOMETER 2

The data from extensometer 2 was collected by a data logger, with a daily measurement reading frequency that recorded displacement measurements to the nearest 0.1 millimetre (Milne, 1993). A plot of the strain over time for extensometer 2 is shown in Figure 4-7.

Figure 4-8 shows plan, cross section, and long section views of the stope and extensometer, before and after being undercut by blast 10. Figure 4-8b shows the estimated limits of sloughing following blasts 10 and 11. Reporting indicated that within 24 hours of the undercutting of extensometer 2 by blast 10, minor sloughing occurred along a discrete foliation plane resulting in the loss of the three anchors closest to the stope hanging wall (Milne, 1993). As a result, only anchor segments 1-2 and 2-3 were able to collect data for the remainder of the stope excavation (Milne, 1993), with anchor 2-3 being located approximately one metre from the opening, after the sloughing due to blast 10 had occurred.

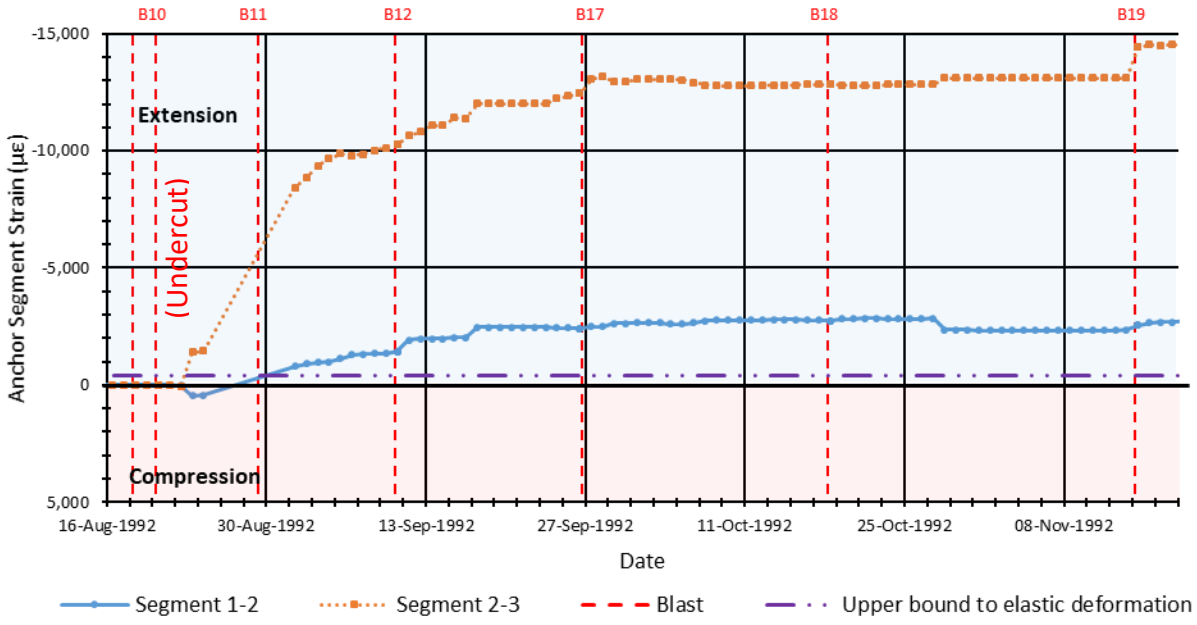

Figure 4-7: Segment strains in Brunswick mine's 13N stope hanging wall measured by extensometer 2.

Figure 4-8 also includes a schematic of areas of expected concentration and relaxation, for stresses generally perpendicular to the ore zone. The measured strain responses for the remaining extensometer 2 anchor segments appear reasonable (Figure 4-7). The compressive response measured in anchor segment 1-2 following blast 10 suggests that the anchor segment is either not undercut or the zone of stress relaxation does not extend to cover the entire segment until after blast 11 when an extension response is measured. This is supported by the cross section (Figure 4-8b) and plan section (Figure 4-8d).

In the plot of segment strain over time (Figure 4-7), it appears that there is a transition to non-linear extension for anchor segment 2-3 associated with blast 10 and a trend update associated with blast 11. For anchor segment 1-2 there appears to be a transition to non-linear extension associated with blast 11 and a possible trend update associated with blast 18, although there are insufficient additional blasts to confirm the trend update. As a result, the dataset for extensometer 2 appears suitable for analysis of both anchor segments 1-2 and 2-3 using the modified SERF method.

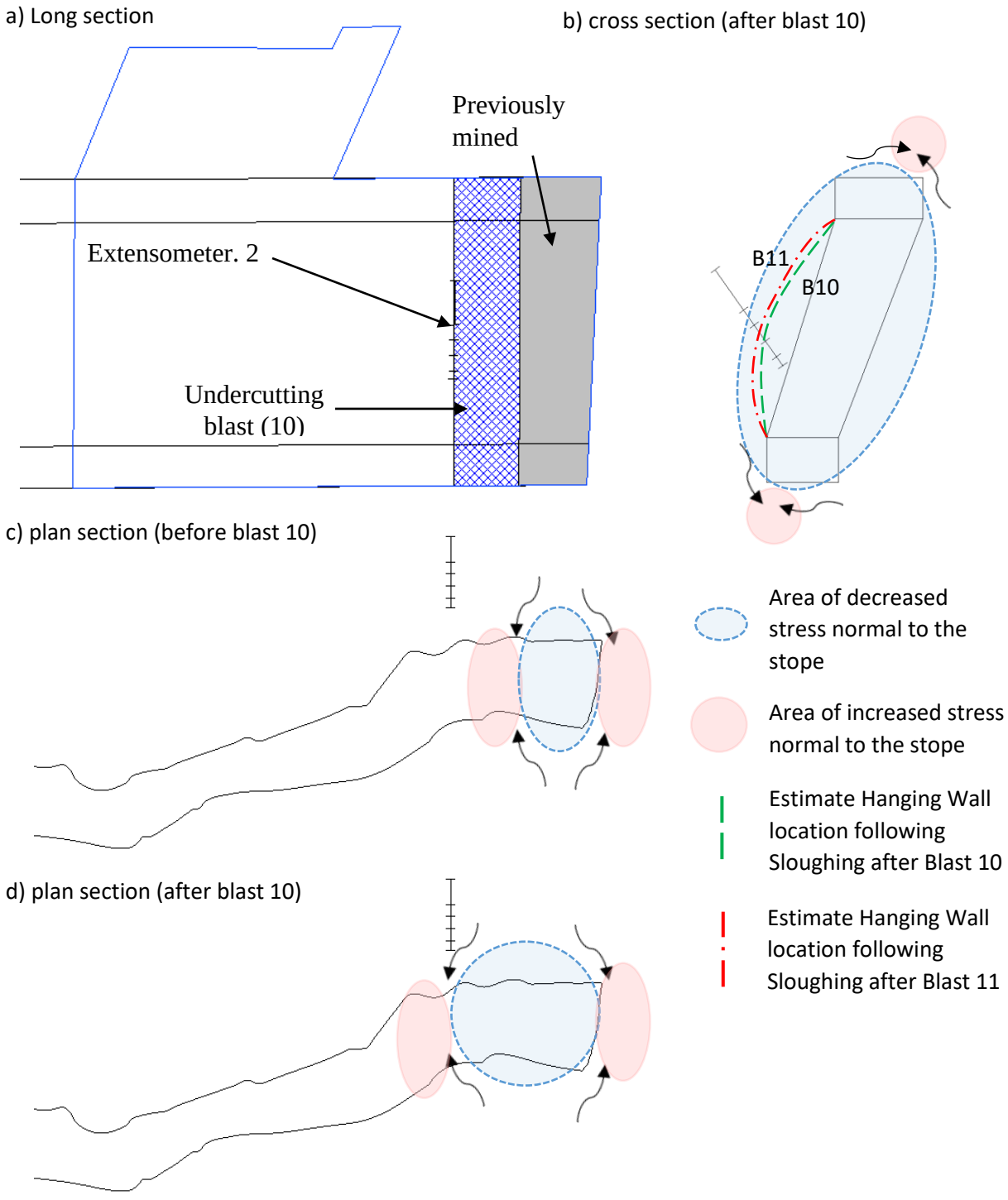

Figure 4-8: Section views of the Brunswick Mine 16N stope showing blast geometries, excavation geometries, expected zones of stress change, and the location of extensometer 2 for: (a) true longitudinal view, (b) cross section after undercutting, (c) plan section prior to undercutting, and (d) plan section after undercutting.

4.1.6 Estimation of Pre-mining stress

The dataset for the 16N stope at Brunswick Mine contained both blast dates and geometries to determine which blast undercut each extensometer. These details are summarized in Table 4-4.

The dataset for the 16N stope contained daily measurements for each extensometer anchor. By comparing successive measurements, the change in strain due to each stope blast could be estimated. The strain changes in each extensometer anchor segment are summarized in Table 4-4. By applying Equation 3-6, and using an elastic modulus of 63 GPa and a Poisson's ratio of 0.22 (Hudyma et al., 1993) the measured changes in strain after undercutting were used to calculate the pre-mining stress in each anchor segment, as summarized in Table 4-4. Results associated with anchors not believed to be fully relaxed are coloured yellow. A sample calculation for anchor segment 2-3 of extensometer 2 is shown below.

$$\sigma_{pre-mining} \cong -\frac{\Delta\varepsilon\, E}{(1-\upsilon)} \cong -\frac{(10\mu\varepsilon)(63\ GPa)}{\big(1-(0.22)\big)} \cong -1\ MPa$$

Following undercutting there was no measured strain response during the first day. Although a strain response was measured following the sloughing event between blast 10 and 11, this was not considered to be part of the initial ground response to undercutting. The perpendicular distances from the hanging wall to the segment anchors reported in Table 4-4, are following the sloughing events that resulted in the loss of anchors 4, 5, and 6. Prior to the sloughing, anchor segment 1-2 and 2-3 were approximately 6.0 and 8.0 metres from the hanging wall respectively. In both cases the ERF is much smaller suggesting that the anchor segments are not fully relaxed, which supports the lack of measured strain response to undercutting by blast 10.

Table 4-4: Summary of the stress and strain change following undercutting for each extensometer segment in the 16N stope hanging wall.

Anchor Segment	Anchor Segment length (m)	Perpendicular distance to hanging wall (m)	ERF (m)	Strain change due to blast (με)	Calculated Pre-mining stress (MPa)
Extensometer 2-	Undercut by Blast 10 on 20-Aug-1992				
1-2	5.0	3.0 – 8.0	1.66	0	0
2-3	2.0	1.0 – 2.0	1.23	10	-1
3-4	2.0	Lost following Blast 10			
4-5	2.0	Lost following Blast 10			
5-6	1.0	Lost following Blast 10			

*yellow highlight- not fully relaxed (ERF< distance of furthest anchor to hanging wall)
*red highlight- unreliable anchor segment

4.1.7 Modified SERF Method

Previous SERF analysis of extensometer 2 data from the 16N stope at Brunswick mine, resulted in a predicted RF of instability (RF_p) of approximately 13.9 metres (R^2=0.93) for anchor segment 2-3 (between one and three metres from the stope hanging wall) and 14.9 metres (R^2=0.79) for anchor segment 1-2 (between three and eight metres from the stope hanging wall) (Figure 4-9). These RF_p were considered to compare favourably to the actual RF of failure (RF_f) of 12.4 metres (Milne and Snell, 2018).

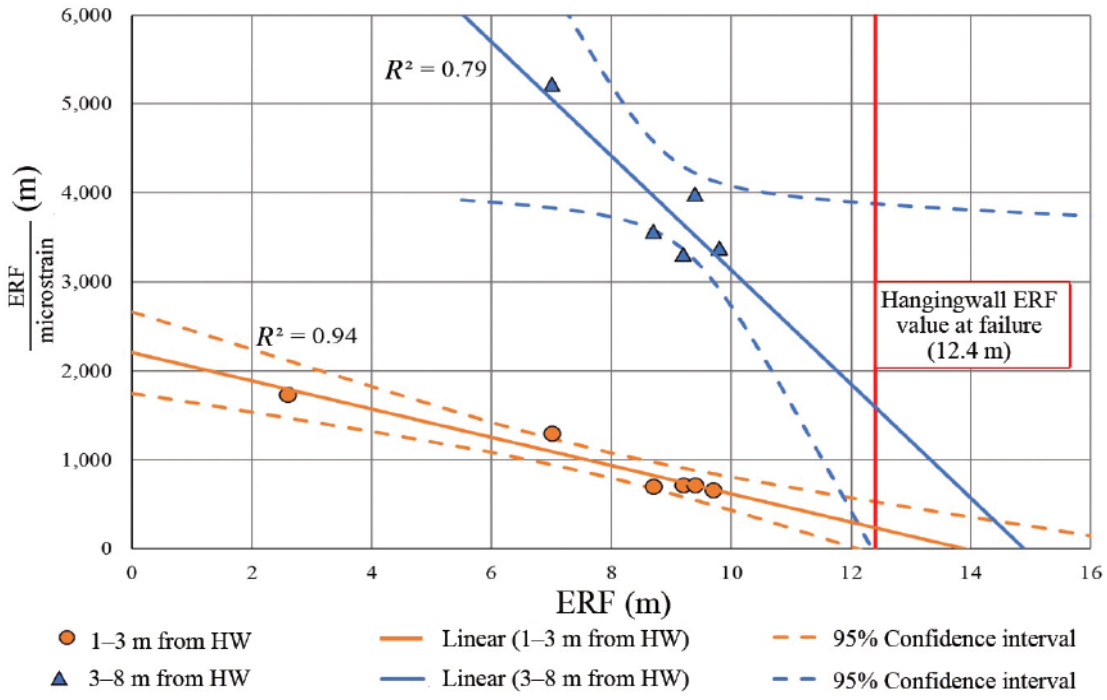

Figure 4-9: Plot of the RF_p for the 16N stope hanging wall at Brunswick mine using the SERF method (from Milne and Snell, 2018).

Since the RF_p are larger than the RF_f, they should be considered an unconservative prediction. Considering the possible applications of the SERF method outlined in Section 3.4.2, the SERF method would not have provided warning of the instability that occurred following blast 19 when the stope RF increased to 12.4 metres.

The degree to which the RF_p is unconservative can be best illustrated by considering the additional production blasts that would need to be taken to reach the RF_p. For the 16N stope, the stope height is limited based on drilling from the upper sublevel and any additional production blasts will only increase the strike length of the opening. It was found that an additional strike length of 16.7 metres (~32%) was required, beyond the final stope strike length, to reach the RF value that predicts instability for anchor segment 2-3 and 32.8 metres (~62%) to reach the RF value that predicts instability for anchor segment 1-2 (Figure 4-10).

Attempts to reproduce the results shown in Figure 4-9, using case history data from Hudyma et al. (1993) and Milne (1993), identified two flaws in the original calculation. The first flaw identified was the inclusion of the data point for blast 19 at which the hanging wall failed. Inclusion of the blast 19 data point results in a slightly larger RF_p. In practice, adding the failure data cannot be used to obtain a failure prediction.

The second flaw relates to the calculation of the ERF values used in the SERF method. Milne and Snell (2018) used ERF values from Milne (1997) which were larger than those in the original case history data (Milne, 1993) and could not be reproduced. Using the ERF values from the original case history data (Milne, 1993), results in a flattening of the segment 2-3 trend and a reduction of the RF_p for segment 1-2 (3-8 metres from the hanging wall) from 14.9 metres to 13.5 metres (Figure 4-11). Detail showing the ERF calculation for each extensometer anchor are shown in Appendix B.

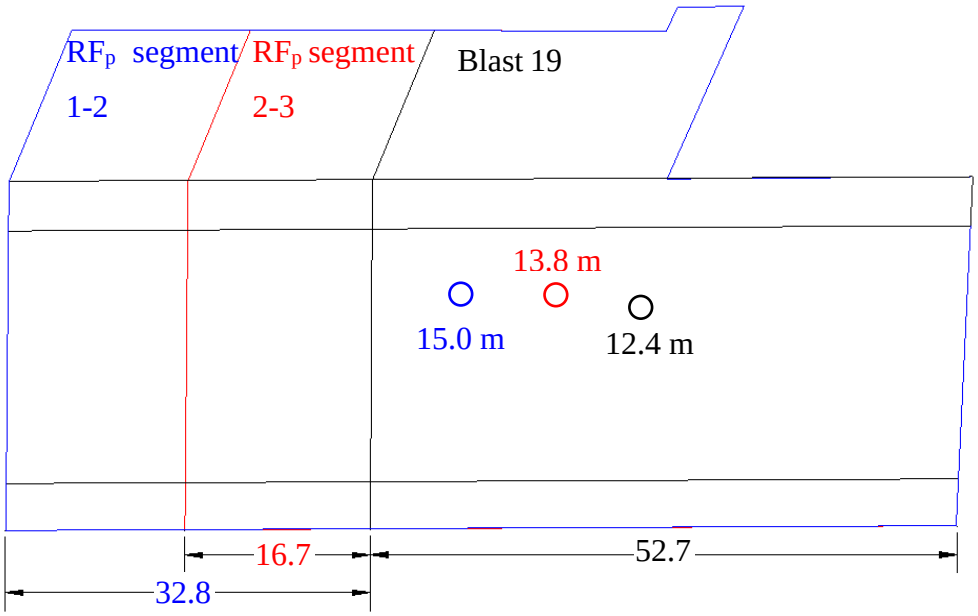

Figure 4-10: Schematic showing geometry increase to reach projected RF_p from Milne and Snell (2018) analysis.

Applying the modified SERF method improves the accuracy of the RF_p. Using the ERF values from Milne (1993) and excluding the deformation measured for the final blast, the modified SERF method resulted in a RF_p of approximately 10.5 metres for anchor segment 1-2 (from 3-8 metres from the hanging wall) and approximately 17.0 for anchor segment 2-3 (from 1-3 metres from the hanging wall) (Figure 4-12). The RF_p associated with the anchor segment further from the hanging wall is within the RF failure zone, between the stable blast 18 geometry (RF = 9.7m) and the failed geometry after blast 19 (RF = 12.4 metres). This suggests that if blast 19 were taken, hanging wall instability could occur extending back to anchor segment 1-2, to a depth of three to eight metres from the current hanging wall.

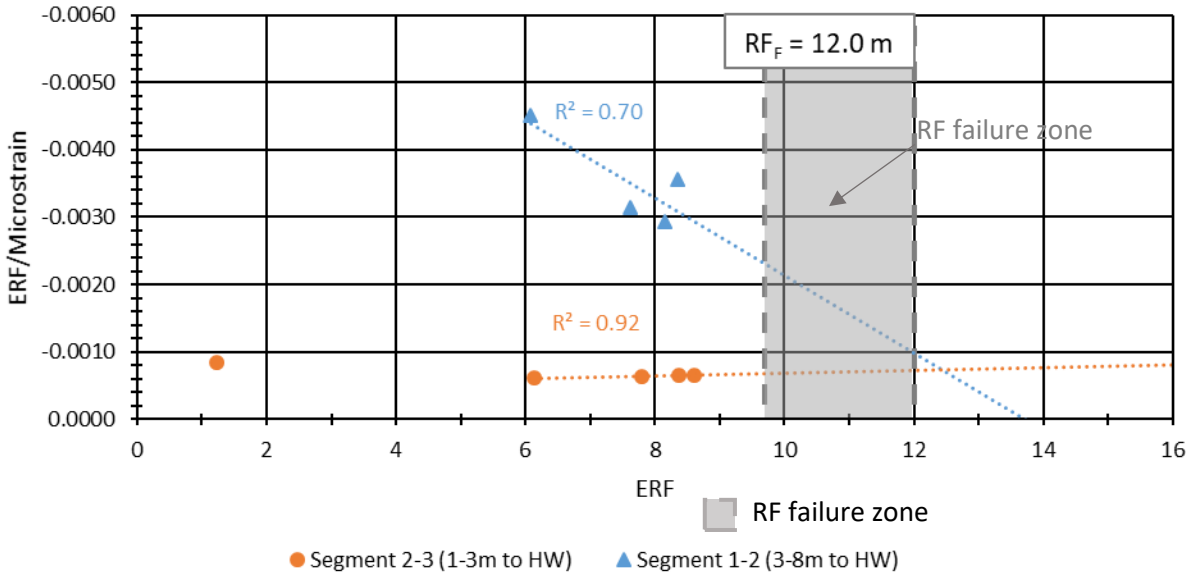

Figure 4-11: Plot of the RF_p for the 16N stope hanging wall at Brunswick mine using the SERF method after correcting the anchor segment ERF values.

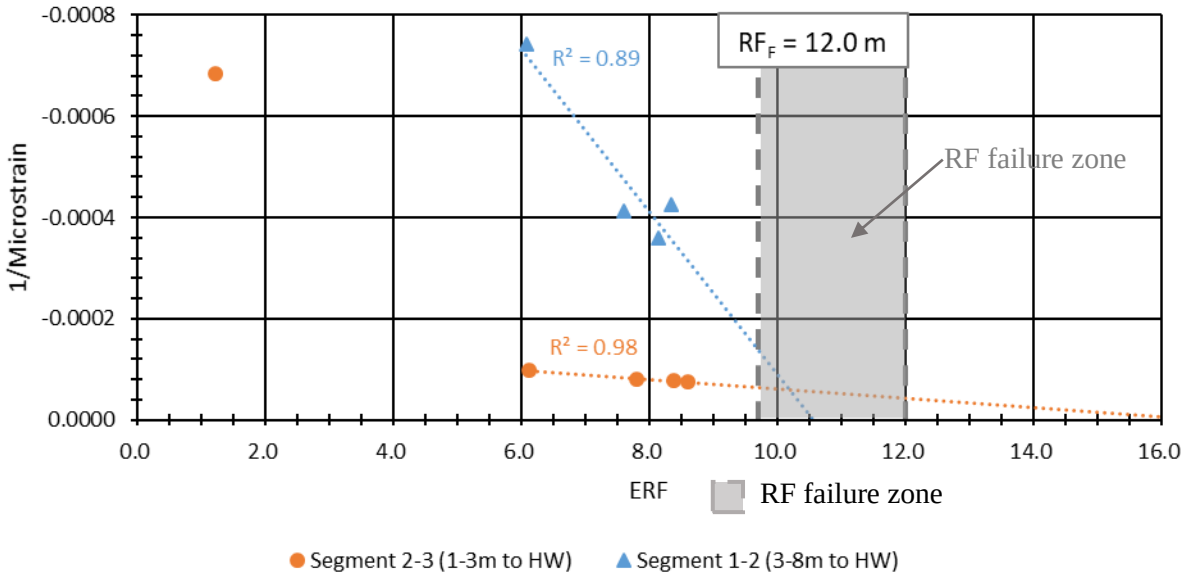

Figure 4-12: Application of the modified SERF method to predict a geometry of instability for the 16N stope at Brunswick Mine.

4.1.8 Summary of Brunswick Mine analysis

No conclusion could be made regarding the estimation of pre-mining stress from extensometer data due to the large distance from the reliable anchor segments to the stope hanging wall at the time of undercutting. Due to this distance being larger than the ERF of the anchors, it is believed that the anchor segment was not fully relaxed, which was supported by the lack of measured strain response by extensometer 2.

Data from the 16N stope provides a suitable case to demonstrate the improvement in predicting a RF_p using the modified SERF method over the previously proposed SERF method. For this dataset, the remaining anchor segment that was furthest from the stope hanging wall predicted a RF_p that fell with the range of RF between the last stable hanging wall geometry and the failed geometry following the next production blast, which was considered a successful application.

4.2 Mount Isa Mine - 5FP1

The Mount Isa mine is located in Mount Isa, Queensland, approximately 780 kilometres west of Townsville, Australia. Mines in the Mount Isa area have been producing copper, lead, silver, and zinc from deposits in parallel seams, within a 1,000-metre-thick sulphide and shale formation, since the 1920's (Villaescusa, 1996). The ore is extracted from deposits with parallel bedding, dipping to the west at approximately 70°. The shale, forming the mineralization and host strata, has varied strength resulting in the stability of the hanging wall, and associated dilution, being the topic of extensive research. Additional details about the Mount Isa Mine at the time of the research program are available in Appendix D.

The 5FP1 stope was located in a high stress abutment and was mined using a bench stoping method. Following excavation, and prior to backfilling, the final stope dimensions were 53 metres up dip and 43 metres along strike with rock abutments surrounding the opening (Milne, 1997).

Figure 4-13 is a schematic showing the location and approximate dimensions of the 5FP1 stope. The 5FP1 stope was the first of the four stopes shown in Figure 4-13b to be mined. Ground support, including cable bolts and split sets, were installed from the development sills to support the hanging wall by pinning bedding layers to effectively create a thicker beam. Bulbed, single strand cable bolts were fully grouted and installed in fan patterns with variable cable bolt length and ring spacing, depending on the ground conditions and opening geometry (Villaescusa et al., 1992; Villaescusa, 1996).

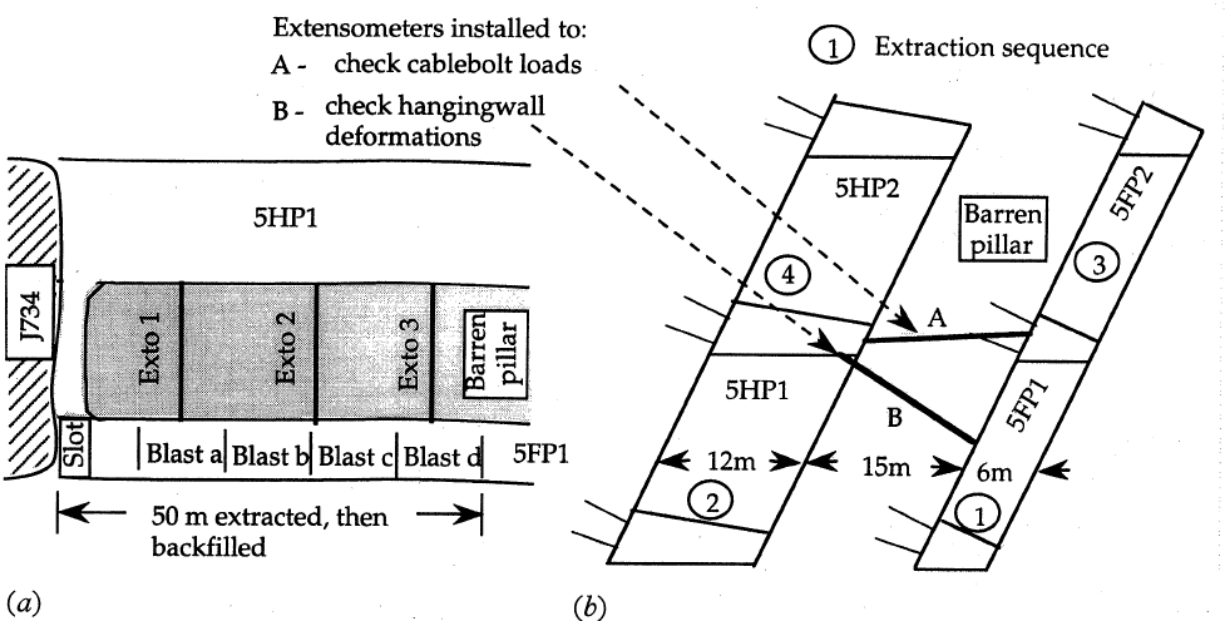

Figure 4-13: (a) Plan view and (b) cross-section, looking north, of the 5HP1 and 5FP1 stopes showing extensometer locations, ground support, blast sequence (from Villaescusa, 1996).

4.2.1 Stope Mining

To control dilution and prevent instability that could jeopardise the 5HP1 stope, mining of the 5FP1 bench stope was split into multiple sub-stopes. Each sub-stope was mined and backfilled before advancing along strike, to the north, to mine the next sub-stope. The instrumented potion of the 5FP1 bench stope was completed with 4 production blast (Figure 4-13a), which began on 11-March, 1993 and concluded on 29-March, 1993.

After the instrumented portion of the stope was mined and backfilled, the remainder of the 5FP1 bench stope was mined in a similar fashion until the entire planned strike length had been mined. Data associated with stope mining after the backfill front had passed the instruments was not available.

4.2.2 Estimation of Pre-Mining Stress

The dataset for the 5FP1 stope contained a small number of manual readings taken following each stope blast. By comparing successive measurements, the change in strain due to each stope blast could be estimated. The strain changes in each anchor segment are summarized in Table 4-5. By applying Equation 3-6, and using an elastic modulus of 25 GPa and a Poisson's ratio of 0.25 (Milne, 1997), the measured changes in strain were used to calculate the pre-mining stress in each anchor segment, as summarized in Table 4-5. Results associated with anchors not believed to be fully relaxed are coloured yellow. A sample calculation for anchor segment 1-3 of extensometer 1 is shown below.

$$\sigma_{pre-mining} \cong -\frac{\Delta\varepsilon\, E}{(1-\upsilon)} \cong -\frac{(-820\mu\varepsilon)(25\ GPa)}{\big(1-(0.25)\big)} \cong 25\ MPa$$

For the closest reliable anchor segment for extensometer 1, the ERF is larger than the distance from the anchors to the opening, suggesting that this anchor segment has relaxed fully (Section 3.2.4). The estimated pre-mining stress for this anchor segment (25 MPa) is approximately 60% of the 40 MPa stress modelled (MIM, 1993).

None of the reliable extensometer 2 anchor segments were considered fully relaxed since the ERF of the anchor segment was smaller than the distance from the hanging wall to at least one of the anchors. The assessment of incomplete stress relaxation appears to be supported by the estimated stress of 20 MPa for extensometer 2 anchor segment 1-3, which was closest to the opening, being smaller than the estimated stress from the fully relaxed extensometer 1 anchor segment 1-3.

Table 4-5: Summary of the stress and strain change following undercutting for each extensometer segment in the Mount Isa 5FP1 stope hanging wall.

Anchor Segment	Anchor Segment length (m)	Perpendicular distance to hanging wall (m)	ERF (m)	Strain change due to blast (με)	Calculated Pre-mining stress (MPa)
Extensometer 1	Undercut by Blast 1 on 11-Mar-1993				
1-2	2.2	0.5-2.5	7.2	-820	25
2-3					
3-4	1.3	2.5-3.5	7.1	-680	25
4-5	4.5	3.5-7.5	7.1	-1,170	40
5-6	13	7.5-18.0	6.9	-140	5
Extensometer 2	Undercut by Blast 3 on 25-Mar-1993				
1-2	2.2	0.5-2.5	2.0	-550	20
2-3					
3-4	1.3	2.5-3.5	2.0	-950	30
4-5	4.5	3.5-7.5	2.0	-850	30
5-6	13	7.5-18.0	2.0	-120	5

*yellow highlight- not fully relaxed (ERF< distance to hanging wall)
*red highlight- unreliable anchor segment

Using Equation 3-6, an elastic modulus of 25 GPa, and Poisson's ratio of 0.25, the difference in stress between the predicted and modelled stress is associated with a displacement of approximately 1.0 millimetres over the 2.2 metre anchor segment length. The variation in stress between the modelled 40 MPa and estimated 25 MPa normal stress could be a result of uncertainty in the accuracy of the manual measurements, although measurements were reported to 0.01 millimetres, and/ or the elastic modulus selected for modelling. An estimate of the pre-mining stress based on the depth and regional K-ratio could not be made due to a lack of information about the stope location. As a result, it is uncertain which of the estimates of pre-mining stress is more reasonable.

4.2.3 Summary of 5FP1 analysis

Although the estimate of pre-mining stress using extensometer strains was smaller than the modelled pre-mining stress by Milne (1997), the results were within 60% of one another. Minor changes to the model inputs, an increase in the measured strain, or a different estimate of the in-situ stresses used for modelling would be enough make up the difference between the two estimates of pre-mining stress.

Backfilling of the 5FP1 stope limited the unsupported geometry of the hanging wall during extraction of the stope and contributed to the observed stability. The small number of stope blasts also meant that a transition to non-linear extension could not be confirmed, and the modified SERF method could not be applied.

4.3 Mount Isa Mine - 5HP1

The 5HP1 stope was located in the same area as the 5FP1 stope (Figure 4-13). The 5HP1 stope was mined following the completion of the 5FP1 stope, which positioned it in the stress shadow of the 5FP1 stope.

A schematic showing the plan and section view for the instrumented portion of the 5HP1 stope is show in Figure 4-14. A pillar was left at the approximate mid point of the stope, beside a second slot raise. This pillar, and the subsequent backfilling of the first half of the stope, served to break up the open geometry of the stope hanging wall and is not shown (Milne, 1994). Excavation of the instrumented portion of the 5HP1 stope cut off access to the extensometers before excavation of the stope was fully completed. The last available extensometer measurements were recorded when the stope dimensions were 55 metres up dip and 53 metres along strike (Milne, 1997), although the final stope geometry, after ring 38 was blasted, was approximately 85 metres along strike (Milne, 1994). The 5HP1 stope used the same ground support measures as the 5FP1 stope.

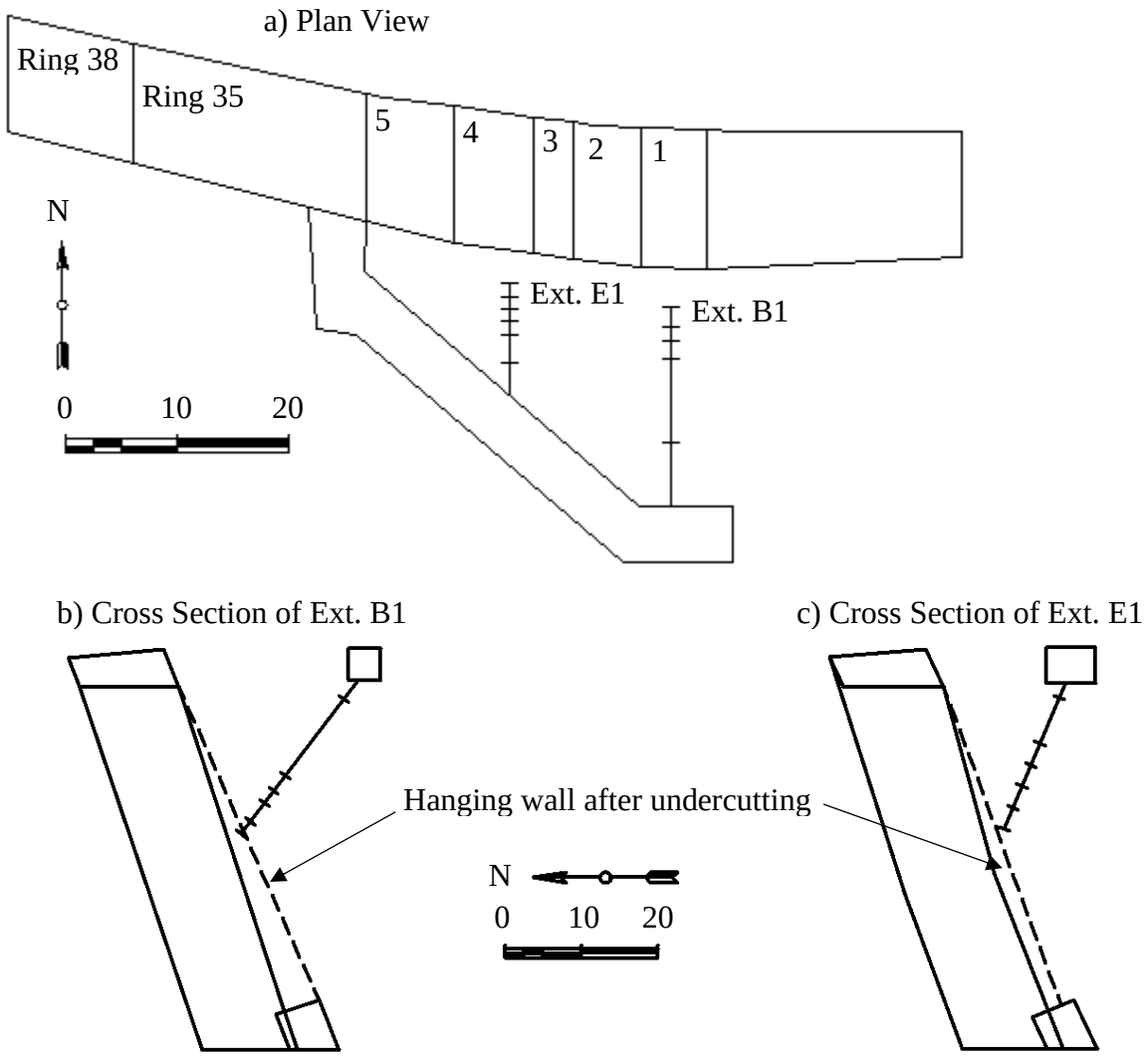

Figure 4-14: Section views of the Mount Isa 5HP1 stope showing the extensometer location and the stope excavation sequence in (a) plan view, (b) cross section of extensometer B1, and (c) cross section of extensometer E1 (after Milne, 1994).

4.3.1 Stope mining

Mining of the instrumented portion of the 5HP1 bench stope at Mount Isa Mine was completed with five production blasts, which progressed from South to North, (Figure 4-14a) before access to the hanging wall instrumentation drift was cut off. As a result, extensometer data is only available from 6-April, 1993 until 13-May, 1993 (Milne, 1994; Milne, 1997). Additional measurements were collected in October 1993, after the stope had been backfilled, however, these are not considered since the measured deformation could not be related to a change in blast geometry (Milne, 1994). For simplicity, the blast numbers discussed in this section are not the overall stope blast number, but rather are related to the blasting sequence of the five blasts for which extensometer measurements were collected.

After access to the hanging wall instrumentation drift was cut off, there were challenges with hanging wall stability. Following blasting up to ring 35, on 23-May, 1993, sloughing was reported along a fault. Prior to this, the last survey of a stable hanging wall was conducted following blasting up to ring 27, by blast 4, on 9-May, 1993. Additional sloughing occurred following the last stope blast which took rings 36 to 38 on 25-May, 1993 (Milne, 1994).

4.3.2 Estimation of Pre-Mining Stress

The dataset for the 5HP1 stope contained a small number of manual readings taken following each stope blast. By comparing successive measurements, the change in strain due to each stope blast could be estimated. The strain changes in each anchor segment are summarized in Table 4-6. By applying Equation 3-6, and using an elastic modulus of 25 GPa and a Poisson's ratio of 0.25 (Milne, 1997) the measured changes in strain after undercutting were used to calculate the pre-mining stress in each anchor segment, as summarized in Table 4-6. Results associated with anchors not believed to be fully relaxed, are coloured yellow. A sample calculation for anchor segment 2-4 of extensometer B1 is shown below.

$$\sigma_{pre-mining} \cong -\frac{\Delta\varepsilon\, E}{(1-\upsilon)} \cong -\frac{(-120\mu\varepsilon)(25\ GPa)}{\big(1-(0.25)\big)} \cong 5\ MPa$$

For the closest reliable anchor segment for extensometer B1, the ERF was smaller than the distance of at least one of the anchors to the opening, suggesting that this anchor segment was not fully relaxed (Section 3.2.4). This is supported by the estimated pre-mining stress for this anchor segment (5 MPa) being approximately one third of the 15 MPa indicated by MIM (1993). Additional details about the 5HP1 stope are available in Appendix D.

For the closest reliable anchor segment for extensometer E1, the ERF is larger than the distance from the anchors to the opening, suggesting that his anchor segment has relaxed fully. The estimated pre-mining stress for this anchor segment (20 MPa) is approximately 30% larger than the 15 MPa indicated.

This stress estimate has a degree of uncertainty related to the accuracy of the manual measurement, which were recorded to the nearest 0.1 millimetre, and uncertainty in the estimate of elastic parameters. Additionally, the model used to estimate stress used approximated input stresses and excavation geometries. Considering these factors, a 30% variation is estimated pre-mining stress can be considered acceptable.

Table 4-6: Summary of the stress and strain change following undercutting for each extensometer segment in the 5HP1 stope hanging wall.

Anchor Segment	Anchor Segment length (m)	Perpendicular distance to hanging wall (m)	ERF (m)	Strain change due to blast (με)	Calculated Pre-mining stress (MPa)
Extensometer B1	Undercut by Blast 1 on 13-Apr-1993				
1-2	2.0	Lost following Blast 1			
2-3	5.0	1.0-5.0	3.7	-120	5
3-4					
4-5	2.5	5.0-7.0	3.7	-150	5
5-6	12.5	7.0-17.5	3.6	10	0
Extensometer E1	Undercut by Blast 4 on 9-May-1993				
1-2	3.0	1.0-2.5	6.4	-530	18
2-3	6.0	2.5-7.0	6.4	0	0
3-4					
4-5	3.0	7.0-9.0	6.3	-50	2
5-6	6.5	9.0-19.0	6.2	30	-1

*yellow highlight- not fully relaxed (ERF< distance to hanging wall)
*red highlight- unreliable anchor segment

4.3.3 Modified SERF Method

Two failure events were noted during mining of the 5HP1 bench stope at Mount Isa Mine. The first was a spalling failure which was observed following the blasting of ring 35 when the hanging wall had a RF of approximately 17.4 m, although the spalling may have initiated earlier. The second, more significant spalling failure was estimated to extend over 10 metres from the original hanging wall location, and was observed following the blasting of rings 36 to 38, when the hanging wall had a RF of approximately 18.2 m.

Due to issues with data reliability, the closest anchor segment on extensometer B1 to the opening was anchor segment 2-4. Applying the modified SERF method to the data following the transition to non-linear extension results in a predicted RF of instability (RF_p) of approximately 19 m for anchor segment 4-5 (between five and seven metres from the stope hanging wall) (Figure 4-15). Although the predicted geometry of instability is larger than both the RF of spalling and the RF of failure (RF_f), it is expected that an improved failure prediction would have been obtained with more data, closer to the point of instability. The presence of the fault, along which sloughing occurred, may have also contributed to the RF_f being smaller than the RF_p.

Similarly, applying the modified SERF method to the data from extensometer E1 results in a RF_p of approximately 19 m (Figure 4-16). This prediction is for anchor segment 1-2, which is closer to the opening than anchor segment 3-4 on extensometer B1. The predicted RF_p is based on two data points and it is expected that the inclusion of additional data points from subsequent blasts, as the geometry of instability was approached, would have resulted in an increase in the slope of the trend line and a decrease in the RF_p.

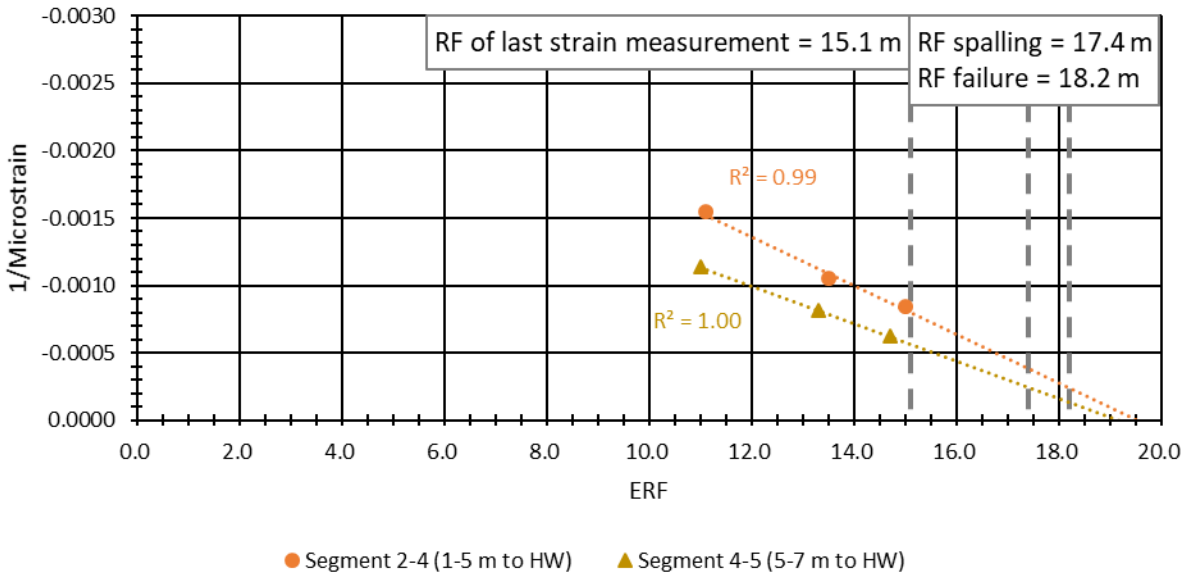

Figure 4-15: Analysis of measurements by extensometer B1 of the 5HP1 stope at Mount Isa Mine using the modified SERF method.

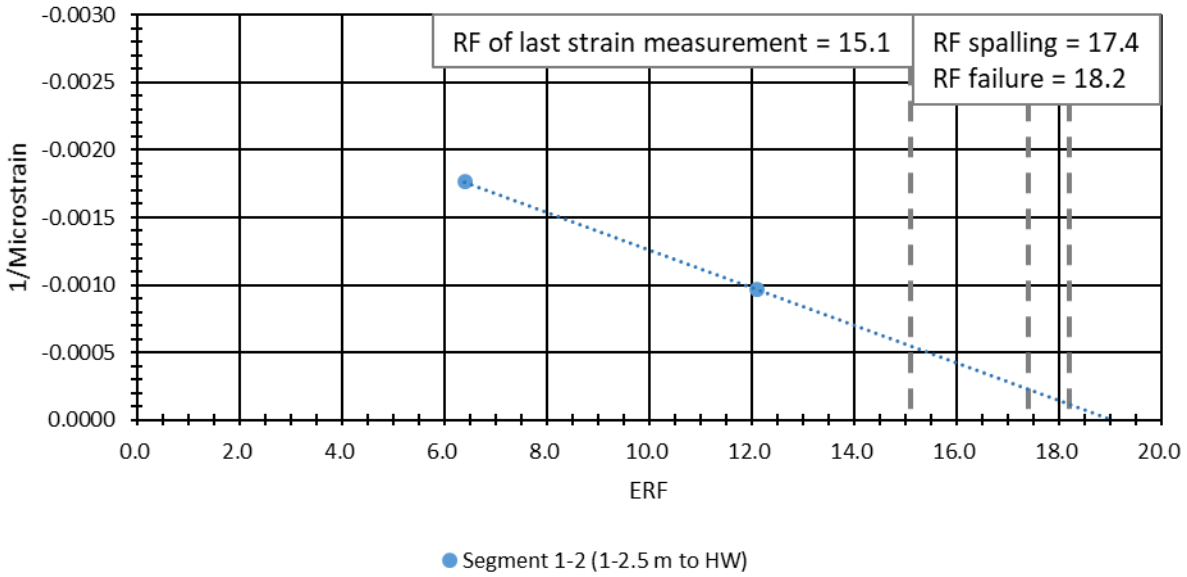

Figure 4-16: Analysis of measurements by extensometer E1 of the 5HP1 stope at Mount Isa Mine using the modified SERF method.

4.3.4 Summary of 5HP1 analysis

Ideally, the estimates of pre-mining stress using extensometer measurements would be compared to measured stresses rather than modelled stresses. The estimates of the pre-mining stress using extensometer measurements appear to reasonably approximate modelled stresses. The differences in values can be associated with incomplete relaxation of the anchor segment, potential measurement errors, and variability between the selected elastic modulus and actual rock mass behaviour as well as the approximate nature of modelling input parameters such as in-situ stress values.

The loss of access to the hanging wall instrumentation drift during stope mining limited the effectiveness of the modified SERF method as additional blasts occurred prior to failure, which could have influenced the predicted instability. Despite this limitation, the modified SERF method appears to provide a reasonable prediction of approaching instability in advance of hanging wall sloughing. It is also seen as a favourable result that both extensometers independently predict a similar RF_p, however, it should be noted that the depth of predicted instability is different for both extensometers. It is also unknown if both extensometers would continue to predict the same RFp as mining continued.

5 SEABEE GOLD OPERATION

The case histories presented in this section were previously summarized in Shacker et al. (2018) and much of the following discussion is taken from this reference.

The Seabee Gold Operation (SGO) is located approximately 125 km northeast of La Ronge near Laonil Lake, Saskatchewan (Figure 5-1). At the time of the study there were two operating mines on site. The instrumentation program took place at Santoy Mine, which is located approximately 14 km east of the Seabee Mine and mill. SGO is located within the Canadian Shield in the Glennie domain (Corrigan et al, 2007). The Santoy deposits are located along the western extent of the Carruthers Lake synform and are hosted in metavolcanics, overlying intrusive complexes, rhyolite, and conglomerates overlain by siliciclastics and metavolcanics and affected by shears trending generally north-south (Morelli and MacLachlan, 2012; Wood, 2016; SRK,2017; Tipton, 2019). Additionally, a suite of pegmatite dykes exists in the region and crosscut mine development and mineralization (Wood, 2016).

2017 production from the combined mines at SGO averaged 905 tonnes of ore per day with Santoy Mine supplying 82% of this tonnage (SSR Mining, 2018).

Figure 5-1: Location of the SGO (after Saskatchewan Geospatial Imagery Collaborative, n.d.)

5.1 General rock mass properties

The typical rock mass at Santoy Mine is an amphibolite with a RMR_{76} ranging from 61 to 80, although there are localized occurrences where the RMR_{76} ranges from 41 to 60. There are three primary joint sets, which influence the RMR_{76} rating, with orientations of approximately 60°/360° (A), 80°/270° (B), and 10-30°/180° (C), as shown in Figure 5-2 (Pakalnis, 2017). The lower RMR_{76} values are associated with areas where either the shallow dipping joint set (C) has tighter

spacing and/or chloritic altered schists are present. Excavations are supported, as needed, with screen, mechanical bolts, and cable bolts.

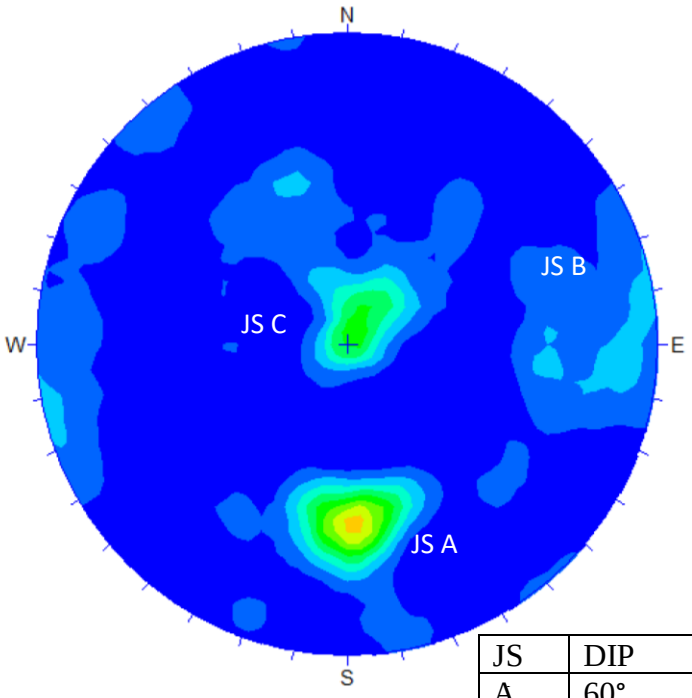

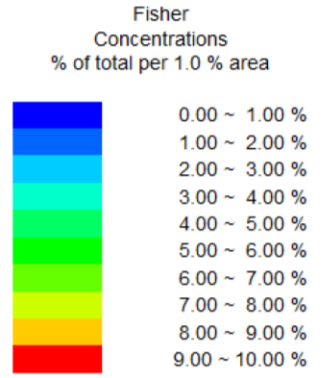

JS	DIP	DDR	
A	60°	360°	Ore structure
B	80°	270°	Release planes
C	10-30°	180°	Shallow

Figure 5-2: Stereonet of Santoy Gap joint orientations and images showing the three primary joint sets present at Santoy Mine (from Pakalnis, 2017)

A RMR_{76} of approximately 75 was observed for the average Santoy rock mass, matching the observations by Pakalnis (2017) and Schartner (2017), which provides an estimated elastic modulus of approximately 50 GPa using Equation 2-17. Other rock mass properties associated with the Santoy mine, measured by laboratory testing, are summarized in Table 5-1. A summary of the comprehensive laboratory program conducted on core from the Santoy Mine (Beneteau et al., 2019) is available in Appendix E.

Table 5-1: Summary of rock mass properties at Santoy Mine from laboratory testing (Beneteau et al., 2019).

Property	Symbol	Value
Average RMR_{76}		75
Elastic modulus	E	75±40 GPa
Poisson's ratio	ν	0.31±0.17
Unit weight	γ	29 kN/m^3
Unconfined compressive strength	UCS	144±42 MPa

5.2 Mining Overview

A long section of Santoy Mine is shown in Figure 5-3. Three sites were instrumented with extensometers, the 24L 411 Alimak Stope, and the 28-30L and 30-31L Longhole stopes. The instrumented portion of the orebody is located between approximately 140 m and 400 m below surface. The mining method uses loose rockfill as backfill and mining panels are developed from the bottom up. The orientation of the major principal horizontal stress is estimated to be near horizontal, aligned with the strike of the mineralization (Paulgaard et al., 2014; SRK, 2017), and can be estimated based on a typical Canadian shield K-ratio of 2 (Herget, 1988). Based on these estimated properties, stresses normal to the stope hanging walls will approximately equal the vertical stress, which ranges between 8 MPa and 23 MPa, based on the weight of the overlying rock mass for depths of 140 m and 400 m respectively. No known in-situ stress measurements have been conducted, at the mine or in the surrounding area, to confirm these estimates.

As shown in Figure 5-3, Santoy uses both longhole open stope and Alimak mining methods to access, develop, and extract ore. For Alimak mining, the Alimak raise serves as access to several sublevels within the overall stope panel. Each sublevel serves as a sill where miners follow the vein along strike until the ore pinches off. Once a sublevel is driven, cable bolts are installed into the hanging wall and, after the ground support is installed, the sublevel serves as an overcut for longhole drilling and blasting, as in conventional longhole open stope mining.

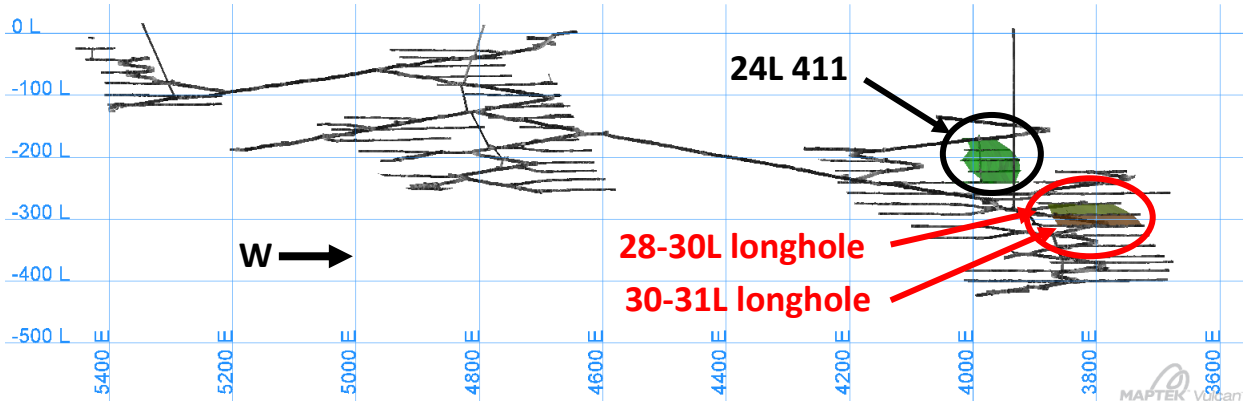

Figure 5-3: Long section, looking south, of Santoy mine development and the location of the instrumented stopes (24L 411 Alimak, 28-30L longhole, and 30-31 longhole).

The instrumentation program was completed using extensometers and dataloggers supplied by MDT. The extensometers used at SGO have a potentiometer length of five inches (127 millimetres) and operate off an input voltage of five volts (MDT, 2017). Two types of datalogger were used in the instrumentation program. The SMART Log has a single port and 10-bit resolution, allowing the return voltage to be split into up to 1,024 sub-units (2^{10}). For an input voltage of five volts (500 centivolts) this provides a measurement interval of 0.49 centivolts, which equates to 0.12 millimetres for a 127 millimetre potentiometer. The SMART Log3 has three ports and 16-bit resolution, allowing the return voltage to be split into up to 65,536 subunits (2^{16}). For an input voltage of five volts (500 centivolts) this provides a measurement interval of 0.0076 centivolts, which equates to 0.0019 millimetres for a 127 millimetre potentiometer (MDT, 2017).

The initial MDT Mine Monitor database, provided by MDT, would truncate exported data to the nearest 0.01 centivolt (0.0025 millimetre), which loses some of the resolution for SMART Log3 recordings. Although future versions of the Mine Monitor Database application improved this

resolution, these changes in the database exports did not influence the results, as data from the SMART Log3 was rounded to the nearest 0.01 millimetre prior to analysis.

For the average Santoy mine elastic modulus (75 GPa), and assuming an anchor segment length of one metre, the SMART Log can measure a strain of approximately 120 microstrain (equivalent to approximately 13.0 MPa), the SMART Log3 can measure a strain of approximately 2 microstrain (approximately 0.2 MPa), and the data rounding of the SMART Log3 results in limiting measured strain to the nearest 10 microstrain (1.1 MPa). This provides a range to the precision of the reported measurements that is reasonable for the magnitude of stresses being considered in the pre-mining stress estimate and analysis using the modified SERF method.

Although three stopes were instrumented, failure of a SMART Log3 prevented the collection of measurements for the 28-30L Longhole Stope. As a result, only data from the remaining two stopes were analysed. The datasets were analyzed following the approach outlined in Section 3 and an overview of the results of the analysis are provided in Table 5-2.

Table 5-2: Overview of the outcome of the estimates of pre-mining stress and a geometry of instability using the SERF method for different stopes.

Mine	Stope	Pre-mining stress	SERF
Santoy Mine	24 411 Alimak	Reasonable	Not applicable
	30-31L Longhole	Reasonable	Not applicable

5.3 Santoy 24L 411 Alimak Stope

The 24L 411 stope at Santoy Mine was considered an Alimak stope based on the method of accessing the sublevels for support and development (Figure 5-4), however, it operated more like a regular longhole open stope with the stope blast holes drilled from sub-levels. Overall, the average stope depth was 205 metres below surface, which corresponds to a vertical stress of approximately 6 MPa. The Alimak stope had an up dip length of approximately 92 metres at an average dip of approximately 54 degrees (Figure 5-5).

Level development in the Alimak stope consisted of an overcut (17L), an undercut (24L), and three sublevel sills that were accessed from the Alimak raise (Figure 5-4). All five sills were driven along strike to follow the gold vein until the grade dropped below cutoff, resulting in sill lengths

that varied between 60 and 93 metres. All mucking was done from 24L since there was no ramp access to the sublevel sills.

SGO mapping data, with limited structural data, was limited to sublevel one, the 17L sill, and the 24L hanging wall mucking drift due to access restrictions (Appendix C). The mapping, conducted as part of this project, resulted in a rock mass classification of (Q' = 20 and RMR'_{76} = 75-80) which was similar to the RMR_{76} value of 79 recorded by the site engineer. This shows consistency between mine site mapping data and data collected for this research. Where mapping was not done for this research, mine site classification data was used. Mapping around the 24L 411 Alimak stope did not identify any local variations to the orientation of the average Santoy Mine joint sets (Figure 5-2) but did identify the presence of a pegmatite dyke in the western portion of the stope.

Site engineers developed a ground support program for the Santoy 24L 411 Alimak stope based on the RMR_{76} values and the designed stope geometry. The ground support included three nine-metre-long double strand, bulbed cable bolts installed into the hanging wall every three metres along the sublevel sills (Figure 5-5) and every 2.4 metres vertically along the Alimak raise (Schartner, 2017).

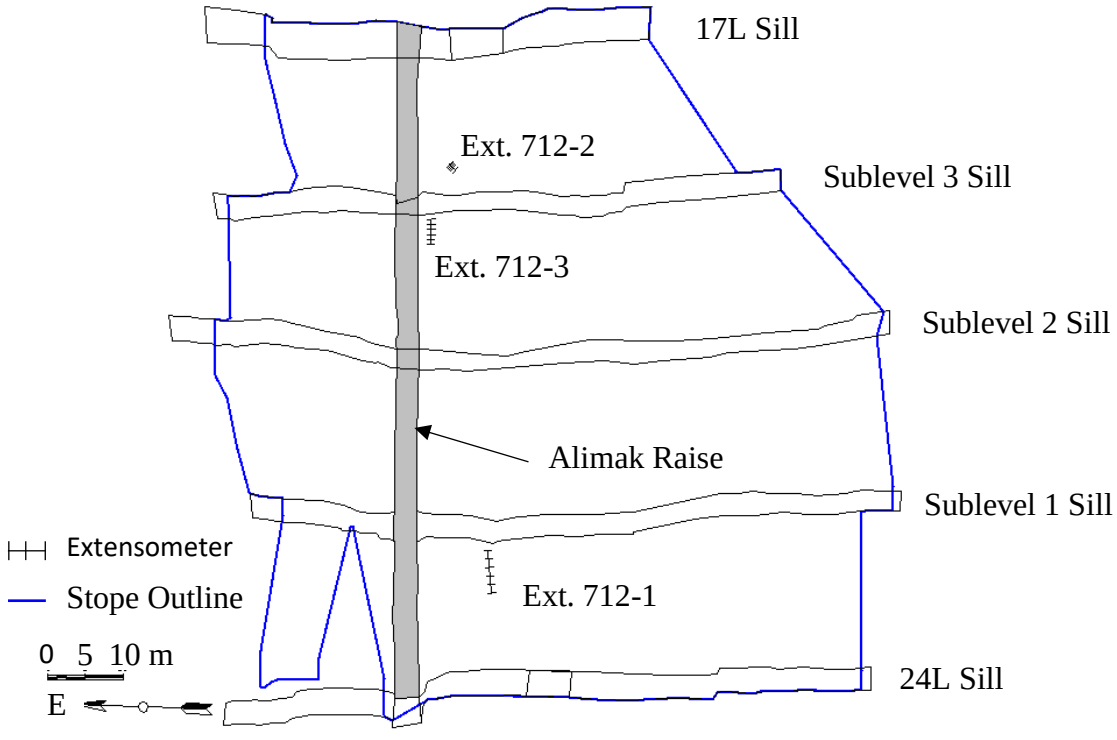

Figure 5-4: True longitudinal section of the Santoy 24L 411 Alimak stope showing existing development, the designed stope outline, and the installed extensometer locations.

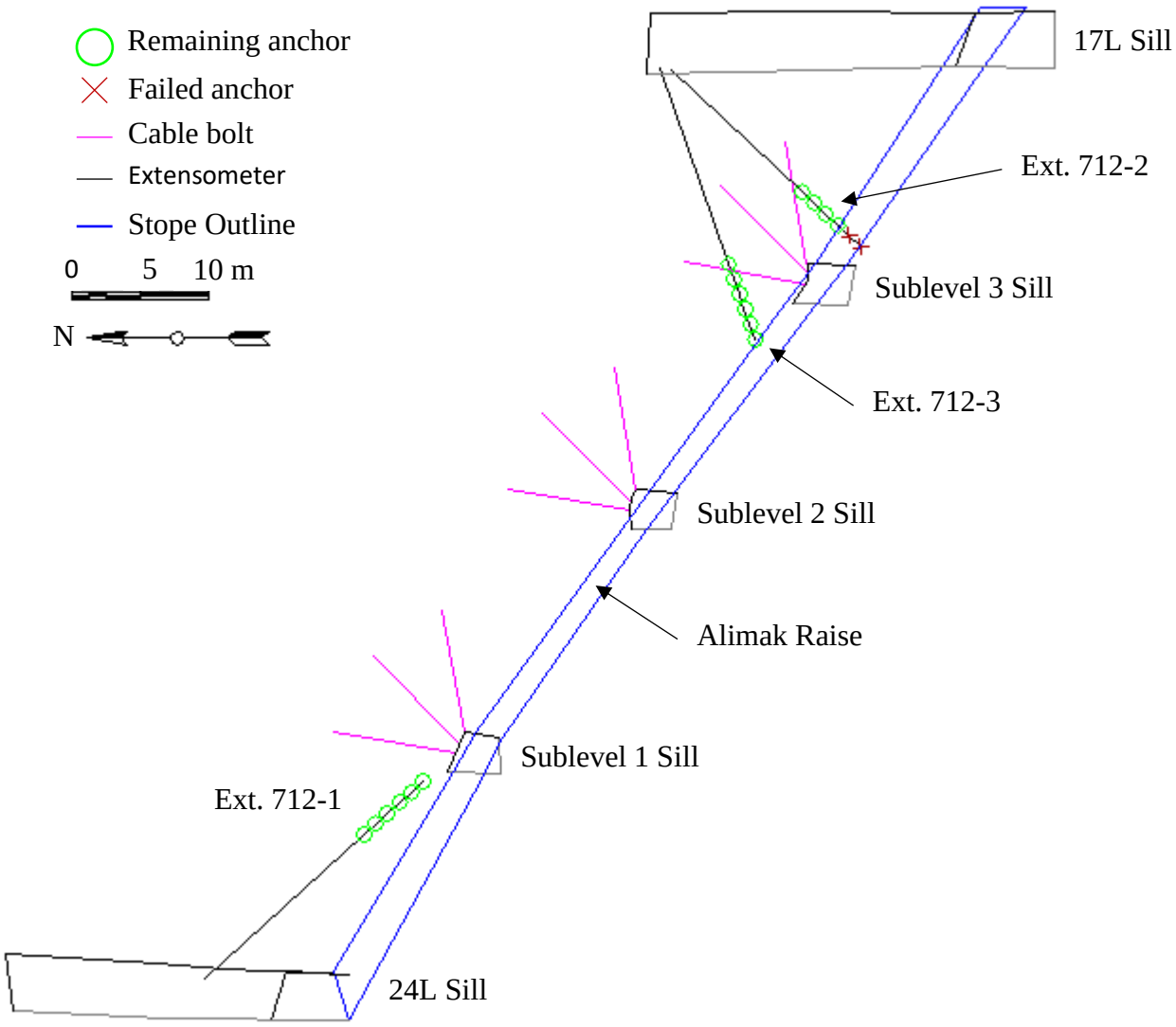

Figure 5-5: Cross section view adjacent to the Alimak raise of the Santoy 24L 411 stope looking east and showing the stope design outline, projected extensometer locations, and ground support,

5.3.1 Instrumentation program design

Extensometer locations were designed to maximize hanging wall coverage, reach the hanging wall within a 25m hole length, and have an orientation ideally perpendicular (± 30°) to the hanging wall contact. Instruments could only be installed and accessed from hanging wall development on 17L and 24L, and the preferred extensometer orientation was only possible from 17 level overcut. The instrumentation design consisted of one extensometer installed up from the 24L haulage drift and two extensometers being installed down from the 17L access. The extensometer locations are

shown in a true long view normal to the stope hanging wall (Figure 5-4) and in a cross section adjacent to the Alimak raise showing projections of the extensometer locations (Figure 5-5).

Due to operational constraints, two of the three extensometers deviated from the design locations and, due to hole conditions, it was not possible to accurately verify the hanging wall contact location with a borehole camera. The instrument installation procedure is summarized in Appendix F. The distances between extensometer anchors are summarized in Table 5-3 and a schematic of the anchor positions relative to the stope and drillhole collar are shown in Figure 5-6.

Extensometer 712-1 was installed on 27-June, 2017 from the Sublevel 1 Sill, to be accessed from the 24L haulage drift, and Extensometers 712-2 and 712-3 were installed on 22-June, 2017 from the 17L Crosscut.

Table 5-3: Distances between anchors for extensometers installed to monitor the Santoy 24L 411 Alimak Stope hanging wall.

Instrument	Distance between anchors (m)					
	1-2	2-3	3-4	4-5	5-6	6-Head
712-1	1.17	1.17	1.17	1.17	1.17	1.17
712-2	1.17	1.17	1.17	1.17	1.17	1.17
712-3	1.17	1.17	1.17	1.17	1.17	1.17

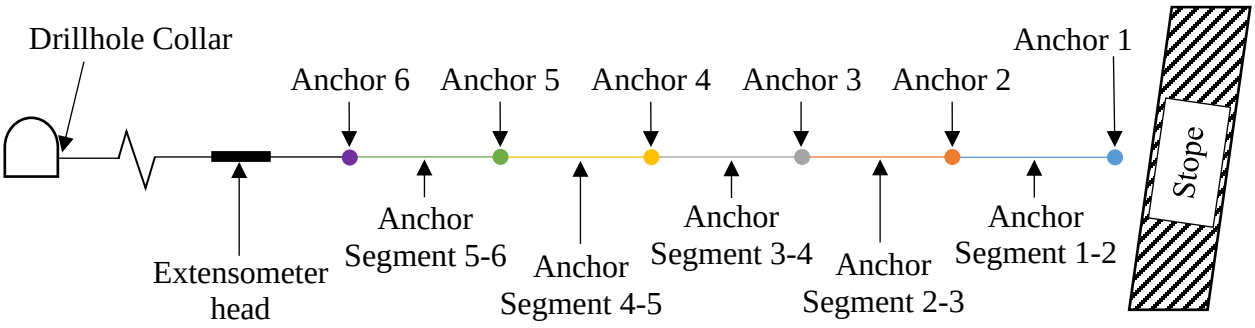

Figure 5-6: Schematic showing the anchor positions relative to the stope and the drillhole collar.

5.3.2 Stope Mining

Mining of the Santoy 24L 411 Alimak stope was completed with 37 production blasts. Production blasting began on 1-July, 2017 and concluded on 22-October, 2017 with the general mining direction retreating towards the Alimak raise on each sublevel and then advancing up dip towards

17L. The blast sequencing and associated blast outlines are shown in a true longitudinal view of the Santoy 24L 411 Alimak stope hanging wall, looking south, in Figure 5-7, along with the instrument locations.

Prior to the start of mining, the mining plan was changed from fully mucking out the stope following each production blast to only removing enough muck to provide a free face for the next production blast, to provide support to the hanging wall. During excavation, more muck was removed than required to provide a free face in order to meet production targets. As a result, the geometry of the unsupported opening could not be confirmed.

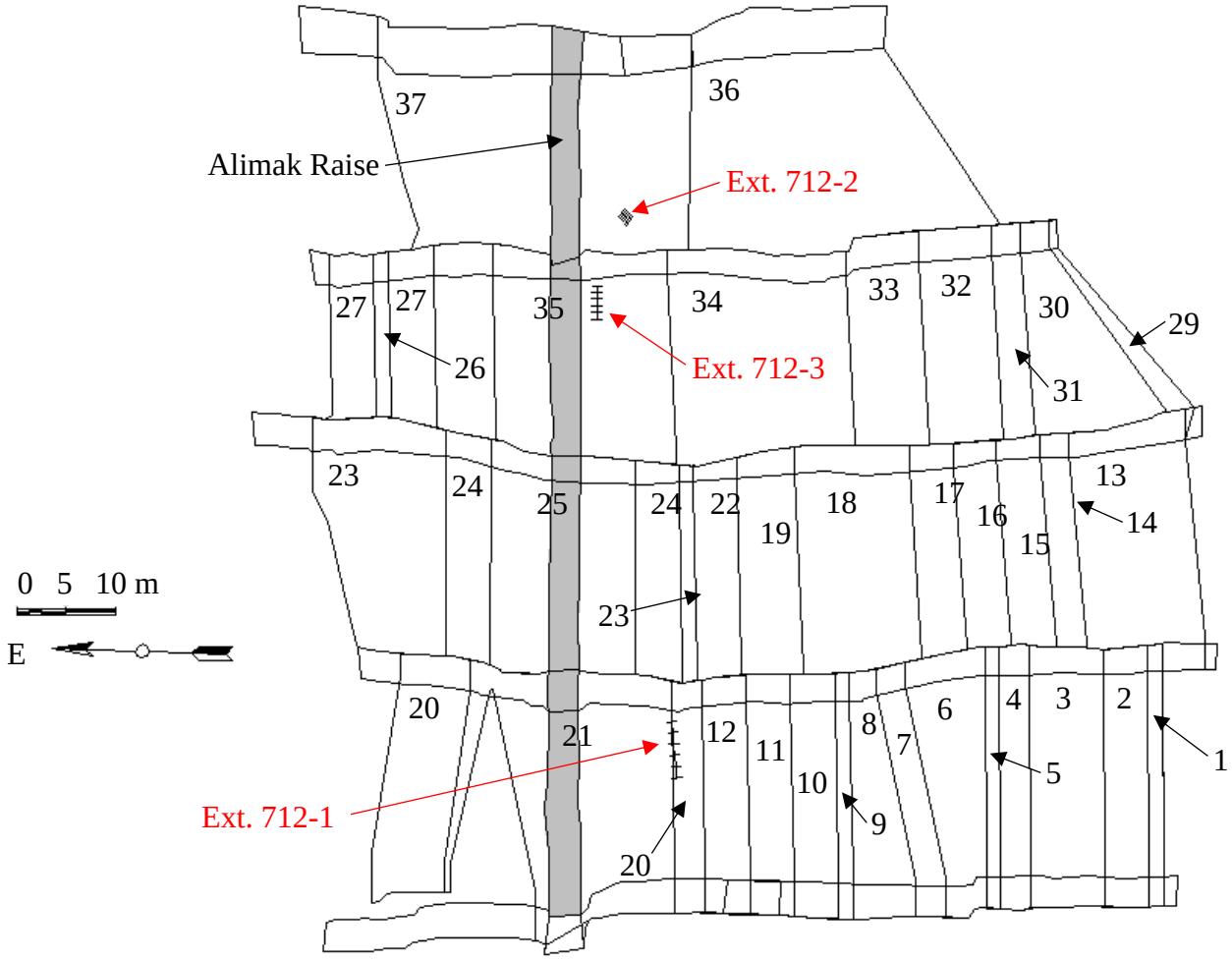

Figure 5-7: True longitudinal section of the Santoy 24L 411 Alimak stope hanging wall looking south and showing stope outlines and instrument locations.

Limited Cavity Monitoring System (CMS) scans were completed for the Santoy 24L 411 Alimak stope to provide final geometries for the stope hanging wall. Four CMS scans were reviewed, however, coverage gaps due to the small number of scans and the narrow stope width, as well as interpretation challenges due to muck left in the stope, limited the utility of the scans.

A site visit was conducted on 4-November 2017, when extraction from the Santoy 24L 411 Alimak stope neared completion. The site visit included a tour of the 24L Sill to observe a large slab that had dropped from the Alimak hanging wall and was bridging the open stope and remaining ore (Figure 5-8). In addition to the large slab, several pieces of oversize were observed in remucks on 24L (Figure 5-9). Unfortunately, the source of the oversize is unknown and could have been from hanging wall instability or large muck due to blasthole deviations. The SERF method is not intended to predict instability in the form of isolated blocks which may have created the oversize muck (~0.2 to 1.0 m^3).

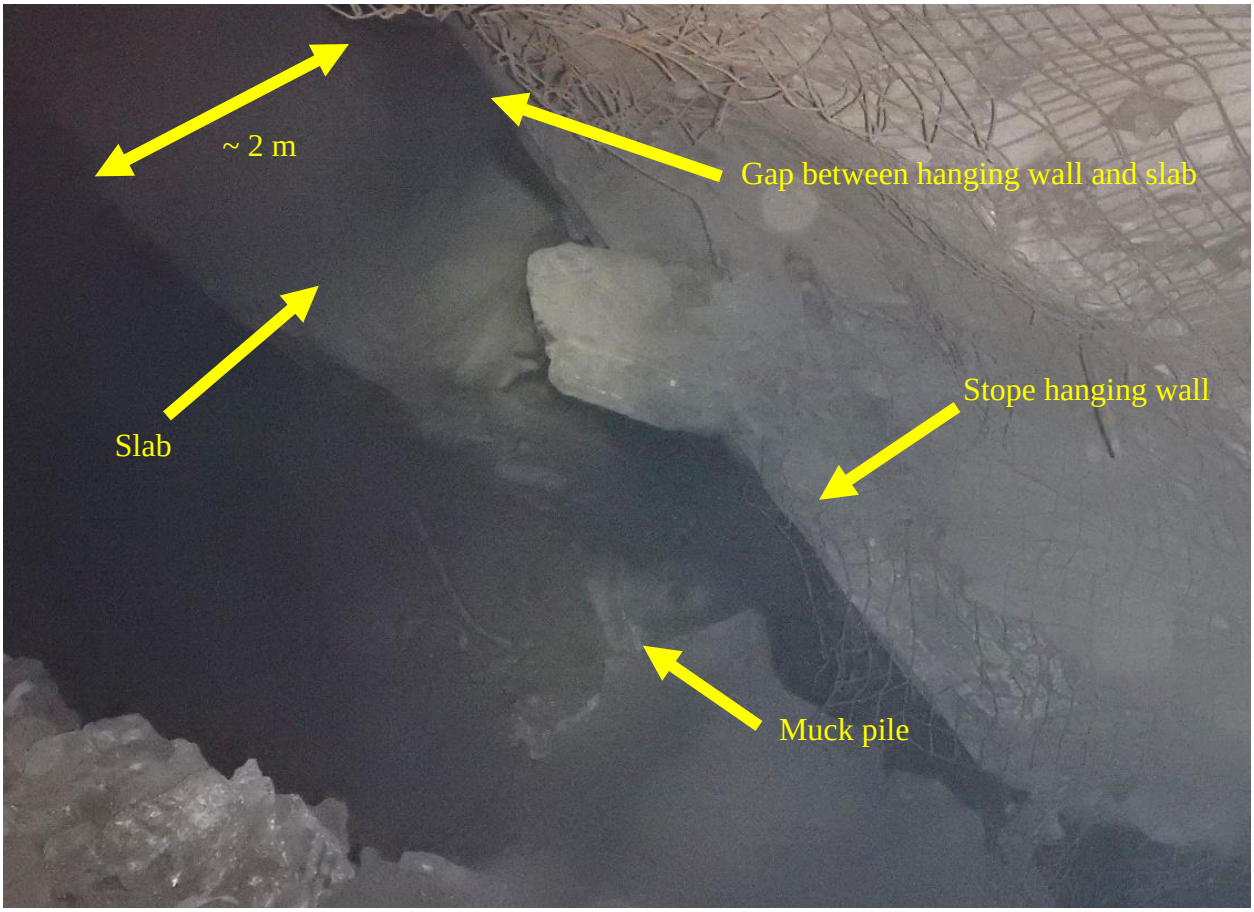

Figure 5-8: Slab from a hanging wall failure bridging the stope.

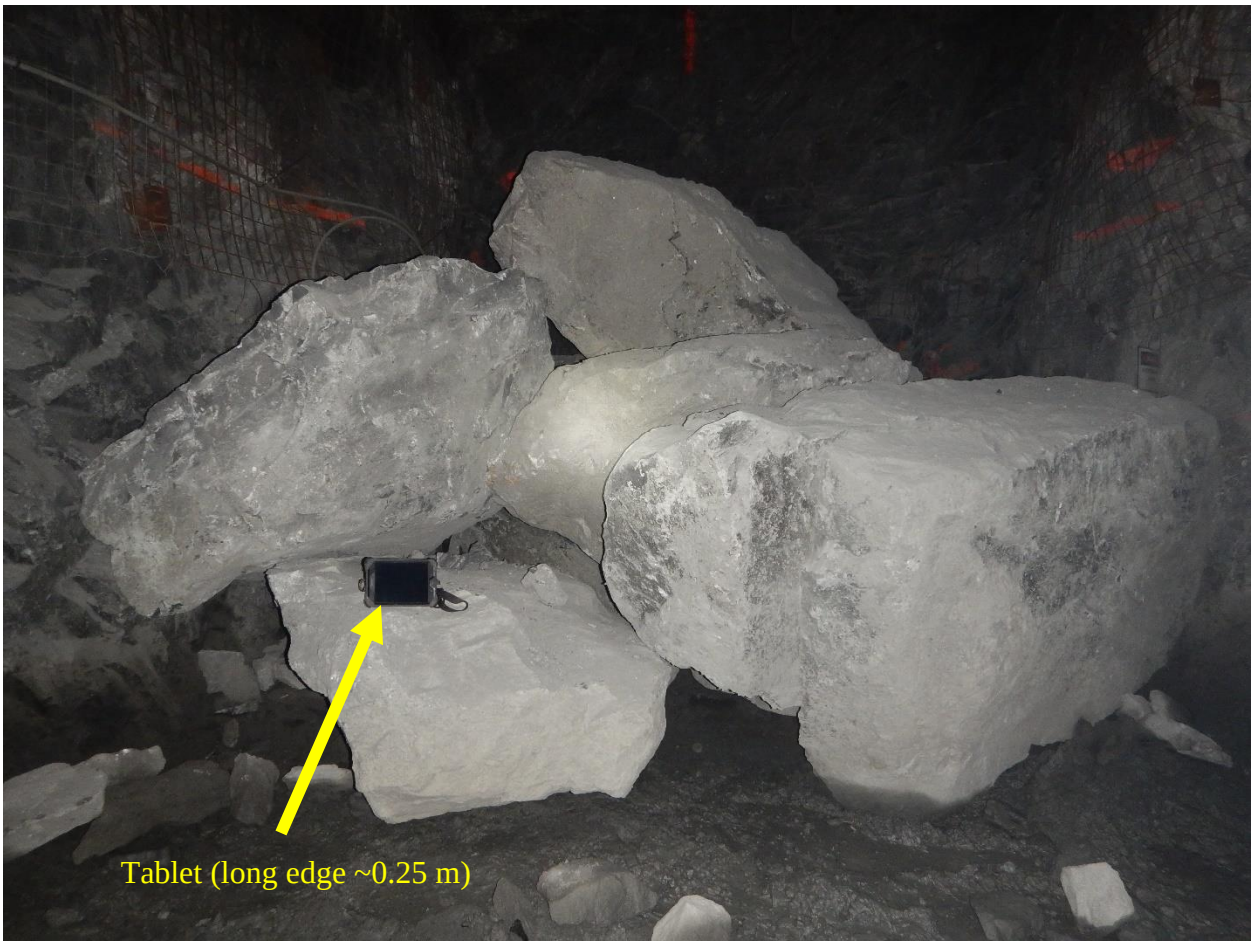

Figure 5-9: Oversize removed from the 24L Alimak stope.

5.3.3 Ground Response to Mining

The 24L 411 Alimak stope (Figure 5-4) is at an average depth of 205 metres, corresponding to a vertical stress of approximately 6 MPa and a stress normal to the hanging wall of 6 MPa, as discussed in Section 5.3. As mining approached the instrument location, a maximum stress increase of up to approximately 20 MPa, approximately 3 times the initial stress normal to the hanging wall, can be feasible (Section 3.1) which is associated with a strain of approximately 200 microstrain for the Santoy rock (75 GPa). It was similarly estimated that the stress concentration would exceed the intact rock strength (144 MPa) for compressive strains larger than approximately 1,300 microstrain. Since compressive failure of the intact rock is not expected due to the low expected stresses, if this magnitude of compressive strain were measured, it could be indicative of potential shearing along structure within the rock mass (Section 3.1).

Applying Equation 3-7, the estimated upper bound to elastic deformation in the hanging wall adjacent and normal to the stope, due to hanging wall stress relaxation following undercutting by stope mining, is estimated to be approximately 50 microstrain of tension. Assuming a one metre anchor segment length, this strain would be associated with a deformation of approximately 0.05 millimetres.

$$\varepsilon_{(a-b)} = \frac{\Delta\sigma_n}{E}(1-\upsilon) = \frac{0-6MPa}{50GPa}(1-0.31) \cong -100\mu\varepsilon$$

5.3.3.1 EXTENSOMETER 712-1

The data from extensometer 712-1 was logged using a SMART Log, providing a resolution of approximately 0.127 millimetres. A plot of the anchor segment strain over time for extensometer 712-1 is shown in Figure 5-10.

Figure 5-11 shows plan, cross section, and long section views of the stope and extensometer, before and after being undercut by blast 20. To obtain instrumentation coverage for the hanging wall, extensometer 712-1 was oriented at an angle of approximately 18° to the stope hanging wall (Figure 5-11b). This was done to gain deformation measurements earlier in the stope excavation sequence, even though it was realized that an orientation closer to perpendicular to the hanging wall is the preferred orientation.

Figure 5-11 also includes a schematic of areas of expected stress concentration and relaxation, for stresses generally perpendicular to the ore zone. After undercutting, the extensometer anchors closest to the stope are within a zone of relaxation, and a tensile strain response can be expected between anchors. Figure 5-10 shows the full range of recorded strain for extensometer 712-1 with anchor segments 1-2 showing approximately 800 microstrain of compression following undercutting. Since this is in a zone of expected tensile response, and anchor 1 was within a metre of the designed hanging wall; it was concluded that this anchor was either damaged or lost in the undercutting blast and data from this anchor segment could not be used after undercutting. Due to the orientation of the extensometer relative to the hanging wall, it is also possible that the deformation is a result of shear movement along a foliation (Section 3.1) which is illustrated in Figure 5-11c.

Due to the suggested shearing and unfavourable extensometer orientation, the dataset from extensometer 712-1 is not considered reliable and was not be analysed further.

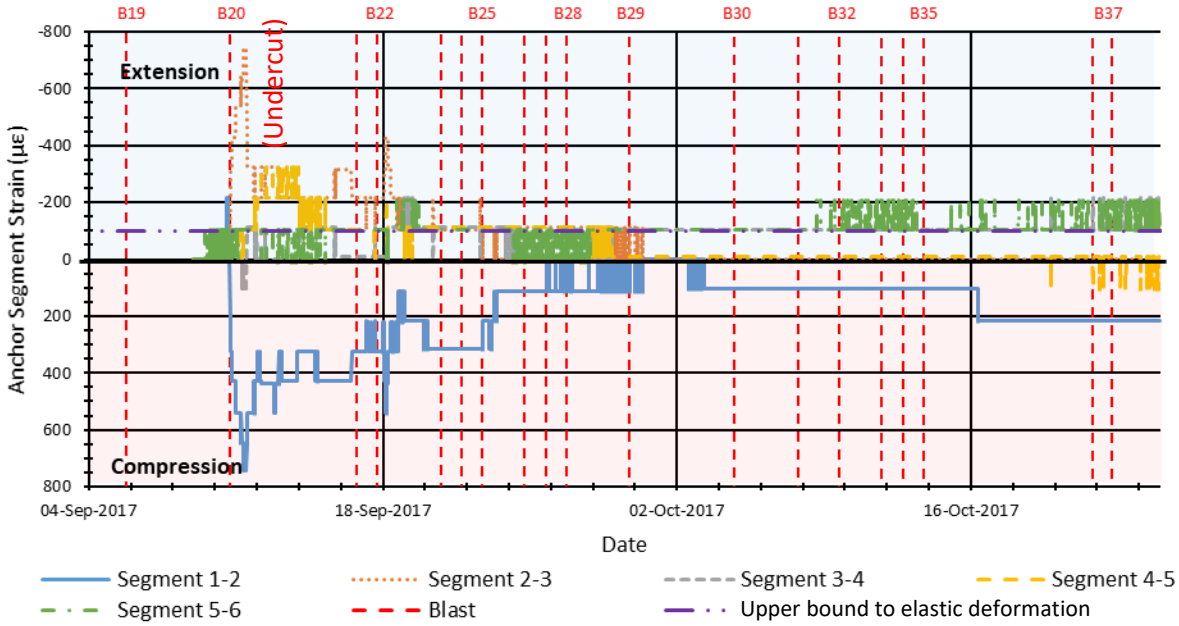

Figure 5-10: Full dataset of segment strains in the 24L 411 stope hanging wall at Santoy mine measured by extensometer 712-1.

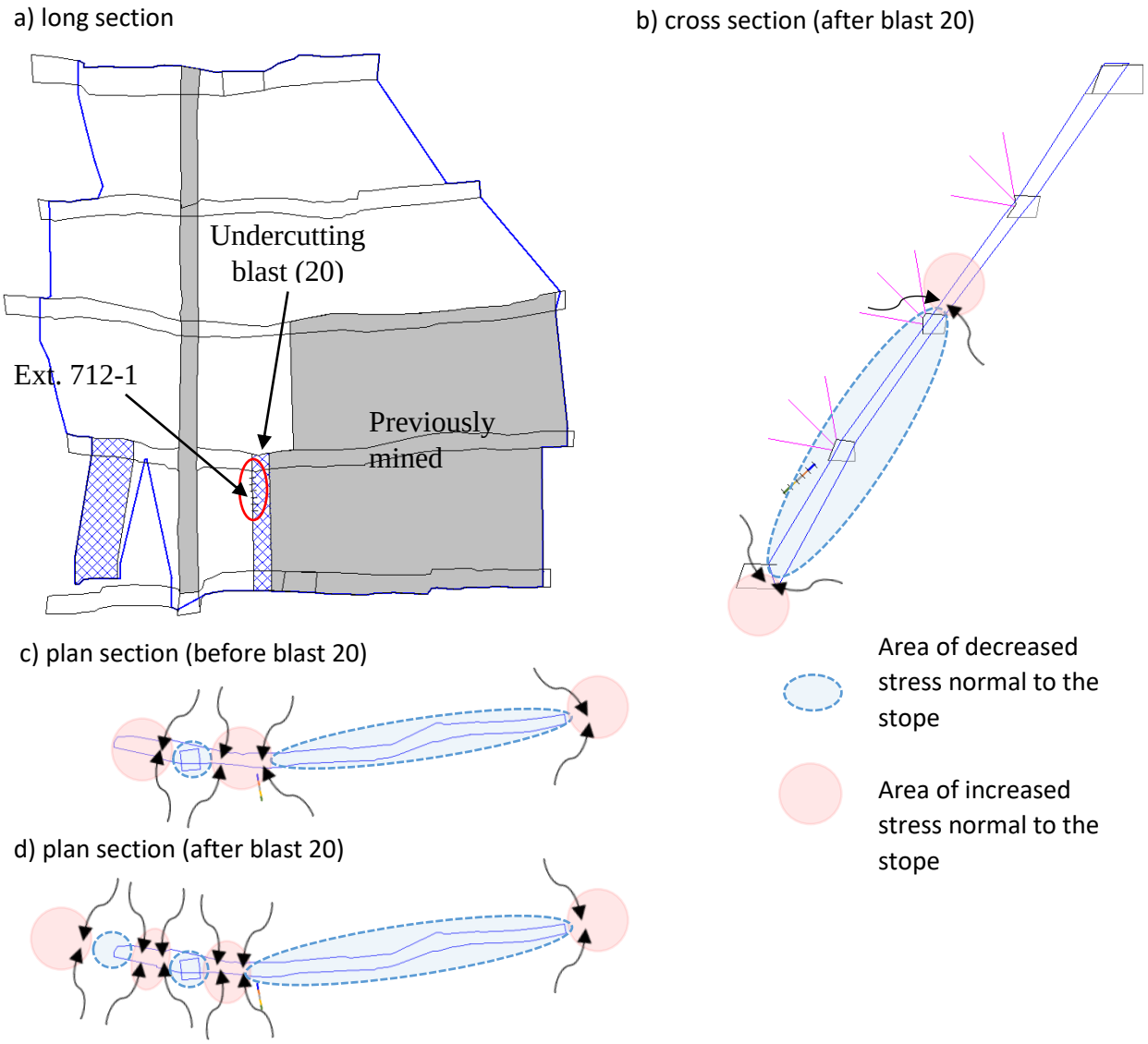

Figure 5-11: Section views of the Santoy 24L 411 Alimak stope showing blast geometries, excavation geometries, expected zones of stress change, and the location of extensometer 712-1 for: (a) true longitudinal view, (b) cross section after undercutting, (c) plan section prior to undercutting, and (d) plan section after undercutting.

5.3.3.2 EXTENSOMETER 712-2

The data from extensometer 712-2 was logged using a SMART Log3, providing a resolution of approximately 0.0025mm, which was rounded to the nearest 0.01 millimetres. A plot of the strain over time for extensometer 712-2 is shown in Figure 5-12.

Figure 5-13 shows plan, cross section and long section views of the stope and extensometer, before and after being undercut by blast 37. Figure 5-13b shows that anchors 1 and 2 for extensometer 712-2 are located within the planned stope. After undercutting anchor segment 1-2 and 2-3 were lost, even though they show approximately 9,000 compressive microstrain and 11,000 tensile microstrain respectively. This left anchor segment 3-4 within one metre of the planned stope.

Figure 5-13 also includes a schematic of areas of expected stress concentration and relaxation, for stresses generally perpendicular to the ore zone. After undercutting, the extensometer anchors closest to the stope are within a zone of relaxation, and a tensile strain response can be expected between anchors. Figure 5-12 shows the full range of recorded strain for extensometer 712-2 with anchor segments 3-4 showing approximately 8,000 microstrain of compression following undercutting. Since this is in a zone of expected tensile response, and anchor 3 was within a metre of the designed hanging wall; it was concluded that this anchor was either damaged or lost in the undercutting blast and data from this anchor segment could not be used after undercutting.

After removing the unreliable anchor segments, the strain response in the remaining anchor segments appear reasonable and a more detailed strain response is shown in Figure 5-13e.

The undercutting blast was the final blast for this stope. No additional stope geometries could be monitored with extensometer 712-2 so there was no opportunity to apply the modified SERF method.

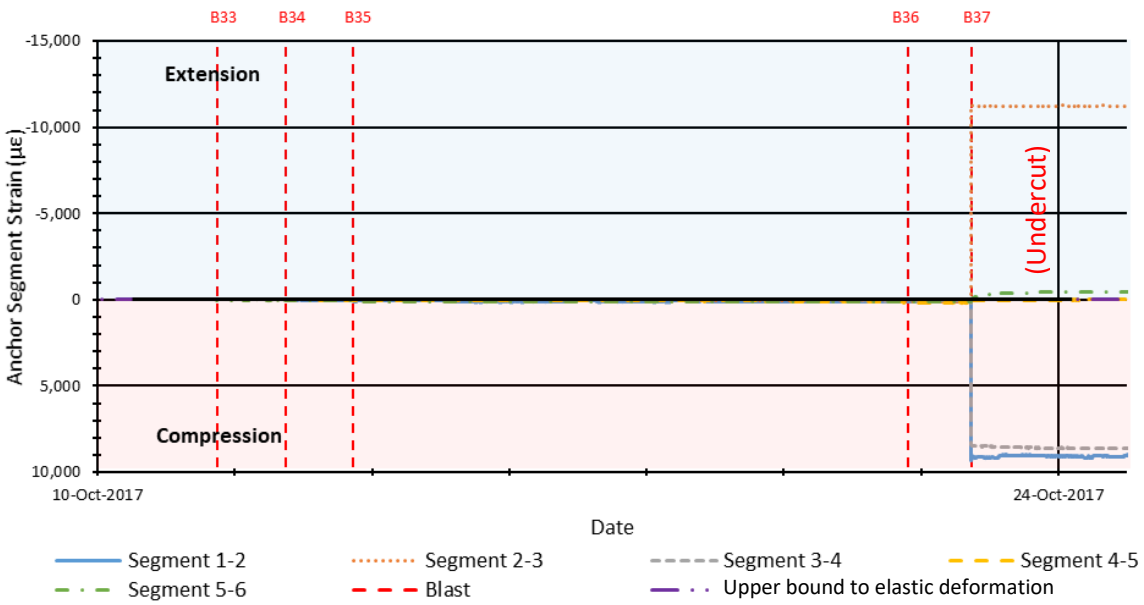

Figure 5-12: Full dataset of segment strains in the 24L 411 stope hanging wall at Santoy mine measured by extensometer 712-2.

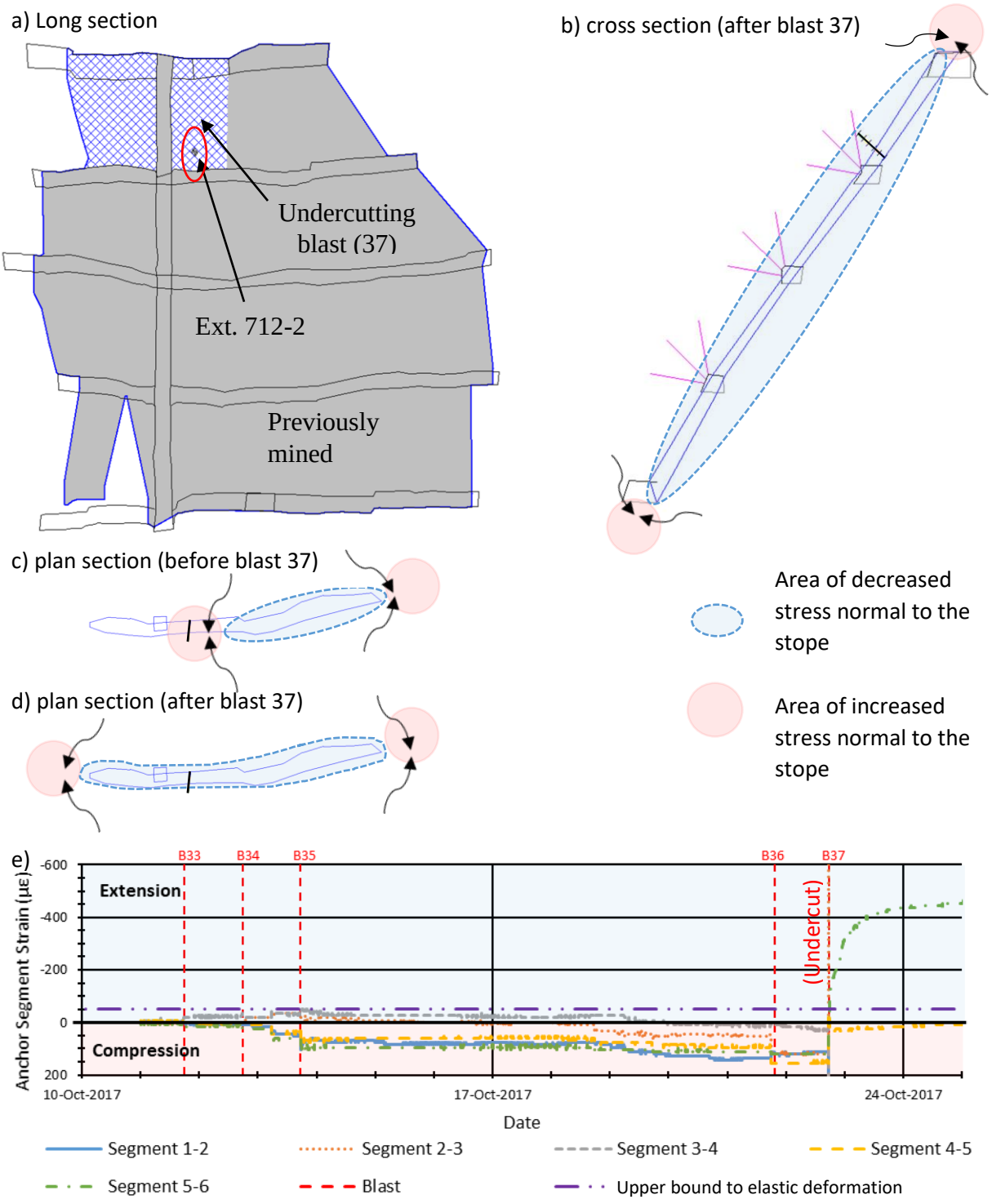

Figure 5-13: Section views of the Santoy 24L 411 Alimak stope showing blast geometries, excavation geometries, expected zones of stress change, and the location of extensometer 712-2 for: (a) true longitudinal view, (b) cross section after undercutting, (c) plan section prior to undercutting, (d) plan section after undercutting, and (e) a plot of strain over time for the reliable anchor segments.

5.3.3.3 EXTENSOMETER 712-3

The data from extensometer 712-3 was logged using a SMART Log3, providing a resolution of approximately 0.0025mm, which was rounded to the nearest 0.01 millimetres. A plot of the strain over time for extensometer 712-3 is shown in Figure 5-14.

Figure 5-15 includes a schematic of areas of expected stress concentration and relaxation, for stresses generally perpendicular to the ore zone. After undercutting, the extensometer anchors closest to the stope are within a zone of relaxation, and a tensile strain response can be expected between anchors. Figure 5-14 shows the full range of recorded strain for extensometer 712-2. While initially the measurements appear reasonable, over a week after undercutting by blast 35 a large strain response in several anchor segments initiated, just prior to blast 36 on 21-October, 2017. Following this event between blasts, anchor segment 2-3 and 3-4 are showing a mirror image as a result of large deformations logged for anchor 3 relative to anchor 2 and anchor 4. Additionally, anchor segment 1-2 measures a compressive response where a tensile response is expected due to the proximity to the opening and anchor segment 5-6 shows a compressive strain that far exceeds the 1,300 microstrain associated with failure of the intact rock, indicating potential shearing (Figure 3-1) or other non-linear behaviour. Considering the results for these anchor segments, the data does not appear to be reliable after 21-October, 2017 which may correspond to the hanging wall slough shown in Figure 5-8.

The earlier data, prior to 21-October, 2017 appears reasonable and is shown in Figure 5-15e. While it is expected that deformation and strain would be largest closest to the opening, Figure 5-15e indicates increasing strain as the distance from the opening increases. Review of the deformation data after undercutting on 13-October, 2017 shows the largest deformation occurring closest to the opening which, coupled with the strain measurements exceeding the estimated elastic limit, suggests non-linear deformation in anchors segment 2-3 and 3-4, possibly due to crack dilation.

The data prior to 21-October, 2017 appears reasonable and can provide information for estimating the pre-mining stress, although the measurements associated with anchor segments 2-3 and 3-4 should not be deforming elastically. Additionally, as the reliable strain plot only contains data from one production blast, there are insufficient reliable results for the dataset to be considered using the modified SERF method.

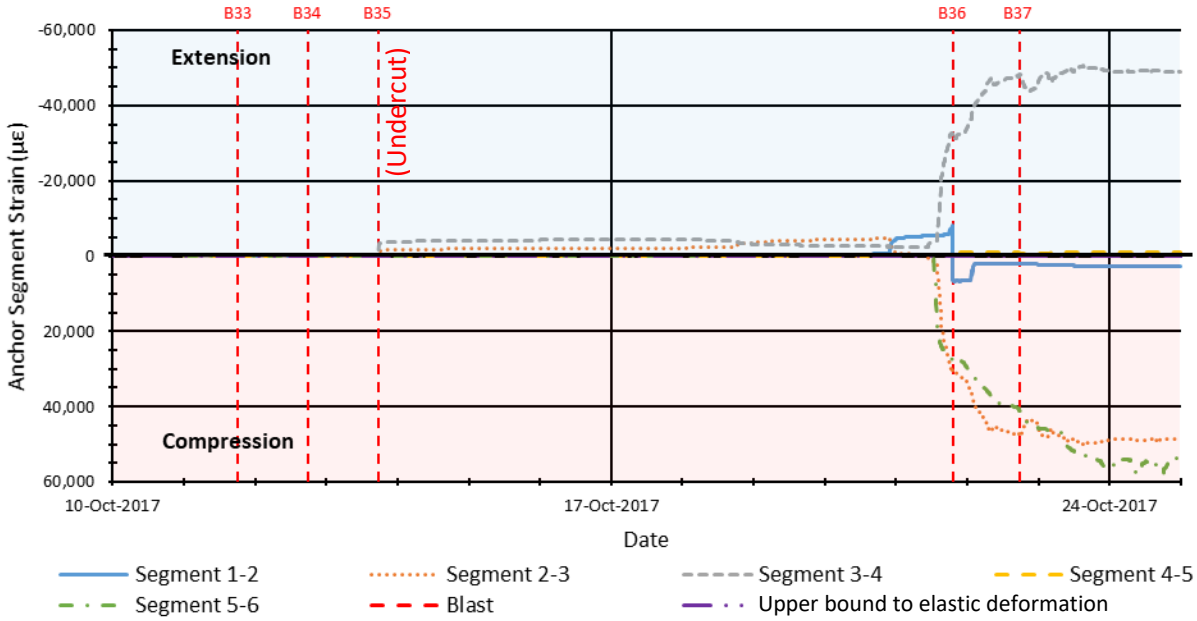

Figure 5-14: Full dataset of segment strains in the 24L 411 stope hanging wall at Santoy mine measured by extensometer 712-3.

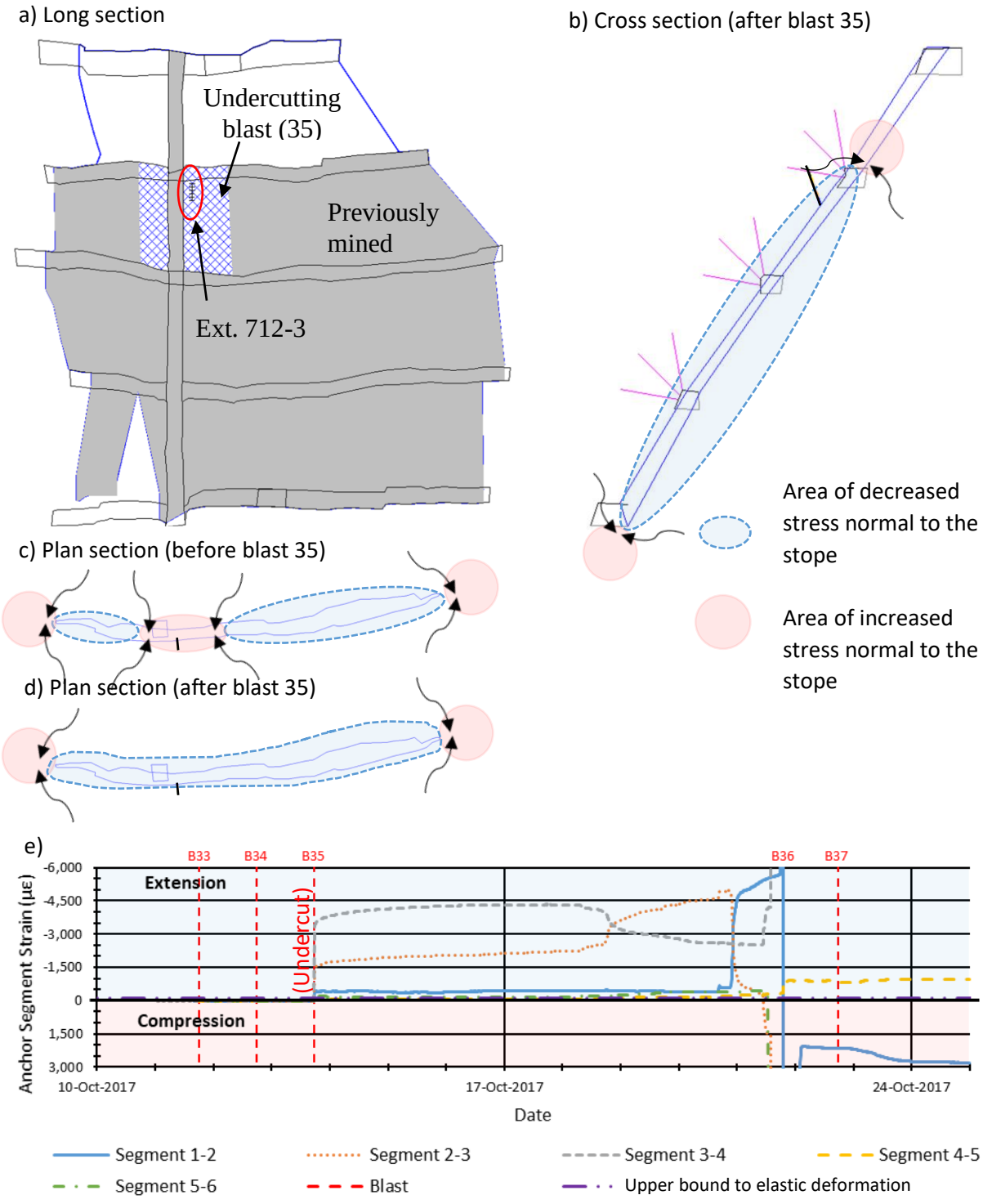

Figure 5-15: Section views of the Santoy 24L 411 Alimak stope showing blast geometries, excavation geometries, expected zones of stress change, and the location of extensometer 712-3 for: (a) true longitudinal view, (b) cross section after undercutting, (c) plan section prior to undercutting, (d) plan section after undercutting, and (e) a plot of strain over time for the reliable anchor segments.

5.3.4 Estimation of Pre-Mining Stress

The dataset for the 24L 411 alimak stope at Santoy mine contained both blast dates and which blast undercut each extensometer. These details are summarized in Table 5-4.

The dataset for the 24L 411 alimak stope contains a large number of readings recorded by dataloggers at regular intervals. By comparing measurements just prior to the undercutting blast and shortly after the blast, the change in strain due to each stope blast was estimated. The strain changes in each extensometer anchor segment are summarized in Table 5-4. All of the measured strains were larger than the estimated upper bound to elastic deformation suggesting that the rock mass was no longer behaving elastically and that the estimated elastic modulus for the rock mass (50 MPa) may be more appropriate than the laboratory elastic modulus (75 MPa). By applying Equation 3-6, and using an elastic modulus of 50 GPa and a Poisson's ratio of 0.31, the measured changes in strain after undercutting were used to calculate the pre-mining stress in each anchor segment as summarized in Table 5-4. Results associated with anchors no believed to be fully relaxed are coloured yellow. A sample calculation for anchor segment 4-5 of extensometer 712-2 is shown below.

$$\sigma_{pre-mining} \cong -\frac{\Delta\varepsilon\, E}{(1-\upsilon)} \cong -\frac{(-110\mu\varepsilon)(50\ GPa)}{\big(1-(0.31)\big)} \cong 8\ MPa$$

For the closest remaining anchor segments on both extensometers, the anchor segment ERF is larger than the distance from the anchors to the stope hanging wall, suggesting that the anchor segment is in the relaxation zone and has relaxed fully (Section 3.2.4). Based on the location of stope below surface, a depth based stress of approximately 6 MPa was estimated for the stress normal to the hanging wall (Section 5.3). This is approximately equal to the pre-mining stress estimates associated with the measured strain change by extensometer 712-2, anchor segment 4-5 (8 MPa), which is the closest reliable anchor segment to the opening as described in Section 5.3.3.

The pre-mining stress estimate associated with extensometer 712-3, anchor segment 1-2 (30 MPa) is a little over three times the depth based estimate of stress normal to the hanging wall. Considering the magnitude of the strain, it is likely that non-linear extension is occurring and that the elastic modulus used in the stress estimate is too high for conditions following undercutting.

Table 5-4: Summary of the stress and strain change following undercutting for each extensometer segment in the Santoy 24L 411 Alimak stope hanging wall.

Anchor Segment	Anchor Segment length (m)	Perpendicular distance to hanging wall (m)	ERF (m)	Strain change due to blast (με)	Calculated Pre-mining stress (MPa)
Extensometer 712-2	Undercut by Blast 37 on 22-Oct-2017				
1-2	1.17	Lost following blast 37			
2-3	1.17	Lost following blast 37			
3-4	1.17	Lost following blast 37			
4-5	1.17	2.1-3.3	16.3	-110	8
5-6	1.17	3.3-4.4	16.2	-280	20
Extensometer 712-3	Undercut by Blast 35 on 13-Oct-2017				
1-2	1.17	1.1-2.1	8.4	-440	30
2-3	1.17	2.1-3.0	7.7	-1,600	120*
3-4	1.17	3.0-4.0	7.0	-3,570	260*
4-5	1.17	4.0-4.9	6.2	-70	5
5-6	1.17	4.9-5.8	5.4	-250	20

*yellow highlight- not fully relaxed (ERF< distance to hanging wall)
*red highlight- unreliable anchor segment
Possible crack dilation indicated by a ””

5.3.5 Modified SERF Instability Analysis

None of the instruments installed in stope 24L 411 could be used for SERF analysis based on the criteria outlined in Section 3.4.1. Due to the orientation of extensometer 712-1 and the possible shear deformation recorded, data from this instrument was not reliable. Extensometer 712-2 provided reasonable results, however, the undercutting blast was the last production blast in the stope, so no relation could be developed between strain and changing stope geometry. Extensometer 712-3 may have captured a failure on 21-October, 2017, as indicated in Figure 5-8, however, there was no identifiable driver of this instability.

Other factors such as time or the presence and removal of stabilizing muck from the stope appear to have been a stronger influence on hanging wall movement in this case. The presence, and subsequent removal, of muck in the stope would alter the RF of the stope hanging wall as the unsupported geometry would be smaller than the blasted geometry.

5.3.6 Summary of the Santoy 24L 411 Alimak stope

Of the three extensometers used to monitor the Santoy 24L 411 Alimak, two provided data that was suitable for estimation of the pre-mining stress. Of the two estimates, one can be discounted due to perceived non-linear deformation, possibly associated with the sloughing being temporarily supported by muck following the undercutting blast. The remaining result from extensometer 712-2 provides a good estimate of the depth based estimate of the pre-mining stress acting normal to the opening suggesting that extensometers may be used to provide useful estimates of pre-mining stress.

The modified SERF method could not be applied for any of the extensometers due to either poor orientation relative to the hanging wall, insufficient blasts following undercutting to provide a dataset for analysis, or deformation not being driven by changes in hanging wall geometry. Due to a lack of detail about the location of muck within the stope during excavation, the influence of muck on the hanging wall RF could not be considered.

5.4 Santoy 30-31L Longhole Stope

The Santoy mine longhole panel covered a portion of the mine from 28L to 38L with an up dip length of 120 metres at an average dip of 55 degrees (Figure 5-16). The overall longhole panel was located at an average depth of approximately 320 metres below surface, which corresponds to an average vertical stress of approximately 9 MPa. The longhole panel was split into six sublevels, with up dip lengths of approximately 26 metres, that were mined in an up dip direction. Each stope level was accessible from surface via a footwall ramp system with crosscut access to overcut and undercut sills.

On each stope level, sills were driven along strike to follow up to three separate gold veins which were extracted separately (Figure 5-17). As mining retreated back towards the ramp access, backfilling of the stope began and advanced along with the mining face, in an Avoca type mining method. Once sufficient backfill was placed, production blasting commenced on the next stope level above the backfilled stope. Ground support was designed by site engineers based on the RMR classification and the opening geometries. The ground support generally included bolts and screen and was augmented by cable bolts in areas with larger spans.

The Santoy 30-31L longhole stope was located near the top of the Santoy 28-30L longhole panel, at an average depth of approximately 300 m below surface, with a vertical stress of approximately 9 MPa (Figure 5-16). The Santoy 30-31L longhole stope had an up dip length of approximately 26 metres, at a dip of approximately 54 degrees, and a strike length of approximately 168 metres. Production drilling and blasting was carried out on 30L and mucking was done from 31L. As mining retreated to the east, towards the ramp access, backfilling of the stope began and advance along with the mining face in an Avoca type mining method.

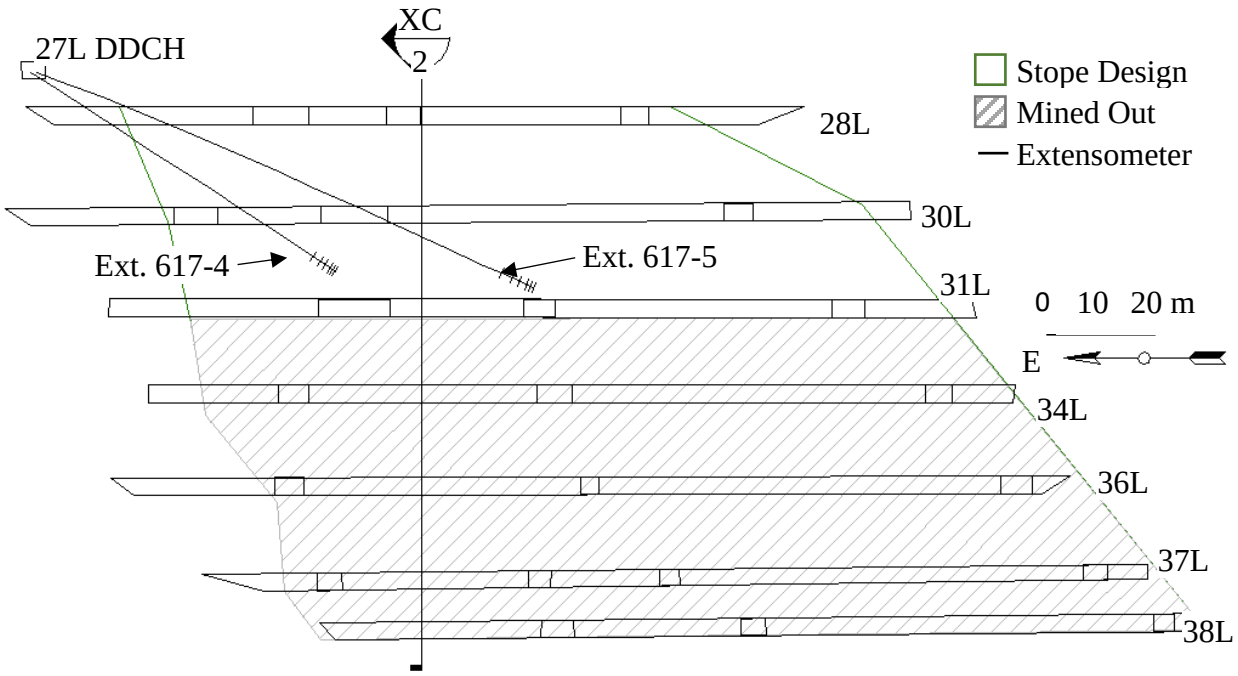

Figure 5-16: Long view of the longhole panel hanging wall looking south and showing level developments, panel outlines, mined out areas, and extensometer locations.

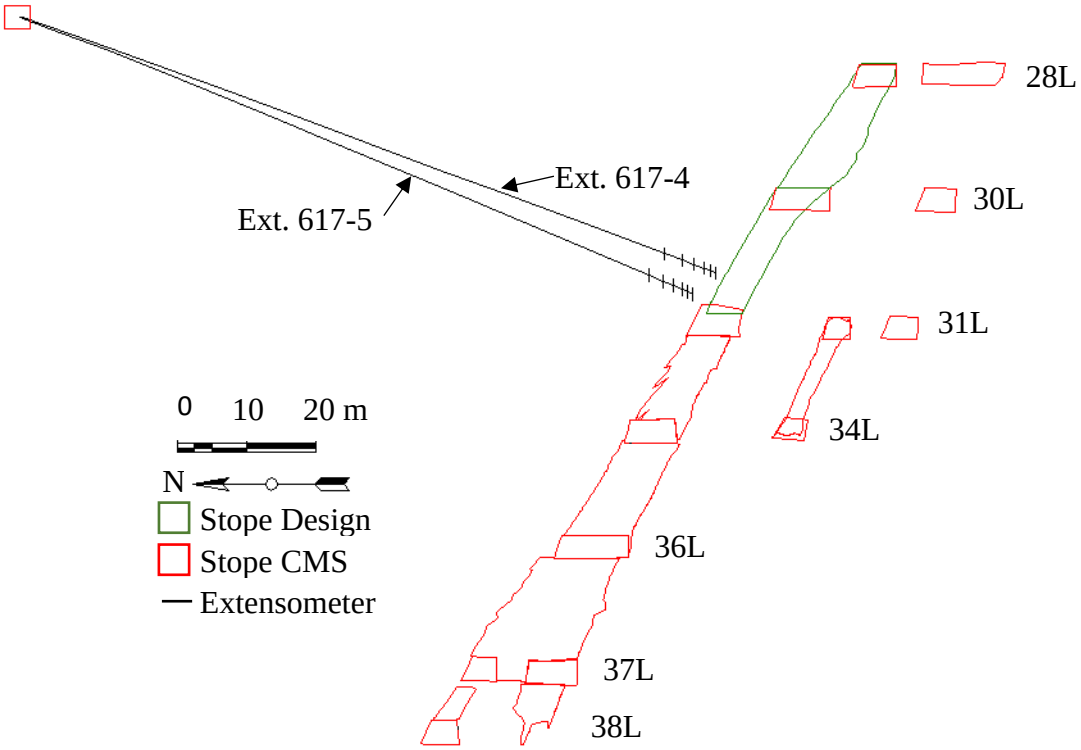

Figure 5-17: Cross section view along XC-2 of Santoy longhole panel looking east showing the stope design outline, extensometer locations, surveys, and CMS.

5.4.1 Instrumentation program design

Due to a lack of hanging wall infrastructure around the longhole panel, new drillholes could not be designed and drilled for the installation of extensometers. Instead, the locations of underground exploration drillholes were reviewed to identify the exploration drillholes that had favourable intersection with the stope hanging wall.

The holes chosen were drilled from a diamond drill chamber on 27 level (27L). The diamond drill holes chosen for instrumentation, corresponding extensometer number, hole length, hole dip, and extensometer length are summarized in Table 5-5. Figure 5-16 and Figure 5-17 show the hole locations and Figure 5-18 shows the work area for the instrument installation including the instrumented hole collars and other unused diamond drill hole collars.

The three extensometers were installed on 21-August, 2017.

Table 5-5: Extensometer drillhole details for the instrumentation of the 30-31L longhole stope.

Drillhole			Extensometer	
Name	Length (m)	Trend/Plunge	Name	Length
SUG-14-029	180	208/-16	617-4	122
SUG-14-046	226	222/-14	617-5	143

The drillholes were identified by probing the hole to measure the trend and plunge and comparing the results to the exploration drillhole database. The drillhole identity was then verified by comparing the physical collar position, relative to other drillholes, to a plot of the planned collar locations. The instrument installation procedure is summarized in Appendix F. The distances between extensometer anchors are summarized in Table 5-6 and a schematic of the anchor positions relative to the stope and drillhole collar are shown in Figure 5-19.

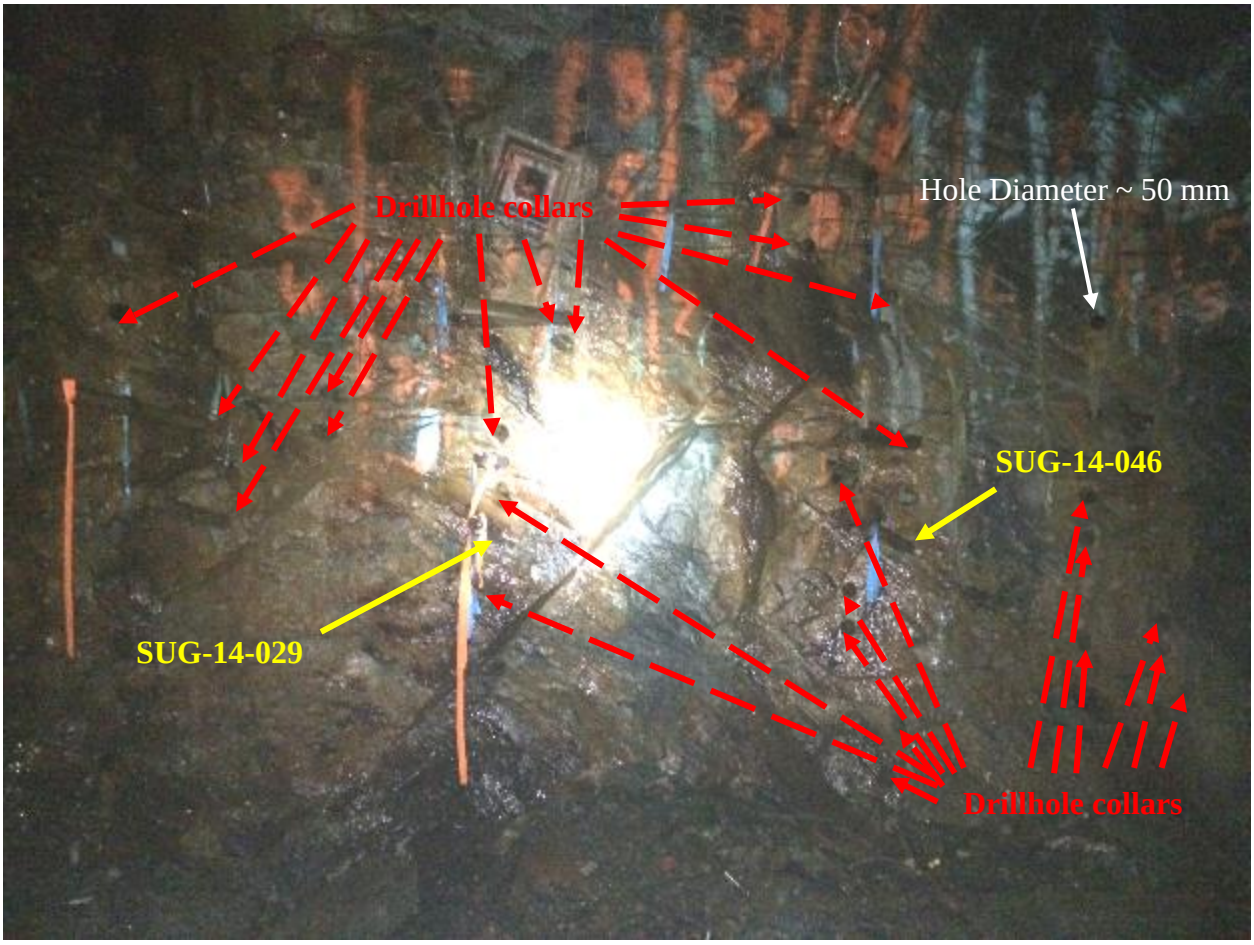

Figure 5-18: Image of the collars of existing exploration holes in the 27L DDCH.

Table 5-6: Distances between anchors for extensometers installed to monitor the Santoy 30-31L longhole stope.

Instrument	Distance between anchors (m)					
	1-2	2-3	3-4	4-5	5-6	6-Head
617-4	1	1	2	2	3	1
617-5	1	1	2	2	3	1

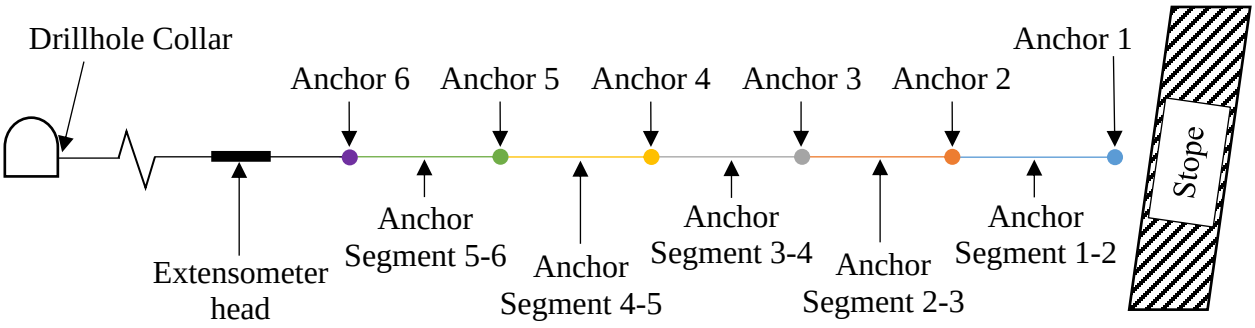

Figure 5-19: Schematic showing the anchor positions relative to the stope and the drillhole collar.

5.4.2 Stope Mining

The monitored portion of the mining of the Santoy 30-31L longhole stope consisted of 20 production blasts, from the 30L sill, starting on 12-March, 2017 and concluding on 10-October, 2017. Several production blasts had been previously taken at the east end of the stope and left open, with the monitored stope blasting beginning at the western end and proceeding to connect to the previous excavation with blast 20 (Figure 5-20). Section view XC-3 is aligned with anchor 1 of extensometer 617-4 (Figure 5-21) and section view XC-4 is aligned with anchor 1 of extensometer 617-5 (Figure 5-22). Prior mining and backfilling of several stopes in the 28-38L panel, with an up dip length of approximately 70 metres, was completed before extraction from the 30-31L stope could be started.

No CMS scan was available for the XC-3 area following the completion of mining activity so it was not possible to confirm the final hanging wall location. There were also insufficient scans to confirm the position of the backfill front during mining activity.

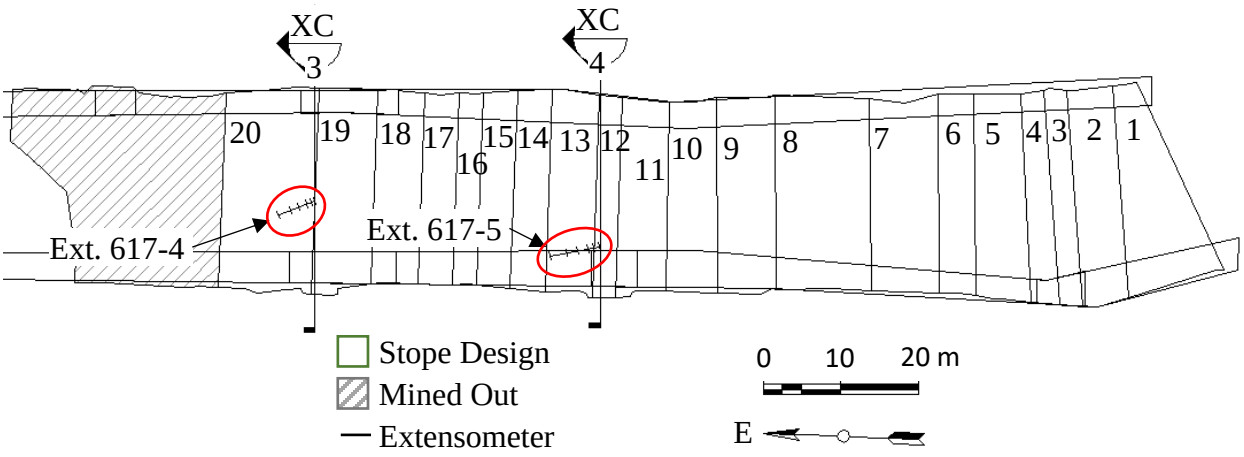

Figure 5-20: True longitudinal view of the Santoy 30-31L longhole stope hanging wall looking south and showing stope outlines and instrument locations.

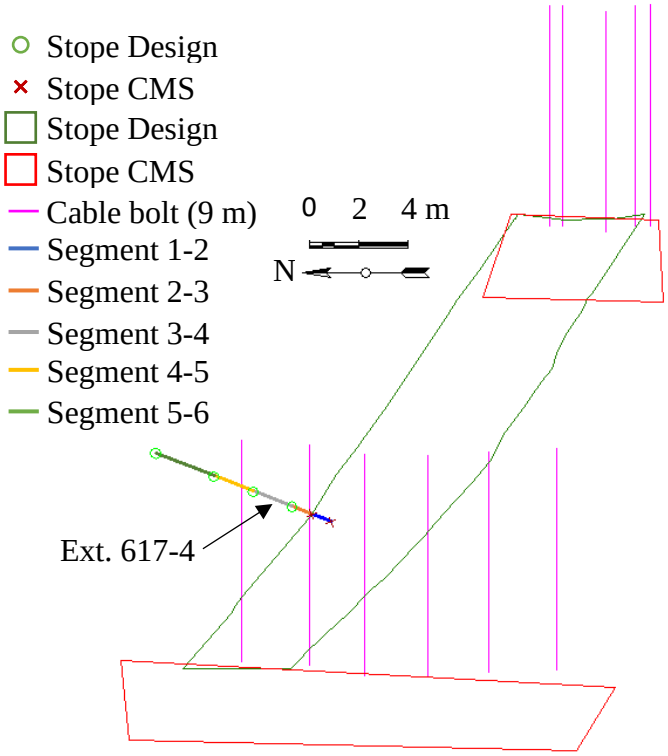

Figure 5-21: Cross section along XC-4 of the Santoy 30-31L longhole stope looking east and showing the stope design outline, extensometer locations, ground support, surveys, and CMS.

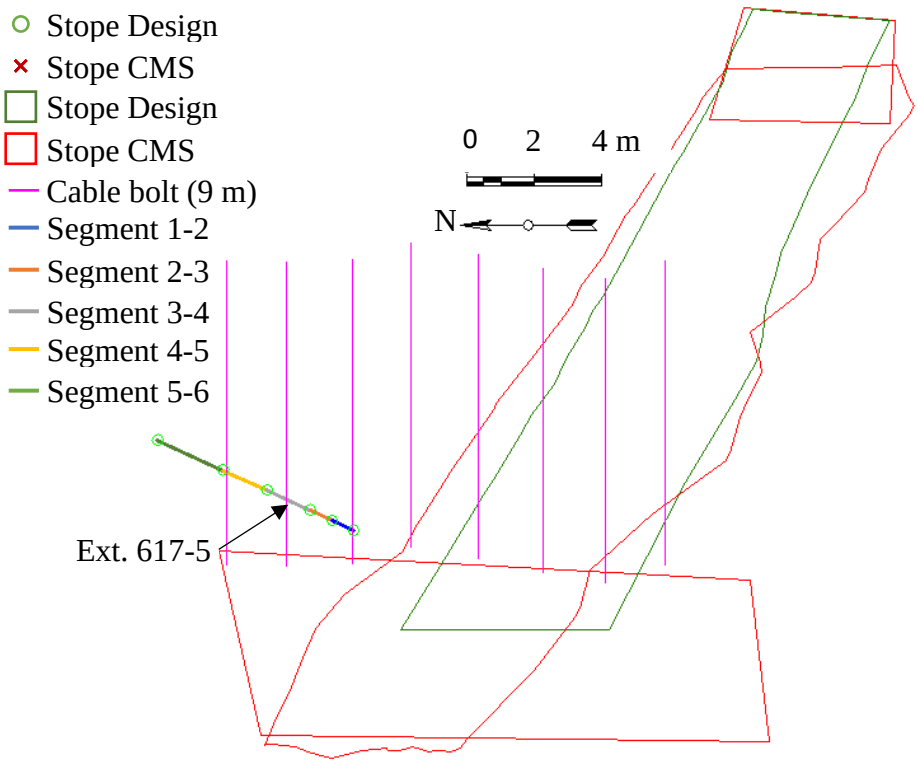

Figure 5-22: Cross section along XC-5 of the Santoy 30-31L longhole stope looking east and showing the stope design outline, extensometer locations, ground support, surveys, and CMS.

A site visit was conducted on 4-November, 2017 after extraction from the Santoy 30-31L longhole stope was completed. Stope access was limited to the 30L cross-cut and backfilled surface. The stope hanging wall appeared to be in good condition and there was no observed evidence of sagging or failed hanging wall (Figure 5-23). Interviews with site personnel confirmed that, although there were a few instances of oversize during mucking, no large dilution events occurred and the hanging wall had stood up well during excavation.

Figure 5-23: Santoy 30-31L longhole stope hanging wall viewed from the 30L crosscut.

5.4.3 Ground Response to Mining

The 30-31L longhole stope (Figure 5-20) is at an average depth of 300 metres, corresponding to a vertical stress, and a stress normal to the hanging wall, of approximately 9 MPa, as discussed in Section 5.4. As mining approaches the instrument location, a stress increase of up to approximately three times the initial stress normal to the hanging wall, could be expected (27 MPa) (Section 3.1) which is associated with a strain of approximately 550 microstrain for the Santoy rock mass (50 GPa). It was estimated that stress concentration would exceed the intact rock strength (144 MPa) for compressive strains larger than approximately 1,300 microstrain. Since compressive failure of the intact rock is not expected due to the shallow mining depth; if this magnitude of compressive strain were measured, it could be indicative of potential shearing along structure within the rock mass (Section 3.1).

Applying Equation 3-7, the estimated upper bound to elastic deformation in the hanging wall adjacent and normal to the stope, due to hanging wall stress relaxation following undercutting by stope mining, is estimated to be approximately 150 microstrain of tension. Assuming a one metre anchor segment length, this strain would be associated with a deformation of approximately 0.15 millimetres.

$$\varepsilon_{(a-b)} = \frac{\Delta\sigma_n}{E}(1-\upsilon) = \frac{0-9MPa}{50GPa}(1-0.31) \cong -150\mu\varepsilon$$

5.4.3.1 EXTENSOMETER 617-4

The data from extensometer 617-4 was logged using a SMART Log3, resulting in a resolution of approximately 0.0025mm, which was rounded to the nearest 0.01 millimetres. A plot of the strain over time for extensometer 617-4 is shown in Figure 5-24.

Figure 5-25 shows plan, cross section and long section views of the stope and extensometer, before and after being undercut by blast 20. Figure 5-25b shows that anchors 1 and 2, for extensometer 617-4, are located within the planned stope. After undercutting anchor segment 1-2 and 2-3 were lost. This left anchor segment 3-4 within one metre of the planned stope.

After removing the unreliable anchor segments, the strain response in the remaining anchor segments appear reasonable and a more detailed strain response is shown in Figure 5-25e.

The undercutting blast was the final blast for this stope. No additional stope geometries could be monitored with extensometer 617-4 so there was no opportunity to apply the modified SERF method.

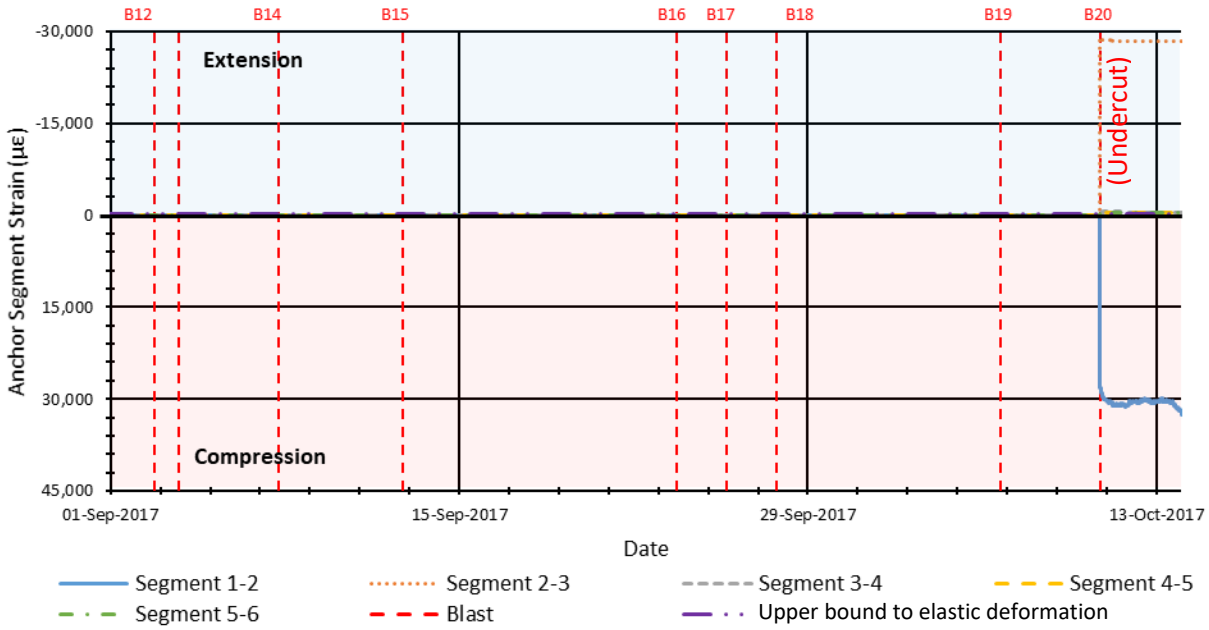

Figure 5-24: Full dataset of segment strains in the 30-31L longhole stope hanging wall at Santoy mine measured by extensometer 617-4.

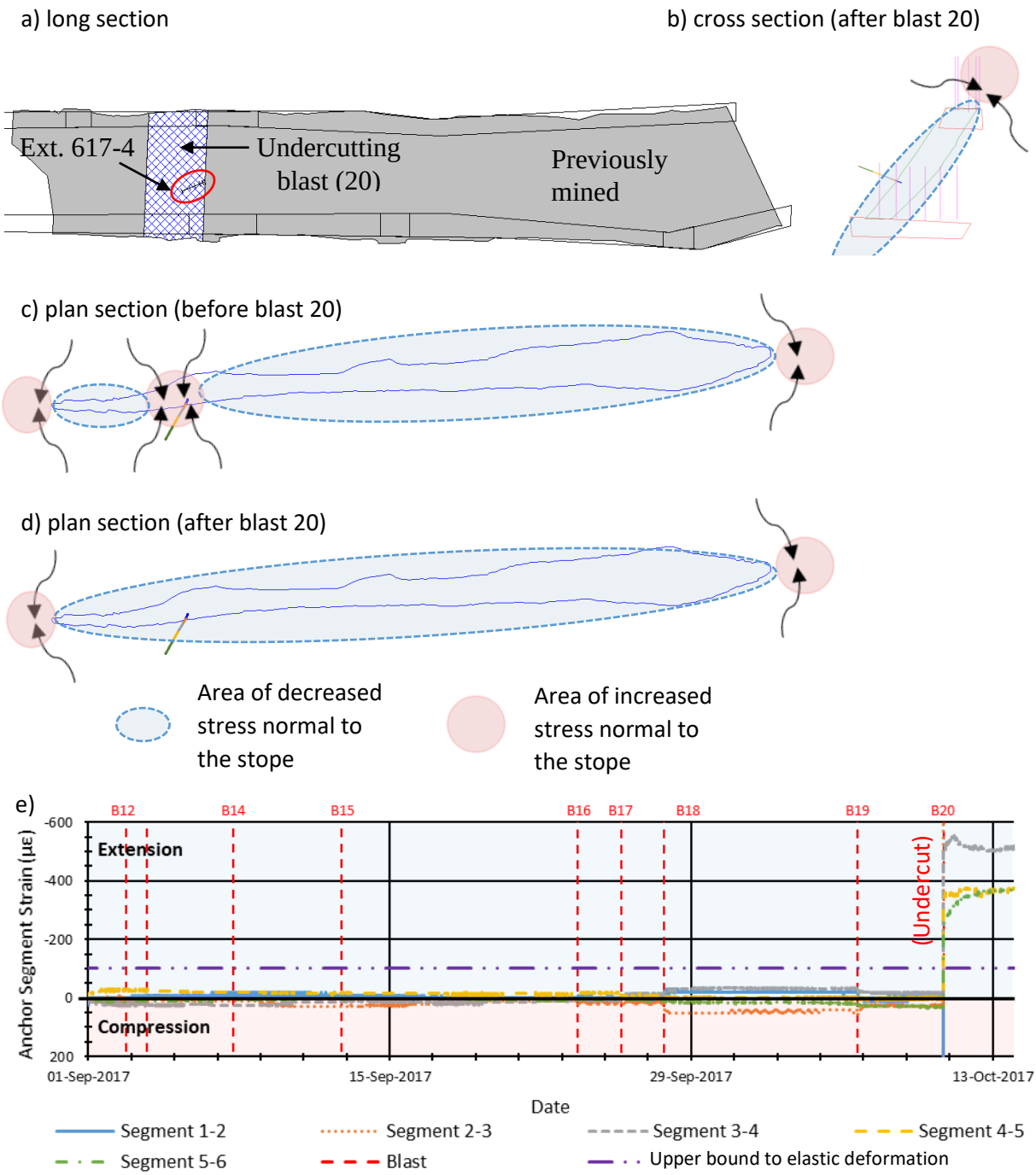

Figure 5-25: Section views of the Santoy 30-31L longhole stope showing blast geometries, excavation geometries, expected zones of stress change, and the location of extensometer 617-4 for: (a) true longitudinal view, (b) cross section after undercutting, (c) plan section prior to undercutting, (d) plan section after undercutting, and (e) a plot of strain over time for the reliable anchor segments.

5.4.3.2 EXTENSOMETER 617-5

The data from extensometer 617-5 was logged using a SMART Log3, resulting in a resolution of approximately 0.0025mm, which was rounded to the nearest 0.01 millimetres. A plot of the strain over time for extensometer 617-5 is shown in Figure 5-26.

Figure 5-27 shows plan, cross section and long section views of the stope and extensometer, before and being undercut by blast 12 and 13. From the plan view shown in Figure 5-27d, extensometer 617-5 is oriented approximately 45° to the strike of the stope hanging wall, which resulted in the zone of relaxation not covering all anchors until after blast 13, and complicates stress interpretation. Figure 5-27b shows that anchors 1, 2, and possibly 3 are just above the 31L sill and the previously excavated 31-34L stope and may fall within the zone of stress influence from this excavation (Figure 5-28).

In the full strain plot for extensometer 617-5 (Figure 5-26), anchor segments 1-2 and 2-3 appear to be mirrored. Review of the deformation data shows that anchor 2 is slipping relative to the measured displacements for anchors 1 and 3, which have a similar magnitude. If strain was considered in anchor segment 1-3, the resultant strain would be smaller than the strain in anchor 3-4 which is contrary to the expectation of larger displacements closer to the opening. As a result, the data for both anchor segment 1-2 and 2-3 are not considered reliable. Although anchor segment 3-4 measures a tensile response following undercutting, the magnitude of anchor segment 4-5, which is further from the opening, is larger. This is contrary to expected behaviour, where deformation and strain are largest closest to the opening, suggesting that anchor segment 3-4 had been influenced by stress redistribution during mining of the 31-34L stope.

After removing the unreliable anchor segments, the strain response in the remaining anchor segments appear reasonable and a more detailed strain response is shown in Figure 5-27e. In this plot, there appears to be a transition to non-linear extension for anchor segment 4-5 associated with blast 13 suggesting that the dataset from extensometer 617-5 is suitable for analysis using the modified SERF method. Following the transition to non-linear extension, there was a trend update associated with blast 16 as the strain begins to stabilize and a second trend update associated with blast 18 and apparent stabilization. This is likely due to the backfill front passing the extensometer location and beginning to provide support to the hanging wall. A similar response can be observed in anchor segment 5-6 although a possible transition to non-linear deformation does not occur until

blast 15 when the measured strain exceeds the estimated upper bound to elastic deformation. As with anchor segment 4-5, a trend update appears to occur for anchor segment 5-6 in association with blast 16 as the measured strains begins to stabilize and blast 18 as the hanging wall stabilizes.

For this extensometer, a trend update due to stabilization would result in the termination of the application of the modified SERF method, until another trend update and continued non-linear deformation occurred. For this dataset the modified SERF method was applied to the dataset prior to the trend update to assess the prediction of instability during earlier stages of stope mining, prior to stabilization of the instrumented location by backfilling.

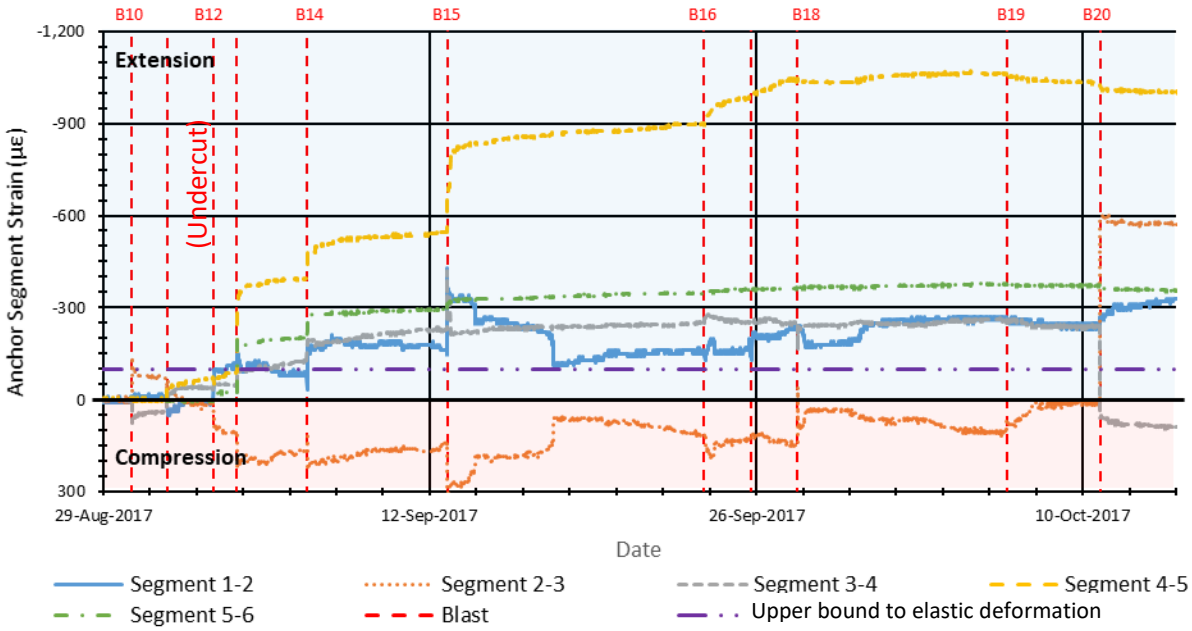

Figure 5-26: Full dataset of segment strains in the 30-31L longhole stope hanging wall at Santoy mine measured by extensometer 617-5.

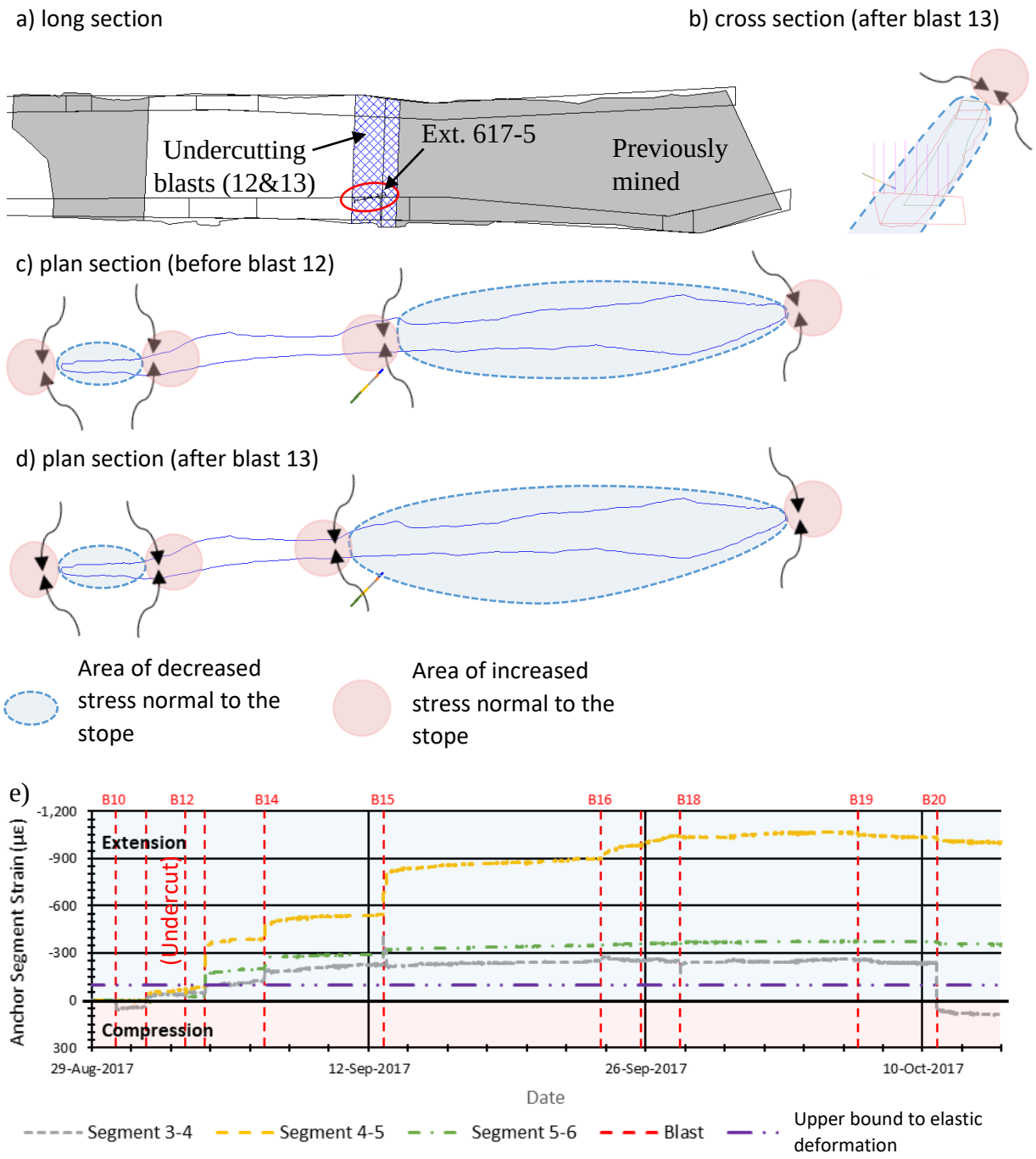

Figure 5-27: Section views of the Santoy 30-31L longhole stope showing blast geometries, excavation geometries, expected zones of stress change, and the location of extensometer 617-5 for: (a) true longitudinal view, (b) cross section after undercutting, (c) plan section prior to undercutting, (d) plan section after undercutting, and (e) a plot of strain over time for the reliable anchor segments.

5.4.4 Estimation of Pre-Mining Stress

The dataset for the 30-31L longhole stope at Santoy mine contained both blast dates and which blast undercut each extensometer. These details have been summarized in Table 5-7.

The dataset for the 30-31L longhole stope contains a large number of readings recorded by a datalogger at regular intervals. By comparing measurements just prior to the undercutting blast and shortly after the blast, the change in strain due to each stope blast was estimated. The strain changes in each extensometer anchor segment are summarized in Table 5-7. All of the measured strains were larger than the upper bound to elastic deformation suggesting that the rock mass was no longer behaving elastically and that the estimated elastic modulus for the rock mass (50 MPa) may be more appropriate than the laboratory elastic modulus (75 MPa). By applying Equation 3-6, and using an elastic modulus of 50 GPa and a Poisson's ratio of 0.20, the measured changes in strain after undercutting were used to calculate the pre-mining stress in each anchor segment as summarized in Table 5-7. Results associated with anchors not believed to be fully relaxed are coloured yellow. A sample calculation for anchor segment 3-4 of extensometer 617-4 is shown below.

$$\sigma_{pre-mining} \cong -\frac{\Delta\varepsilon\, E}{(1-\upsilon)} \cong -\frac{(-500\mu\varepsilon)(50\ GPa)}{\big(1-(0.31)\big)} \cong 35\ MPa$$

For the closest remaining anchor segments on both extensometers, as described in Section 5.4.3, the anchor segment ERF is larger than the distance from the segment anchors to the stope hanging wall. This suggests that the anchor segments have relaxed fully (Section 3.2.4). The pre-mining stress estimated for anchor segment 3-4 of extensometer 617-4 (35 MPa) was approximately triple the depth based estimate of stress (9 MPa). The difference between the measured response and the estimate could be due to a combination of incorrect assumptions about the K-ratio used in the depth based estimate, concentration of stresses from mining the 30-31L stope and the previous stope in the 28-38L panel, or non-linear deformation of the hanging wall and a lower elastic modulus than was used in the estimate of pre-mining stress. The presence of previously excavated and backfilled stopes, with a cumulative up dip length of approximately 70 metres, ten metres down dip from the extensometer would also have increased the virgin stress normal to the stope area, prior to installation of the extensometer.

The pre-mining stress estimate associated with anchor segment 3-4 of extensometer 617-5, is approximately equal to the depth based stress estimate. The validity of this estimate is not immediately clear since anchor segments further from the opening measured more strain and it is possible that the anchor segment was partially relaxed due to previous mining activity (Section 5.4.3). Sectional analysis of the extensometer installation location show that the extensometer had been undercut by a crosscut on 31L (Figure 5-28). As a result, it is possible that stress concentration may have occurred in the back prior to the installation of the instruments, due to stress redistribution around the previous stope.

Table 5-7: Summary of the stress and strain change following undercutting for each extensometer segment in the Santoy 30-31L longhole stope hanging wall.

Extensometer 617-4	Undercut by Blast 20 on 10-Oct-2017				
Anchor Segment	Anchor Segment length (m)	Perpendicular distance to hanging wall (m)	ERF (m)	Strain change due to blast (με)	Pre-mining stress (MPa)
1-2	1.0	Lost following blast 20			
2-3	1.0	Lost following blast 20			
3-4	2.0	0.8-2.5	9.3	-500	35
4-5	2.0	2.5-4.0	9.4	-340	25
5-6	3.0	4.0-6.5	9.5	-300	20
Extensometer 617-5	Undercut by Blast 13 on 3-Sep-2017				
Anchor Segment	Anchor Segment length (m)	Perpendicular distance to hanging wall (m)	ERF (m)	Strain change (με)	Pre-mining stress (MPa)
1-2	1.0	Unreliable following blast 12			
2-3	1.0	Unreliable following blast 12			
3-4	2.0	2.7-4.0	4.6	-150	10
4-5	2.0	4.0-5.4	3.9	-300	20
5-6	3.0	5.4-7.3	2.9	-200	15

*yellow highlight- not fully relaxed (ERF< distance to hanging wall)
*red highlight- unreliable anchor segment

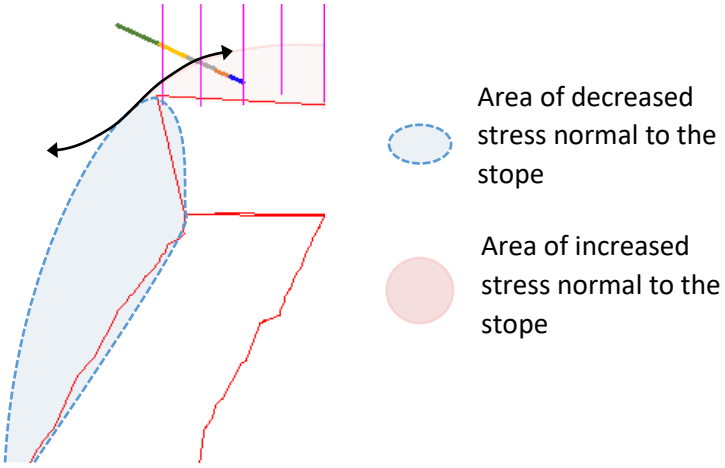

Figure 5-28: Potential stress deviation around the 31L sill resulting in a pre mining stress greater than the estimated 9 MPa in-situ or virgin stress.

5.4.5 Modified SERF Instability Analysis

Although the dataset of measurements recorded by extensometer 617-5 stabilized as the backfill front passed the extensometer location, the modified SERF method can be applied to earlier data to provide a predicted RF of instability (RF_p) for the hanging wall, prior to backfilling. Limiting the dataset to only consider data prior to blast 18 provides a RF_p of approximately 10.5 metres for anchor segment 4-5 (between 4.0 and 5.4 metres from the stope hanging wall) and 14.5 metres for anchor segment 5-6 (between 5.4 and 7.3 metres from the stope hanging wall) using the modified SERF method (Figure 5-29).

For both anchor segments the RF_p is larger than the final stope RF and, as a result, no instability was predicted based on the modified SERF method. It should also be noted that this is believed to be a conservative prediction as the final RF, and the ERF for both anchor segments are smaller than recorded in this study due to the advancing backfill front serving as an abutment and limiting the unsupported strike length of the stope hanging wall. Due to the limited number of CMS scans during excavation of the 30-31L longhole stope, the location of the backfill front could not be confirmed to support the proper calculation of the RF and ERF associated with the stope.

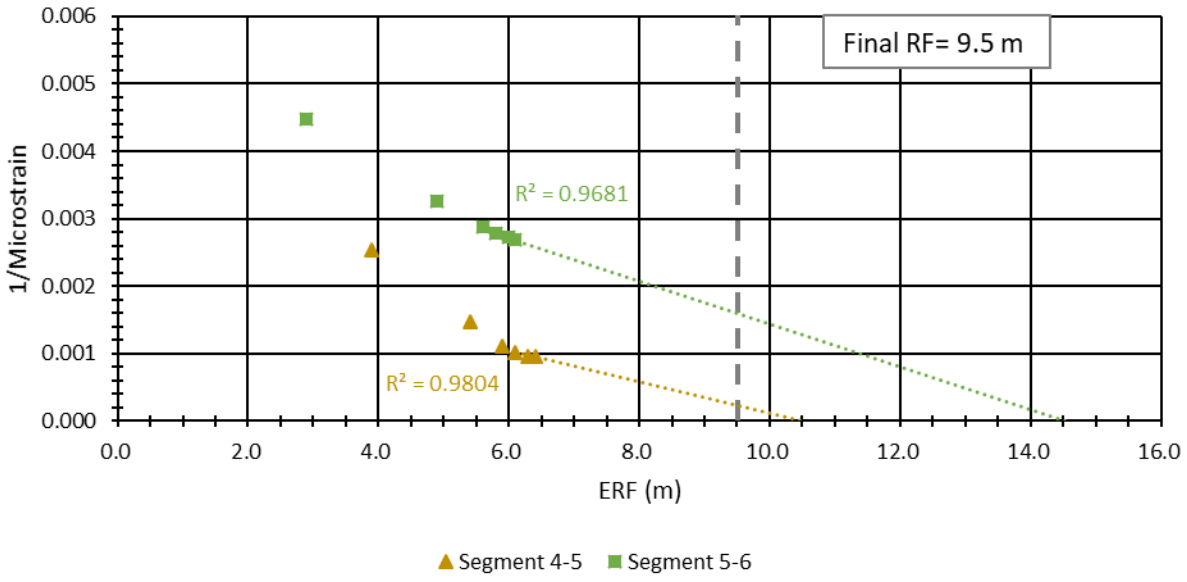

Figure 5-29: Analysis of measurements by extensometer SBGO-M0617-5 of the Santoy 30-31L longhole stope hanging wall using the modified SERF method.

5.4.6 Summary of the Santoy 30-31L Longhole Stope

Both extensometers used to monitor the Santoy 30-31L longhole stope provided data that was suitable for estimation of the pre-mining stress. Depending on the position of the extensometer relative to openings prior to undercutting, the pre-mining stress ranged from a magnitude of approximately one to three times the stress based on depth. In both cases, analysis suggests that the pre-mining stress is larger than the depth based estimate indicating that the K-ratio may have changed due to excavation of deeper sublevels. Previous mining of longhole stopes from 31L to 38L may also have resulted in stress concentration in the 30-31L longhole stope resulting in higher initial stresses. Non-linear deformation may also have been taking place.

When the modified SERF method was applied to the data before the trend update associated with stabilization, no instability was predicted for the stope hanging wall. Additionally, the modified Avoca method resulted in a backfill front advancing along with the mining face serving as an abutment and effectively reducing the geometry of the unsupported hanging wall. Unfortunately, insufficient data was available about the location of the backfill front to calculate revised RF and ERF for the hanging wall for use in the modified SERF method.

5.5 Summary of SGO Results

The use of extensometers to estimate the pre-mining stress as stopes are excavated showed promise. Interpretation challenges occurred in some areas where previous stress changes likely occurred due to adjacent mining activity, prior to extensometer installations. Despite these challenges, the estimation of pre-mining stress from extensometer measurements appears to provide a useful tool for understanding the rock mass behaviour.

Although the SGO case study was not able to validate or invalidate the modified SERF method, it did serve to reinforce conditions for the method to be applied. They are:

- The orientation of the extensometer should be as near normal to the hanging wall as possible,
- Extensometers should be located such that there are sufficient production blasts following undercutting to identify a trend of increasing non-linear deformation, and
- If the hanging wall is to be supported by muck or backfill, the location of the supporting material should be known so the RF and ERF can be calculated properly.

6 CONCLUSIONS

This study has outlined techniques for interpreting extensometer data from underground open stope mines. Analysis considered five stopes from three underground mining operations that had been instrumented with at least one hanging wall extensometer. The conclusions associated with the primary techniques being applied to interpret extensometer data are as follows.

6.1 Estimation of Pre-Mining Stress

Numerical modelling has supported the development of a simple equation to estimate pre-mining stress normal to a stope hanging wall from a normal strain and elastic rock mass properties (Equation 3-5). This formula can be applied to estimate a pre-mining stress, based on the assumption that surface stresses reduce to zero following undercutting.

When applied to underground open stope scenarios, the formula appears to reasonably estimate the modelled or measured pre-mining stress when an elastic deformation response is measured by extensometers. Discrepancies between the estimated stress and modelled or measured response can occur when previous excavation around the instrument location, prior to installation of the extensometer, alter the virgin stress conditions, the rock mass has deteriorated due to reduced confinement, or non-linear deformation is measured. Depending on the case, reducing the elastic modulus to reflect the deterioration of the rock mass, in association with the reduction of clamping forces and dilation of joint infilling, can reduce the discrepancy. As with other analysis requiring the use of rock mass properties, selecting a reasonable elastic modulus for use can be challenging.

6.2 Modified SERF method

When applied to suitable open stope environments, the modified SERF method appears to be an effective tool for predicting a geometry and depth of instability. The modified SERF method improves the SERF method by removing the ERF factor in the numerator of the vertical axis. This removes the bias introduced due to the initial rapid increases in the ERF which approaches a maximum as the stope size increases.

The review of the case histories supported the definition of suitable applications for the modified SERF method. Criteria to be considered when designing and implementing an instrumentation program to apply the modified SERF method include:

- Extensometers are placed far enough from abutments that the ERF continues to increase during stope excavation,
- Extensometers are undercut early during stope excavation,
- Extensometer should be oriented as near perpendicular to the hanging wall as possible,
- Extensometer measurements can be collected throughout the active life of the stope,
- The hanging wall undergoes non-linear deformation,
- The location of backfill is known, to allow accurate calculation of the ERF of the unsupported hanging wall, and
- There are sufficient stope blasts to identify a trend of increasing strain.

Once instrumentation is installed and excavation has begun, site engineers can quickly import new extensometer data and update the empirical plots associated with the modified SERF method. This can provide the mine with active insight into hanging wall movement, and potentially approaching instability, allowing informed decisions to be made to control stope dilution.

6.3 Recommendations for Future Work

Datasets for failed hanging walls including hanging wall extensometer measurements, reliable blast dates and geometries, and backfilling details are not common. Of the datasets considered during this study, only two of the stope hanging walls failed and of these two stopes, the dataset was incomplete for one. Further case histories of failed hanging walls should be considered to confirm the ability of the modified SERF method to predict a geometry of hanging wall instability and the criteria defining suitable applications.

The estimation of elastic stress from a measured strain and elastic rock mass properties is useful in limited applications since the transition from elastic to non-linear deformation can be challenging to identify. Testing the ability of the formula to estimate stresses associated with non-linear deformation would be useful for defining the limits of the applicability of the formula to estimate stresses from strains. The equation used was correlated to historical numerical modelling, as well as modelling conducted as part of this research. The modelling included tensile stresses induced tangential to the hanging wall stope surfaces. It is recommended that future tests be combined with the installation of stress cells to correlate the technique with field data instead of modelling results.

REFERENCES

Barton, N., Lien, R., & Lunde, J. (1974). Engineering classification of rock masses for the design of tunnel support. *Rock mechanics*, *6*(4), 189-236.

Beer, G., Meek, J. L., & Cowling, R. (1983, January). Prediction of the behaviour of shale hanging walls in deep underground excavations. In *5th ISRM Congress*. International Society for Rock Mechanics and Rock Engineering.

Beneteau D., Prefontaine, J., Szczepanik, Z. (2019). Rock mechanics laboratory testing results for Santoy Mine. University of Saskatchewan.

Barton, N., Lien, R., & Lunde, J. (1974). Engineering classification of rock masses for the design of tunnel support. *Rock mechanics*, *6*(4), 189-236.

Bieniawski, Z. T. (1974). Estimating the strength of rock materials. *Journal of the Southern African Institute of Mining and Metallurgy*, *74*(8), 312-320.

Bieniawski, Z.T. (1976). Rock mass classification in rock engineering. *Exploration for Rock Engineering*, Johannesburg, Balkema, 97-106.

Bieniawski, Z. T. (1978, October). Determining rock mass deformability: experience from case histories. *International journal of rock mechanics and mining sciences & geomechanics abstract* (Vol. 15, No. 5, pp. 237-247). Pergamon.

Bozzano, F., Mazzanti, P., & Moretto, S. (2018). Discussion to: 'Guidelines on the use of inverse velocity method as a tool for setting alarm thresholds and forecasting landslides and structure collapses' by T. Carlà, E. Intrieri, F. Di Traglia, T. Nolesini, G. Gigli and N. Casagli. *Landslides*, 1-5.

Brady, B., & Brown, E. (1985). Rock mechanics for underground mining. London: George Allen & Unwin.

Brady, B., Brown, E.T. author, & SpringerLink. (2006). Rock Mechanics for underground mining: Third edition.

Carlà, T., Intrieri, E., Di Traglia, F., Nolesini, T., Gigli, G., & Casagli, N. (2017a). Guidelines on the use of inverse velocity method as a tool for setting alarm thresholds and forecasting landslides and structure collapses. *Landslides*, *14*(2), 517-534.

Carlà, T., Intrieri, E., Farina, P., & Casagli, N. (2017b). A new method to identify impending failure in rock slopes. *International Journal of Rock Mechanics and Mining Sciences, 93*, 76.

Carlà, T., Intrieri, E., Di Traglia, F., Nolesini, T., Gigli, G., & Casagli, N. (2018). Reply to discussion on "Guidelines on the use of inverse velocity method as a tool for setting alarm thresholds and forecasting landslides and structure collapses" by F. Bozzano, P. Mazzanti, and S. Moretto. *Landslides*, *15*(7), 1443-1444.

Corrigan, D., Galley, A. G., Pehrsson, S., & Goodfellow, W. D. (2007). Tectonic evolution and metallogeny of the southwestern Trans-Hudson orogen. *Geological Association of Canada, Mineral Deposits Division*, 881-902.

Crosta, G. B., & Agliardi, F. (2003). Failure forecast for large rock slides by surface displacement measurements. *Canadian Geotechnical Journal*, *40*(1), 176-191.

Deere, D. U. (1964). Technical description of rock cores for engineering purpose. *Rock Mechanics and Engineering Geology*, *1*(1), 17-22.

Dick, G. J., Eberhardt, E., Cabrejo-Liévano, A. G., Stead, D., & Rose, N. D. (2014). Development of an early-warning time-of-failure analysis methodology for open-pit mine slopes utilizing ground-based slope stability radar monitoring data. *Canadian Geotechnical Journal*, *52*(4), 515-529.

Esmaeili, K., Hadjigeorgiou, J., & Grenon, M. (2010). Estimating geometrical and mechanical REV based on synthetic rock mass models at Brunswick Mine. *International Journal of Rock Mechanics and Mining Sciences*, *47*(6), 915-926.

Saskatchewan Geospatial Imagery Collaborative (n.d.). Retrieved on February 6, 2019 from: flysask2.ca

Fukuzono, T. (1985). A new method for predicting the failure time of a slope. In *Proceedings of 4th International Conference and Field Workshop on Landslide, 1985* (pp. 145-150).

Google (n.d.). Map of Brunswick mine area.

Herget, G. (1987, February). Stress assumptions for underground excavations in the Canadian Shield. In *International Journal of Rock Mechanics and Mining Sciences & Geomechanics Abstracts* (Vol. 24, No. 1, pp. 95-97). Pergamon.

Herget, G. (1988). *Stresses in rock* (p. 179). Rotterdam: Balkema.

Hoek, E., & Brown, E. T. (1980). *Underground excavations in rock*. CRC Press.

Hoek, E. (2006). Practical Rock Engineering.

Hutchinson, D. J., & Diederichs, M. S. (1995). Cablebolting in underground hard rock mines, A practical guide and final report of a joint research project through the Mining Research Directorate and the Australian Mineral Industries Research Association (AMIRA). Mount Isa Mines (1984). *Unpublished internal document*.

Hudyma, M., Grant, D., Potvin, Y., Brummer, R., & Milne, D. (1993). Geomechanics of sill pillar mining in rock burst prone conditions. *Unpublished internal document*, Noranda Technology Centre.

Hudyma, M., Potvin, Y., Milne, D., Brummer, R., Grant, D., & Board, M. (1994). Geomechanics of sill pillar mining. in A. A. Balkema (Ed.), *Proceedings of the 1st North American Rock Mechanics Symposium*, Austin, Texas, 969–976.

Kanduth, H., Germain, P., & Jacob, D. (1993). in situ stress determinations at the Brunswick Mine. *Unpublished internal document*, Noranda Technology Centre.

Kilburn, C. R., & Petley, D. N. (2003). Forecasting giant, catastrophic slope collapse: lessons from Vajont, Northern Italy. *Geomorphology*, *54*(1-2), 21-32.

Kirsch, C. (1898). Die theorie der elastizitat und die bedurfnisse der festigkeitslehre. *Zeitschrift des Vereines Deutscher Ingenieure*, *42*, 797-807.

Laubscher, D.H. (1977). Geomechanics classification of jointed rock masses - mining applications. *Transactions, Institute of Mining and Metallurgy*, Section A, Vol. 86, pp. A1-8

Martin, D., & Stacey, P. (Eds.). (2018). *Guidelines for Open Pit Slope Design in Weak Rocks*. CSIRO PUBLISHING.

Mazzanti, P., Bozzano, F., Cipriani, I., & Prestininzi, A. (2015). New insights into the temporal prediction of landslides by a terrestrial SAR interferometry monitoring case study. *Landslides*, *12*(1), 55-68.

Milne, D. (1993). Interpretation of the Brunswick mine instrumentation program. *Unpublished internal report*, Noranda Technology Centre.

Milne, D. (1994). Summary of observations by visiting rock mechanics engineer. *Unpublished internal report*, Mount Isa Mines.

Milne, D. (1997). *Underground design and deformation based on surface geometry* (Doctoral dissertation, University of British Columbia).

Milne, D., Pakalnis, R. C., & Lunder, P. J. (1996). Approach to the quantification of hanging-wall behaviour. *Transactions of the Institution of Mining and Metallurgy. Section A. Mining Industry*, *105*.

Milne, D., Pakalnis, R., Grant, D., & Sharma, J. (2004). Interpreting hanging wall deformation in mines. *International Journal of Rock Mechanics and Mining Sciences*, *41*(7), 1139-1151.

Milne, D. & Snell, G. (2016). Interpreting measured hanging wall deformation. *Presentation at the 2016 CIM annual general meeting, Vancouver, BC*.

Milne, D & Snell, G. (2018). New failure prediction method for underground excavations. *CIM Journal*, Vol. 9, No. 1, 2018. https://doi.org/10.15834/cimj.2018.4

MIM (1993). Unnamed internal documents. *Unpublished internal report*, Mount Isa Mines.

Saskatchewan Geological Survey, Morelli, R. M., & MacLachlan, K. (2012). *Saskatchewan Gold: Mineralization Styles and Mining History*. Saskatchewan Geological Survey.

Pakalnis, R. (2017). Report on Site Visit - Santoy Mine, Seabee Gold Operation Silver Standard, No. SGM-01/17. *Unpublished internal report*, SSR Mining.

Palmström, A. (1982). The volumetric joint count-a useful and simple measure of the degree of rock jointing. *Proc. 4th Int. Cong. Int. Assoc. Eng. Geol*, *5*, 221-228.

Paulgaard, T., Garrison, S., Murray, S., and Smith, T. (2014). Santoy gap development project, Phase 2 (Capstone Design Project). University of Saskatchewan.

Potvin, Y. (1988). *Empirical open stope design in Canada* (Doctoral dissertation, University of British Columbia).

Potvin, Y., & Hudyma, M. (2000). Open stope mining in Canada. *Proceedings of the MassMin2000, Brisbane. Carlton: AusIMM*, 661e74.

Poulos, H. G., & Davis, E. H. (1974). *Elastic solutions for soil and rock mechanics* (No. BOOK). John Wiley.

Read, J., & Stacey, P. (2009). Guidelines for open pit slope design.

Examine 2D 8.0, 2D stress analysis for underground excavations. (n.d. a) Retrieved April 10, 2019, from Rocscience website: file:///C:/Program%20Files/Rocscience/Examine2D%208.0/WebHelp/Examine2D.htm

RS3 V2.0, 3D Geotechnical Finite Element Analysis. (n.d. b) Retrieved April 10, 2019, from Rocscience website: file:///C:/Program%20Files/Rocscience/RS3%202.0/WebHelp/RS3.htm#t=Getting_Started%2FGetting_Started.htm

Rose, N. D., & Hungr, O. (2007). Forecasting potential rock slope failure in open pit mines using the inverse-velocity method. *International Journal of Rock Mechanics and Mining Sciences*, *2*(44), 308-320.

Schartner, N. (2017). Internal ground support designs. *Unpublished internal report*. SSR Mining.

Schartner, N. P. (2018). *Causes and Methods of Reducing Dilution at Seabee Gold Mine* (Masters dissertation, University of Saskatchewan).

Shacker, D., Milne, D., Hughes, P., & Schartner, N. (2018). Prediction of Hanging Wall Instability Using the Strain Effective Radius Factor Method. In *52nd US Rock Mechanics/Geomechanics Symposium*. American Rock Mechanics Association.

SRK Mining Consultants (2017). NI 43-101 Technical Report for the Seabee Gold Operation, Saskatchewan, Canada. Retrieved January 18, 2018 from: http://www.ssrmining.com/_resources/2017-10-20-Seabeey-Gold-Operation-Technical-Report.pdf

SSR Mining (2018). SSR Mining Reports Forth Quarter and Year-End 2017 Results. February 22, 2018. News Release 18-03. Retrieved on March 7, 2018 from: http://s22.q4cdn.com/546540291/files/doc_news/2018/2018-02-22-Q4-YE-2017-Results-FINAL.PDF

Stewart, S. B. V., & Forsyth, W. W. (1995). The Mathew's method for open stope design. *CIM bulletin*, *88*(992), 45-53.

Stewart, P & Trueman, R. (2003). Applying the extended Mathews stability graph: Quantifying case history requirements and site-specific effects, *First AGCM Conference, Sydney*, Australia, 2003.

Suorineni, F. (2010). The stability graph after three decades in use: experiences and the way forward. *International journal of mining, Reclamation and Environment*, *24*(4), 307-339.

Tipton, K. Personal communication, February, 2019

Villaescusa, E., Sandy, M. P., & Bywater, S. (1992). Ground support investigations and practices at Mount Isa. Rock support in mining and construction, Balkema, Rotterdam, 185-193.

Villaescusa, E. (1996). Excavation design for bench stoping at Mount Isa mine, Queensland, Australia. Transactions of the Institution of Mining and Metallurgy-Section A-Mining Industry, 105, A1.

Voight, B. (1988). A method for prediction of volcanic eruptions. *Nature*, *332*(6160), 125.

Voight, B. (1989). A relation to describe rate-dependent material failure. *Science*, *243*(4888), 200-203.

Wang, J. (2004). *Influence of stress, undercutting, blasting, and time on open stope stability and dilution* (Doctoral dissertation, University of Saskatchewan).

Wang, J., Milne, D., Wegner, L., & Reeves, M. (2007). Numerical evaluation of the effects of stress and excavation surface geometry on the zone of relaxation around open stope hanging walls. *International Journal of Rock Mechanics and Mining Sciences*, *2*(44), 289-298.

Wikipedia (n.d. a) Brunswick 6 mine. Retrieved on February 8, 2019, from: https://en.wikipedia.org/wiki/Brunswick_6_mine

Wikipedia (n.d. b) Mount Isa Mines. Retrieved on February 8, 2019, from: https://en.wikipedia.org/wiki/Mount_Isa_Mines

Wood, C. R. (2016). *Structural study of the auriferous Santoy shear zone, northeastern Glennie domain, Saskatchewan* (Doctoral dissertation, Faculty of Graduate Studies and Research, University of Regina).

APPENDIX A MODEL RESULTS FOR CYLINDRICAL AND TABULAR OPENINGS

Examine 2D model of a cylindrical opening

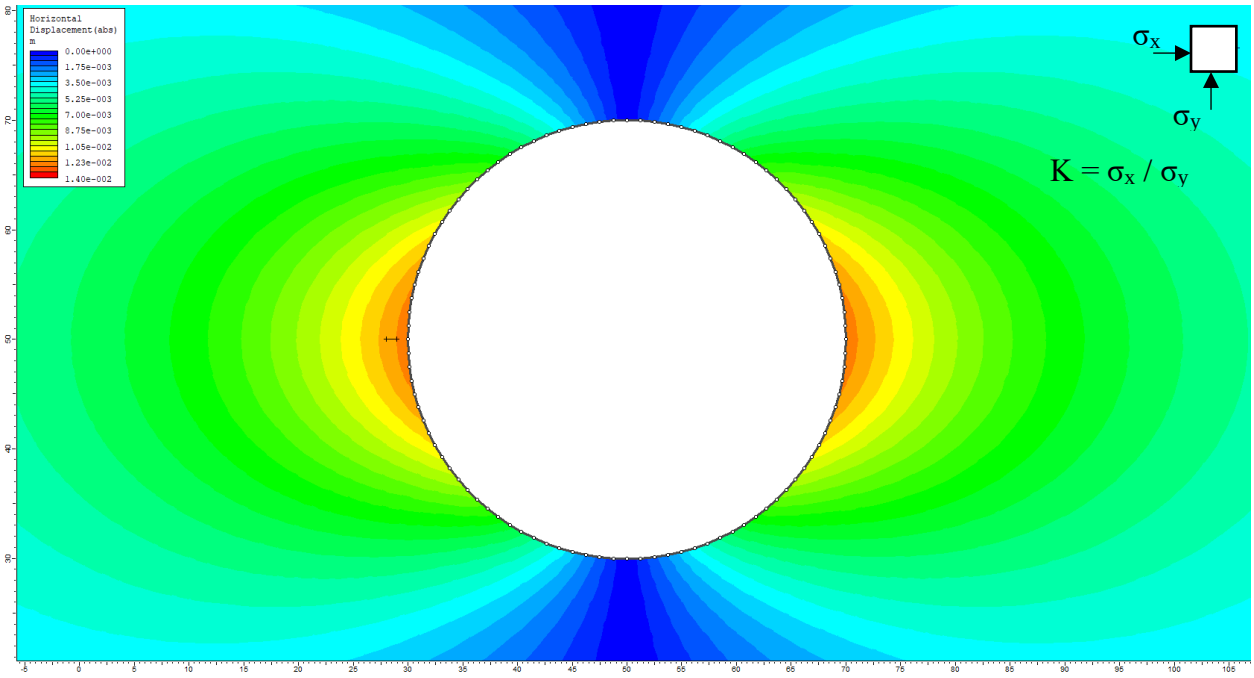

Figure A-1: View of the horizontal displacement around a cylindrical opening (radius = 20 metres) in Examine 2D.

Table A-1: Summary of the results from Examine 2D modelling of horizontal displacement around a cylindrical opening.

ν	E (MPa)	σ (x) (MPa)	K	r_1 (m)	r_2 (m)	Displacement (mm)			με
						r_1	r_2	Delta	
0.25	50000	5	0.5	21	22	1.10	0.96	-0.14	-143
0.25	50000	10	1.0	21	22	4.82	4.61	-0.22	-219
0.25	50000	20	2.0	21	22	12.28	11.91	-0.37	-372
0.25	50000	30	3.0	21	22	19.73	19.21	-0.52	-524
0.25	50000	40	4.0	21	22	27.19	26.51	-0.68	-677

Examine2D Analysis Information

Document Name:

- SERF-Theory-Stress-CircleTunnel-v01.exa

Project Summary:

- Job Title: Examine2D - 2D Stress Analysis for Excavations
- Date Created: 2019-03-04, 3:36:57 PM

Project Settings

General

- Units: Metric, stress as MPa
- Number of Excavation Elements: 100
- Boundary Element Type: Constant
- Analysis Type: Plane Strain
- Matrix Solver Type: Jacobi Bi-Conjugate Gradient

Field Stress

	K=0.5	K=1.0	K=2.0	K=3.0	K=4.0
Type	Constant Stress	Constant Stress	Constant Stress	Constant Stress	Constant Stress
Sigma 1 (MPa)	5.00	10.00	20.00	30.00	40.00
Sigma 3 (MPa)	10.00	10.00	10.00	10.00	10.00
Sigma Z (MPa)	10.00	10.00	10.00	10.00	10.00
Angle (deg)	0.00	0.00	0.00	0.00	0.00

Rock Mass Elastic Properties

Type	Isotropic
Em (MPa)	50000.00
Poisson's Ratio	0.25

Rock Mass Strength

Type	Mohr-Coulomb
Tensile Strength (MPa)	0.30
Cohesion (MPa)	2.00
Friction Angle (deg)	50.00

Joint Strength

Type	Elastic
Joint Normal Stiffness (MPa/m)	10000.00
Joint Shear Stiffness (MPa/m)	1000.00

List of All Coordinates

Stress Grid

#	X	Y
1	-30.000	-30.000
2	130.000	-30.000
3	130.000	130.000
4	-30.000	130.000

Excavation Boundary

	X	Y
Origin	50	50
Radius	20	

Material Query

#	X	Y
1	29.000	50.000
2	28.000	50.000

Examine 2D model of a tabular opening

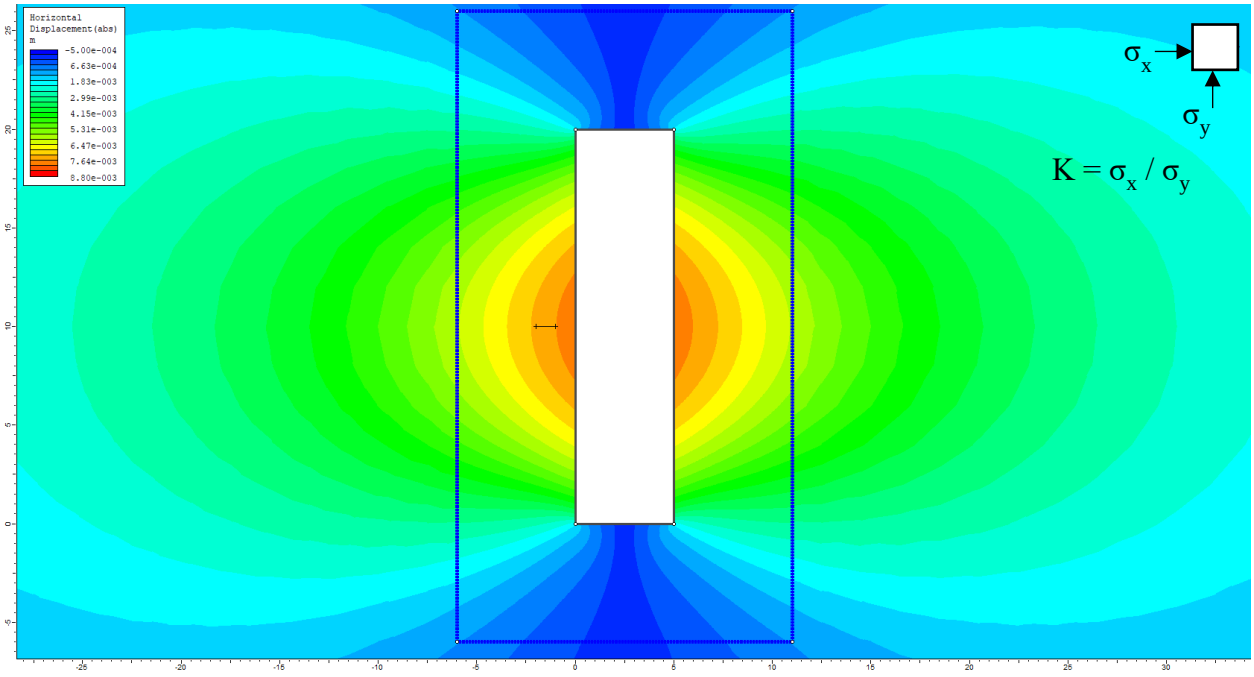

Figure A-2: View of the horizontal displacement around a tabular opening (height = 20 metres, width =5 metres) in Examine 2D.

Table A-2: Summary of the results from Examine 2D modelling of horizontal displacement around a tabular opening.

v	E (MPa)	σ (x) (MPa)	K	Distance to HW (m)		Displacement (mm)			με
				r_1	r_2	r_1	r_2	Delta	
0.25	50000	5	0.5	1	2	1.76	1.68	-0.08	-85
0.25	50000	10	1.0	1	2	3.71	3.56	-0.16	-157
0.25	50000	20	2.0	1	2	7.62	7.32	-0.30	-301
0.25	50000	30	3.0	1	2	11.53	11.08	-0.45	-446
0.25	50000	40	4.0	1	2	15.44	14.85	-0.59	-590

Examine2D Analysis Information

Document Name:

- Stress-Theory(5x20)-v03b.exa

Project Summary:

- Job Title: SERF Method
- Analysis: Stress at a boundary
- Author: Dylan Shacker
- Company: UofS
- Date Created: 2018-11-28, 3:57:24 PM

Project Settings

General

- Units: Metric, stress as MPa
- Number of Excavation Elements: 100
- Boundary Element Type: Constant
- Analysis Type: Plane Strain
- Matrix Solver Type: Jacobi Bi-Conjugate Gradient

Field Stress

	K=0.5	K=1.0	K=2.0	K=3.0	K=4.0
Type	Constant Stress	Constant Stress	Constant Stress	Constant Stress	Constant Stress
Sigma 1 (MPa)	5.00	10.00	20.00	30.00	40.00
Sigma 3 (MPa)	10.00	10.00	10.00	10.00	10.00
Sigma Z (MPa)	10.00	10.00	10.00	10.00	10.00
Angle (deg)	0.00	0.00	0.00	0.00	0.00

Rock Mass Elastic Properties

Type	Isotropic
Em (MPa)	50000.00
Poisson's Ratio	0.25

Rock Mass Strength

Type	Mohr-Coulomb
Tensile Strength (MPa)	0.30
Cohesion (MPa)	2.00
Friction Angle (deg)	50.00

Joint Strength

Type	Elastic
Joint Normal Stiffness (MPa/m)	10000.00
Joint Shear Stiffness (MPa/m)	1000.00

Advanced Joint Properties

Initial Joint Deformation	Yes
Consider Joint Aperture	No

List of All Coordinates

Stress Grid

#	X	Y
1	-37.500	-30.000
2	42.500	-30.000
3	42.500	50.000
4	-37.500	50.000

Stress Grid

#	X	Y
1	-6.000	-6.000
2	11.000	-6.000
3	11.000	26.000
4	-6.000	26.000

Excavation Boundary

#	X	Y
1	5.000	0.000
2	5.000	20.000
3	0.000	20.000
4	0.000	0.000

Material Query

#	X	Y
1	-1.000	10.000
2	-2.000	10.000

RS3 model of a tabular opening

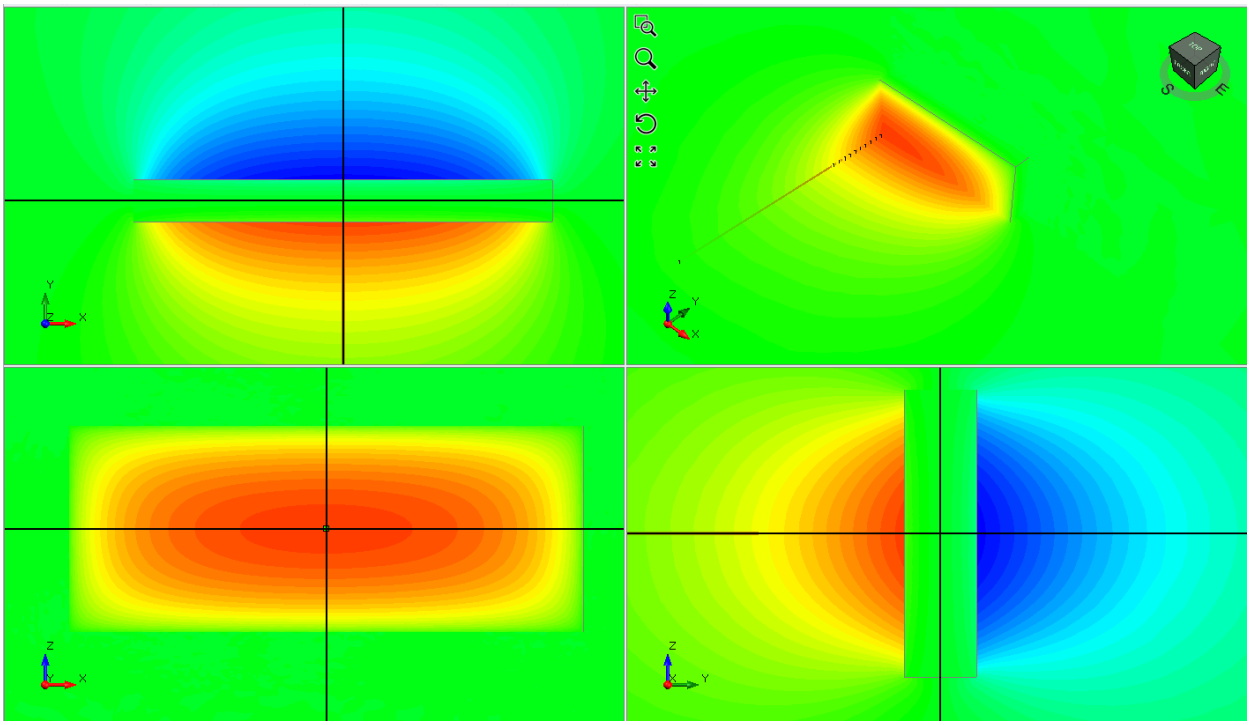

Figure A-3: Views of the horizontal displacement around a tabular opening (height = 20 metres, length = 50 metres, width =5 metres) in RS3.

Table A-3: Summary of the results from RS3 modelling of horizontal displacement around a tabular opening.

v	E (MPa)	σ_1 (y) (MPa)	K	Distance to HW (m)		Displacement (mm)			με
				r_1	r_2	r_1	r_2	Delta	
0.25	50000	5	0.5	1	2	1.55	1.46	-0.09	-86
0.25	50000	10	1.0	1	2	3.27	3.11	-0.16	-160
0.25	50000	20	2.0	1	2	6.72	6.41	-0.31	-306
0.25	50000	30	3.0	1	2	10.16	9.71	-0.45	-453
0.25	50000	40	4.0	1	2	13.60	13.00	-0.60	-599

RS³ Analysis Information

Project Settings

Document Name:	SERF-Theory-v03.2
Project Title:	SERF-Theory
Analysis:	SERF Theory-v01
Author:	Dylan Shacker
Company:	UofS

Units

Units:	Metric, stress as MPa
Time Units:	Days
Permeability Units:	Meters/second
Coordinate:	Cartesian x,y,z

Boreholes

Stage Information

Number of Stages: 2

#	Name
1	Stage 1
2	Stage 2

Stress Analysis

Maximum Number of Iterations:	500
Tolerance:	0.001
Load Steps:	Automatic
Convergence Type:	Absolute Force & Energy
Accelerate Initial Stiffness:	Yes
Min. Alpha:	0.1
Max. Alpha:	10
Tensile failure reduces Hoek-Brown tensile strength to zero:	No
Tensile failure reduces shear strength to residual:	Yes
Abort calculation when non-convergence detected:	No

Solver Options

Analysis Type:	Uncoupled
Solver Type:	Automatic

Groundwater Settings

Method:	None
Pore Fluid Unit Weight:	0.00981 MN/m3

Shear Strength Reduction

Determine Strength Reduction Factor: No

Mesh Setup

Element Type:	10-Noded Tetrahedra
Mesh Gradation:	Graded

Material Properties

General	
Name:	Material 1
Color:	
Initial Element Loading:	Field Stress Only
Material Behavior:	Drained
Strength	
Failure Criterion:	Mohr Coulomb
Material Type:	Elastic
Peak Tensile Strength (MPa):	0.3
Peak Friction Angle (Degrees):	50
Peak Cohesion (MPa):	2
Unsaturated Shear Strength - Phi B:	0
Unsaturated Shear Strength - Air Entry (MPa):	0
Stiffness	
Type:	Linear Isotropic
Young's Modulus (MPa):	25000
Poisson's Ratio:	0.25
Using Unloading Condition:	No

General	
Name:	Material 4
Color:	
Initial Element Loading:	Field Stress Only
Material Behavior:	Drained
Strength	
Failure Criterion:	Mohr Coulomb
Material Type:	Elastic
Peak Tensile Strength (MPa):	0.3
Peak Friction Angle (Degrees):	50
Peak Cohesion (MPa):	2
Unsaturated Shear Strength - Phi B:	0
Unsaturated Shear Strength - Air Entry (MPa):	0
Stiffness	
Type:	Linear Isotropic
Young's Modulus (MPa):	50000
Poisson's Ratio:	0.25
Using Unloading Condition:	No

APPENDIX B CALCULATION OF THE ERF VALUES FOR THE 16N STOPE AT BRUNSWICK MINE

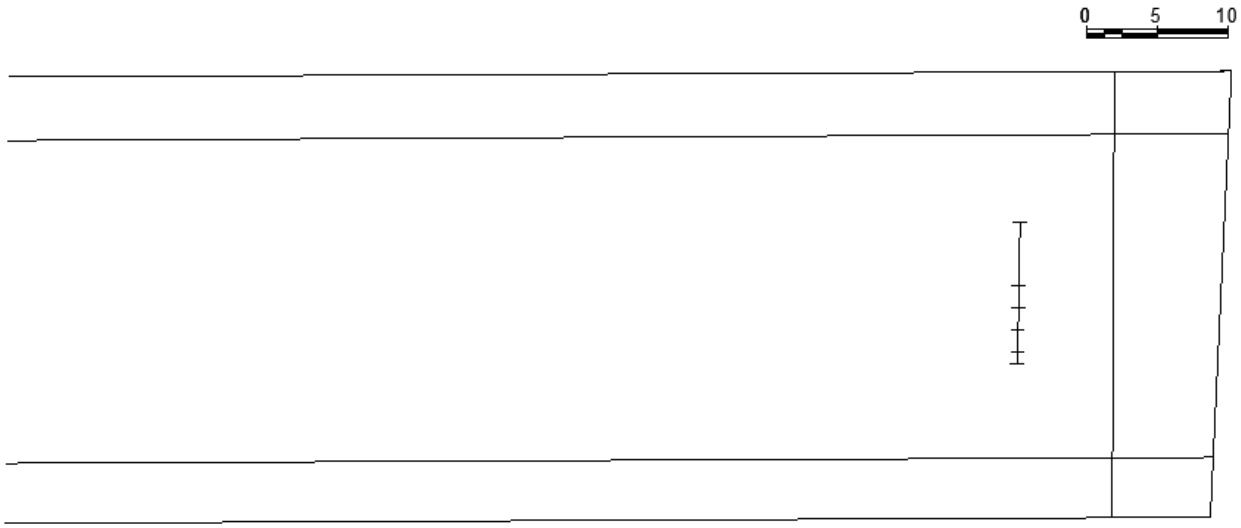

Figure B-1: True long view of the 16N Stope hanging wall after Blast 9 prior to undercutting of extensometer 2.

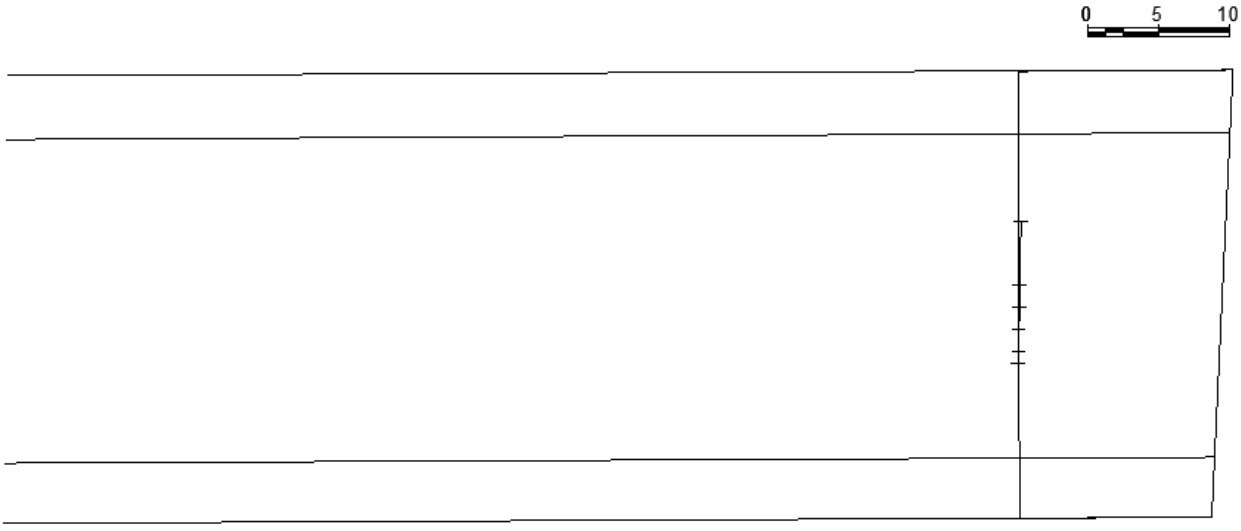

Figure B-2: True long view of the 16N Stope hanging wall after Blast 10 showing partial undercutting of extensometer 2.

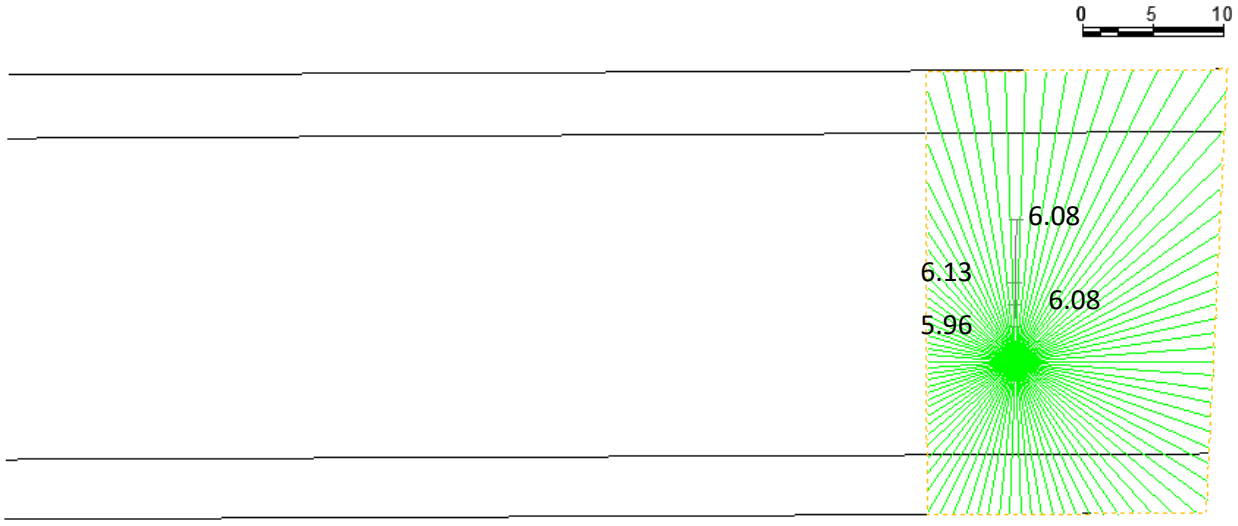

Figure B-3: True long view of the 16N Stope hanging wall after Blast 11 showing the ERF calculation for anchor 6.

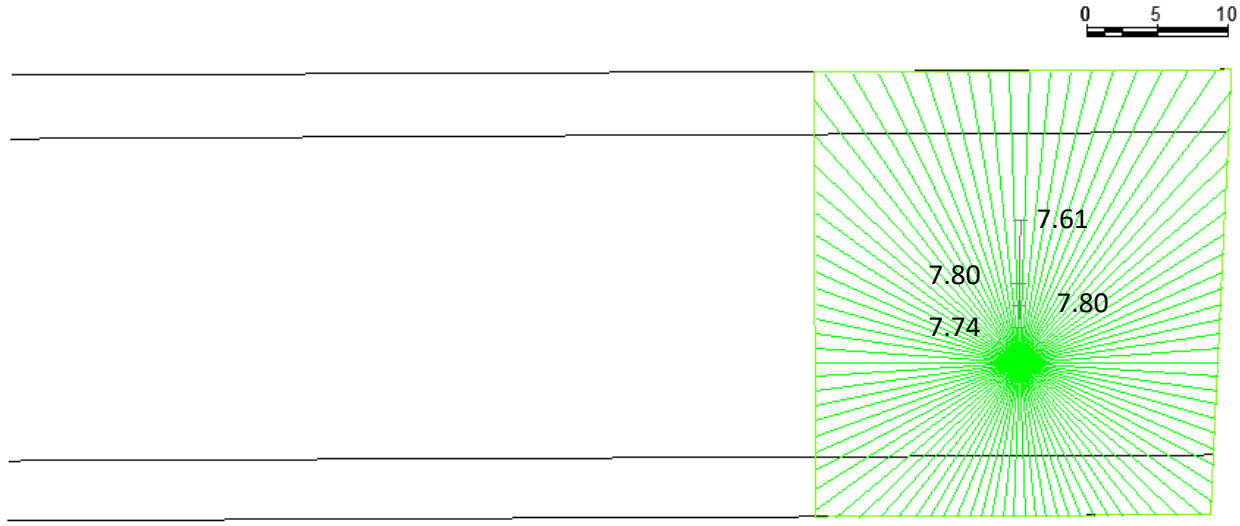

Figure B-4: True long view of the 16N Stope hanging wall after Blast 12 showing the ERF calculation for anchor 6.

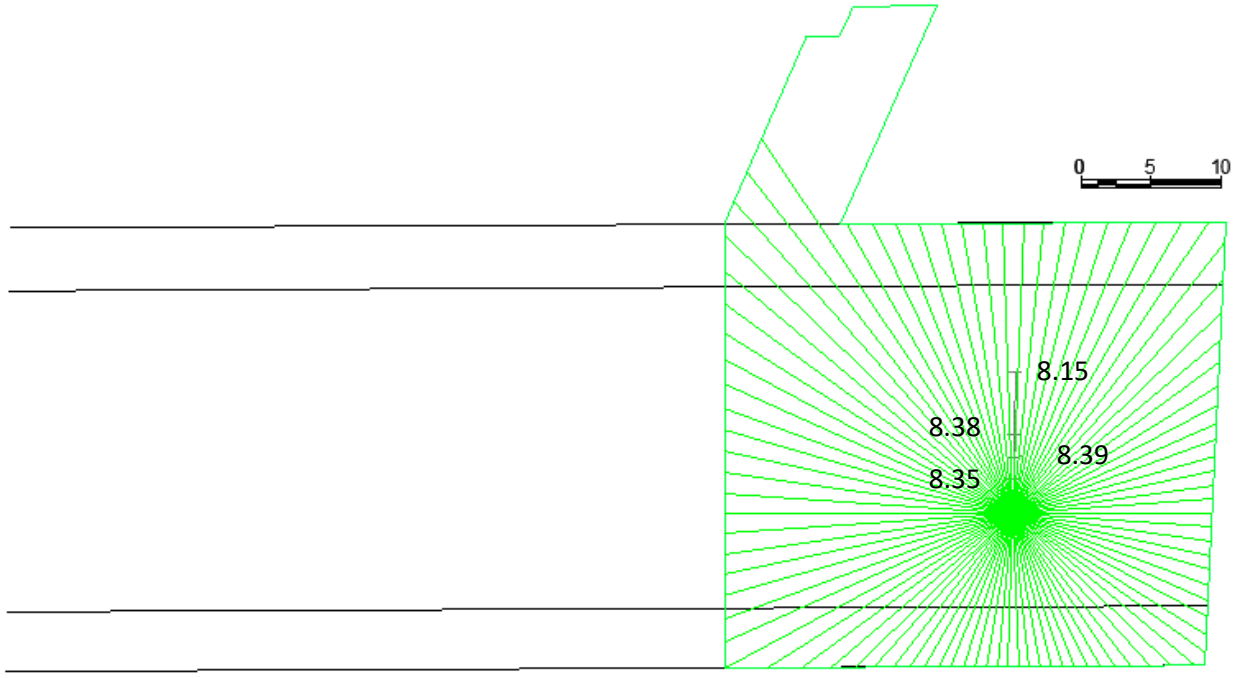

Figure B-5: True long view of the 16N Stope hanging wall after Blast 17 showing the ERF calculation for anchor 6.

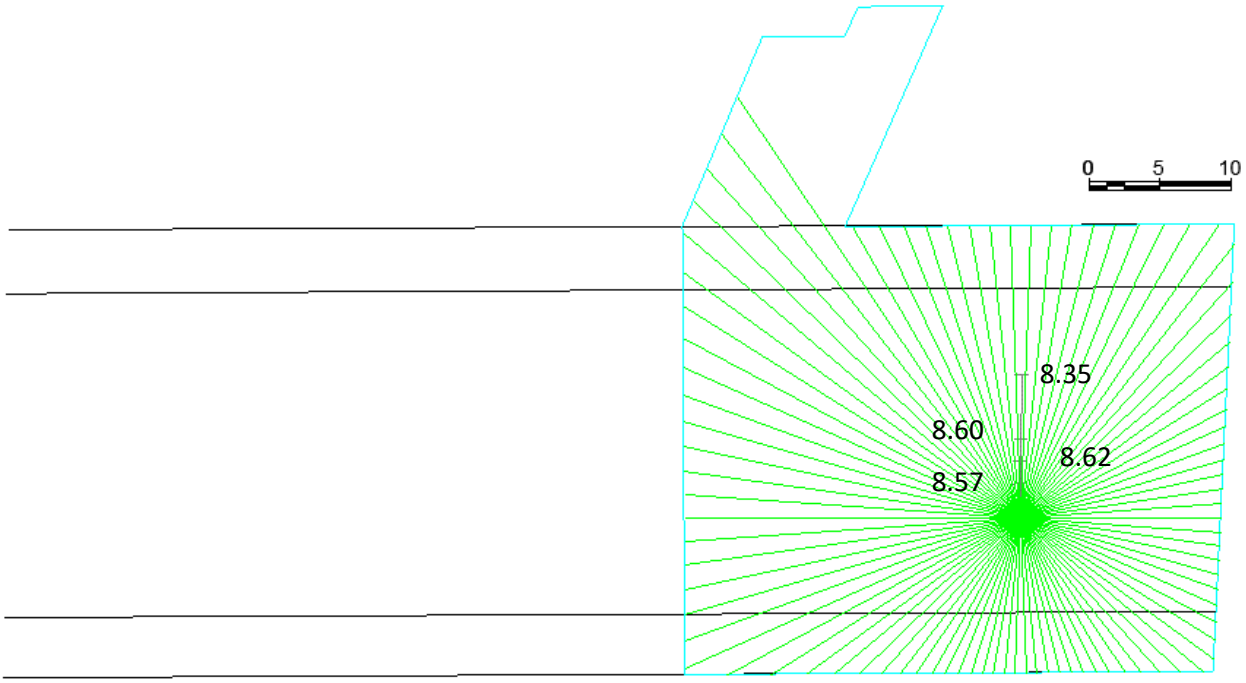

Figure B-6: True long view of the 16N Stope hanging wall after Blast 18 showing the ERF calculation for anchor 6.

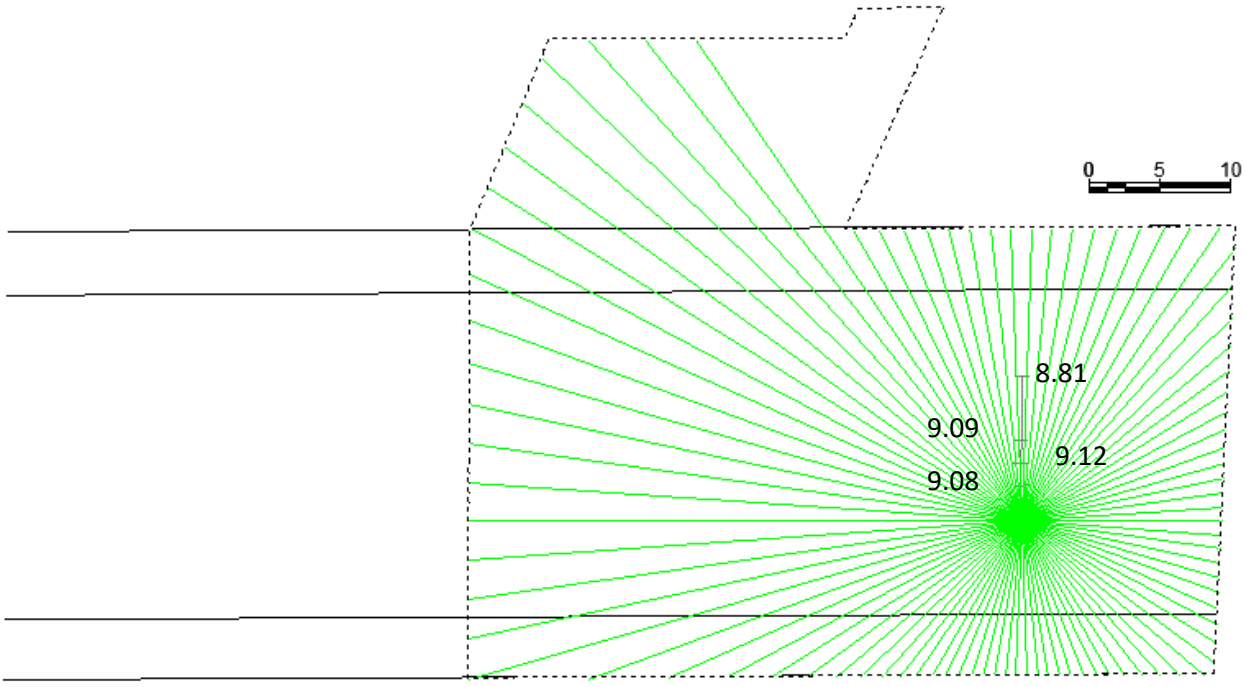

Figure B-7: True long view of the 16N Stope hanging wall after Blast 19 showing the ERF calculation for anchor 6.

APPENDIX C RMR MAPPING AT SANTOY MINE

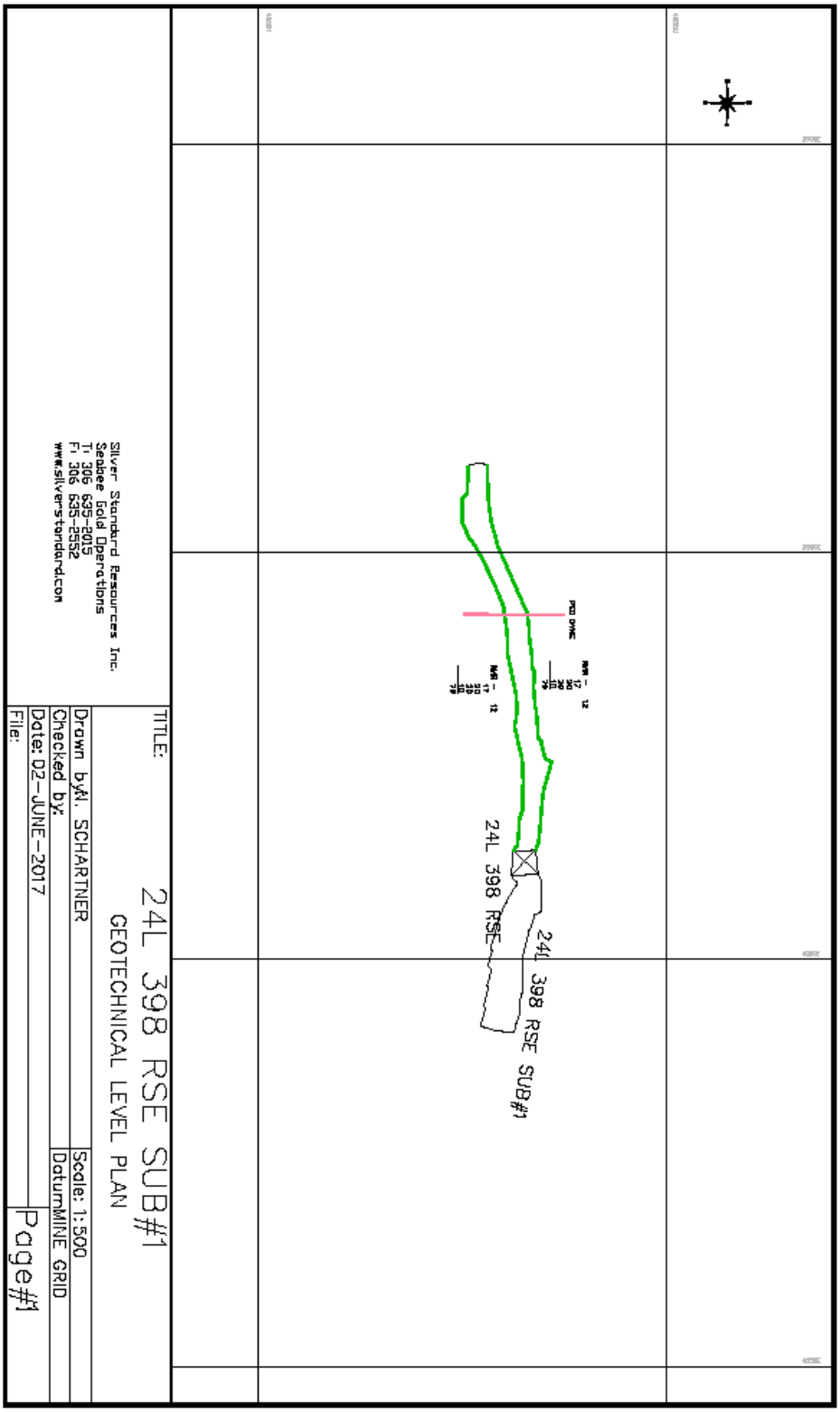

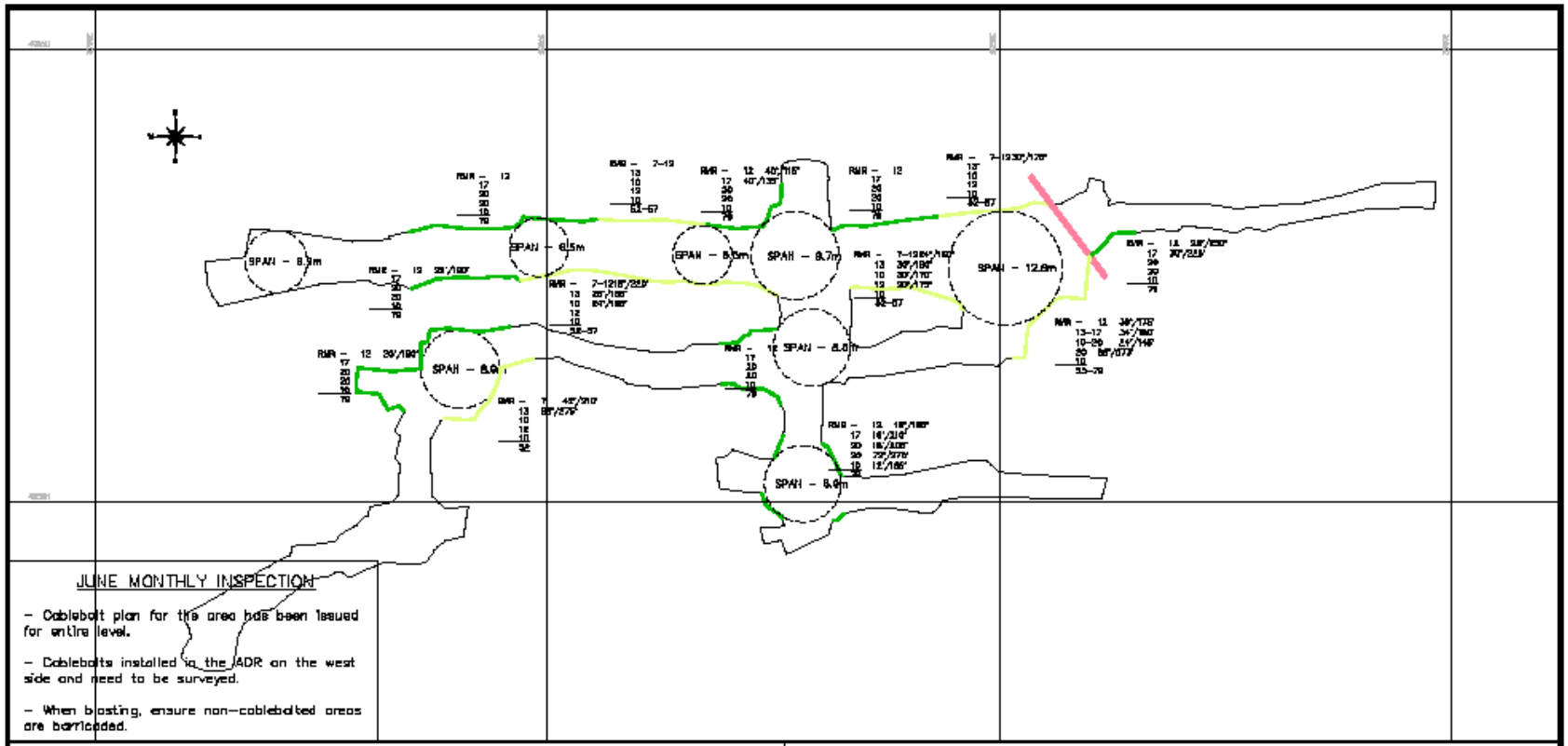

JUNE MONTHLY INSPECTION

- Cablebolt plan for the area has been issued for entire level.
- Cablebolts installed in the ADR on the west side and need to be surveyed.
- When blasting, ensure non-cablebolted areas are barricaded.

Silver Standard Resources Inc.
Seabee Gold Operations
T: 306 635-2015
F: 306 635-2552
www.silverstandard.com

TITLE: 28L 382 SILLS
GEOTECHNICAL LEVEL PLAN

Drawn by: N. SCHARTNER	Scale: 1:500
Checked by:	Datum: MINE GRID
Date: 07-JULY-2017	Page#1
File:	

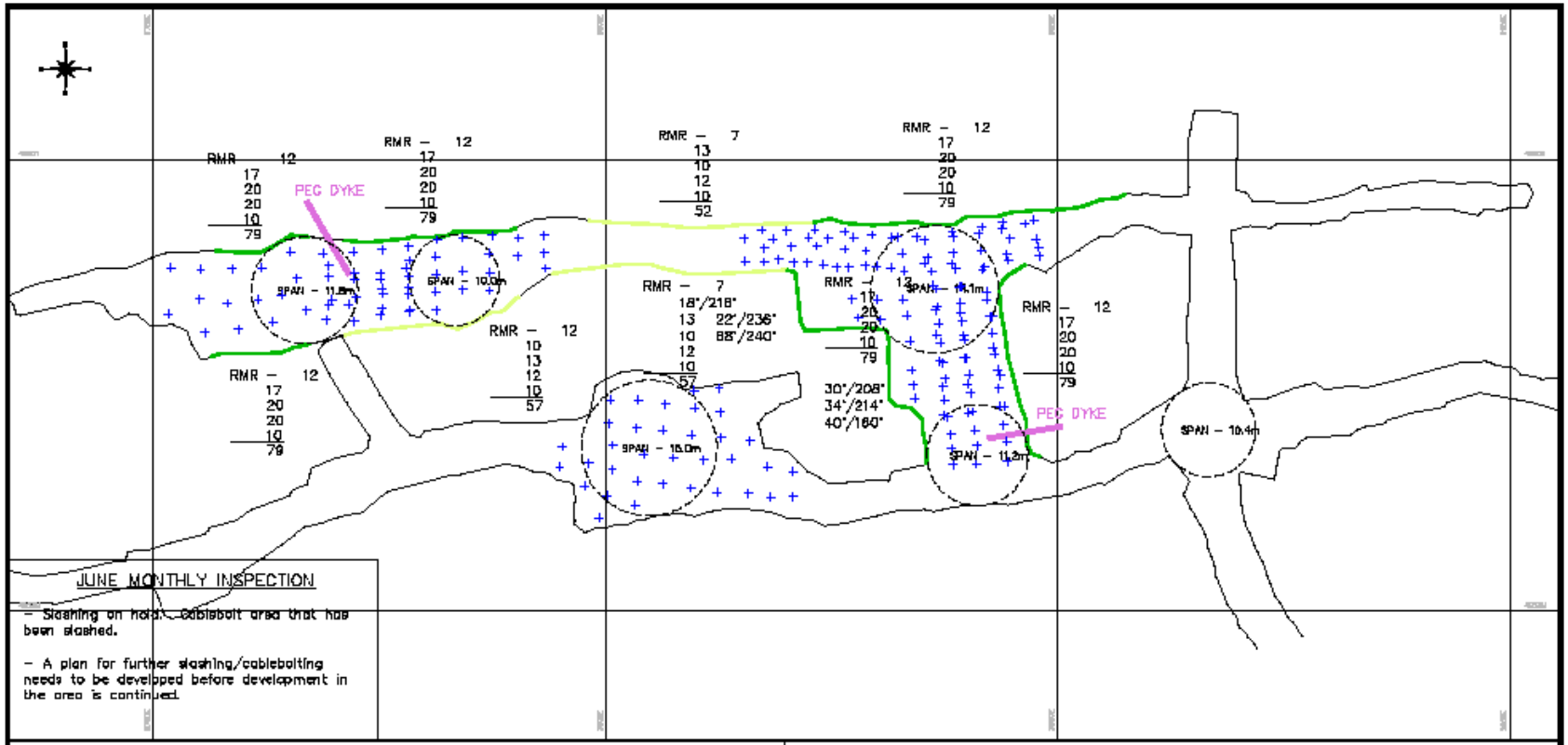

Silver Standard Resources Inc.
Seabee Gold Operations
T: 306 635-2015
F: 306 635-2552
www.silverstandard.com

TITLE: 30L 385 SILLS
GEOTECHNICAL LEVEL PLAN

Drawn by: N. SCHARTNER	Scale: 1:500
Checked by:	Datum: MINE GRID
Date: 07-JULY-2017	Page#1
File:	

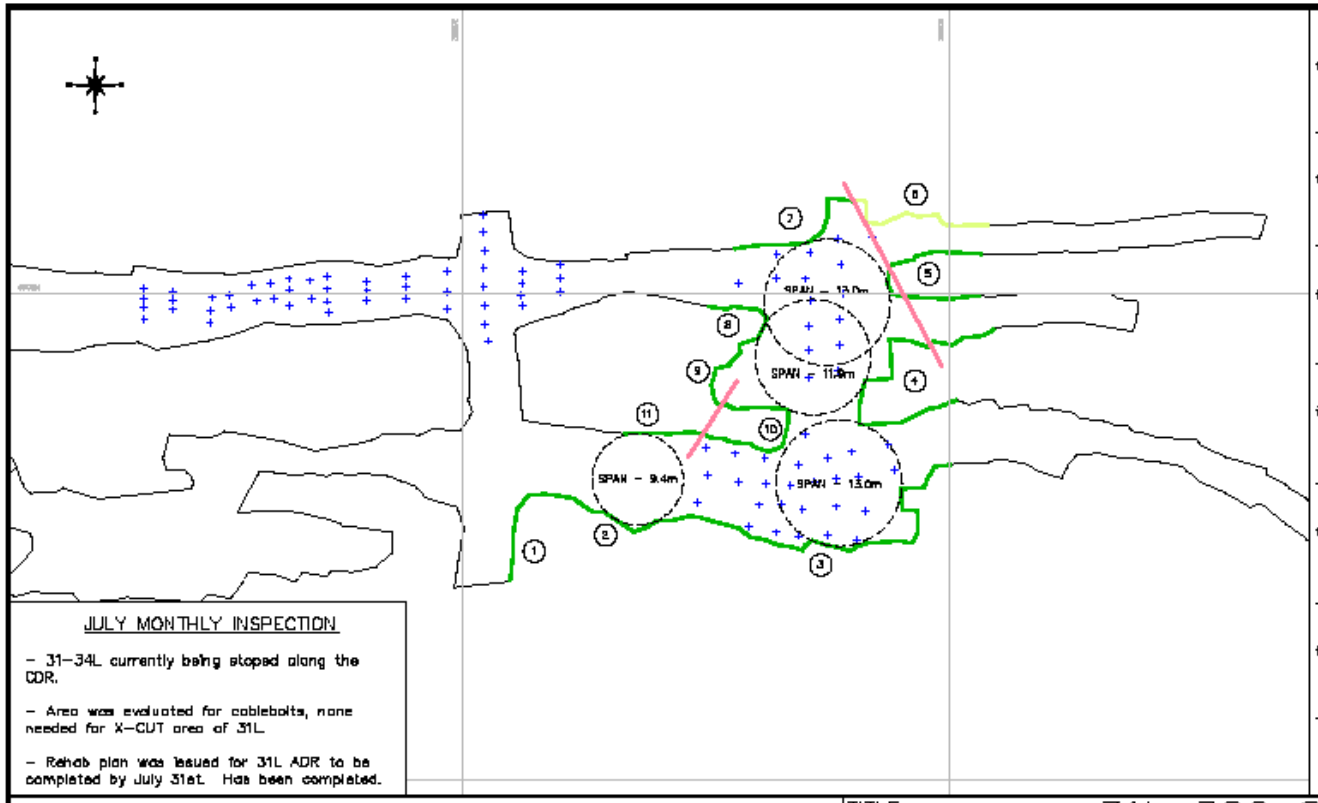

ROCKMASS QUALITY AND STRUCTURAL MAPPING

#1	12	16°/180°	#7	12	88°/238°
	17			17	08°/246°
	20			20	
	20			20	
	10			10	
	79			79	
#2	12		#8	12	10°/170°
	17			17	
	20			20	
	20			20	
	10			10	
	79			79	
#3	12	80°/240°	#9	12	90°/115°
	17	56°/348°		17	70°/010°
	20			20	20°/200°
	12–20			20	64°/004°
	10			10	
	71–79			79	
#4	12	44°/190°	#10	12	
	17	42°/176°		17	
	20	64°/254°		20	
	20	38°/176°		20	
	10			10	
	79			79	
#5	12	28°/228°	#11	12	28°/204°
	17	58°/115°		17	26°/210°
	20	48°/190°		20	
	20			20	
	10			10	
	79			79	
#6	12	30°/190°			
	13				
	10				
	12				
	10				
	57				

JULY MONTHLY INSPECTION

- 31–34L currently being stoped along the CDR.
- Area was evaluated for cablebolts, none needed for X–CUT area of 31L.
- Rehab plan was issued for 31L ADR to be completed by July 31st. Has been completed.

Silver Standard Resources Inc.
Seabee Gold Operations
T: 306 635-2015
F: 306 635-2552
www.silverstandard.com

TITLE: 31L 380 SILLS
GEOTECHNICAL LEVEL PLAN

Drawn by: N. SCHARTNER	Scale: 1:500
Checked by:	Datum: MINE GRID
Date: 20–JULY–2017	Page#1
File:	

APPENDIX D MOUNT ISA MINE

The Mount Isa mine is located in Mount Isa, Queensland, approximately 780 kilometres west of Townsville, Australia (Figure D-1). Mines in the Mount Isa area have been producing copper, lead, silver, and zinc from deposits in parallel seams, within a 1,000-metre-thick sulphide and shale formation, since the 1920's (Villaescusa, 1996). The ore is extracted from deposits with parallel bedding, dipping to the west at approximately 70°. The shale, forming the mineralization and host strata, has varied strength resulting in the stability of the hanging wall, and associated dilution, being the topic of extensive research.

The data considered during this case study was summarized by Milne (1994). The case study from the Mount Isa mine focuses on the location, conditions, and practices at the time the data was collected. Current site conditions and practices may differ. This study provides only the details required to review the ground response to mining, estimate pre-mining stresses from extensometer data, and apply the modified SERF method to predict hanging wall instability, if applicable.

Figure D-1: Location of the Mount Isa Mine (Wikipedia, n.d. b)

General rock mass properties

Mapping identified a bedding plane set and four major joint sets (Figure D-2), which are primarily smooth and planar with either a chloritic or thin carbonate infilling (Villaescusa et al., 1992; Villaescusa 1996; Milne, 1997). An Elastic modulus of 25 GPa and Poisson's ratio of 0.25 were estimated for the shale.

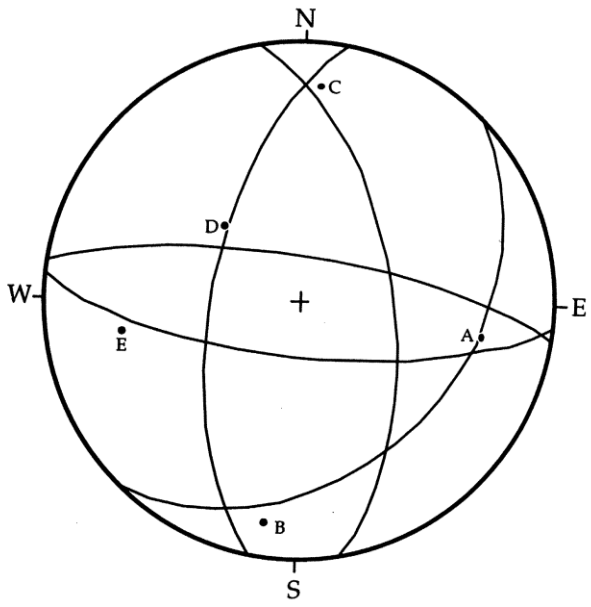

JS	DIP	DDR	
A	62°	280°	Bedding
B	76°	8°	Joint
C	72°	185°	Joint
D	34°	134°	Joint
E	60°	80°	Joint, often calcite infilling

Figure D-2: Stereographic project of bedding and primary joints at Mount Isa Mine (after Villaescusa, 1996).

Mining Overview

Mining at Mount Isa Mine was generally completed using either cut and fill stoping, open stoping, or bench stoping. After 1991, improved understanding of the behaviour of the hanging wall allowed cut and fill to be replaced by bench and open stoping, although the stability and dilution control of the exposed hanging wall remained a concern (Villaescusa et al., 1992; Villaescusa, 1996). The generally accepted hanging wall failure mode at Mount Isa mine is mid-span buckling of the unsupported bedding planes. Numerous stope hanging walls failed once the unsupported excavation geometry became too large. A combination of pillars, ground support, and backfill were utilized to provide stability to mining blocks (Villaescusa, 1996).

Numerical modelling suggested the maximum principal stress was oriented approximately normal to the bedding and thus, the stope hanging wall (Villaescusa, 1996). Instrumentation data was available from the 5FP1 and 5HP1 stope instrumentation programs and is described and analysed in Section 0 and 0 respectively.

5FP1

The 5FP1 stope was located in a high stress abutment and was mined using a bench stoping method. Following excavation, and prior to backfilling, the final stope dimensions were 53 metres up dip and 43 metres along strike with rock abutments surrounding the opening (Milne, 1997).

Figure D-3 is a schematic showing the location and approximate dimensions of the 5FP1 stope. The 5FP1 stope was the first stope to be mined in this area following the completion of overcut and undercut developments (Villaescusa, 1996). Ground support, including cable bolts and split sets, were installed from the development sills to support the hanging wall by pinning bedding layers to effectively create a thicker beam. Bulbed, single strand cable bolts were fully grouted and installed in fan patterns with variable cable bolt length and ring spacing, depending on the ground conditions and opening geometry (Villaescusa et al., 1992; Villaescusa, 1996).

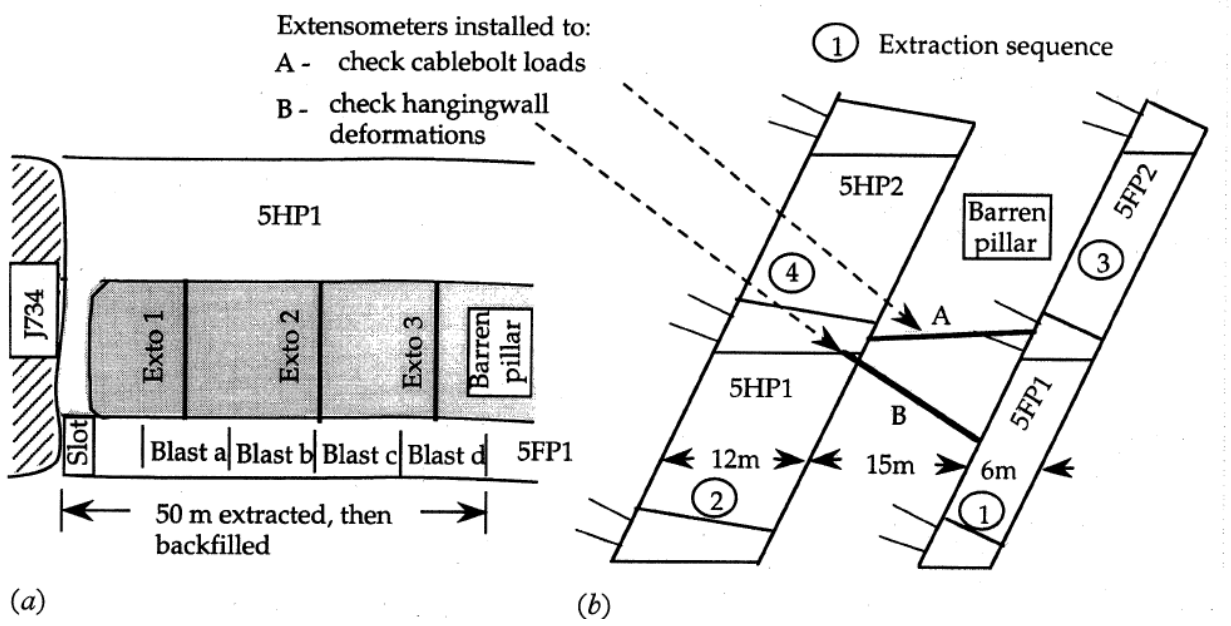

Figure D-3: (a) Plan view and (b) cross-section, looking north, of the 5HP1 and 5FP1 stopes showing extensometer locations, ground support, blast sequence (from Villaescusa, 1996).

Instrumentation program design

Data was available for only 2 of the 6 planned extensometers for the 5FP1 stope. Both extensometer 1 and extensometer 2 consisted of six anchors and were installed from the 5HP1 overcut, with the deepest anchors positioned approximately 0.5 metres from the planned hanging wall (Figure D-3b) (Milne, 1994; Milne, 1997). The distances between extensometer anchors are summarized in Table D-1 and a schematic of the anchor positions relative to the stope and drillhole collar are shown in Figure D-4.

Table D-1: Extensometer layout for extensometers installed in the Mount Isa Mine 5FP1 Stope hanging wall.

Instrument	Distance between anchors (m)					
	1-2	2-3	3-4	4-5	5-6	6-Head
Extensometer 1	1.0	1.0	1.0	4.0	15.0	3.0
Extensometer 2	1.0	1.2	1.3	4.5	13.0	3.0

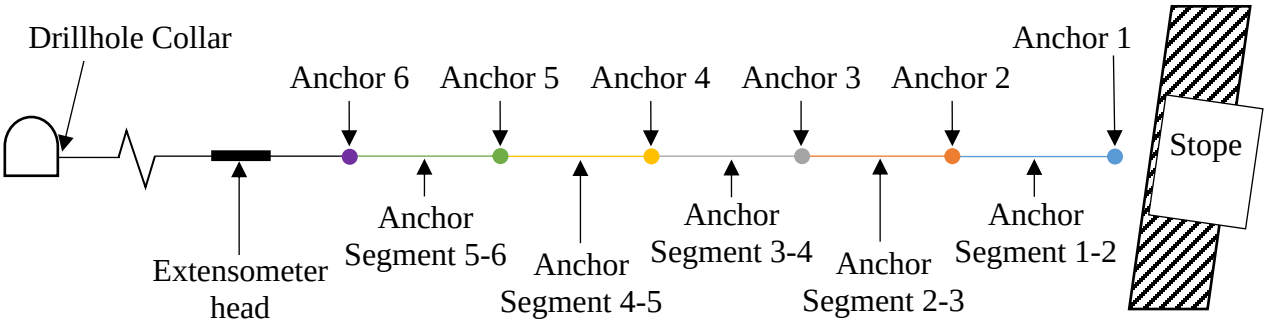

Figure D-4: Schematic showing the anchor positions relative to the stope and the drillhole collar.

Stope Mining

To control dilution and prevent instability that could jeopardise the 5HP1 stope, mining of the 5FP1 bench stope was split into multiple sub-stopes. Each sub-stope was mined and backfilled before advancing along strike, to the north, to mine the next sub-stope. The instrumented potion of the 5FP1 bench stope was completed with 4 production blast (Figure D-3a), which began on 11-March, 1993 and concluded on 29-March, 1993.

After the instrumented portion of the stope was mined and backfilled, the remainder of the 5FP1 bench stope was mined in similar fashion until the entire planned strike length had been mined. Data associated with stope mining after the backfill front had passed the instruments was not available.

Ground Response to Mining

For the stope location, a pre-mining stress of approximately 40 MPa, oriented normal to the hanging wall, was estimated by Milne (1997). Prior to undercutting, there was no measured concentration of compressive strain indicated by the data from either extensometer 1 or 2.

Applying Equation 3-7, the estimated upper bound to elastic deformation in the hanging wall adjacent and normal to the stope, due to hanging wall stress relaxation following undercutting by stope mining, is estimated to be approximately 1200 microstrain of tension. Assuming a one metre anchor segment length, this strain would be associated with a deformation of approximately 1.2 millimetres.

$$\varepsilon_{(a-b)} = \frac{\Delta\sigma_n}{E}(1-\upsilon) = \frac{0-40MPa}{25GPa}(1-0.25) \cong -1200\mu\varepsilon$$

EXTENSOMETER 1

The data from extensometer 1 was collected manually and recorded to the nearest 0.01 millimetre (Milne, 1994). A plot of the strain over time for extensometer 1 is shown in Figure D-5.

Figure D-6 shows plan, cross section, and long section views of the stope and extensometer, before and after being undercut by blast 1. Figure D-6b shows a schematic of areas of expected stress concentration and relaxation, for stresses generally perpendicular to the ore zone. Reviewing the displacement data, measured from the collar, the largest initial displacement occurs closest to the hanging wall with progressively smaller deformation as the distance from the opening to the anchor increases. This indicates that the anchors are labelled correctly and appear to be functioning normally. There is some variability in the strain measurements between anchors, within the expected zone of relaxation. Averaging the strain response over a longer distance requires less measurement accuracy and averages any variations in Elastic Modulus over the entire segment length. Figure D-6e shows a revised plot of strain over time with the strain calculated over anchor segment 1-3, instead of separately over anchor segment 1-2 and 2-3, to average the lower strain

levels initially measured by the anchor segment with those believed to be more representative of the in-situ stress conditions.

Although several extensometer 1 anchor segments exceed the estimated upper bound to elastic deformation of 1,200 microstrain, none of the anchor segments established a trend of increasing non-linear extension for subsequent production blasts. As a result, no transition to non-linear extension can be determined and the data from extensometer 1 is not considered suitable for analysis using the modified SERF method.

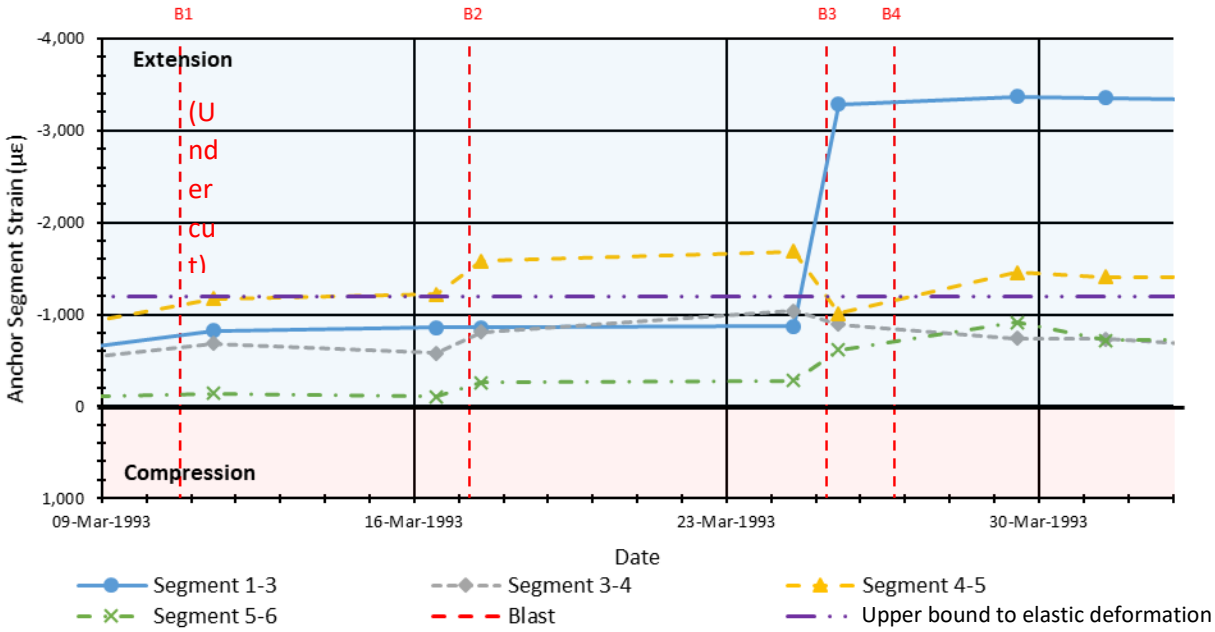

Figure D-5: Segment strains in Mount Isa Mine 5FP1 stope hanging wall measured by extensometer 1.

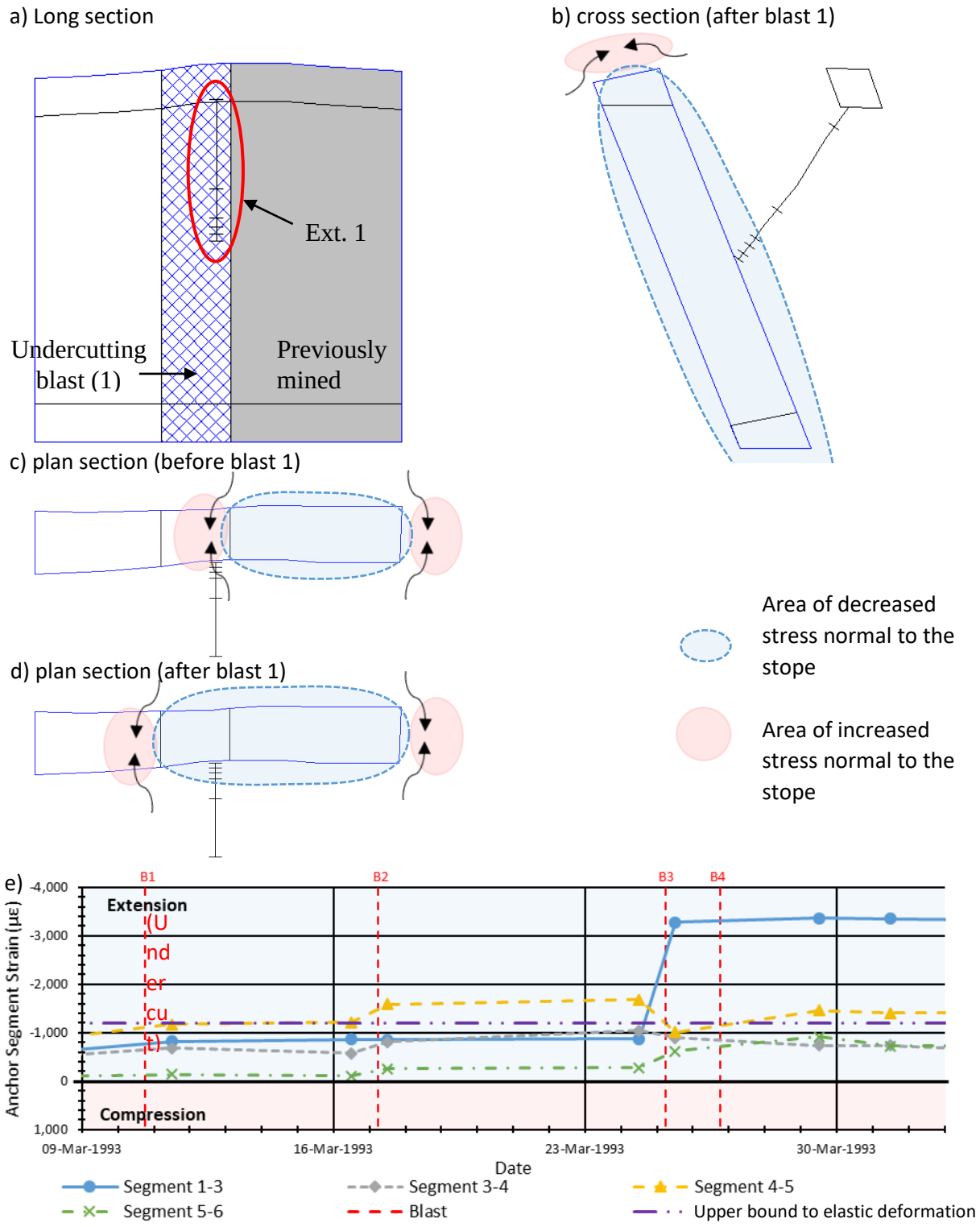

Figure D-6: Section views of the Mount Isa Mine 5FP1 bench stope showing blast geometries, excavation geometries, expected zones of stress change, and the location of extensometer 1 for: (a) true longitudinal view, (b) cross section after undercutting, (c) plan section prior to undercutting, (d) plan section after undercutting, and (e) a plot of strain over time for the reliable anchor segments.

EXTENSOMETER 2

As with extensometer 1, the data from extensometer 2 was collected manually and recorded to the nearest 0.01 millimetre (Milne, 1994). A plot of the strain over time for extensometer 2 is shown in Figure D-7.

Figure D-8 shows plan, cross section, and long section views of the stope and extensometer, before and after being undercut by blast 3. Figure D-8b also includes a schematic of areas of expected stress concentration and relaxation, for stresses generally perpendicular to the ore zone. As with extensometer 1, averaging strain values for extensometer 2 over a longer distance is believed to improve the reporting accuracy by reducing sensitivity to measurement accuracy and variations in Elastic Modulus. Figure D-8e shows a revised plot of strain over time with the measurements taken over anchor segment 1-3, instead of separately over anchor segment 1-2 and 2-3, to consider strains over a longer interval.

Production blasts do not undercut extensometer 2 until blast 3 of 4. This resulted in only two stope geometries with associated data points so no trend could be established, and the modified SERF method could not be applied.

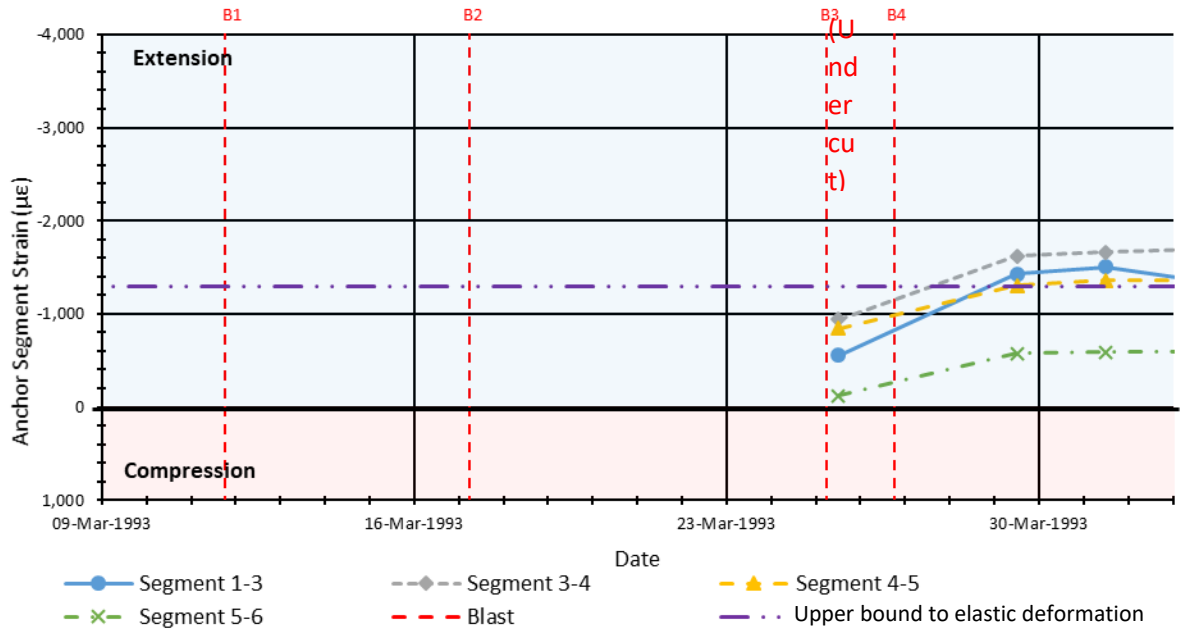

Figure D-7: Segment strains in Mount Isa Mine 5FP1 stope hanging wall measured by Extensometer 2.

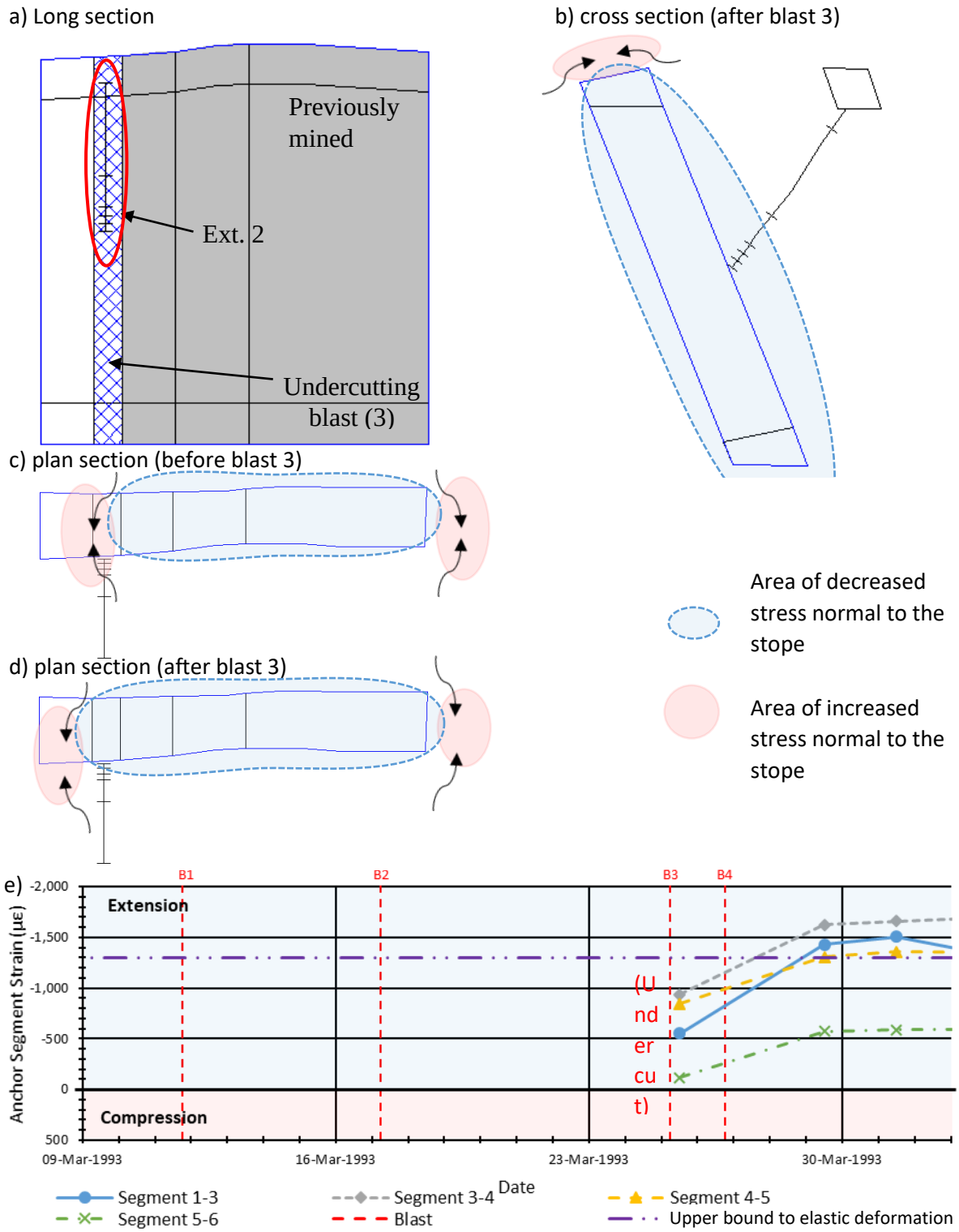

Figure D-8: Section views of the Mount Isa Mine 5FP1 bench stope showing blast geometries, excavation geometries, expected zones of stress change, and the location of extensometer 2 for: (a) true longitudinal view, (b) cross section after undercutting, (c) plan section prior to undercutting, (d) plan section after undercutting, and (e) a plot of strain over time for the reliable anchor segments.

Estimation of Pre-Mining Stress

The dataset for the Mount Isa Mine 5FP1 stope contained both blast dates and which blast undercut each extensometer. These details have been summarized in Table D-2.

The dataset for the 5FP1 stope contained a small number of manual readings taken following each stope blast. By comparing successive measurements, the change in strain due to each stope blast could be estimated. The strain changes in each anchor segment are summarized in Table D-2. By applying Equation 3-6, and using an Elastic modulus of 25 GPa and a Poisson's ratio of 0.25 (Milne, 1997), the measured changes in strain were used to calculate the pre-mining stress in each anchor segment as summarized in Table D-2. Results associated with anchors not believed to be fully relaxed are coloured yellow. A sample calculation for Anchor Segment 1-2 of Extensometer 1 is shown below.

$$\sigma_{pre-mining} \cong -\frac{\Delta\varepsilon\, E}{(1-\upsilon)} \cong -\frac{(-820\mu\varepsilon)(25\ GPa)}{\big(1-(0.25)\big)} \cong 25\ MPa$$

The closest reliable anchor segment for extensometer 1, as described in Section 0, is anchor segment 1-3. the ERF of this anchor segment is larger than the distance from the anchors to the opening, suggesting that this anchor segment has relaxed fully (Section 3.2.4). The estimated pre-mining stress for this anchor segment (25 MPa) is approximately 60% of the 40 MPa stress modelled by MIM (1993).

None of the reliable extensometer 2 anchor segments were considered fully relaxed since the ERF of the anchor segment was smaller than the distance from the hanging wall to at least one of the anchors. The assessment of incomplete stress relaxation appears to be supported by the estimated stress of 20 MPa for extensometer 2 anchor segment 1-3, which was closest to the opening, being smaller than the estimated stress from the fully relaxed extensometer 1 anchor segment 1-3.

Using Equation 3-6, an Elastic modulus of 25 GPa, and Poisson's ratio of 0.25, a difference in stress of 15 MPa between the predicted and modelled stress is associated with a displacement of approximately 1.0 millimetres over the 2.2 metre anchor segment length. The variation in stress could between the modelled 40 MPa and estimated 25 MPa normal stress could be a result of uncertainty in the accuracy of the manual measurements, although measurements were reported to

0.01 millimetres, and/ or the Elastic modulus selected for modelling. An estimate of the pre-mining stress based on the depth and regional K-ratio could not be made due to a lack of information about the stope location. As a result, it is uncertain which of the estimates of pre-mining stress is more reasonable.

Table D-2: Summary of the stress and strain change following undercutting for each extensometer segment in the Mount Isa 5FP1 stope hanging wall.

Anchor Segment	Anchor Segment length (m)	Perpendicular distance to hanging wall (m)	ERF (m)	Strain change due to blast (με)	Calculated Pre-mining stress (MPa)
Extensometer 1-	Undercut by Blast 1 on 11-Mar-1993				
1-2	2.2	0.5-2.5	7.2	-820	25
2-3					
3-4	1.3	2.5-3.5	7.1	-680	25
4-5	4.5	3.5-7.5	7.1	-1,170	40
5-6	13	7.5-18.0	6.9	-140	5
Extensometer 2-	Undercut by Blast 3 on 25-Mar-1993				
1-2	2.2	0.5-2.5	2.0	-550	20
2-3					
3-4	1.3	2.5-3.5	2.0	-950	30
4-5	4.5	3.5-7.5	2.0	-850	30
5-6	13	7.5-18.0	2.0	-120	5

*yellow highlight- not fully relaxed (ERF< distance to hanging wall)
*red highlight- unreliable anchor segment

Summary of 5FP1 analysis

Although the estimate of pre-mining stress using extensometer strains was smaller than the modelled pre-mining stress by Milne (1997), the results were within 60% of one another. Minor changes to the model inputs or an increase in the measured strain would be enough make up the difference between the two estimates of pre-mining stress.

Backfilling of the 5FP1 stope limited the unsupported geometry of the hanging wall during extraction of the stope and contributed to the observed stability. The small number of stope blasts also meant that a transition to non-linear extension could not be confirmed, and the modified SERF method could not be applied.

5HP1

The 5HP1 stope was located in the same area as the 5FP1 stope (Figure D-3). The 5HP1 stope was mined following the completion of the 5FP1 stope, which positioned it in the stress shadow of the 5FP1 stope.

A schematic showing the plan and section view for the instrumented portion of the 5HP1 stope is show in Figure D-9. A pillar was left at the approximate mid point of the stope, beside a second slot raise. This pillar, and the subsequent backfilling of the first half of the stope served to break up the open geometry of the stope hanging wall and is not shown (Milne, 1994). Excavation of the instrumented portion of the 5HP1 stope cut off access to the extensometers before excavation of the stope was fully completed. The last available extensometer measurements were recorded when the stope dimensions were 55 metres up dip and 53 metres along strike (Milne, 1997), although the final stope geometry, after ring 38 was blasted, was approximately 85 metres along strike (Milne, 1994). The 5HP1 stope used the same ground support measures as the 5FP1 stope.

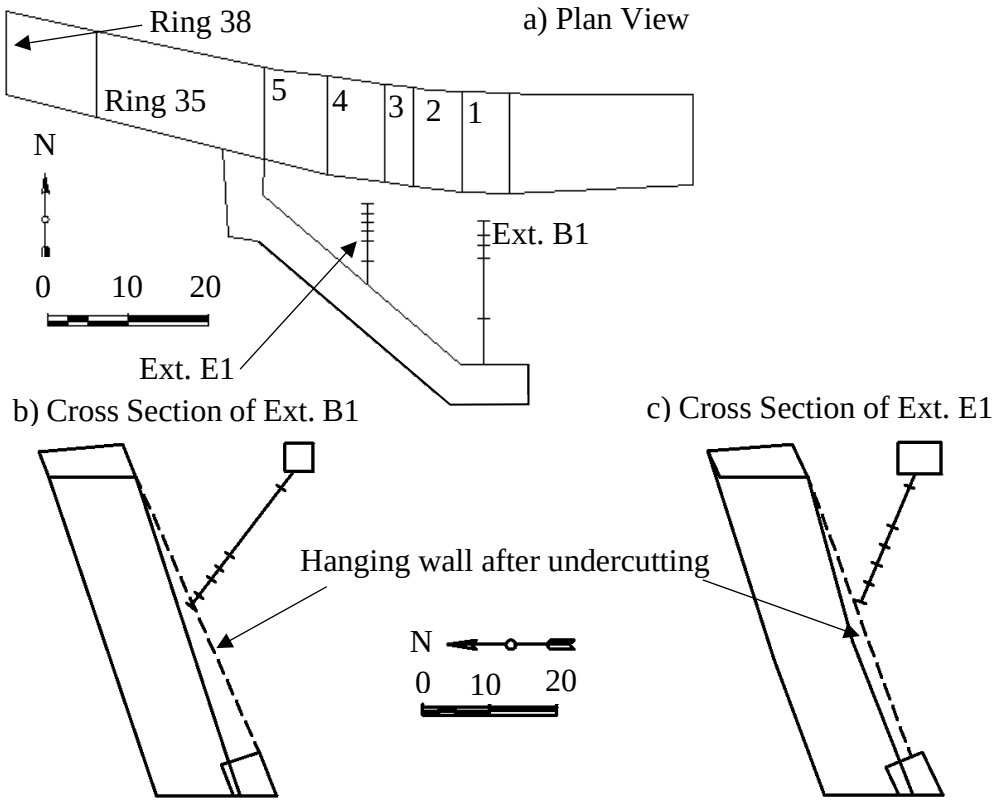

Figure D-9: Section views of the Mount Isa 5HP1 stope showing the extensometer location and the stope excavation sequence in (a) plan view, (b) cross section of extensometer B1, and (c) cross section of extensometer E1 (after Milne, 1994).

Instrumentation program design

The instrumentation dataset for the 5HP1 stope at Mount Isa Mine included two extensometers. The distances between extensometer anchors are summarized in Table D-3 and a schematic of the anchor positions relative to the stope and drillhole collar are shown in Figure D-10.

Table D-3: Extensometer layout for extensometers installed in the Mount Isa Mine 5HP1 Stope hanging wall.

Instrument	Distance between anchors (m)					
	1-2	2-3	3-4	4-5	5-6	6-Head
Extensometer B1	2.0	3.0	2.0	2.5	12.5	3.0
Extensometer E1	3.0	3.0	3.0	3.0	6.5	2.0

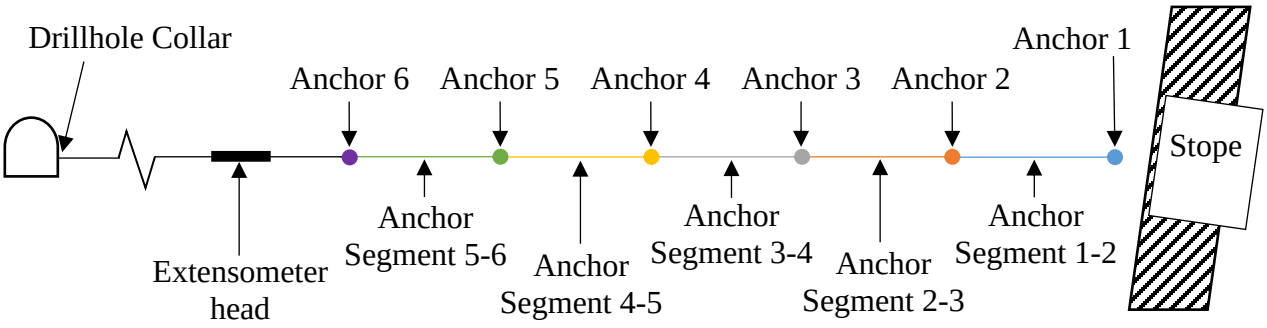

Figure D-10: Schematic showing the anchor positions relative to the stope and the drillhole collar.

Stope mining

Mining of the instrumented portion of the5HP1 bench stope at Mount Isa Mine was completed with five production blasts, progressed from South to North, (Figure D-9a) before access to the hanging wall instrumentation drift was cut off. As a result, extensometer data is only available from 6-April, 1993 until 13-May, 1993 (Milne, 1994; Milne, 1997). Additional measurements were collected in October 1993, after the stope had been backfilled, however, these are not considered since the measured deformation could not be related to a change in blast geometry (Milne, 1994). For simplicity, the blast numbers discussed in this section are not the overall stope blast number, but rather are related to the blasting sequence of the five blasts for which extensometer measurements were collected.

After access to the hanging wall instrumentation drift was cut off, there were challenges with hanging wall stability. Following blasting up to ring 35, on 23-May, 1993, sloughing was reported along a fault. Prior to this, the last survey of a stable hanging wall was conducted following blasting up to ring 27, by blast 4, on 9-May, 1993. Additional sloughing occurred following the last stope blast took rings 36 to 38 on 25-May, 1993 (Milne, 1994).

Ground Response to Mining

The 5HP1 stope is located within the stress shadow of the 5FP1 stope detailed in Section 0. Milne (1997) estimated that the stress shadow resulted in a decrease in the stress normal to the hanging wall to approximately 15 MPa. As mining approaches the instrument location, a maximum stress increase of up to approximately 45 MPa, approximately three times the initial stress normal to the hanging wall, could be expected (Section 3.1) which is associated with a strain of approximately 1,800 microstrain for the Mount Isa rock mass (25 GPa).

Applying Equation 3-7, the estimated upper bound to elastic deformation in the hanging wall adjacent and normal to the stope, due to hanging wall stress relaxation following undercutting by stope mining, is estimated to be approximately 450 microstrain of tension. Assuming a one metre anchor segment length, this strain would be associated with a deformation of approximately 0.5 millimetres.

$$\varepsilon_{(a-b)} = \frac{\Delta\sigma_n}{E}(1-\upsilon) = \frac{0-15MPa}{25GPa}(1-0.25) \cong -450\mu\varepsilon$$

EXTENSOMETER B1

The data from extensometer B1 was collected manually and recorded to the nearest 0.01 millimetre (Milne, 1994). A plot of the strain over time for extensometer B1 is shown in Figure D-11.

Figure D-12 shows plan, cross section, and long section views of the stope and extensometer, before and after being undercut by blast 1. Figure D-12b includes a schematic of areas of expected stress concentration and relaxation, for stresses generally perpendicular to the ore zone. Following blast 1, no additional measurements could be collected from anchor 1 and the hanging wall was anticipated to be located approximately one metre from anchor 2 (Milne, 1994).

Figure D-11 shows the full range of recorded strain for extensometer B1. Following undercutting, anchor segments 2-3 and 3-4 are showing a mirrored suggesting a problem with anchor 2. Figure D-12e shows a revised plot of strain over time with the measurements taken over anchor segment 2-4 to provide a reliable value for the closest reliable anchor segment to the stope hanging wall.

The plot of reliable segment strain over time for extensometer B1 (Figure D-12e) shows a series of increasing strain measurements following undercutting. Based on the estimated upper bound to elastic deformation, it appears that a transition to non-linear extension may occur as a result of blast 3 meaning that the extensometer B1 dataset appears suitable for analysis using the modified SERF method.

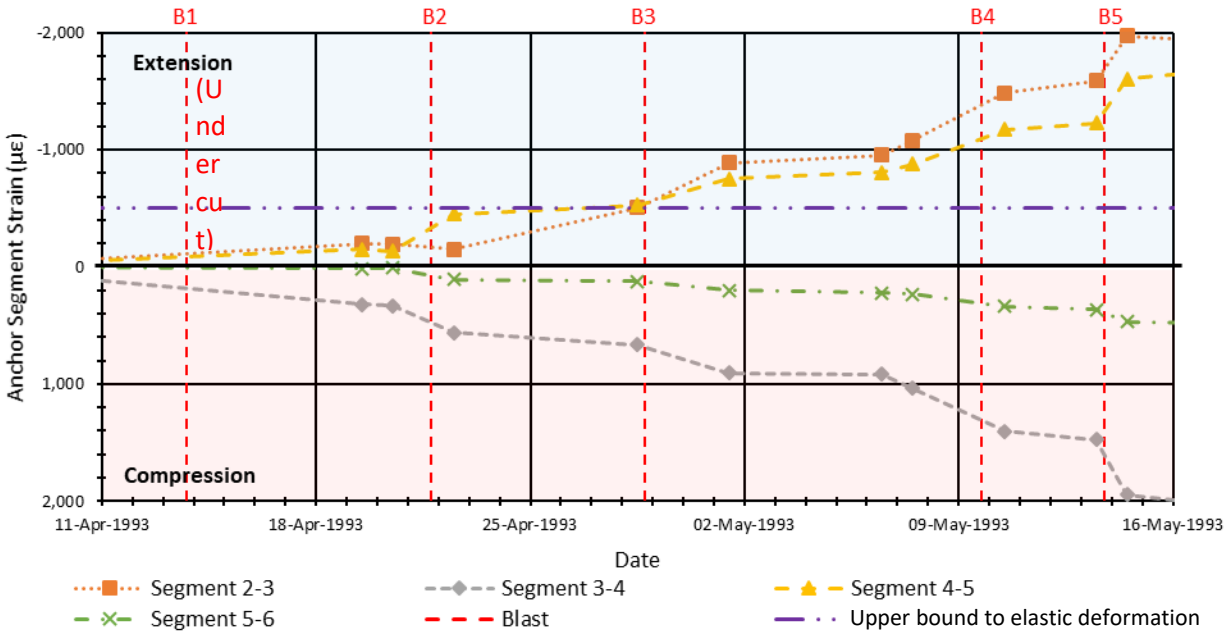

Figure D-11: Segment strains in Mount Isa Mine 5HP1 stope by extensometer B1.

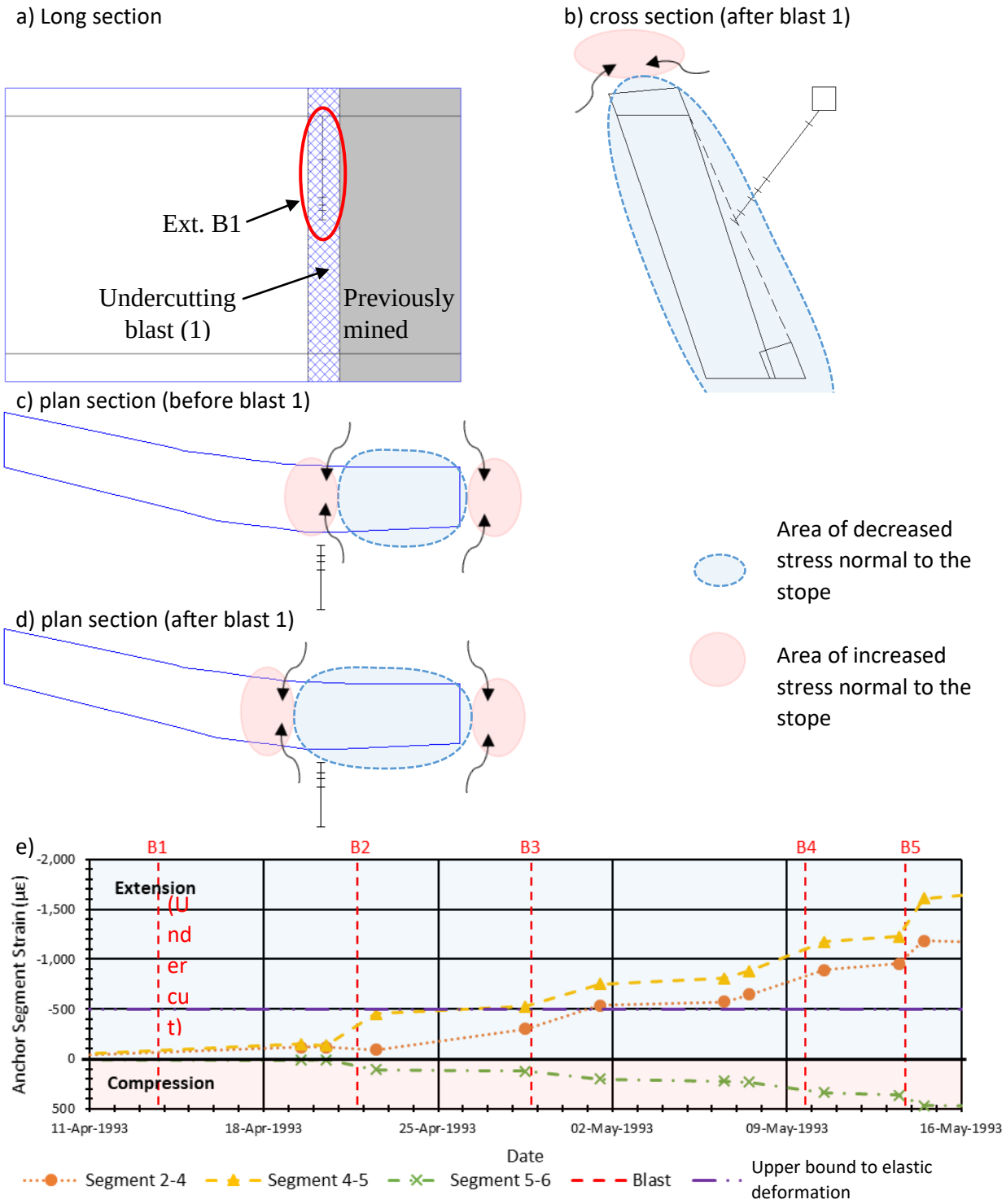

Figure D-12: Section views of the Mount Isa Mine 5HP1 bench stope showing blast geometries, excavation geometries, expected zones of stress change, and the location of extensometer B1 for: (a) true longitudinal view, (b) cross section after undercutting, (c) plan section prior to undercutting, (d) plan section after undercutting, and (e) a plot of strain over time for the reliable anchor segments.

EXTENSOMETER E1

The data from extensometer E1 was collected manually and recorded to the nearest 0.1 millimetre (Milne, 1997). A plot of the strain over time for extensometer E1 is shown in Figure D-13.

Figure D-14 shows plan, cross section, and long section views of the stope and extensometer, before and after being undercut by blast 4. Figure D-14b also includes a schematic of areas of expected concentration and relaxation, for stresses generally perpendicular to the ore zone.

Figure D-13 shows the full range of recorded strain for extensometer E1. Following undercutting, anchor segments 1-2 shows an increasing, non-linear, tensile strain measurements as expected. The remaining anchor segments do not measure any notable strain until after the final stope blast for which the response of anchor segments 2-3 and 3-4 appear to be mirrored. Review of the deformation data shows anchor 3 is slipping relative to the larger displacements measured by anchors 2 and 4, which have similar magnitudes.

The plot of segment strain over time for extensometer E1 (Figure D-14e) shows increasing strain measurements following undercutting in anchor segment 1-2. The strain exceeds the estimated upper bound to elastic deformation following apparent undercutting by blast 4, suggesting a transition to non-linear extension. As a result, the dataset for extensometer E1 appears suitable for analysis using the modified SERF method, although ideally there would be additional stope blasts to establish a trend.

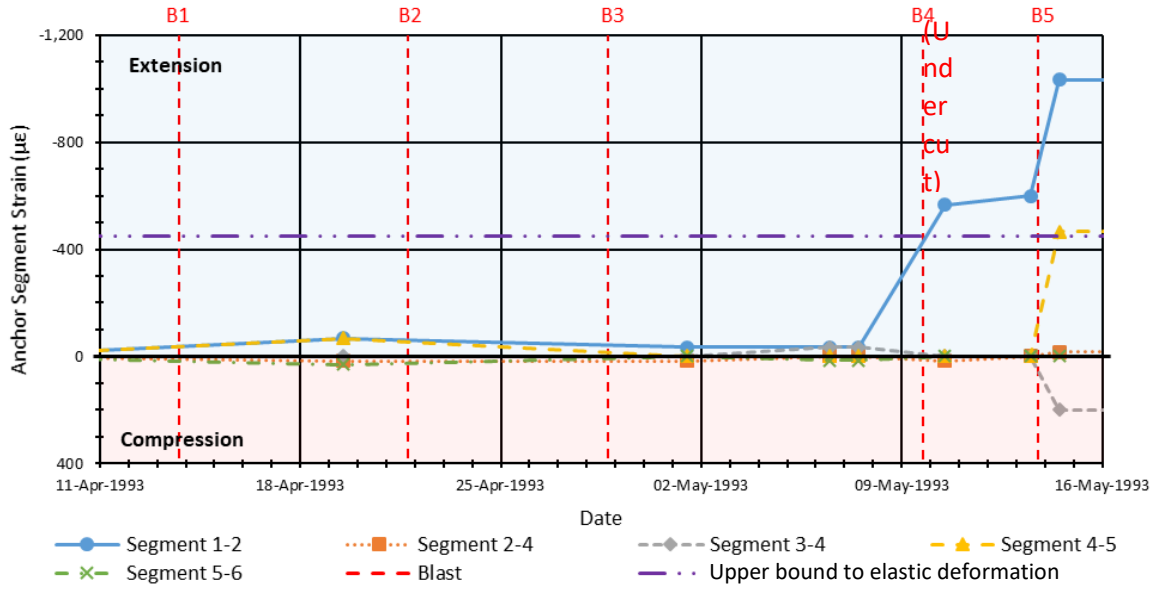

Figure D-13: Segment strains in Mount Isa Mine 5HP1 stope by extensometer E1.

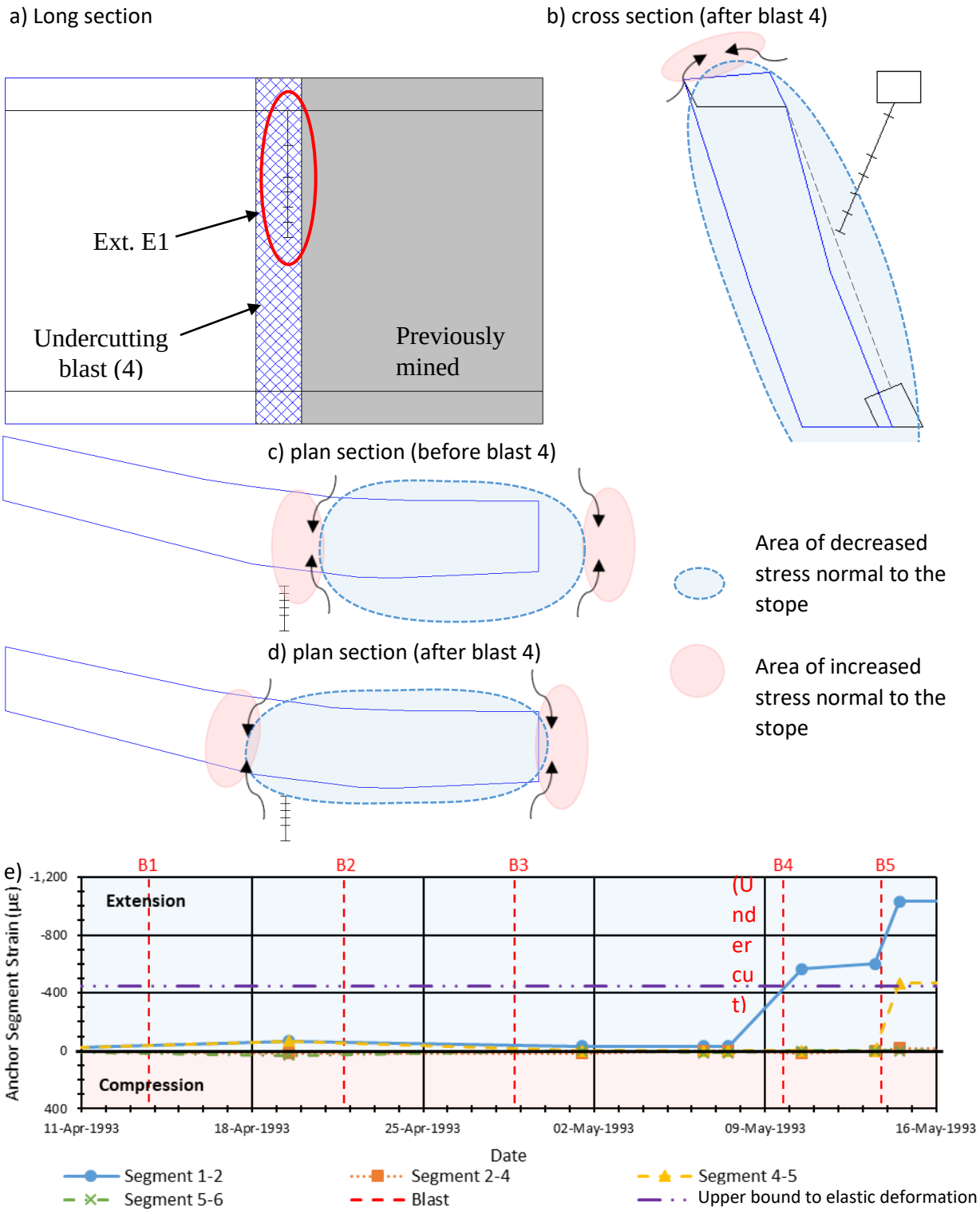

Figure D-14: Section views of the Mount Isa Mine 5HP1 bench stope showing blast geometries, excavation geometries, expected zones of stress change, and the location of extensometer E1 for: (a) true longitudinal view, (b) cross section after undercutting, (c) plan section prior to undercutting, (d) plan section after undercutting, and (e) a plot of strain over time for the reliable anchor segments.

Estimation of Pre-Mining Stress

The dataset for the Mount Isa Mine 5HP1 stope contained both blast dates and which blast undercut each extensometer. These details have been summarized in Table D-4.

The dataset for the 5HP1 stope contained a small number of manual readings taken following each stope blast. By comparing successive measurements, the change in strain due to each stope blast could be estimated. The strain changes in each anchor segment are summarized in Table D-4. By applying Equation 3-6, and using an Elastic modulus of 25 GPa and a Poisson's ratio of 0.25 (Milne, 1997) the measured changes in strain after undercutting were used to calculate the pre-mining stress in each anchor segment, as summarized in Table D-4. Results associated with anchors no believed to be fully relaxed are coloured yellow. A sample calculation for Anchor Segment 2-4 of Extensometer B1 is shown below.

$$\sigma_{pre-mining} \cong -\frac{\Delta\varepsilon\, E}{(1-\upsilon)} \cong -\frac{(-120\mu\varepsilon)(25\ GPa)}{\big(1-(0.25)\big)} \cong 5\ MPa$$

For the closest reliable anchor segment for extensometer B1, as described in Section 0, the ERF was smaller than the distance of at least one of the anchors to the opening, suggesting that this anchor segment was not fully relaxed (Section 3.2.4). This is supported by the estimated pre-mining stress for this anchor segment (5 MPa) being approximately one third of the 15 MPa indicated by MIM (1993).

For the closest reliable anchor segment for extensometer E1, the ERF is larger than the distance from the anchors to the opening, suggesting that his anchor segment has relaxed fully. The estimated pre-mining stress for this anchor segment (20 MPa) is approximately 20% larger than the 15 MPa indicated.

Considering the pre-mining stress estimate associated with the fully relaxed measurement from extensometer E1, by using Equation 3-6, an Elastic modulus of 25 GPa, and Poisson's ratio of 0.25, the difference in stress between the predicted and modelled stress is associated with a displacement of approximately 0.5 millimetres over the 3.0 metre anchor segment length. This could be a result of uncertainty in the accuracy of the manual measurement, which were recorded to the nearest 0.1 millimetre, and/ or the deterioration of the Elastic modulus used for the pre-mining stress estimate due to mining activity.

Table D-4: Summary of the stress and strain change following undercutting for each extensometer segment in the 5HP1 stope hanging wall.

Anchor Segment	Anchor Segment length (m)	Perpendicular distance to hanging wall (m)	ERF (m)	Strain change due to blast (με)	Calculated Pre-mining stress (MPa)
Extensometer B1-	Undercut by Blast 1 on 13-Apr-1993				
1-2	2.0	Lost following Blast 1			
2-3	5.0	1.0-5.0	3.7	-120	20
3-4					
4-5	2.5	5.0-7.0	3.7	-150	5
5-6	12.5	7.0-17.5	3.6	10	0
Extensometer E1-	Undercut by Blast 4 on 9-May-1993				
1-2	3.0	1.0-2.5	6.4	-530	18
2-3	6.0	2.5-7.0	6.4	0	0
3-4					
4-5	3.0	7.0-9.0	6.3	-50	2
5-6	6.5	9.0-19.0	6.2	30	-1

*yellow highlight- not fully relaxed (ERF< distance to hanging wall)
*red highlight- unreliable anchor segment

Modified SERF Method

Two failure events were noted during mining of the 5HP1 bench stope at Mount Isa Mine. The first was a spalling failure which was observed following the blasting of ring 35 when the hanging wall had a RF of approximately 17.4 m, although the spalling may have initiated earlier. The second, more significant spalling failure estimated to extend over 10 metres from the original hanging wall location, was observed following the blasting of rings 36 to 38 when the hanging wall had a RF of approximately 18.2 m.

Due to issues with data reliability, the closest anchor segment on extensometer B1 to the opening was anchor segment 2-4. Applying the modified SERF method to the data following the transition to non-linear extension results in a predicted RF of instability (RF_p) of approximately 19 for anchor segment 4-5 (between five and seven metres from the stope hanging wall) (Figure D-15). Although the predicted geometry of instability is larger than both the RF of spalling and the RF of failure (RF_f), it is expected that an improved failure prediction would have been obtained with more data, closer to the point of instability. The presence of the fault, along which sloughing occurred, may have also contributed to the RF_f being smaller than the RF_p.

Similarly, applying the modified SERF method to the data from extensometer E1 results in a RF_p of approximately 19 (Figure D-16). This prediction is for anchor segment 1-2, which is closer to the opening than anchor segment 3-4 on extensometer B1. The predicted RF_p is based on two data points and it is expected that the inclusion of additional data points from subsequent blasts, as the geometry of instability was approached, would have resulted in an increase in the slope of the trend line and a decrease in the RF_p.

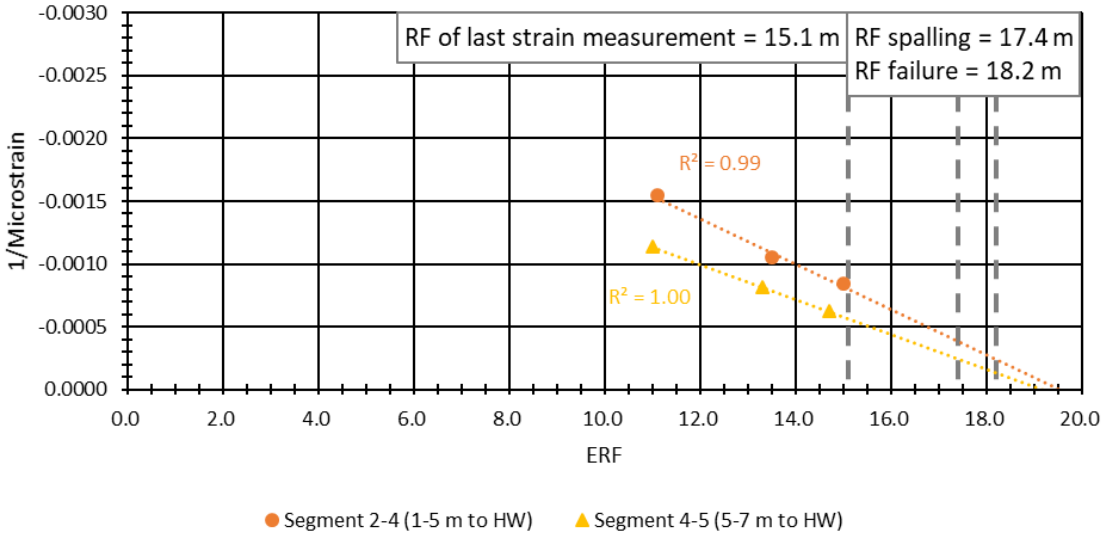

Figure D-15: Analysis of measurements by extensometer B1 of the 5HP1 stope at Mount Isa Mine using the modified SERF method.

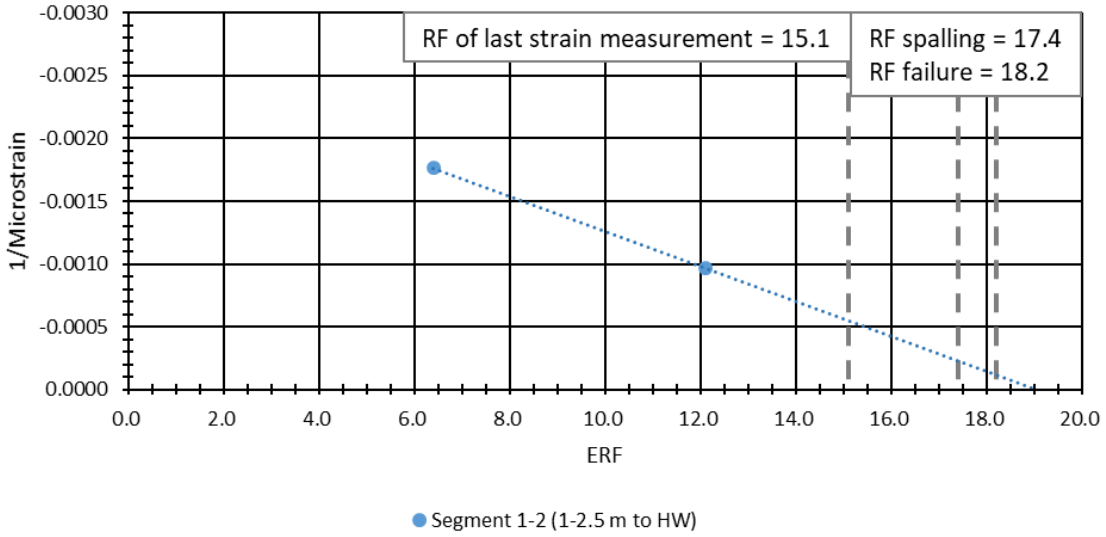

Figure D-16: Analysis of measurements by extensometer E1 of the 5HP1 stope at Mount Isa Mine using the modified SERF method.

Summary of 5HP1 analysis

Ideally, the estimates of pre-mining stress using extensometer measurements would be compared to measured stresses rather than modelled stresses. The estimates of the pre-mining stress using extensometer measurements appear to reasonably approximate stresses modelled by Milne (1997). The differences in values can be associated with incomplete relaxation of the anchor segment, potential measurement errors, and variability between the selected Elastic modulus and actual rock mass behaviour.

The loss of access to the hanging wall instrumentation drift during stope mining limited the effectiveness of the modified SERF method as measurements leading up to the reported instability could not be considered. Despite this limitation, the modified SERF method appears to provide a reasonable prediction of approaching instability in advance of hanging wall sloughing. It is also seen as a favourable result that both extensometers independently predict a similar RF_p, however, it should be noted that the depth of predicted instability is different for both extensometers. It is also unknown if both extensometers would continue to predict the same RFp as mining continued.

Summary of Mount Isa Results

The use of extensometers to estimate the pre-mining stress as stopes are excavated shows promise as reasonable results were obtained for several extensometers, after unreliable data was discounted.

The 5HP1 bench stope produces an unconservative prediction of stope hanging wall instability based on a limited dataset. It is expected that if a full dataset, including the blasts closer to actual instability the result would improve.

APPENDIX E SUMMARY OF SANTOY MINE LABORATORY TEST RESULTS

Table E-1: Acoustic velocity testing results for hanging wall rock types.

Rock Type	Sample	P-wave velocity (km/sec.)	S-wave velocity (km/sec.)	Young's Modulus Dynamic (GPa)	Poisson's Ratio Dynamic
Diorite	SUG-2-1-B	4.36	2.50	47	0.21
Diorite	SUG-2-2-A	5.37	3.31	73	0.19
Diorite	SUG-2-3-A	4.34	2.56	47	0.23
Diorite	SUG-2-3-B	4.50	2.73	53	0.21
Mafic Volcanic	SUG-1-1-A	4.93	2.87	58	0.24
Mafic Volcanic	SUG-1-2-A	4.26	2.82	53	0.11
Mafic Volcanic	SUG-1-4-A	6.11	3.63	96	0.18
Mafic Volcanic	SUG-3-4-A	5.72	3.60	90	0.17
Mafic Volcanic	SUG-4-1-A	4.43	3.06	59	0.04
Mafic Volcanic	SUG-4-1-B	4.65	2.87	60	0.15
Mafic Volcanic	SUG-4-4-A	5.30	3.13	71	0.23
Mafic Volcanic	SUG-4-4-B	4.76	3.11	63	0.12
Mafic Volcanic	SUG-5-1-A	3.85	2.46	42	0.16
Mafic Volcanic	SUG-5-1-B	3.73	2.56	41	0.05
Mafic Volcanic	SUG-5-2-A	3.35	2.33	34	0.03
Mafic Volcanic	SUG-5-2-B	4.67	2.56	50	0.23
Mafic Volcanic	SUG-7-1-A	4.31	2.58	49	0.17
Mafic Volcanic	SUG-7-1-B	4.23	2.76	52	0.13
Mafic Volcanic	SUG-7-3-A	4.78	3.28	68	0.05
Mafic Volcanic	SUG-8-1-A	5.68	3.49	87	0.20
Mafic Volcanic	SUG-8-1-B	6.00	3.71	98	0.15
Mafic Volcanic	SUG-8-2-A	5.04	3.41	75	0.08
Mafic Volcanic	SUG-8-2-B	5.48	3.55	87	0.14
Mafic Volcanic	SUG-8-4-A	6.25	3.85	107	0.19
Mafic Volcanic	SUG-9-3-A	6.43	3.86	105	0.22
Mafic Volcanic	SUG-9-3-B	6.55	3.74	102	0.26

Table E-2: Acoustic velocity testing results for ore rock types.

Rock Type	Sample	P-wave velocity (km/sec.)	S-wave velocity (km/sec.)	Young's Modulus Dynamic (GPa)	Poisson's Ratio Dynamic
Altered Mafic Volcanic	SUG-6-5-A	5.32	3.37	80	0.16
Altered Mafic Volcanic with Diopside	SUG-5-5-A	4.00	2.63	47	0.12
Altered Mafic Volcanic with Diopside	SUG-5-5-B	4.73	3.03	63	0.15
Diorite	SUG-1-5-A	5.39	3.32	70	0.19
Diorite	SUG-2-5-A	5.38	3.23	68	0.22
Diorite	SUG-2-5-B	5.08	3.19	64	0.17
Diorite	SUG-3-5-A	5.43	3.32	70	0.20
Diorite	SUG-9-5-A	5.52	3.32	71	0.22
Diorite	SUG-9-5-B	5.70	3.39	75	0.23
Mafic Volcanic	SUG-10-5-A	5.13	3.38	77	0.12
Mafic Volcanic	SUG-10-5-B	5.90	3.74	100	0.16
Quartz Vein	SUG-7-5-E	5.64	3.21	69	0.21
Quartz Vein	SUG-8-5-A	5.80	3.83	86	0.08
Quartz Vein	SUG-8-5-B	5.71	3.69	82	0.14
Silicified Diorite	SUG-4-5-A	5.46	3.31	70	0.21
Silicified Diorite	SUG-4-5-B	5.51	3.35	72	0.21

Table E-3: Brazilian testing results for hanging wall rock types.

Rock Type	Sample	Brazilian (parallel) (MPa)	Brazilian (perpendicular) (MPa)
Mafic Volcanic	SUG-1-4-C	12	
Mafic Volcanic	SUG-3-3-E	17	
Mafic Volcanic	SUG-4-1-F	14	
Mafic Volcanic	SUG-7-3-C	15	
Mafic Volcanic	SUG-8-2-C	13	
Mafic Volcanic	SUG-8-4-C	13	
Mafic Volcanic	SUG-9-3-D	21	
Diorite	SUG-2-2-D		16
Diorite	SUG-2-3-E		10
Mafic Volcanic	SUG-1-2-D		10
Mafic Volcanic	SUG-4-1-E		15
Mafic Volcanic	SUG-7-3-B		12
Mafic Volcanic	SUG-8-4-B		19
Mafic Volcanic	SUG-8-4-D		11

Table E-4: Brazilian testing results for ore rock types.

Rock Type	Sample	Brazilian (parallel) (MPa)	Brazilian (perpendicular) (MPa)
Altered Mafic Volcanic	SUG-6-5-G	17	
Altered Mafic Volcanic with Diopside	SUG-5-5-D	11	
Diorite	SUG-2-5-C	13	
Diorite	SUG-3-5-E	19	
Mafic Volcanic	SUG-10-5-D	12	
Altered Mafic Volcanic	SUG-6-5-F		12
Diorite	SUG-1-5-E		11
Diorite	SUG-3-5-D		21
Quartz Vein	SUG-7-5-D		16
Silicified Diorite	SUG-4-5-D		21

Table E-5: Direct shear testing results for hanging wall rock types.

Rock Type	Sample	Direct Shear (MPa)
Altered Mafic Volcanic with Diopside	SUG-7-4-A1	44
Diorite	SUG-2-1-A	38
Diorite	SUG-2-4-A	30
Diorite	SUG-2-4-Aa	23
Mafic Volcanic	SUG-3-2-A	36
Mafic Volcanic	SUG-3-2-Aa	29
Mafic Volcanic	SUG-3-3-D	18
Mafic Volcanic	SUG-5-3-A1	33
Mafic Volcanic	SUG-6-1-A1	35
Mafic Volcanic	SUG-6-3-A1	33
Mafic Volcanic	SUG-8-3-A1	37
Mafic Volcanic	SUG-9-4-A1	36
Mafic Volcanic	SUG-10-1-A1	37

Table E-6: Corrected Point Load testing results for hanging wall rock types.

Rock Type	Sample	Corrected Point Load Is(50) (MPa)	K Conversion Factor	UCS (MPa)
Diorite	SUG-2-1-C	9	8	73
Diorite	SUG-2-2-B	8	8	66
Diorite	SUG-2-2-C	8	8	68
Diorite	SUG-2-3-C	5	8	42
Diorite	SUG-2-3-D	6	8	51
Mafic Volcanic	SUG-1-1-B	6	8	45
Mafic Volcanic	SUG-1-1-C	6	8	46
Mafic Volcanic	SUG-1-1-D	5	8	41
Mafic Volcanic	SUG-1-2-B	5	8	44
Mafic Volcanic	SUG-1-2-C	6	8	46
Mafic Volcanic	SUG-1-4-B	8	8	64
Mafic Volcanic	SUG-3-3-A	7	8	58
Mafic Volcanic	SUG-3-3-B	9	8	69
Mafic Volcanic	SUG-3-3-C	6	8	47
Mafic Volcanic	SUG-3-4-B	10	8	79
Mafic Volcanic	SUG-3-4-C	7	8	60
Mafic Volcanic	SUG-3-4-D	8	8	63
Mafic Volcanic	SUG-4-1-C	9	8	73
Mafic Volcanic	SUG-4-1-D	8	8	60
Mafic Volcanic	SUG-5-1-C	7	8	54
Mafic Volcanic	SUG-5-2-C	6	8	51
Mafic Volcanic	SUG-7-1-C	4	8	31
Mafic Volcanic	SUG-7-1-D	6	8	44
Mafic Volcanic	SUG-9-3-C	8	8	62

Table E-7: Corrected Point Load testing results for ore rock types.

Rock Type	Sample	Corrected Point Load Is(50) (MPa)	K Conversion Factor	UCS (MPa)
Altered Mafic Volcanic	SUG-6-5-B	7	8	56
Altered Mafic Volcanic	SUG-6-5-C	7	8	58
Altered Mafic Volcanic	SUG-6-5-D	7	8	57
Altered Mafic Volcanic	SUG-6-5-E	7	8	55
Altered Mafic Volcanic with Diopside	SUG-5-5-C	7	8	52
Diorite	SUG-1-5-B	3	8	27
Diorite	SUG-1-5-C	2	8	20
Diorite	SUG-1-5-D	1	8	7
Diorite	SUG-3-5-B	8	8	68
Diorite	SUG-3-5-C	8	8	66
Mafic Volcanic	SUG-10-5-C	7	8	54
Quartz Vein	SUG-7-5-A	8	8	62
Quartz Vein	SUG-7-5-B	7	8	58
Quartz Vein	SUG-7-5-C	8	8	66
Quartz Vein	SUG-8-5-C	3	8	26
Silicified Diorite	SUG-4-5-C	10	8	81

Table E-8: Unconfined Compressive Strength testing results for hanging wall rock types.

Rock Type	Sample	UCS (MPa)	Youngs Modulus Static (MPa)	Poisson's Ratio Static
Diorite	SUG-2-1-B	124	n/a	n/a
Diorite	SUG-2-3-B	90	90	0.23
Mafic Volcanic	SUG-1-1-A	139	57	0.32
Mafic Volcanic	SUG-1-4-A	150	n/a	n/a
Mafic Volcanic	SUG-3-4-A	180	81	0.38
Mafic Volcanic	SUG-4-1-B	125	n/a	n/a
Mafic Volcanic	SUG-4-4-A	98	73	0.23
Mafic Volcanic	SUG-5-2-A	209	66	0.47
Mafic Volcanic	SUG-5-2-B	231	n/a	n/a
Mafic Volcanic	SUG-7-1-A	167	n/a	n/a
Mafic Volcanic	SUG-7-3-A	89	55	n/a
Mafic Volcanic	SUG-8-1-A	144	90	0.27
Mafic Volcanic	SUG-8-1-B	125	n/a	n/a
Mafic Volcanic	SUG-9-3-A	141	91	0.28

Table E-9: Unconfined Compressive Strength testing results for ore rock types.

Rock Type	Sample	UCS (MPa)	Youngs Modulus Static (MPa)	Poisson's Ratio Static
Altered Mafic Volcanic with Diopside	SUG-5-5-A	129	57	0.33
Diorite	SUG-1-5-A	170	72	0.26
Diorite	SUG-2-5-A	94	76	0.23
Diorite	SUG-9-5-B	145	80	0.28
Quartz Vein	SUG-7-5-E	128	n/a	n/a
Quartz Vein	SUG-8-5-A	230	n/a	n/a
Silicified Diorite	SUG-4-5-A	175	70	0.31

Table E-10: Triaxial testing results for hanging wall rock types.

Rock Type	Sample	Confining Stress (MPa)	Strength (MPa)	Youngs Modulus Static (MPa)	Poisson's Ratio Static
Diorite	SUG-2-2-A	5	220	82	0.21
Diorite	SUG-2-3-A	1	139	48	0.12
Mafic Volcanic	SUG-1-2-A	3	99	51	0.23
Mafic Volcanic	SUG-4-1-A	7	339	86	0.31
Mafic Volcanic	SUG-4-4-B	5	247	78	0.24
Mafic Volcanic	SUG-5-1-A	3	331	75	0.46
Mafic Volcanic	SUG-5-1-B	1	297	85	0.27
Mafic Volcanic	SUG-7-1-B	5	238	75	0.42
Mafic Volcanic	SUG-8-2-A	1	234	89	0.36
Mafic Volcanic	SUG-8-2-B	3	253	95	0.48
Mafic Volcanic	SUG-8-4-A	5	248	100	0.36
Mafic Volcanic	SUG-9-3-B	5	211	80	0.26

Table E-11: Triaxial testing results for ore rock types.

Rock Type	Sample	Confining Stress (MPa)	Strength (MPa)	Youngs Modulus Static (MPa)	Poisson's Ratio Static
Altered Mafic Volcanic	SUG-6-5-A	5	231	72	0.24
Altered Mafic Volcanic with Diopside	SUG-5-5-B	1	227	n/a	n/a
Diorite	SUG-2-5-B	3	272	71	0.27
Diorite	SUG-3-5-A	1	148	71	0.22
Diorite	SUG-9-5-A	5	211	79	0.39
Mafic Volcanic	SUG-10-5-A	3	92	64	0.48
Mafic Volcanic	SUG-10-5-B	7	167	82	0.24
Quartz Vein	SUG-8-5-B	1	249	93	0.08
Silicified Diorite	SUG-4-5-B	3	289	74	0.27

APPENDIX F SEABEE GOLD OPERATION EXTENSOMETER INSTALLATION PROGRAM

Seabee Gold Operation's Santoy 24L 411 Alimak Stope

Due to scheduling and communication challenges, the initial instrumentation holes drilled for the Santoy 24L 411 Alimak stope from the 17L access drift were drilled in the wrong direction. The re-drilled holes also deviated from the planned orientation but could be used. Prior to the installation of extensometers in the new drill holes, the holes from the 17L access drift were logged with a borehole camera to confirm the location of the hanging wall contact. Although the quartz veining was easily identified by the borehole camera (Figure F-1), it was not possible to locate the contact in the partially water/mud filled hole (Figure F-2).

The second instrumentation hole was full of the same opaque water as the first instrumentation hole. Based on the borehole camera results from the first instrumentation hole, no attempt was made to locate the hanging wall contact in the second water filled instrumentation hole. Since the depth of the hanging wall contact could not be determined with the borehole camera, the installation depth was determined from the orebody model and the actual instrumentation hole orientation at the instrumentation hole collar. Using the revised installation depths, the two extensometers were inserted into the instrumentation holes and grouted in place. Once the grouting was completed a board was placed along the 17L access drift to make the instrumentation hole collars more obvious and reduce the risk of vehicle damage (Figure F-3).

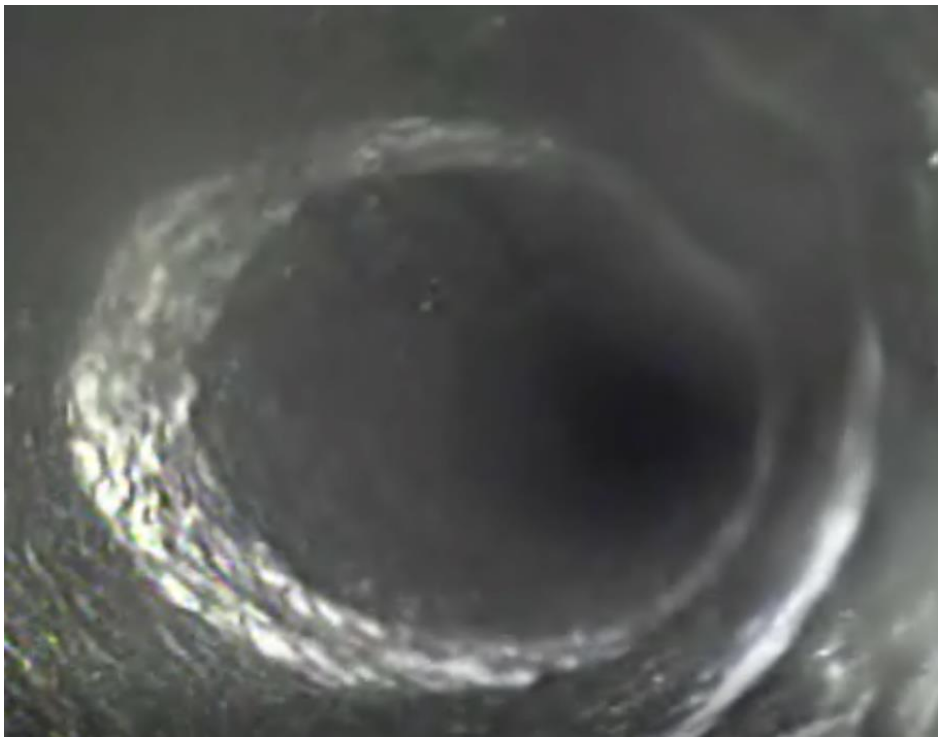

Figure F-1:Borehole camera image showing quartz veining in the hanging wall of the Alimak panel.

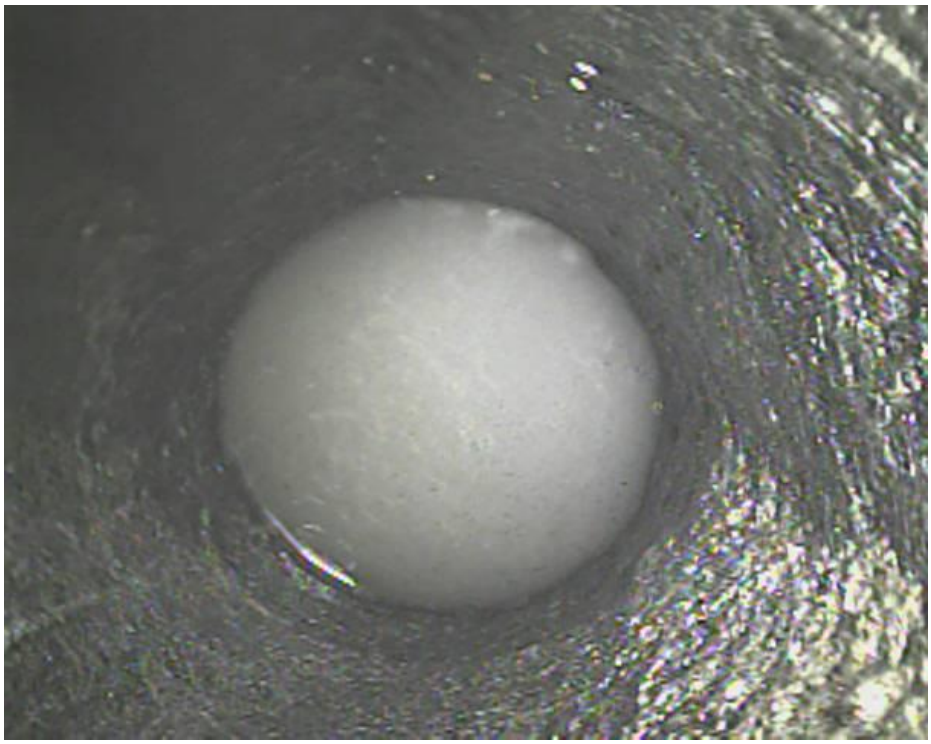

Figure F-2: Borehole camera image of the opaque water below a depth of 22.3 m.

Figure F-3: Instrumentation hole collar(s) showing the extensometer casing and grout tube being secured by wooden wedges both before (left) and after grouting (right).

The instrumentation hole was not drilled from the 24L haulage drift before the drill was mobilized to the sublevel 1 sill to begin the installation of ground support. As a result, the initial design was modified to drill the instrumentation hole from the sublevel 1 sill to breakthrough on in the 24L sill. Installation and grouting of the extensometer were also completed from the sublevel 1 sill. Since data collection would occur from the 24L haulage drift, the extensometer had to be installed in reverse. The extensometer readout connector was inserted into the instrumentation hole followed by the head and finally the extensometer anchors. The result was that anchor one of the extensometer was located just below the drillhole collar in the sublevel 1 sill and the connector for taking readings was accessible from the 24L haulage drift.

After the extensometer was oriented correctly in the instrumentation hole, the construction crew plugged the toe of the instrumentation hole with rags while standing in the 24L haulage drift. After the instrumentation hole was plugged approximately a third of the instrumentation hole length was filled with grout and allowed time to set to form a secondary plug that would support the weight of the remainder of the grout column before filling the remainder of the instrumentation hole.

Over the time that the 24L 411 Alimak stope was being mined three instances of cable damage occurred. The first two instances occurred in the 24L sill when the cable was pinched between the sill wall and the bucket of heavy equipment during stope mucking (Figure F-4). One of the instances was noted during a data collection trip and the other was reported by the equipment operator. Following both instances, site electricians repaired the damage cable using butt splicing and the location of the cable was changed to protect against future contact.

Following the second instance of cable damage, the position of the cable was altered more dramatically and no additional damage occurred during mucking. Both of the damage events occurred prior to undercutting of the extensometer and are not believed to have influenced the integrity of the data collected by extensometer SASK-M0712-1. The third instance of cable damage occurred in the 17L sill where the extensometer cable was cut and the datalogger placed on the floor of the crosscut. Fortunately, the stope had been fully excavated by this point and the damage had no impact on the data collection program.

Figure F-4: Cable damage noted on 13-July, 2017 (left) and 20-August, 2017 (right) to the lead wire of the extensometer on 24L.

Seabee Gold Operation's Santoy 28-30L Longhole Stope

Prior to installation of the extensometer SBGO-M0617-3 in exploration drillhole SUG-14-027 to monitor the Santoy 28-30L stope, the drillhole was probed using combined lengths of ¾" grout tube. Due to the depth of the hanging wall contact, the available borehole camera could not be used to confirm the installation depth which was calculated based upon the stope's reserve solid. The extensometer was also uncoiled in the diamond drill chamber and a tape measure was attached to the lead wire PVC using electrical tape. During uncoiling and attachment of the measuring tape, a coil in the lead wire did not straighten cleanly resulting in a kink forming in the PVC around the lead wire. The kinked PVC was straightened by hand and then reinforced using metal strips and electrical tape as shown in Figure F-5.

Figure F-5: Image showing the reinforcement of a bent portion of the extensometer casing using steel strips and electrical tape.

The supplier instructions state that the instrumentation drillhole have a minimum diameter of 50 mm (Mine Design Technologies, 2017), which equates to a BQ or larger size hole (Canuck Drilling Systems, 2017). The exploration drillholes in the 27L DDCH had a diameter of just under 50 mm (Figure F-6), which equates to an AQ size hole. As a result, it was not possible to install the extensometer using the typical configuration of affixing a grout tube along the length of the extensometer to allow toe grouting. Figure F-7 shows an attempt to insert the grout tube and extensometer anchor at the same time. Although the grout tube would not fit into the drillhole when attached to the extensometer anchor, it was noted that the grout tube and extensometer lead wire PVC segments could be inserted together.

Figure F-6: Image showing the dimension of the exploration drillholes.

Figure F-7: Image of an attempt to insert a grout tube affixed beside the extensometer anchor into an exploration drillhole.

Due to the small exploration drillhole diameter the extensometer was initially inserted into the drillhole on its own. Exploration drillhole SUG-14-027 plunged gently at an angle of -5 degrees and installation stalled at a depth of 80 metres. Initially the extensometer could be inserted deeper into the drillhole following a delay in the installation to allow the instrument to straighten within the hole. The revised installation procedure was slow and ultimately failed to allow installation to a depth of more than 100 metres. A second revision was made to the installation method to attach the grout tube to the PVC lead wire case up-hole from the extensometer head using electrical tape (Figure F-8). As the extensometer and grout tube were inserted into the exploration drillhole, the PVC lead wire and grout tube were bonded together every five metres using electrical tape to provide additional stiffness when pushing on the PVC. This method proved successful and the extensometer was inserted to the target installation depth.

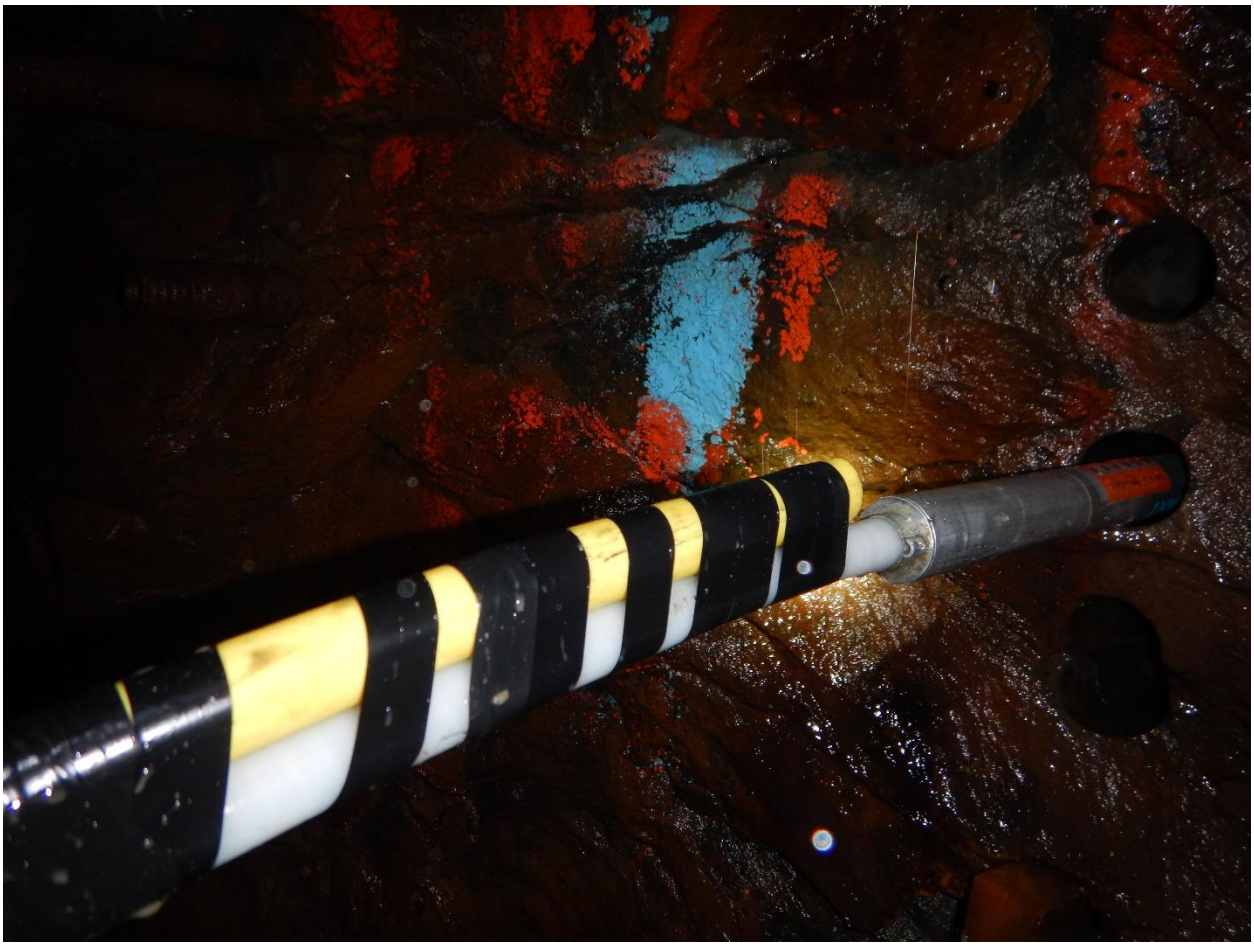

Figure F-8: Image showing the attachment of a grout tube to the lead wire casing.

Following insertion of the extensometer, grout was pumped into the exploration drillhole until there was grout return at surface. The grout water content ranged from 0.5 to 0.6 as multiple batches of grout were required to complete grouting of all the extensometers in the 27L DDCH. The grout water content was estimated using the glove based approach described by Hutchinson and Diederichs (1995).

Once all the extensometers were grouted in place the lead wires were connected to a datalogger located in the 27L DDCH.

Seabee Gold Operation's Stantoy 30-31L Longhole Stope

The same process was followed to prepare the extensometers for installation in the Santoy 30-31L longhole stope as was used for installing the extensometer to monitor the Santoy 28-30L longhole stope hanging wall.

Installation of extensometer SBGO-M0617-4 into drillhole SUG-14-029, which plunged at -15 degrees, was completed to the target depth without issue. During the installation of extensometer SBGO-M0617-5 into drillhole SUG-14-046, which plunged at -15 degrees, challenges arose in reaching the target installation depth. Similar to the approach used during the installation of extensometer SBGO-M0617-3 into drillhole SUG-14-027, grout tube was attached to the extensometer PVC casing which allowed the extensometer to be inserted to a depth of 140 m. At this point an obstruction was contacted that could not be cleared resulting in the installation of the extensometer two metres short of the target installation depth.

Both extensometers installed to monitor the Santoy 30-31L longhole stope hanging wall were grouted until there was grout return using the same process as the Santoy 28-30L longhole stope. After grouting was completed both extensometers were attached to a data logger as well.